A versatile scaffold:

The binding specificities of the Par3 PDZ domains mediate multiple interactions with polarity proteins.

Dissertation

der Mathematisch-Naturwissenschaftlichen Fakultät

der Eberhard Karls Universität Tübingen

zur Erlangung des Grades eines

Doktors der Naturwissenschaften

(Dr. rer. nat.)

vorgelegt von

Dipl. Biochem. Fabian Alexander Renschler

aus Sindelfingen

Tübingen 2018

Gedruckt mit der Genehmigung der Mathematisch-Naturwissenschaftlichen Fakultät der Eberhard Karls Universität Tübingen.

Tag der mündlichen Qualifikation:	23.07.2018
Dekan:	Prof. Dr. Wolfgang Rosenstiel
1. Berichterstatter:	Dr. Silke Wiesner
2. Berichterstatter:	Prof. Dr. Thilo Stehle

Summary

The asymmetric distribution of RNA, lipids and proteins is the basis of cell polarity. Polarized cells are vital for the organization of multicellular organism. Malfunctions in the processes generating cell polarity are linked with cancer and developmental defects. For cell polarization, the PAR complex, consisting of atypical protein kinase C, Par3 and Par6, is essential. Par3 is the central scaffold of the PAR complex. Par3 comprises of an N-terminal oligomerization domain, three Postsynaptic density protein-95, Disk large, Zonula occludens 1 (PDZ) domains, a kinase binding domain and an unstructured C-terminus. Its PDZ domains are the major protein-protein interaction domains. However, a detailed analysis of their specificities towards PDZ binding motifs (PBMs) occurring in Par3 interaction partners in the environment of cell polarity is missing.

Here, I present the structural basis of the interaction of Par3 with Par6. I identified a PBM in Par6 that is essential for Par3 interaction and interacts with the PDZ1 and PDZ3, but not the PDZ2 domains *in vitro*. Together with my coauthors, I showed that the Par6 PBM interacts with Par3 via a canonical PDZ:PBM interaction and functions together with the Par6 PDZ domain in Par6 localization *in vivo*.

In addition, I investigated the specificities of the individual Par3 PDZ domains for cell polarity proteins. My analysis revealed a unique binding profile for the *dm*Par3 PDZ1 and PDZ2 domains, while the binding profile of the *dm*Par3 PDZ3 domain is very promiscuous and overlaps with the specificities of the other two Par3 PDZ domains. These overlapping specificities enable Par3 to mediate multivalent interactions and thereby enable Par3 to form large protein networks with many different cell polarity proteins.

In a third project, I discovered a hitherto unknown short motif N-terminal of the third PDZ domain of *dm*Par3, denoted FID-motif. I was able to show that the FID-motif folds back onto the *dm*Par3 PDZ3 domain in close vicinity of the PBM binding groove thereby reducing the affinities of the PDZ3 domain towards various PBMs in polarity proteins. These reductions in affinity prevent a subset of the previous identified PDZ3 ligands to interact with the PDZ3 domain. Hence, the FID-motif seems to fine-tune the recruitment of PBM-carrying polarity proteins via the *dm*Par3 PDZ3 domain.

The detailed analyses presented in this thesis provide important insights into the individual roles of the Par3 PDZ domains in the assembly of polarity protein complexes. I present new clues in regard of functional redundancies within the Par3 PDZ module and provide the further evidence for Par3 acting as a central scaffold of polarity protein networks. Therefore, the function of the Par3 protein during establishment, maintenance and disruption of cell polarity during development and the related process of cancer metastasis can be understood in greater detail.

Zusammenfassung

Die asymmetrische Verteilung von RNS, Lipiden und Proteinen ist die Grundlage für die Polarität von Zellen. Die Zellpolarität ist essentiell für die Organisation multizellulärer Organismen. Fehler in den Vorgängen, die der Polarisation von Zellen zugrunde liegen, stehen in Verbindung mit Krebs und Entwicklungsstörungen. Für die Zellpolarität ist der PAR-Komplex, bestehend aus der atypischen Proteinkinase C, Par3 und Par6, essentiell. Hierbei ist Par3 das zentrale Gerüstprotein des PAR-Komplexes und besteht aus einer Oligomerisierungsdomäne am Aminoende, drei Postsynaptic density protein-95, Disk large, Zonula occludens 1 (PDZ) Domänen, einer Kinasebindedomäne und einem unstrukturiertem Carboxylende. Die drei PDZ-Domänen sind die wichtigsten Proteininteraktionsdomänen von Par3. Es fehlt jedoch eine detaillierte Analyse ihrer Spezifitäten in Bezug auf PDZ-Bindungsmotiven (PBM) von Par3 Interaktionspartner, die im Kontext der Zellpolarisation vorkommen.

Ich stelle hier die strukturelle Grundlage der Interaktion von Par3 und Par6 vor. Ich habe ein PBM, das essentiell für die Interaktion mit Par3 ist, in Par6 identifiziert. Das Par6 PBM interagiert mit der ersten und dritten Par3 PDZ-Domäne *in vitro*, wohingegen es nicht mit der PDZ2-Domäne interagiert. Zusammen mit meinen Koautoren konnte ich zeigen, dass das Par6 PBM mit Par3 mittels einer kanonischen PDZ:PBM-Bindung interagiert und dass das Par6 PBM zusammen mit der Par6 PDZ-Domäne *in vivo* eine Rolle bei der Par6-Lokalisation spielt.

Des Weiteren führte ich Untersuchungen über die Spezifitäten der einzelnen Par3 PDZ-Domänen im Hinblick auf die PBM von Zellpolaritätsproteinen durch. Meine Analyse ergab eindeutige Bindeprofile für die *dm*Par3 PDZ2- und PDZ3-Domänen, wohingegen das Bindeprofil der *dm*Par3 PDZ3-Domäne sehr promisk war und sich mit den Spezifitäten der anderen beiden Par3 PDZ-Domänen überschnitt. Diese Überschneidungen ermöglichen es Par3 multivalente Interaktionen mit vielen verschiedenen Zellpolaritätsproteinen ein zu gehen. Dadurch wird es Par3 gestattet weitreichende Proteinnetzwerke mit vielen unterschiedlichen Zellpolaritätsproteinen zu formen.

Während eines dritten Forschungsprojektes habe ich ein bis dahin unbekanntes, kurzes Motiv, als FID-Motiv benannt, am Aminoende der dritten Par3 PDZ-Domäne entdeckt. Ich konnte zeigen, dass sich das FID-Motiv auf die *dm*Par3 PDZ3-Domäne zurück faltet und dadurch die Affinitäten der PDZ3-Domäne für die PBM einiger Zellpolaritätsproteine reduziert. Diese Verringerung der Affinitäten hindert einige der zuvor identifizierten PDZ3-Liganden an der Interaktion mit der PDZ3-Domäne. Daher scheint das FID-Motiv ein Feinregler der PBM-vermittelten Rekrutierung von Zellpolaritätsproteinen durch die *dm*Par3 PDZ3-Domäne zu sein.

Die detaillierte Studie der Bindeeigenschaften der *dm*Par3 PDZ-Domänen, die in dieser Dissertation vorgestellt werden, liefert wichtige Einblicke in die Rollen der einzelnen Par3 PDZ-Domänen beim

Aufbau von Polaritätsproteinkomplexen. Ich stelle neue Hinweise in Bezug auf die funktionale Redundanz innerhalb des Par3 PDZ-Moduls vor und bringe weitere Beweise für die These, dass Par3 das zentrale Gerüstprotein von Polaritätsproteinkomplexen ist, dar. Infolgedessen kann die Funktion des Par3-Proteins bei der Etablierung, dem Aufrechterhalten und der Auflösung der Zellpolarität während der Embryonalentwicklung und der damit verwandten Metastasenbildung bei Krebserkrankungen besser verstanden werden.

Table of Contents

List of abbreviations and symbols

Table 1: Abbreviations and symbols used in this thesis.

abbreviation	meaning
aa	amino acid
ABR	Actin binding region
AJ	adherens junctions
aPKC	atypical protein kinase C
Arm	Armadillo
Baz	Bazooka
BMRB	Biological Magnetic Resonance Bank
C. elegans	*Caenorhabditis elegans*
CA repeats	Cadherin repeats
CC	coiled coil
Cdc42	Cell division control protein 42 homolog
Cno	Canoe
Crb	Crumbs
CRIB	Cdc42/Rac interactive binding domain
CSPs	chemical shift perturbations
D. melanogaster	*Drosophila melanogaster*
Dlg	Discs large
Dlt	Discs lost
dm	*Drosophila melanogaster*
E. coli	*Escherichia coli*
Ed	Echinoid
EGF	epidermal growth factor
EMT	epithelial-mesenchymal transition
ϕ	hydophobic amino acid
FBD	4.1 protein, Ezrin, Radixin and Moesin binding domain
FHA	Forkhead associated domain
FID	free induction decay
GB1	protein G B1 domain
GF	gel filtration
GSH	Glutathione
GST	Glutathione-S-Transferase
Gu-Kinase	Guanylate kinase
Gαi	G protein αi subunit
h	hours
HA	hemaglutinin
hs	*Homo sapiens*
IEX	ion exchange
Ig	Immunoglobulin domain
INEPT	Insensitive nuclei enhanced by polarization transfer
Insc	Inscutable
kb	Kilobases/ 1000 nt

KBD	Kinase binding domain
Khc-73	Kinesin heavy chain 73
L27	LIN2/7 binding
LamG	Laminin G domain
Lgl	Lethal giant larvae
LIM	Zinc-binding domain present in Lin-11, Isl-1, Mec-3
LRR	Leucine-rich repeats
MET	mesenchymal-epithelial transition
min	minutes
mm	*Mus musculus*
MW	molecular weight
n.d.	not detectable
Ni-NTA	Ni^{2+}-nitrilotriacetic acid
NMR	nuclear magnetic resonance
nt	nucleotide
NTD	N-terminal domain
o/n	over night
OD	oligomerization domain
Par	partition defective
PB1	Phox and Bem1 domain
PBM	PDZ binding motif
PDZ	Postsynaptic density protein-95, Disk large, Zonula occludens 1
Pins	Partner of Inscutable
Pyd	Polychaetoid
RA	Ras association (RalGDS/AF-6) domain
RF	restriction free
Scrib	Scribble
SDS-PAGE	sodium dodecyl sulfate polyacrylamide gel electrophoresis
SH3	Src homology 3 domain
Shg	Shotgun
SJ	septate junctions
Smash	Smallish
Stan	Starry night
Std	Stardust
TEV	tobacco etch virus
TJ	tight junctions
TM	transmembrane domain
V	Volt
VH	Vinculin homology
x	any amino acid
ZU5	Domain present in ZO-1 and Unc5-like netrin receptors
α-cat	α-catenin

Table of Figures

List of Tables

1. Introduction

1.1 Cell polarity

Multicellular organisms contain many different cell types that display an asymmetric distribution of their components that is crucial for their cellular function. These asymmetric distributions of proteins, RNAs and lipids give rise to cell polarity. These asymmetries inside cells are important in a huge variety of biological processes. For instance, during development, asymmetric cell division can give rise to distinct daughter and mother cells, each with unique cell fates (Figure 1A). Moreover, migratory cells, neurons as well as epithelia cells also display asymmetries (Figure 1A). Not surprisingly, the proper asymmetric distribution of the involved factors has to be established and maintained and under certain circumstances be reverted in a tightly controlled fashion to avoid detrimental outcomes such as cancer (Figure 1B) (Nelson 2003; Tepass 2012).

All these examples of polarized cells are the basis of tissues and organs with highly specialized functions in multicellular organisms. However, to fulfill these specific functions properly, the organization of the polarized cells must be maintained. Moreover, this tissues organization relies on tissue compartments which are physically separated and allow at the same time communication as well as transport between neighboring compartments. Usually, epithelia are found at tissue borders which satisfy all these needs. In addition, epithelia are also present at the boundaries of the body lining the skin and body cavities. Epithelia are sheets of polarized cells and separate different compartments of an organism such as organs, body cavities or the outside. Hence, epithelia face two sides, one inner side and one outer side. The apical membrane of epithelia cells face the outside whereas the basolateral membrane faces the inside which is defined by the extracellular matrix (Figure 1A). In addition, epithelia cells are connected with each other by cell junctions. Hence, the cell-cell contacts define a third domain of the membrane called the lateral membrane. Each membrane domain is defined by the presence of characteristic proteins and lipids.

Yet, epithelia are no static assemblies but are dynamic. They are able to adapt to changes in their environment and to change their environment. For example, during development and wound healing, the transition from stationary epithelia cells to mobile mesenchymal cells (epithelial-mesenchymal transition, EMT) and vice versa (mesenchymal-epithelial transition, MET) are crucial events (Figure 1B). The first hallmark event of EMT is the loss of tight junctions (TJ) followed by the dissolution of adherens junctions (AJ) (Figure 1B). Of note, MET begins with the assembly of spot AJ followed by maturation of those cell contacts as well as assembly of TJ. Noteworthy, the same processes as in EMT and MET are involved in cancer metastasis (Muthuswamy & Xue 2012).

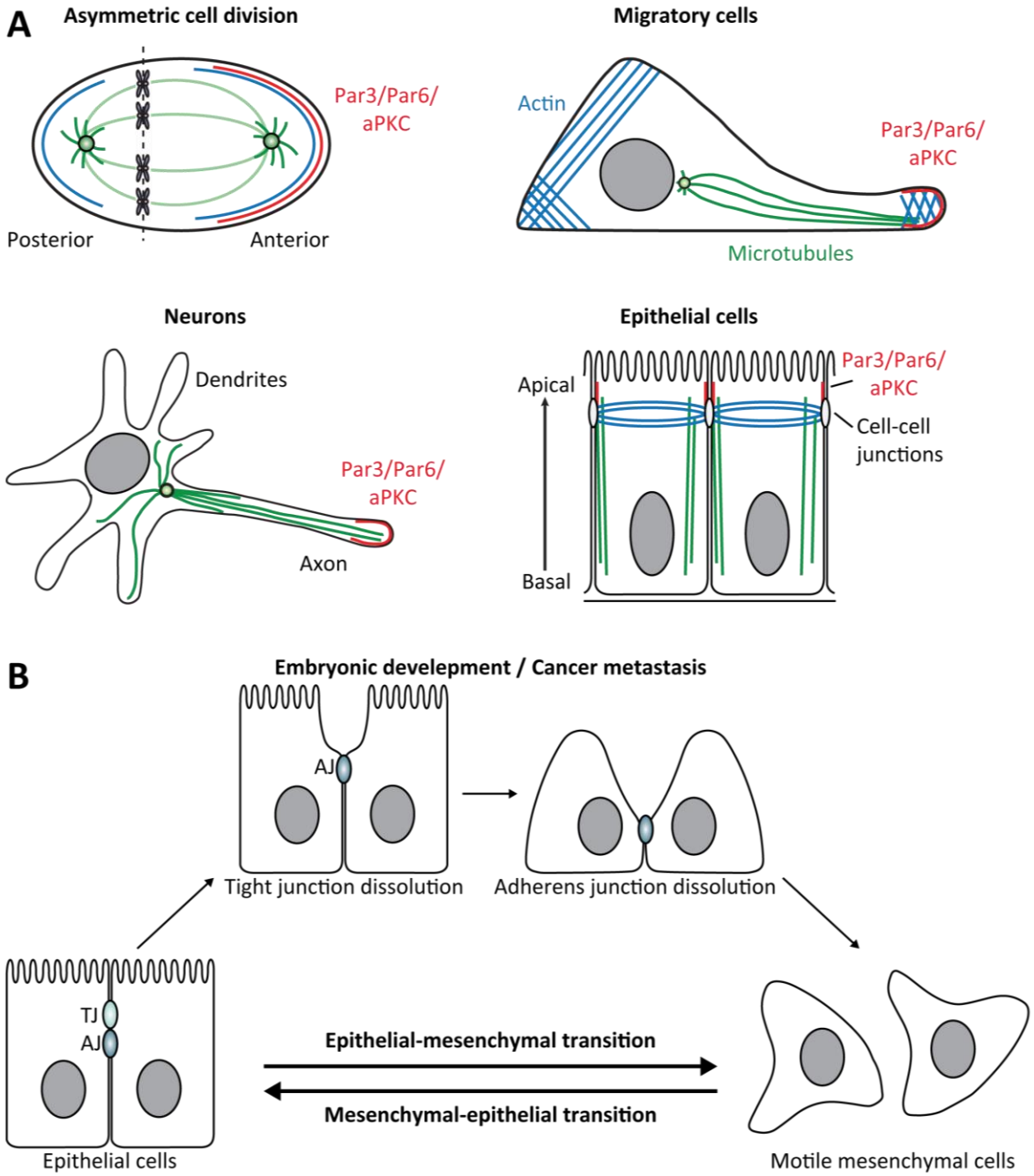

Figure 1: Different examples of polarized cells and remodeling of cell polarity during development and cancer metastasis. (A) Asymmetries of cellular components are crucial for the function of various cell types and cellular functions. As an example, the distribution of the cell polarity proteins Par3, Par3 and aPKC as well as cytoskeletal elements such as actin fibrils and microtubules are shown in red, blue and green, respectively, to highlight the asymmetric distributions of cellular components during asymmetric cell division, in migratory cells, neurons and epithelial cells. **(B)** Cell polarity is not a static but a dynamic process. Epithelial-mesenchymal transition is initiated by tight junction dissolution followed by adherens junction dissolution (top). Mesenchymal-epithelial transition occurs in reverse that is assembly of adherens junctions followed by tight junction assembly.

It is thus of utmost importance to understand the molecular mechanisms underlying the establishment and maintenance of cell polarity.

1.2 Invertebrate epithelia as a model system to study cell polarity

1.2.1 Establishment and maintenance of cell polarity in *Drosophila* epithelia

The first genes connected with cell polarity were identified in screens for mutants with affected asymmetric cell division in the zygote of *C. elegans*. These genes as well as their expressed proteins were named after the observed PARtition-defective phenotype (Kemphues et al. 1988; Watts et al. 1996; Tabuse et al. 1998). Noteworthy, all eight proteins identified in *C. elegans* are conserved in eukaryotes with the exception of Par2 (Macara 2004). Additionally, the pathways by which epithelial polarity is established and maintained is conserved from worm to humans (Macara 2004; Elsum et al. 2012). However, the organization of cell-cell junctions differs between invertebrates and vertebrates. In vertebrates, the tight junctions localize apically to the adherens junctions whereas in flies, the adherens junctions localize apical to the septate junctions (Figure 2) which fulfill similar roles as the vertebrate tight junctions (Macara 2004).

During the formation of epithelia, Par3 localization to the apical part of the cell is the landmark of the initial stages of epitheliogenesis. First, Par3 localizes to early spot-like cell-cell contacts were it serves as transient recruitment hub for Par6 and atypical protein kinase C (aPKC), to assemble the PAR complex. Additionally, Par3 serves as an assembly hub of the Crumbs complex, interacting with Crumbs (Crb) and Stardust (Sdt) (Figure 2A and Figure 3) (Tepass 2012; Lang & Munro 2017).

After the formation of epithelia and maturation of the cell-cell contacts, Par3 is excluded from the apical domain by aPKC dependent phosphorylation and localizes to the adherens junction belt whereas the Par6/aPKC module associates with the Crumbs complex (Tepass 2012; Lang & Munro 2017). The Crumbs complex defines the apical domain of mature epithelia cell and consists of the transmembrane protein Crb, the scaffold protein disc-lost (Dlt) and the Guanylate kinase Std (Figure 2A and Figure 3) (Tepass 2012). However, a fraction of Par6/aPKC still interacts with Par3 but aPKC is inactivated by the Par3 KBD (Lang & Munro 2017). Of note, in vertebrate epithelia Par3 is not associated with the adherens junctions but localizes to the more apical tight junctions (Macara 2004).

In mature epithelia, the basolateral sides are enriched with the kinase Par1 as well as members of the Scribble complex comprising of the scaffold proteins Scribble (Scrib), Lethal giant larvae (Lgl) and the guanylate kinase Disc large (Dlg) (Figure 2 and Figure 3). The Scribble complex is localized with the septate junctions in flies (Figure 2) and basal to adherens junctions in vertebrates (Macara 2004; Elsum et al. 2012). Par1 phosphorylates apical polarity proteins such as Par3. Next, Par5, a 14-3-3 protein, binds those phosphorylated proteins and facilitates their exclusion from the basolateral domain (Macara 2004; McCaffrey & Macara 2009) thereby maintaining their asymmetric distribution. Moreover, the Scribble complex, acts antagonistic to the Par complex via a Lgl mediated

inhibition of aPKC thereby inactivating aPKC at the basolateral domain (Elsum et al. 2012). Of note, aPKC is able to phosphorylate Par1, thereby priming Par1 for exclusion from the apical domain via a Par5 mediated mechanism (Goldstein & Macara 2007) thereby generating a mutual exclusion mechanisms between aPKC and Par1.

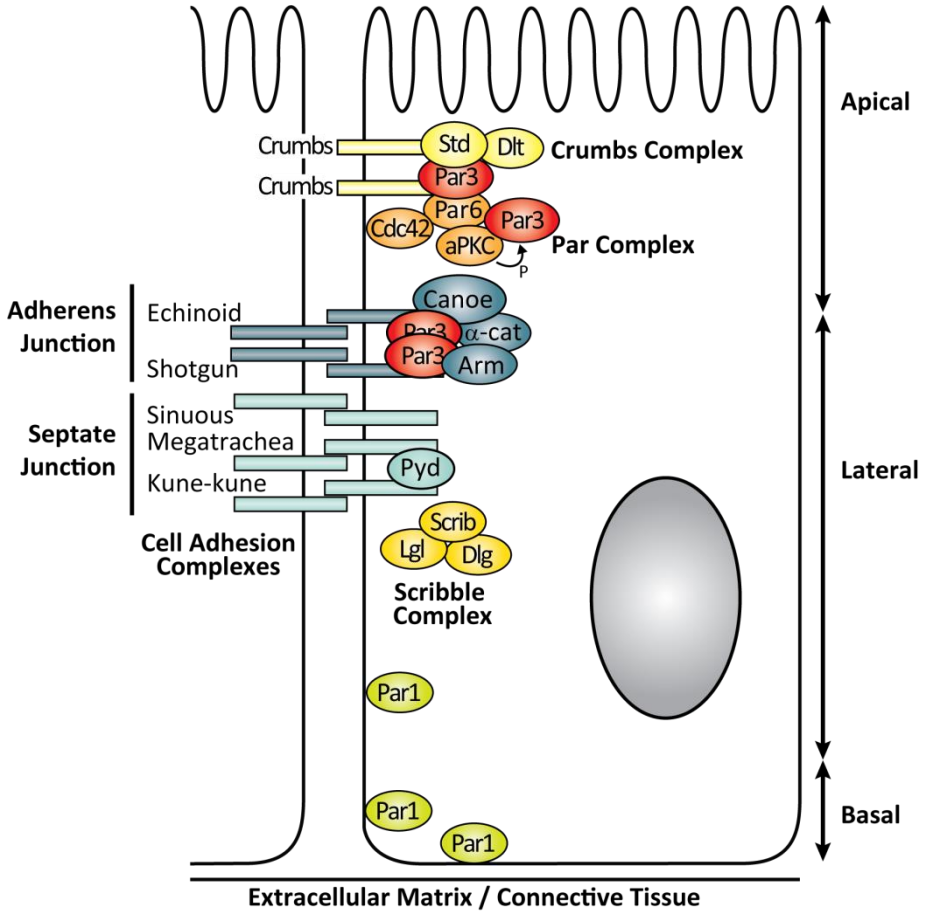

Figure 2: The PAR complex in *Drosophila* epithelia cells. The PAR complex localizes subapically in mature invertebrate epithelia cells. Std, Stardust; Dlt, Discs-lost; Cdc42, Cell division control protein 42; Par3, Partitioning defective 3; aPKC, atypical protein kinase C; α-cat, α-catenin; Arm, Armadillo; Pyd, Polychaetoid; Scrib, Scribble; Lgl, Lethal giant larvae; Dlg, Disc-large; Par1, Partitioning defective 1.

Interestingly, flies can maintain cell polarity in mature epithelia by the presence of either the Crumbs complex or Par3 (Tanentzapf & Tepass 2003; Fletcher et al. 2012), indicating a high degree of complementary in the functions of the PAR and Crumbs complexes. Thereby this functional redundancy convolutes the analysis of the individual functions of those complexes in mature epithelia. Nevertheless, the *Drosophila* embryo and its epithelia offer partial solutions for this problem. Since Std is expresses at earlier stages of *Drosophila* embryogenesis compared to Crb (Krahn, Bückers, et al. 2010; Sen et al. 2015; Renschler et al. 2018) whereas there is a strong maternal expression of Par3 (Wieschaus & Noell 1986; Müller & Wieschaus 1996; Kuchinke et al. 1998), it is feasible to partially dissect the individual contributions.

1.2.2 Polarity proteins and the PAR complex

As in all biological processes, protein complexes play a vital role in the organization of cell polarity. The PAR complex serves as central scaffold involved in cell polarity and consists of Par3, Par6 and aPKC (Macara 2004; McCaffrey & Macara 2009; Lang & Munro 2017). While a single set of genes encodes each of the proteins associated with the PAR complex in invertebrates, the number of genes has been expanded in vertebrates. Hence, two Par3 proteins (Par3 and Par3L), three Par6 proteins (Par6α, Par6β and Par6γ) as well as two aPKC proteins (aPKCλ/ι and aPKCζ) are present in higher eukaryotes (Noda et al. 2001; Gao et al. 2002; Suzuki et al. 2003).

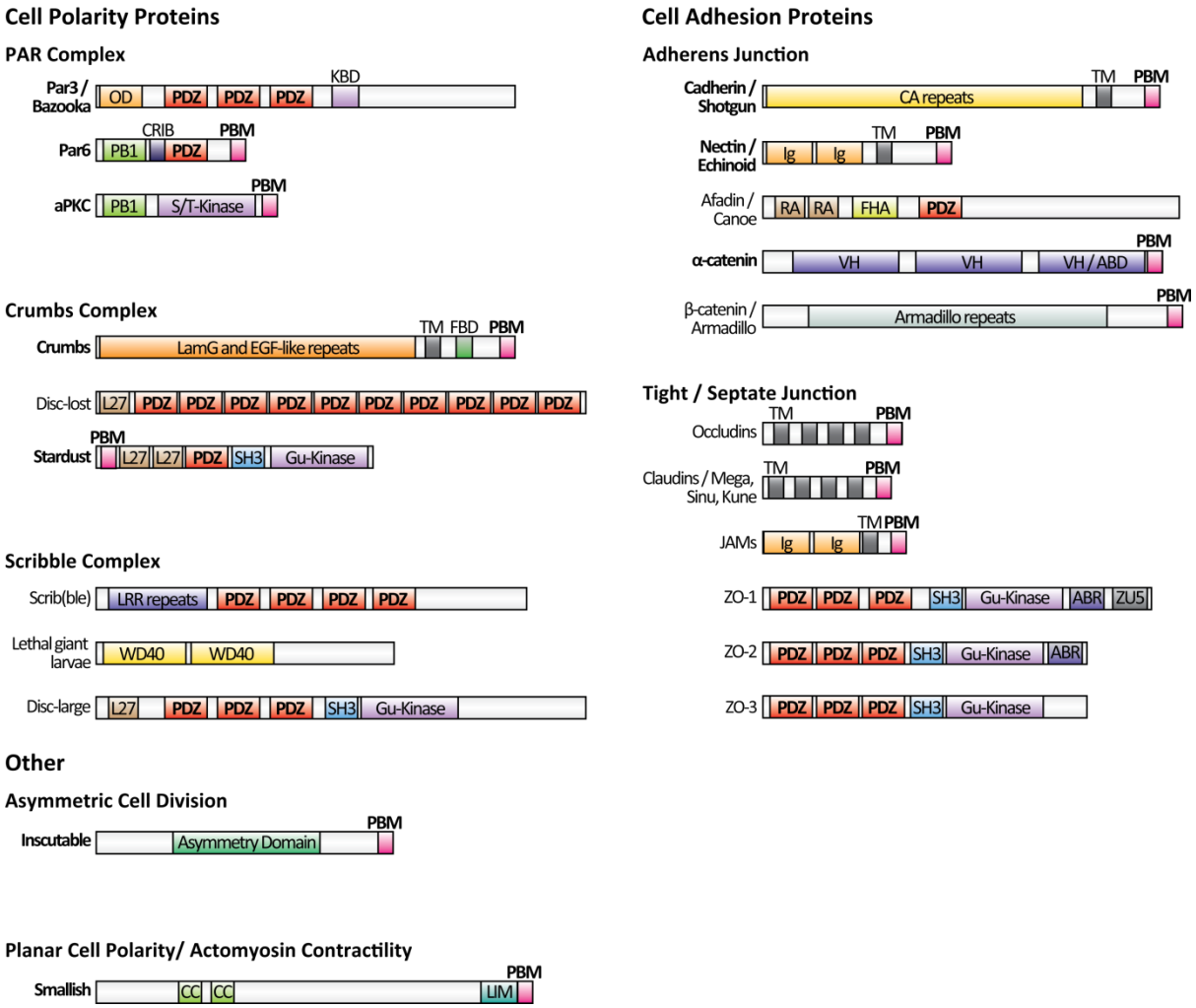

Figure 3: Domain organization of polarity proteins. Known Par3 PDZ domain ligands used in this study are highlighted in bold. OD, oligomerization domain; PDZ, Postsynaptic density protein-95, Disk large, Zonula occludens 1; KBD, kinase binding domain; PB1, Phox and Bem1 domain; CRIB, Cdc42/Rac interactive binding domain; PBM, PDZ binding motif; LamG, Laminin G; EGF, epidermal growth factor; TM, transmembrane domain; FBD, Ferm binding domain; L27, LIN2/7 binding domain; SH3, Src-homology-3 domain; Gu-Kinase, Guanylate kinase; LRR, Leucine-rich repeats; CC, coiled coil; LIM, Zinc-binding domain present in Lin-11, Isl-1, Mec-3; CA repeats, Cadherin repeats; Ig, Immunoglobulin domain; RA, Ras association (RalGDS/AF-6) domain; FHA, Forkhead associated domain; VH, Vinculin homology domain; ABR, actin binding region; ZU5, Domain present in ZO-1 and Unc5-like netrin receptors

Par3 or Bazooka (Baz) in *Drosophila* is the main scaffold protein inside the PAR complex. It consists of an N-terminal oligomerization domain (OD), followed by three Postsynaptic density protein-95, Disk large, Zonula occludens 1 (PDZ) domains. Additionally, a kinase binding domain (KBD) interacting with aPKC is present in its large unstructured C-terminus (Figure 3 and Figure 4) (Tepass 2012; Lang & Munro 2017). Of note, a region in C-terminal vicinity of the KBD was reported to interact with phosphatidylinositol phosphate (PIP) (Krahn, Klopfenstein, et al. 2010).

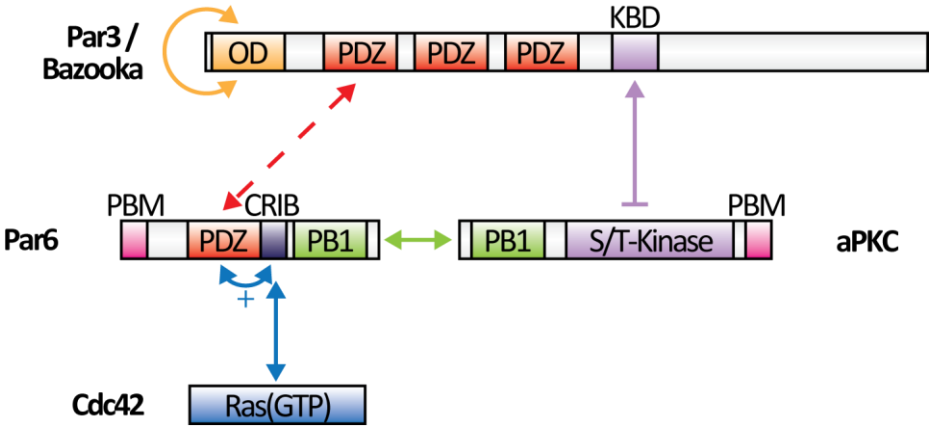

Figure 4: The interactions inside the PAR complex. The Par complex consists of Par3, Par6 and aPKC. Par3 oligomerizes with its N-terminal oligomerization domain (Zhang et al. 2013). It is suggested that the Par3 PDZ1 domain and the Par6 PDZ domain interact with each other (Joberty et al. 2000; Lin et al. 2000; Li et al. 2010). Par6 and aPKC dimerize via their N-terminal PB1 domains (Hirano et al. 2005). The S/T-kinase domain of aPKC is inhibited by the Par3 KBD. At the same time, the Par3 KBD can be phosphorylated by aPKC releasing aPKC inhibition (Wang et al. 2012; Soriano et al. 2016). The small Ras-like GTPase Cdc42 can bind in its GTP-bound state to the Par6 CRIB motif which results in an affinity increase of the Par6 PDZ domain for some of its ligands (Garrard et al. 2003; Peterson et al. 2004; Whitney et al. 2011; Whitney et al. 2016). Domain abbreviations according to Figure 3.

Currently, three functions are associated with Par3 (Harris 2017). First, Par3 is involved in adherens junction assembly during epithelialization (Figure 2). Next, Par3 sequesters the Par6/aPKC module in an inhibited state at the apical-basolateral border (Figure 2). Last, in asymmetric cell division, Par3 acts as assembly site at the cell cortex for the Pins (Partner of Inscutable) complex (Figure 5) (Culurgioni & Mapelli 2013). For example, in asymmetric cell division of *Drosophila* neuroblasts, Pins associates with G protein α i subunits (Gαi) at the apical site. The Gαi subunits are membrane anchored by myristoyl groups and thus recruit Pins to the membrane. In addition, Pins interacts with Inscutable (Insc) via the Insc asymmetry domain (Figure 3) (Culurgioni & Mapelli 2013). With this interaction, Insc links Pins to Par3. However, the details of the Par3:Insc interaction are not well understood (Culurgioni & Mapelli 2013). Finally, Pins orients the mitotic spindle via Discs large (Dlg) mediated interaction with the Kinesin heavy chain 73 motor protein (Khc-73) (Figure 5) (Lu & Johnston 2013; Culurgioni & Mapelli 2013).

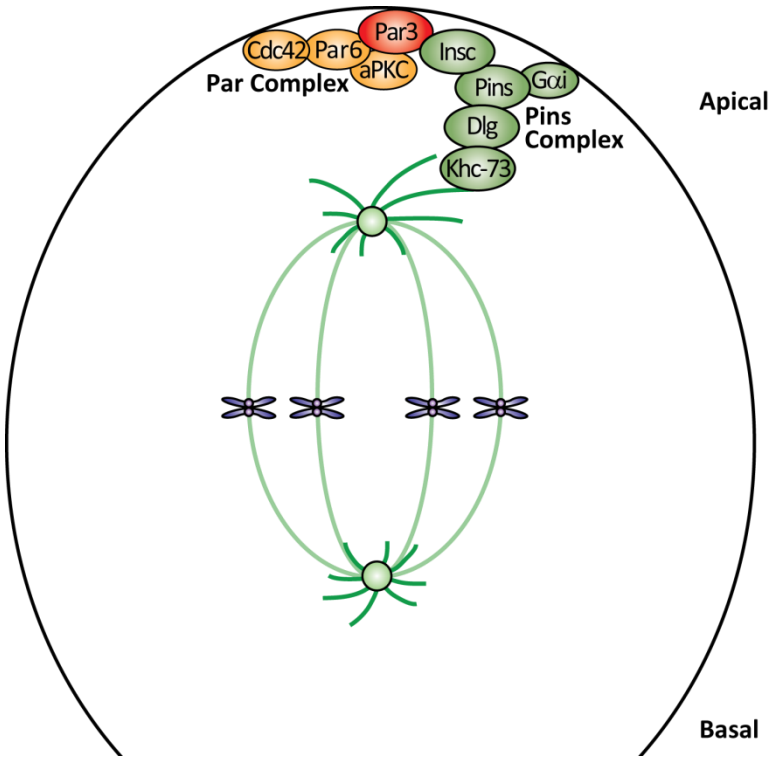

Figure 5: The PAR complex localizes the Pins complex to the apical site during asymmetric cell division of *Drosophila* neuroblast cells. Cdc42, Cell division control protein 42; Par3, Partitioning defective 3; aPKC, atypical protein kinase C; Dlg, Disc-large; Insc, Inscutable; Pins, Partner of Inscutable; Dlg, Discs large; Gαi, G protein αi subunit; Khc-73, Kinesin heavy chain 73.

In recent publications, it was shown that all these roles rely on the oligomerization of Par3 into large clusters (Harris 2017; Rodriguez et al. 2017; Dickinson et al. 2017; Wang et al. 2017). This clustering is mediated by the N-terminal OD domain which is able to form large fibrillar structures *in vitro* (Zhang et al. 2013). Yet, inhibition of Par3 clustering severely inhibits proper Par3 function (Harris 2017). In addition, deletion of other domains also impairs specific Par3 functions. For instance, the inhibition of aPKC is mediated by regions in direct vicinity of the Par3 KBD (Wang et al. 2012; Soriano et al. 2016). Whereas the three PDZ domains have been shown to have specialized functions (McKinley et al. 2012). In short, this study addressed the effects of deletions of single *dm*Par3 domains or multiple domain combinations on the Par3 function and analyzed the resulting phenotype with fluorescence microscopy. With this analysis, the authors concluded that PDZ1 and PDZ3 are important for *dm*Par3 recruitment to the apical domain whereas downstream effects on epithelial structure are mediated by PDZ2. In addition, PDZ1 increases *dm*Par3 turnover thereby decreasing Par3 levels. However, Par3 oligomerization is important for all those functions. Therefore, Par3 clustering has to act together with additional Par3 domains to fulfill all Par3 functions. Of note, the most interaction partners of Par3 are recruited via its PDZ domains. A

detailed description of PDZ domains and especially the ligands of the Par3 PDZ domains can be found in the following paragraphs.

Par6 acts as an adapter between Par3 and aPKC. Par6 heterodimerizes with its N-terminal Phox and Bem1 domain (PB1) domain (Figure 4) with the N-terminal PB1 domain of aPKC (Hirano et al. 2005), generating the Par6/aPKC module. Besides the PB1 domain, Par6 comprises a PDZ domain with a Cdc42/Rac interactive binding domain (CRIB) domain directly N-terminal to its PDZ domain (Figure 3 and Figure 4). Interestingly, the Par6 PDZ domain partially unfolds to adopt high affinity state (Whitney et al. 2013). This high affinity state is induced by the interaction of the small GTPase Cell division control protein 42 (Cdc42) in its GTP bound state with the CRIB domain directly N-terminal of the Par6 PDZ domain (Garrard et al. 2003; Peterson et al. 2004). Thereby, Cdc42 enhances the affinity of the Par6 PDZ domain for the Crb PBM (Whitney et al. 2016) as well as for synthetic ligands (Whitney et al. 2011) (Figure 4). The Cdc42 induced affinity switch probably results in the localization of the Par6/aPKC module with the Crumbs complex (Figure 2 and Figure 4). Previous studies reported the Par3:Par6 interaction to be dependent on the PDZ1 domain of Par3 and the PDZ domain of Par6 (Joberty et al. 2000; Lin et al. 2000; Li et al. 2010) (Figure 4). Conversely, all these reports disputed whether or not the interaction relies additionally on the Par6 Crib-motif in front its PDZ domain. Besides, the *in vivo* relevance was not established without doubt (Li et al. 2010) and aPKC has been reported as linker, proposing an indirect Par3:Par6 interaction (Suzuki et al. 2001; Nagai-Tamai et al. 2002).

The key enzyme of the PAR complex is the serine/threonine atypical protein kinase C (aPKC). It is an atypical member of the protein kinase C family since its N-terminal regulatory domain is truncated and a PB1 domain is present at its N-terminus (Figure 3 and Figure 4) (Drummond & Prehoda 2016). In addition, the kinase domain of aPKC has only two out of three conserved phosphorylation activation sites. Of note, a PDZ binding motif (PBM) is present at its C-terminus (Drummond & Prehoda 2016). Besides the Par3 KBD, aPKC substrates are involved in a variety of signaling pathways such as cell cycle control, cell fate decision via the Hedgehog pathway, tissue homeostasis via Wnt signaling or depolarization via JAK/Stat signaling (Drummond & Prehoda 2016). Of note, several aPKC substrates are phosphorylated in motifs associated with phospholipid interactions, such as the Par3 KBD, and are impaired from membrane binding upon phosphorylation (Drummond & Prehoda 2016; Soriano et al. 2016).

1.3 PDZ domains and PDZ binding motifs

1.3.1 PDZ domains interact with short peptide motifs

Many polarity proteins contain so-called Postsynaptic density protein-95, Disk large, Zonula occludens 1 (PDZ) domains (Figure 3). PDZ domains can be found in various signaling complexes in the animal kingdom (Ivarsson 2012) where they usually act as protein-protein interaction scaffolds. PDZ domains contain about 90 amino acids and fold into an antiparallel β-barrel with 5-6 β-strands and 1-2 α-helices (Luck et al. 2012; Ivarsson 2012; Ye & Zhang 2013) (Figure 6).

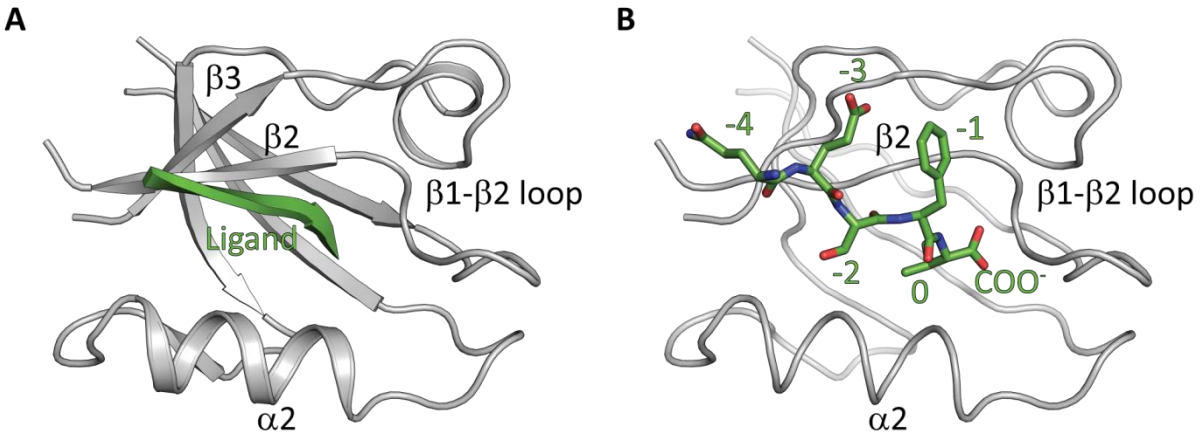

Figure 6: PDZ domain ligand recognition. (A) Cartoon representation of a canonical PDZ:PBM interaction based on the *dm*Par3 PDZ2:Insc PBM structure solved in this study (for details see Figure 29 and Table 32). The PBM augments the β-sheet consisting of the β2- and β3-strand. Together the α2-helix and the β2-strand form the PBM binding groove. The PDZ domain is depicted in grey and the PBM in green, respectively. **(B)** Representation of a canonical PDZ:PBM interaction. The PBM is depicted as green sticks to highlight the PBM classification based on the -2 residue (Lee & Zheng 2010; Ivarsson 2012). The PDZ domain is displayed as grey tube, otherwise as in **(A)**.

The two α-helices cap the open sites of the β-sheets. Canonical PDZ:ligand interaction are based on short motifs, called PDZ binding motifs (PBMs), at the C-terminus of the ligand protein. In a PDZ:PBM interaction, the PBM augments the PDZ β-sheet at the β2-strand (Figure 6). The carboxy terminus of the PBM interacts extensively with a highly conserved GXGL motif inside the loop between the β1- and β2-strands. This loop is therefore called the carboxy-binding loop. Since the last and third last residue of the PBM directly face towards the PDZ domain, the identity of those residues can be used to assign classes to the PBMs (Table 2) (Lee & Zheng 2010; Ivarsson 2012). Moreover, the residues of a PBM are numbered starting at the most C-terminal residue as position 0, the second most C-terminal as position -1, the third most C-terminal as position -2 and so on. Hence, class I PBMs have serine or threonine residues at their -2 position, class II PBMs have hydrophobic residues at position -2, whereas the -2 position of class III PBMs is acidic. Nonetheless, this classification scheme seems to suggest a strict selectivity of PDZ domains towards certain PBMs or ligand classes. Yet, it has been shown in mice, that the PDZ domain selectivity is not restricted to discrete classes, but evenly

distributed through the sequence space (Stiffler et al. 2007). Despite this fact, I will use this classification of PBMs into those three classes for clarity.

Table 2: PDZ ligand classes

PBM class	Consensus sequence
I	X-**T/S**-X-**φ**-COO$^-$
II	X- **φ** -X-**φ**-COO$^-$
III	X-**D/E**-X-**φ**-COO$^-$

X depicts any amino acid, φ depicts hydrophobic amino acids, (Lee & Zheng 2010; Ivarsson 2012)

Besides the canonical PDZ:PBM interaction, various other PDZ domain binding modes have been revealed (Luck et al. 2012; Ivarsson 2012; Ye & Zhang 2013). The most similar to the conventional PDZ:PBM β-sheet augmentation, are internal PBMs (Figure 7).

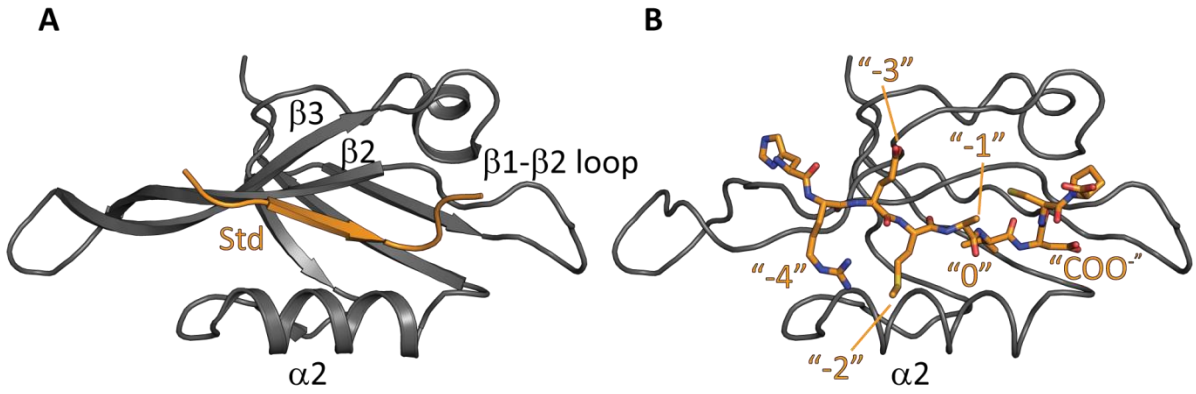

Figure 7: Interaction of internal PBMs with PDZ domains. (A) Cartoon representation of the interaction of the internal PBM of Stardust (Std) with the *dm*Par6 PDZ domain (Penkert et al. 2004) (PDB ID: 1x8s). The internal PBM augments the β-sheet consisting of the β2- and β3-strand. Together the α2-helix and the β2-strand form the PBM binding groove. The PDZ domain is depicted in dark grey and the internal PBM in orange, respectively. **(B)** Cartoon representation of the interaction of the internal PBM of Stardust (Std) with the *dm*Par6 PDZ domain. The PBM is depicted as orange sticks to highlight the mimic of the C-terminus by the aspartic acid side chain ("COO$^-$"). PBM positions in parenthesis indicate equivalent positions of C-terminal PBMs (Figure 6B) The PDZ domain is displayed as dark grey tube, otherwise as in **(A)**.

As suggested by their name, internal PBMs are not at the very C-terminal position of a protein. Nevertheless, they also interact with PDZ domains via a β-sheet augmentation. Here, internal PBMs mimic the C-terminal carboxyl group with an aspartic acid side chain (Ivarsson 2012). Additionally, they usually mitigate steric clashes with the carboxy-binding loop by formation of a β-hairpin of the internal PBM (Ivarsson 2012). Interestingly, some PDZ domains can interact with both canonical and internal PBMs. For example, a recent study (Merino-Gracia et al. 2016) has shown that the PDZ domain of neuronal Nitric Oxide Synthase can interact with classI, II and II ligands as well as internal ligands. Moreover, the Par6 PDZ is known to interact with canonical and internal PBMs of Crumbs (Whitney et al. 2016; Lemmers et al. 2004) and Stardust (Figure 7) (Penkert et al. 2004; Kempkens et al. 2006; Wang et al. 2004), respectively.

Besides the importance of the core PBM consisting of the four last amino acids, upstream residues have been shown to influence PDZ:PBM interactions. These interactions are occasionally found outside the PBM binding groove and are located in the β2-β3-loop or within extensions of the PDZ domain (Luck et al. 2012). Interestingly, the majority of the extended PBM:PDZ interactions are observed within PBM positions -7 and -4 (Luck et al. 2012). In rare cases such as the Par3 PDZ3 domain of rats and mice, the interaction between the PDZ domain and the PBM can extend to position -10. Most strikingly, these distal interactions observed in the rat Par3 PDZ3 domain with the class I PBM of VE-cadherin (Feng et al. 2008) as well as in the mouse Par3 PDZ3 domain with the class II PBM of the phosphatase PTEN (Tyler et al. 2010) seem to be important for the dual specificity of the rodent Par3 PDZ3 domain. Of note, phosphorylation sites are found in these upstream sequences and various examples exist where phosphorylation inside the extended PBM contributes to an increase or decrease in affinity (Luck et al. 2012). In addition, an elegant study by Amacher *et al.* could show that both, the presence of residues in the PBM which interact with the PDZ domain as well as the absence of negative modulators, that is residues lowering the PDZ:PBM affinity by repulsive interactions (e.g. electrostatic repulsion), are necessary for high affinity PDZ:PBM interactions (Amacher et al. 2014).

Beyond the recognition of short motifs, PDZ domains can form homo- and heterodimers (Ivarsson 2012; Ye & Zhang 2013). PDZ dimerization can occur in different modes, ranging from elaborated β-strand swap interactions (Figure 8A) to simple back to back dimerization (Figure 8B) (Ivarsson 2012). In general, PDZ dimers can have various functions such as providing addition interaction sites for ligands, stabilization of the PDZ domains or protein dimerization (Ivarsson 2012; Ye & Zhang 2013).

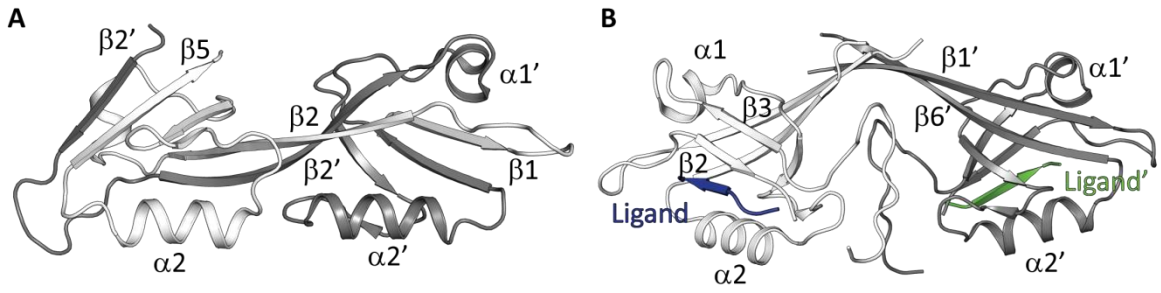

Figure 8: Examples of PDZ dimerization. (A) Cartoon representation of ZO-1 PDZ dimer (Fanning et al. 2007) (PDB ID: 2rcz) illustrating β-strand swap dimers. The individual PDZ domains are colored white and dark grey, respectively. **(B)** Cartoon representation of the Shank1 PDZ dimer in complex with the guanylate kinase associated protein (GKAP1a) PBM (Im et al. 2003) (pdb ID: 1q3p) illustrating back-to-back dimerization. The individual PDZ domains are colored white and dark grey, respectively. The bound ligands are colored in dark blue and green, respectively.

In addition to protein-protein interactions, PDZ domains also mediate protein-lipid interactions. Several different interaction modes between PDZ domains and phospholipids have been published

(Gallardo et al. 2010; Ivarsson 2012). These interactions are based on electrostatic membrane interactions, membrane penetration or specific binding to phosphoinositide head groups (Figure 9). In contrast to the conserved PBM binding groove, the lipid interaction surfaces are more diverse (Gallardo et al. 2010; Chen et al. 2012) and seem to be acquired convergent in the evolution of PDZ domains (Chen et al. 2012). For example, studies investigating the lipid-interactions of the second Par3 PDZ domain in rat revealed three distinct interaction surfaces interacting with lipids (Figure 9). A binding site for phosphoinositide head groups is present in close proximity of the carboxy-binding loop. In addition, residues next to the α1-helix can be inserted into the cell membrane. Moreover, the authors also proposed the presence of positively charged clusters responsible for membrane association (Wu et al. 2007). Of note, all residues reported are conserved between rat and fly (Wu et al. 2007). Worth mentioning, initial, systematic studies addressing the lipid binding properties of PDZ domains revealed that approximately 30-40% of PDZ domains are able to bind to various lipids including phosphoinositides (Chen et al. 2012). Yet, for the majority of those PDZ domains it is unclear if and how those PDZ-lipid interactions are involved in biological processes.

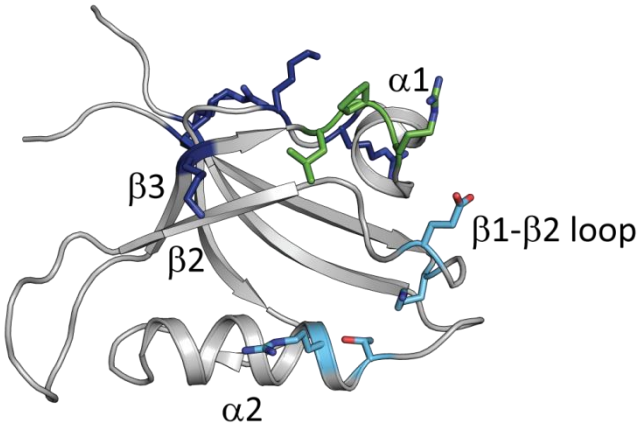

Figure 9: Phospholipid interaction surfaces of the rat Par3 PDZ2 domain. Cartoon representation of the rat Par3 PDZ2 domain (Wu et al. 2007) (PDB ID: 2ogp). Residues interacting with phosphoinositide head groups are shown as light blue sticks. Residues inserting into the membrane are shown as green sticks. Residues forming positively charged clusters are shown as dark blue sticks.

In sum, PDZ domains can mediate protein-protein interactions between short linear motifs such as C-terminal PBMs (Figure 6) and internal PBMs (Figure 7). In addition, dimerization is a well-known interaction mechanism between PDZ domains (Figure 8). Moreover, some PDZ domains possess the ability to interact with certain lipids (Figure 9). All those interaction possibilities highlight the versatility of PDZ domains as organizers of signaling complexes.

1.3.2 Extensions at the termini of PDZ domains and regulation of PDZ:PBM interactions

N- and C-terminal extensions can influence the dynamics, stability and solubility of PDZ domains as well as provide additional ligand interaction sites or regulate the PDZ domain function (Wang et al. 2010; Luck et al. 2012; Ivarsson 2012; Ye & Zhang 2013). Similar to their broad functions, the structures of PDZ extensions can vary and include additional α-helices and β-strands at both termini. Besides, secondary structure based predictions assessed that approximately 40% of all PDZ domains contain extensions on at least one of their termini (Wang et al. 2010).

A well-studied example of a PDZ extension in the context of cell polarity is the CRIB domain N-terminal of the Par6 PDZ domain (Figure 3). The unstructured CRIB domain forms two additional β-strands upon interaction of the Par6 PDZ domain with GTP-bound Cdc42 (Garrard et al. 2003; Peterson et al. 2004; Whitney et al. 2011; Whitney et al. 2013). This structural rearrangement allows the PDZ to transit via partial unfolding into a high affinity state with enhanced affinity for the Crb PBM (Whitney et al. 2011; Whitney et al. 2016).

In addition to extensions at the termini, PDZ domains can also form supramodules. There are two types of supramodules (Luck et al. 2012; Ye & Zhang 2013). Homotypic PDZ domain supramodules only consist of PDZ domains which form larger complexes. Those larger PDZ domain assemblies form tandems and usually a short, conserved linker sequence can be found between the two PDZ domains. Of note, PDZ tandems may not be confused with PDZ dimers as the later occur between PDZ domains of different protein chains whereas PDZ tandems occur in one protein chain. The functions of those PDZ tandems are similar to the short extensions as they can stabilize the fold of one of the involved PDZ domains and provide additional ligand binding sites such as in the PDZ1:PDZ2 and PDZ4:PDZ5 tandem of the multiple PDZ domain protein Glutamate receptor-interacting protein 1 (Luck et al. 2012; Ye & Zhang 2013).

Another kind of PDZ supramodules are heterotypic PDZ domain supramodules. As the name suggests, heterotypic supramodules contain other domains besides PDZ domains. Herein, the additional domains serve similar purposes as in homotypic PDZ domain supramodules. For example, they can stabilize the PDZ domain and generate additional ligand binding interfaces, as in the Harmonin N domain and PDZ domain supramodule (Ye & Zhang 2013). One more example in the contex of cell polarity are the PDZ-SH3-GK supramodules found in members of the membrane-associated guanylate kinase (MAGUK) family such as ZO-1 or Std/Pals1 (Figure 3) (Ye & Zhang 2013; Li et al. 2014). In PDZ-SH3-GK supramodules, a PDZ domain forms with C-terminal SH3- and GK-domains an elaborate binding surface which include canonical PDZ:PBM interactions as well as additional binding surfaces provided by the SH3- and GK domains.

There are various examples present in which regulation of PDZ:PBM interactions occur. Non-surprising, phosphorylation of residues inside the PBM or inside the PBM binding groove of a PDZ domain as well as inside PDZ extensions is reported to weaken or disrupt PDZ:PBM interactions (Luck et al. 2012; Ivarsson 2012; Ye & Zhang 2013). In addition, allosteric changes as induced by the binding of Cdc42 to the Par6 CRIB domain N-terminal of its PDZ domain (Figure 4) also influence the binding properties of PDZ domains (Luck et al. 2012; Ivarsson 2012; Ye & Zhang 2013).

1.3.3 Investigating PDZ specificity

Much effort has been taken to investigate the specificity of PDZ domains. Over the years, several high through-put studies have been published investigating selected PDZ domains or investigating the PDZ specificity on a proteome-wide scale with large efforts on predicting PDZ specificity.

The first study quantifying PDZ domain specificities on a larger scale used peptide arrays to screen the interactions of three PDZ domain with 6223 human C-terminal peptide sequences. Subsequently, the authors used surface plasmon resonance and NMR spectroscopy to investigate the basis of the ligand affinities of the PDZ domains (Wiedemann et al. 2004) and to identify areas of the PDZ domain influencing PBM recognition. These areas included the carboxy-binding loop, the α2-helix as well as residues from β2- and β3-strand (Figure 6). Afterwards, systematic mutational studies were applied to separate the relative affinity contributions of each PBM side chain. Thereby the authors identified regions on the PDZ domains which are responsible for the interactions with the individual PBM position. This knowledge was finally used to design high affinity ligands.

In order to address the specificities of PDZ domains on a larger scale, proteome-wide studies investigating the PDZ specificity in mice were performed (Stiffler et al. 2007). To this end, 157 PDZ of the 270 human PDZ domains (Luck et al. 2012) were screened against 217 PBMs in a protein microarray. The authors used their protein microarray data together with fluorescence polarization data to train and refine a prediction model. At the end, their prediction model suggested an even distribution of PDZ specificity across the proteome. This even distribution suggests that PDZ:PBM interaction do not fall into discrete classes but rather have evolved to use as much sequence diversity as possible to ensure non-overlapping specificities between PDZ:PBM interactions. In addition, a further study from the same lab provided an improved sequence based prediction of PDZ:PBM pairs (Chen et al. 2008). However, the suggested prediction methods are based on a highly underdetermined training data set. Although, the authors tried to bypass the effects of the underdetermined training data set, the prediction method seems to be limited to prediction interactions of PDZ domains sharing high sequence identity with the training data (Chen et al. 2008).

A similar approach investigating the specificities of 82 human and worm PDZ domains used phage display selected ligands to correlate the sequence of the PDZ domain, especially the residues surrounding the PBM binding pocket, with the sequence of the PBM (Tonikian et al. 2008). Since the authors used optimal ligands selected by phage display, the predicted ligand sequence is a prediction of the optimal ligand. However, due to the fact that natural PDZ ligands are usually not optimal, the predicted ligand is just a suggestion (Tonikian et al. 2008). Later studies using structural information to predict PDZ:PBM interactions suggested that the sequence and structure based approaches are complementary and largely depend on the sequence identity between the test and training PDZ domains (Hui et al. 2013). Another approach to predict PDZ specificities was developed combining clustering of PDZ domains into families according to their sequence as well as a machine learning for predication and generation of negative training data derived (Kundu & Backofen 2014). The negative training data derived from machine learning was used to balance the positive interaction data present in the literature (Kundu & Backofen 2014). However, the authors published predictions for the PDZ domains present in the training data set and therefore do not cover all PDZ domains.

Yet, the structure based as well as the sequence based prediction methods are unable to detect the established interaction between the *dm*Par6 PDZ domain and the Crb PBM (Whitney et al. 2016; Lemmers et al. 2004). Of note, the Par6 PDZ domain shares only low identity with the PDZ domains used to generate the prediction algorithms. Therefore, prediction of PDZ:PBM interactions is still an unsolved problem and thorough analysis of PDZ:PBM interactions are inevitable.

Most strikingly, all prediction methods only investigated the core PBM as well as PDZ domain without N- or C-terminal extensions (Wiedemann et al. 2004; Stiffler et al. 2007; Chen et al. 2008; Tonikian et al. 2008; Hui et al. 2013; Kundu & Backofen 2014). Not surprisingly, this limits the predication capabilities since it is estimated for 40% of all PDZ domains to have extensions at one of their termini (Wang et al. 2010). Moreover, residues upstream of the core PBM can influence PDZ:PBM interactions quite dramatically (Luck et al. 2012; Ivarsson 2012; Ye & Zhang 2013).

A comprehensive structural study was performed investigating high affinity PDZ:PBM interactions (Ernst et al. 2014). The aim of this study was to provide structural information on non-class I PBMs bound to PDZ domains since the available structural information was previously dominated by class I PBMs. Noteworthy, this study was based on phage display derived PDZ:PBM pairs reported previously (Tonikian et al. 2008) and therefore selects artificially tight interaction partners. Nevertheless, the authors provide detailed information about specificity generating mechanisms concerning PBM positions 0 to -3.

Interestingly, a phage display screen to identify the ligand specificities of the *dm*Par3 PDZ domains was performed (Yu et al. 2014). However, the data presented seems to be biased towards tryptophan residues. It is known that phage display data can be enriched in hydrophobic residues and therefore comprise prediction algorithms based on phage display data (Luck & Travé 2011).

Moreover, the first screen of a library containing all unique C-termini in the human proteome as well as all unique C-termini of selected viruses was published recently (Ivarsson et al. 2014). However, only nine human PDZ domains were tested. Nevertheless, this screening method renders predictions obsolete since it includes all possible ligands. However, only a very small subset of the 270 PDZ domains present in humans (Luck et al. 2012) have been tested so far.

Taken together, much progress has been made over the past years in understanding PDZ:PBM interactions. It became obvious that PDZ:PBM interactions are fine-tuned between specificity and optimal affinity in their biological context. Furthermore, it turned out to be close to impossible to predict all PDZ:PBM interactions present in nature. In addition, studies addressing the interactions of PDZ domains with several ligands to overcome the limitations of prediction are still sparse.

1.4 The role of the Par3 PDZ domains in cell polarity

Par3 is the central scaffold of the PAR complex and contains three PDZ domains as central interaction modules (Figure 4). Since PDZ domains are known to be promiscuous in regard of ligand recognition, it is not surprising that several ligands for the Par3 PDZ domains were suggested in the literature. Still, the question arises how the Par3 PDZ domains and other PDZ domains present in cell polarity associated proteins can discriminate between their ligands in an environment enriched with PBMs (Figure 3).

Of note, some interactions of the Par3 PDZ domains are already well studied. For example, structural studies investigating the interactions of the rodent Par3 PDZ3 domain revealed its ability to interact with the class I ligand VE-cadherin in rats (Feng et al. 2008) as well as with the class II ligand PTEN in mice (Tyler et al. 2010). Both interactions rely on an additional binding site in the β2-β3-loop besides the PBM binding groove. Of note, the β2-β3-loop is only conserved in vertebrate Par3 PDZ3 domains. In contrast, invertebrate Par3 PDZ3 domains do not contain this conserved loop (Figure 27). In the *Drosophila* Par3 protein, this loop has a unique sequence consisting of glycine and serine residues. Furthermore, previous studies in the lab of Silke Wiesner showed that the β2-β3-loop does not influence the fold of the *dm*Par3 PDZ3 domain (Renschler 2013; Brückner 2014). This suggests that the extended β2-β3-loop is probably dispensable for *dm*Par3 PDZ3 function.

Additionally, the rat Par3 PDZ2 domain can interact with phosphatidylinositol lipids (Figure 9) and the residues mediating this interaction are conserved in the *Drosophila* protein (Wu et al. 2007). In

addition, the PDZ domains and the PIP binding region in the vicinity of the KBD (Krahn, Klopfenstein, et al. 2010) seem to be involved in Par3 oligomerization dependent membrane association in the *Drosophila* embryo ectoderm (McKinley et al. 2012). However, the phospholipid interactions of the second Par3 PDZ domain alone are not sufficient for membrane recruitment (McKinley et al. 2012).

In this study, I investigated the interactions of the *dm*Par3 PDZ domains with different PBMs in greater detail to dissect their specificities. To this end, I searched the literature for ligands reported to interact with at least one of the Par3 PDZ domains. These interactions should be at least proven by biochemical data such as pulldown assays. In order to test also PBMs not listed as Par3 PDZ ligands but present in the cellular environment of Par3, I included several PBMs found in members of the PAR and Crumbs complexes. Therefore, I choose to investigate the interactions of the *dm*Par3 PDZ domains with the class I PBMs of Smallish (Smash), Inscutable (Insc), Crumbs (Crb) and Starry night (Stan) as well as the class II PBMs of Echinoid (Ed), Shotgun (Shg) and *dm*Par6 (Table 5). Furthermore, the class III PBMs of α-catenin (α-cat) and aPKC as well as the internal PBM of Stardust (Std) have been included in my analysis (Figure 10).

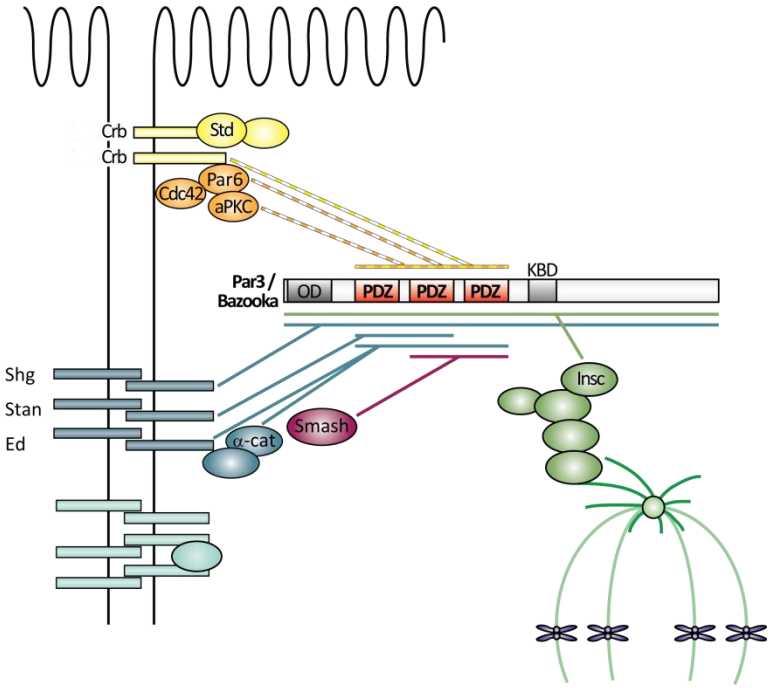

Figure 10: The Par3 PDZ domains in cell polarity. Known interaction partners of the *dm*Par3 PDZ domains are indicated with solid lines whereas possible interaction partners are indicated with dashed lines. Approximate subcellular localizations of the interaction partners are indicated. Abbreviations according to Figure 2 and Figure 3.

The PBM of the LIM domain containing protein Smash was recently identified as an interaction partner of the *dm*Par3 PDZ2 and PDZ3 domains as well as of the Canoe PDZ domain (Beati et al. 2018). This initial study suggested Smash as a mediator between *dm*Par3, the Src family kinase Src42A, Canoe, the *Drosophila* afadin, and the apical actomyosin network (Figure 10) regulating cell shape as well as cortical tension during epitheliogenesis.

Inscutable (Insc) is the link of the PAR complex to asymmetric cell division (Lu & Johnston 2013; Lang & Munro 2017). Insc is an adaptor protein which directly associates with Par3 (Figure 5 and Figure 10) (Wodarz et al. 1999; Schober et al. 1999; Culurgioni & Mapelli 2013; Lu & Johnston 2013) and the Partner of Inscutable (Pins) which is the major scaffolding protein of the Pins complex (Figure 5). Additionally, the Pins complex comprises of the heterotrimeric G-protein Gαi, Disk large (Dlg) and the kinesin motor protein KHC-73 (Lu & Johnston 2013). In short, the Pins complex facilitates the localization of one centromere of the mitotic spindle at a distinct cell cortex thereby aligning the division plane of the asymmetric cell division (Culurgioni & Mapelli 2013).

The Crb PBM is a known interaction partner of the Par6 PDZ domain (Whitney et al. 2016; Lemmers et al. 2004). Moreover, this interaction is enhanced by the interaction of Cdc42 with the Par6 CRIB domain (Whitney et al. 2016). However, since Par3 recruits members of the Crumbs complex during epitheliogenesis (Tepass 2012; Lang & Munro 2017), I tested whether the Crb PBM is able to interact with the Par3 PDZ domains. Additionally, determining the affinities of the interactions of the Crb PBM with the Par3 PDZ domains might shed light on the molecular basis for the later displacement of Crb from initial adherens junctions and establishment of the Crumbs complex. Of note, the interaction of Crb and Std (or its vertebrate homolog Pals1) is a high affinity interaction between the PBM and upstream sequences of Crb C-terminus with the PDZ-SH3-GK module of Std/Pals1 (Li et al. 2014; Ivanova et al. 2015).

Starry night (Stan) is the splice isoform of the *flamingo* gene in *Drosophila* containing a class I PBM at its C-terminus (Wasserscheid et al. 2007). The *flamingo* gene encodes a cadherin that promotes hemophilic cell adhesion and is required for planar cell polarity. The C-terminus of Stan has been shown to interact with the first and second *dm*Par3 PDZ domain (Figure 10) (Wasserscheid et al. 2007).

The C-termini of nectins bind to all Par3 PDZ domains in mouse (Takekuni et al. 2003; Ooshio et al. 2007). Although, no nectin orthologs are present in *Drosophila*, the transmembrane protein Echinoid (Ed) fulfills similar functions in flies (Harris & Tepass 2010). Furthermore, it was shown, that the Ed PBM indeed interacts with the *dm*Par3 PDZ domains (Figure 10) (Wei et al. 2005).

The *Drosophila* DE-Cadherin Shotgun (Shg) was reported to interact with the *dm*Par3 PDZ domains (Figure 10) (Wei et al. 2005; Bulgakova et al. 2013). Besides, a similar interaction between the human VE-Cadherin and the third PDZ of human Par3 was shown to be dependent not only on a classic PBM but also involves interactions upstream of the C-terminal PBM (Iden et al. 2006; Tyler et al. 2010).

A PDZ-PDZ heterodimerization between Par3 with Par6 has been controversially discussed in literature (Joberty et al. 2000; Lin et al. 2000; Suzuki et al. 2001; Nagai-Tamai et al. 2002; Li et al.

2010). However, the presence of a conserved class II PBM at the C-terminus of Par6 proposes an alternative worth investigating (Figure 10).

α-catenin, a member of the catenin family, a protein family defined by the association of its members with cadherins, have been shown to interact with all three Par3 PDZ domains (Figure 10) (Iden et al. 2006). Furthermore, α-catenin and Par3 seem to be involved in VE-cadherin and Par3 mediated orientation of the Golgi apparatus (Odell et al. 2012). In addition, recent studies suggested that α-catenin participates in the front-rear determination of migratory cells (Vassilev et al. 2017).

As a class III PBM is present at the C-terminus of aPKC, I investigated whether the aPKC PBM acts as an additional interaction site between Par3 and aPKC. As it is known for the KBD of Par3 to be a substrate and inhibitor of the kinase domain of aPKC (Wang et al. 2012; Soriano et al. 2016), the interaction of the aPKC PBM with a Par3 PDZ domain (Figure 10) would add an additional interaction mechanism which would ensure association of aPKC with Par3 after phosphorylation of the inhibitory Par3 KBD.

The internal PBM of Std, a member of the Crumbs complex, is the notable exception in this list. Although it is a known ligand of the Par6 PDZ which is not regulated by Cdc42 (Penkert et al. 2004; Kempkens et al. 2006; Wang et al. 2004), it was not selected as a possible Par3 PDZ domain interaction partner with redundant PDZ specificities inside the PAR complex as the Crb PBM. It was rather selected as a negative control since Std recruitment to adherens junctions is dependent on the Std PDZ domain as well as a region C-terminal of the Par3 KBD (Krahn, Bückers, et al. 2010).

Taken together, many different ligands of the *dm*Par3 PDZ domains can be found in literature. However, in many cases the PDZ:PBM interactions were not mapped to individual PDZ domains or described as PDZ:PBM interactions. In addition, the individual specificities of the *dm*Par3 PDZ domains have not been investigated thoroughly. For that reason, I want to investigate the *dm*Par3 PDZ domains and their ligand interactions in greater detail.

2. Aims and significance

Three distinct activities of Par3 clusters have been suggested (Harris 2017). First, Par3 acts as a scaffold for adherens junction assembly (Figure 2A). Second, Par3 inhibits aPKC at the apical-basolateral border by sequestration (Figure 2A). Third, Par 3 acts as a cortical assembly site for the Pins complex during asymmetric cell division (Figure 2B). Recently, it became obvious that those functions rely on the one hand on distinct OD mediated clustering of Par3 (Harris 2017; Rodriguez et al. 2017; Dickinson et al. 2017; Wang et al. 2017). Yet, a thorough investigation of the Par3 PDZ domain mediated protein-protein interactions (Figure 10) underlying the various functions of the Par3 clusters remained absent. In addition, there is only limited information about the specificities of the *dm*Par3 PDZ domains available (Yu et al. 2014). Therefore, I investigated the following two topics in my PhD thesis in order to provide more details for the interactions of the Par3 PDZ domains.

1. Investigate the molecular details of the controversial interaction of Par3 and Par6.
2. Investigate specificities of the individual Par3 PDZ domains in order to reveal a specificity profile against physiological relevant PBMs in the context of the different Par3 functions.

3. NMR spectroscopy and x-ray crystallography

3.1 Nuclear magnetic resonance spectroscopy as a tool to study protein interactions

3.1.1 Fundamentals of NMR spectroscopy

The nuclei of atoms have a quantum mechanical property called nuclear spin I. This spin is the sum of the orbital total angular momenta and the intrinsic spins of all protons composing the nucleus (Table 3). Each proton and neutron has an interger orbital angular momentum and a spin of 1/2. Therefore, in nuclei with even numbers of protons and neutrons (e.g. ^{12}C), the nuclear spin is 0 due to spin pairing. If the numbers of both protons and neutrons is uneven, two unpaired spins are present and result in an integer nuclear spin e.g. 1 in the case of ^{14}N. Moreover, nuclei where the sum of protons and neutrons is odd (e.g. ^{15}N), I is half-integer since one unpaired spin is present. In addition, the nuclear spin results in the nuclear magnetic moment which can be depicted as a magnetic dipole. Hence, the nuclear magnetic moment leads to the interactions of nuclei with magnetic fields. However, if no magnetic field is present, all spins are oriented randomly.

Table 3: Properties of atoms used in protein NMR spectroscopy

Element	Isotope	Nuclear spin (I)	Natural Abundance	Gyromagnetic ratio[1] γ
Hydrogen	^{1}H	1/2	99.98 %	26.75
Deuterium	^{2}H	1	0.02 %	4.10
Carbon	^{12}C	0	98.90 %	0.00
	^{13}C	1/2	1.11 %	6.73
Nitrogen	^{14}N	1	99.63 %	1.93
	^{15}N	1/2	0.37 %	-2.71

[1] in 10^7 $T^{-1}s^{-1}$, (Rattle 1995; Czeslik et al. 2007)

If a sample containing nuclei with I = 1/2 is placed into an external magnetic field with a field strength of B_0 in the direction of the z-axis, the spins of the nuclei will align along B_0 after an equilibration period. Since 2*I+1 orientations are possible, spin 1/2 nuclei can orient themselves in two directions, one parallel (α state) and one anti-parallel (β state) to B_0 (Figure 11A).

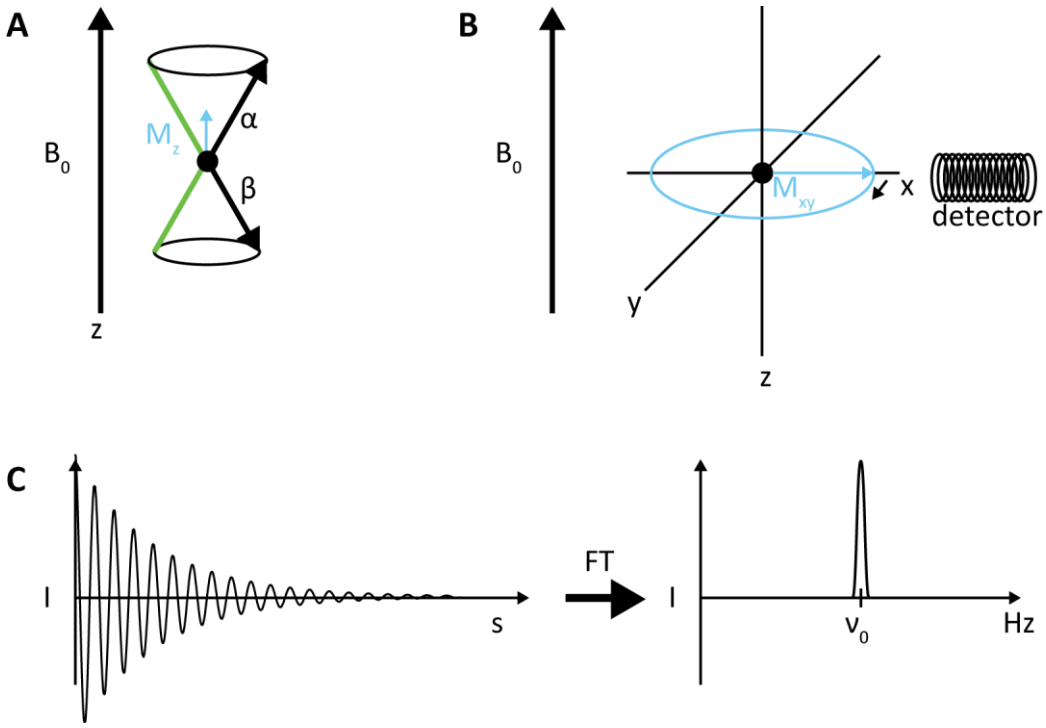

Figure 11: Fundamentals of NMR spectroscopy. (A) The nuclear spins of the atomic nuclei inside a magnetic field B_0 along the z-axis align parallel (α state) and antiparallel (β state) along B_0. The α state is slightly more populated due to its lower energy. The bulk magnetization (cyan arrow) points along the magnetic field. **(B)** The bulk magnetization moves around the z-axis after a short radiofrequency pulse flipped it along the x-axis. The precession motion (black arrow) of the bulk magnetization in the xy-plane (M_{xy}) can be detected by detector coils along the x-axis (black). **(C)** The recorded signal oscillates and decays over time since the magnetization finally returns to equilibrium. After Fourier transformation (FT) the time depend signal is converted to a frequency signal (ν_0).

After equilibration, the population of the α state will be populated slightly more due to its lower energy level. Furthermore, the spins describe a precession motion around the B_0 field which can be described by their Larmor frequency. The velocity ω_0 of this precession motion is given by

Equation 1:

$$\omega_0 = -B_0\gamma$$

with γ being the gyromagnetic ratio. γ is thus a sensitivity measure of the observed nuclei for the magnetic field (Table 3). The frequency ν_0 (in Hz) by which the spins rotate in the xy-plane can be derived from Equation 1:

Equation 2:

$$\nu_0 = \frac{\omega_0}{2\pi} = -\frac{B_0\gamma}{2\pi}$$

The spins add up to the so-called equilibrium magnetization or bulk magnetization M_z of the sample that is aligned along B_0 (M_z) (Figure 11A, cyan arrow). The equilibrium magnetization can be manipulated by a magnetic field B_1 perpendicular to B_0. To this end, electromagnetic waves usually

in the frequency range of radiofrequencies are used. A short radiofrequency pulse will tilt M_z away from the z-axis since the spins start to align with the B_1 field and therefore are in phase coherence with the B_1 field. If this pulse is long enough to tilt the M_z magnetization completely into the xy-plane, it is called a 90° pulse. After the pulse, the magnetization moves around a circle in the xy-plane (Figure 11B black arrow) and induces an electric current in a receiver coil along the x-axis. However, the magnetization will slowly return towards the equilibrium and therefore, the detectable magnetization in the xy-plane will decline exponentially over time (Figure 11C left). This is called the free induction decay (FID).

The time dependent decay of the magnetization ρ of a single 1/2 spin in the xy-plane can be described as a first order differential equation:

Equation 3:

$$\frac{\partial}{\partial t}\rho = (iv_0 - R_2)\rho$$

with R_2 being the decay (relaxation) rate of the transverse magnetization. Equation 3 can be solved as

Equation 4:

$$\rho(t) = \rho(0)e^{iv_0 t}e^{-R_2 t}$$

Equation 4 tells us that ρ oscillates with ω_0 and decays with R_2. The spectrum in the frequency domain in Figure 11 C (right) is the result of the Fourier transformation of Equation 4 as a function of the frequency ω:

Equation 5:

$$\rho(v) = \rho(0)\frac{1}{i(v_0 - v) - R_2} = -\rho(0)\left(\frac{r}{(v_0 - v)^2 + {R_2}^2} + i\frac{(v_0 - v)}{(v_0 - v)^2 + {R_2}^2}\right)$$

Equation 5 describes a Lorentzian line at v_0 with a line width determined by R_2. After phase correction in order to display the real part of Equation 5 the absorption spectra can be displayed (Figure 11 C right).

However, in a molecule, each atom has a unique chemical environment. This local chemical environment is determined by charges in proximity and shielding effects (e.g. ring currents induced in aromatic ring systems) among others which result in a local magnetic field B_{local}. Therefore, each nucleus inside a molecule has its own resonance frequency v_{local} determined by B_{local} and hence gives rise to an individual peak in a NMR spectrum.

Equation 6:

$$v_{local} = -\frac{B_{local}\gamma}{2\pi}$$

Nonetheless, in all equations which describe a single atom spin (Equation 3 – Equation 5), ω_0 can be replaced by ω_{local} in order to describe the nuclei of the same isotope inside a molecule. The local magnetic field and the consequently unique resonance frequencies of atoms in a molecule form the basis for the structural information that can be gained with NMR spectroscopy.

The loss of magnetization or coherence, to be precise the return of the M_{xy} magnetization to the M_z magnetization is called relaxation. There are two processes involved in relaxation. Longitudinal relaxation, T_1 or spin-lattice relaxation is caused by the Brownian motions of molecules. Since Brownian motion is random, all molecules and therefore all nuclei inside a molecule experience random reorientation and thus eventually return to thermal equilibrium. This reorientation of nuclei causes the spins to realign with the B_0 field in the absence of a B_1 field. Transversal relaxation, T_2 or spin-spin relaxation describes the loss of phase coherence. During the duration of the pulse, the spins orient themselves along the B_1 field. After the pulse, the spins start to rotate (Figure 11B). However, not all spins rotate at exactly the same frequency since local inhomogeneities of the B_0 field are present and lead to the loss of phase coherence.

3.1.2 J-coupling and protein NMR

Not only are external magnetic fields able influence the spin of a nucleus. Phase coherence can also be interchanged between atom nuclei with the same spin quantum numbers. This process is called J-coupling. In order to achieve J-coupling, two prerequisites have to be met. First, the coupling nuclei have to be connected by covalent bonds since J-coupling is a scalar coupling, i.e. it occurs through bonds. Second, J-coupling has not to be suppressed i.e. no decoupling pulses are present in the pulse sequence (see below). Each coupling constant is characteristic and depends on the nature of the nuclei involved as well as their distance in terms of separating chemical bonds (Table 3 and Figure 12) and their conformation. In small molecule NMR spectroscopy, J-couplings are used to decipher details about the structure directly from one-dimensional experiments where J-coupling causes single peaks to split into multiplets. In protein NMR however, the use of one-dimensional spectra is limited due to the fact that proteins usually contain far more nuclei than small molecules. Therefore, multidimensional correlation spectra have been developed (Aue et al. 1976; Ernst et al. 1987). Multidimensional correlation spectra use J-couplings to selectively transfer the magnetization form one nucleus (e.g. ^{1}H) to another (e.g. ^{15}N) in order to record the resonance frequencies of both nuclei in correlation with each other. These correlation spectra have proven to be very useful for structure determination of small proteins (≥ 30 kDa) (Kwan et al. 2011) as well as for investigating dynamic processes such as folding, conformational sampling and ligand binding (Bieri et al. 2011; Wiesner & Sprangers 2015; Barrett et al. 2013).

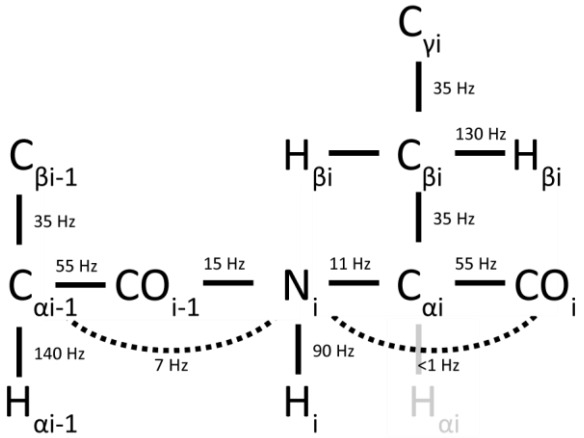

Figure 12: J-couplings inside proteins. ^{1}J-couplings (J-couplings via one chemical bond) are depicted as solid black lines whereas ^{2}J-couplings are depicted as dashed black lines. In order to have J-couplings, all nuclei have to have the same spin of 1/2, that is ^{1}H, ^{15}N and ^{13}C. The figure was adapted from van de Ven (van de Ven 1995).

3.1.3 ^{1}H,^{15}N-HSQC experiments

One of the most frequently used NMR experiments for proteins smaller than 30 kDa is the heteronuclear single quantum coherence (HSQC) experiment. In a ^{1}H,^{15}N-HSQC experiment, each HN atom pair of a uniformly ^{15}N-labeled protein gives rise to one cross peak in the spectrum since a ^{1}H,^{15}N-HSQC experiments correlates the proton chemical shifts with covalently bound nitrogen atoms via ^{1}J-coupling of the HN-bond (Figure 12). Therefore, all backbone amides except Prolines as well as HN pairs occurring in Asparagine, Glutamine, Histidine, Arginine and Lysine can be observed in a ^{1}H,^{15}N-HSQC spectrum. However, due to the proton exchange at neutral pH of Histidine, Lysine and Arginine HN pairs with water molecules, these protons be difficult to observe. Hence, only cross peaks from backbone amides as well as Asparagine and Glutamine side chain amides are usually present in a ^{1}H,^{15}N-HSQC spectrum. In addition, the presence of at least one cross peak per residue gives the possibility to resolve structural and dynamic changes in a protein by ^{1}H,^{15}N-HSQC experiments on a per residue basis. This resolution can be used to track changes in the protein such as binding events, structural changes, chemical or conformational exchange processes and aggregation. The basis of these observations is the same as for all NMR measurements that is that the chemical environment of the observed spin system determines it resonance frequency. If the chemical environment of a HN pair changes, e.g. due to ligand binding, the position of the corresponding cross peak in a ^{1}H,^{15}N-HSQC spectrum will change in the absence and presence of ligand. The following pulse sequence is used to transfer the magnetization in order to observe HN cross peaks in a ^{1}H,^{15}N-HSQC spectrum (Figure 13).

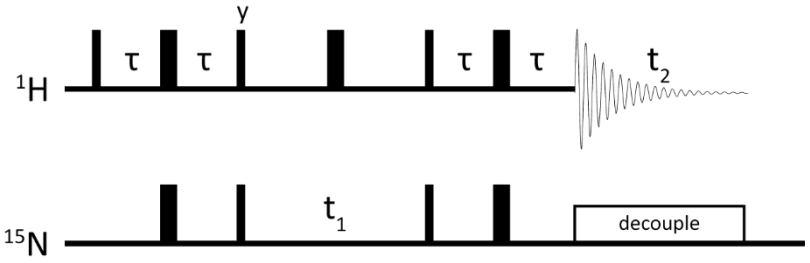

$$H_z \xrightarrow{\frac{H}{x}90} H_y \xrightarrow{-J_{2\tau}} -H_x N_z \xrightarrow{\frac{H}{y}90\ \frac{N}{x}90} -H_z N_y \xrightarrow{N_z(t_1)} -H_z N_y \cos(\omega_N t_1)$$

$$\xrightarrow{\frac{H}{x}90\ \frac{N}{x}90} H_y N_z \cos(\omega_N t_1) \xrightarrow{-J_{2\tau}} -H_x \cos(\omega_N t_1) \xrightarrow{H_z(t_2)} -H_y \cos(\omega_N t_1) \sin(\omega_H t_2)$$

Figure 13: Pulse sequence and coherence transfer pathway of a 2D ^{1}H,^{15}N-HSQC experiment. The narrow bars represent 90° pulses, the wide bars 180° pulses. If no pulse phases are indicated, pulses are along the x-axis. The coherence pathway leading to the observed cross peaks is represented ignoring the relaxation. $\boldsymbol{\tau = {}^{1}/_{4J_{HN}}}$.

First, the magnetization is transferred from protons to nitrogen via ^{1}J-couplings ($^{1}J_{2\tau}$) in a so-called insensitive nuclei enhanced by polarization transfer (INEPT) step (Morris & Freeman 1979). Next, chemical shift evolution of the nitrogen chemical shifts (ω_N) is detected during delay t_1. At the same time, HN ^{1}J-coupling is suppressed by a 180° pulse in the middle of t_1. Then, the magnetization is transferred back to the protons via another INEPT step. Finally, the FID containing proton chemical shifts (ω_H) is recorded during t_2 with decoupling of nitrogen by a series of 180° pulses in the nitrogen dimension in order to suppress HN ^{1}J-coupling. Due to the decoupling of protons and nitrogens during data acquisition, only one peak per HN pair is visible in the HSQC spectrum.

3.1.4 ^{1}H,^{15}N-TROSY experiments

The quality of NMR spectra of large proteins (> 30 kDa) is poor for two reasons. First, large proteins contain more residues leading to an increased number of peaks in the spectra. Second, large proteins tumble slower in solution. The average tumbling time of a 50 kDa protein is around 20 ns whereas the tumbling time of a 150 kDa protein is around 60 ns. Hence, large proteins have an increased transverse spin relaxation leading to line broadening. Both reasons result in poor peak dispersion (signal overlap) in the NMR spectra of large proteins. Therefore, methods have been developed to circumvent these problems. Transverse relaxation-optimized spectroscopy (TROSY) enhances transverse relaxation by selection of the slow relaxing component of a spin system. If two spins are coupled (e.g. a backbone HN pair) only the slow relaxing component of the multiplet can be selected by TROSY pulse sequences (Figure 14) (Pervushin 2000; Keeler 2010).

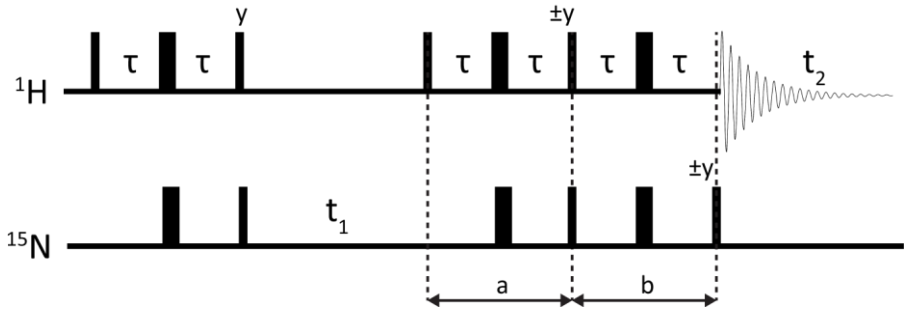

Figure 14: Pulse sequence of a 2D ^{1}H,^{15}N-TROSY experiment. The narrow bars represent 90° pulses, the wide bars 180° pulses. If no pulse phases are indicated, pulses are along the x-axis. $\tau = {}^{1}/_{4J_{HN}}$.

As in the HSQC experiment, the magnetization is first transferred from a proton to a nitrogen via an INEPT step. Then, chemical shift evolution of the nitrogen chemical shifts is recorded. At the same time ^{1}J-coupling between protons and nitrogen ($^{1}J_{HN}$) takes place during delay t_1. In contrast to a HSQC pulse sequence (Figure 13), the HN coupling is retained in each dimension. Therefore, the multiplet does not collapse and the slow relaxing components can be selected. In TROSY experiments, the selection of slow relaxing components is facilitated by the implementation of line-selective pulse elements (Figure 14, sequence a and b) to select only one of the two spin doublets. By alternating the doublet selection by changing the phases of the last 90° pulses in sequence a and b (Figure 14), respectively, and subsequent processing of the acquired data, selection of the slow relaxing components is achieved (Keeler 2010).

3.1.5 Observing protein-protein interactions by NMR spectroscopy

NMR is a useful tool to investigate protein-protein interactions since it offers a close to atomic resolution of interaction surfaces as well as the underlying kinetics (Bieri et al. 2011; Kwan et al. 2011). Since the position of a cross peak inside a two dimensional NMR correlation spectrum is determined by the chemical environment of the observed nuclei, every change in this environment is reflected by a change of the position inside the NMR spectrum. Therefore, binding events can be observed by NMR spectroscopy. In addition, investigation of binding events by NMR spectroscopy do not only provide a spatial resolution via the assignments of the affected cross peaks but also allow to deduce kinetic parameters such as binding affinities (Barrett et al. 2013).

When observing protein interactions by NMR spectroscopy of small proteins (< 30 kDa) or larger proteins (30-45 kDa), ^{1}H,^{15}N-correlation spectra such as ^{1}H,^{15}N-HSQC or ^{1}H,^{15}N-TROSY are used which contain information about each backbone amide inside a ^{15}N-labeled protein (Figure 15). First, a reference spectrum is recorded in the absence of the ligand. In combination with backbone assignment experiments, the cross peaks can be assigned to the amino acids of the protein. Next, unlabeled ligand is added step-wise and chemical shift perturbations (CSPs) that depend on the

ligand concentration are observed on a subset of peaks since only a subset of the chemical environments of the amino acids inside the protein experience changes upon ligand binding (Figure 15). If the linear CSPs can be tracked, the interaction surface can now be mapped using the assignment of the free protein. Otherwise a resonance assignment of the saturated complex has to be performed.

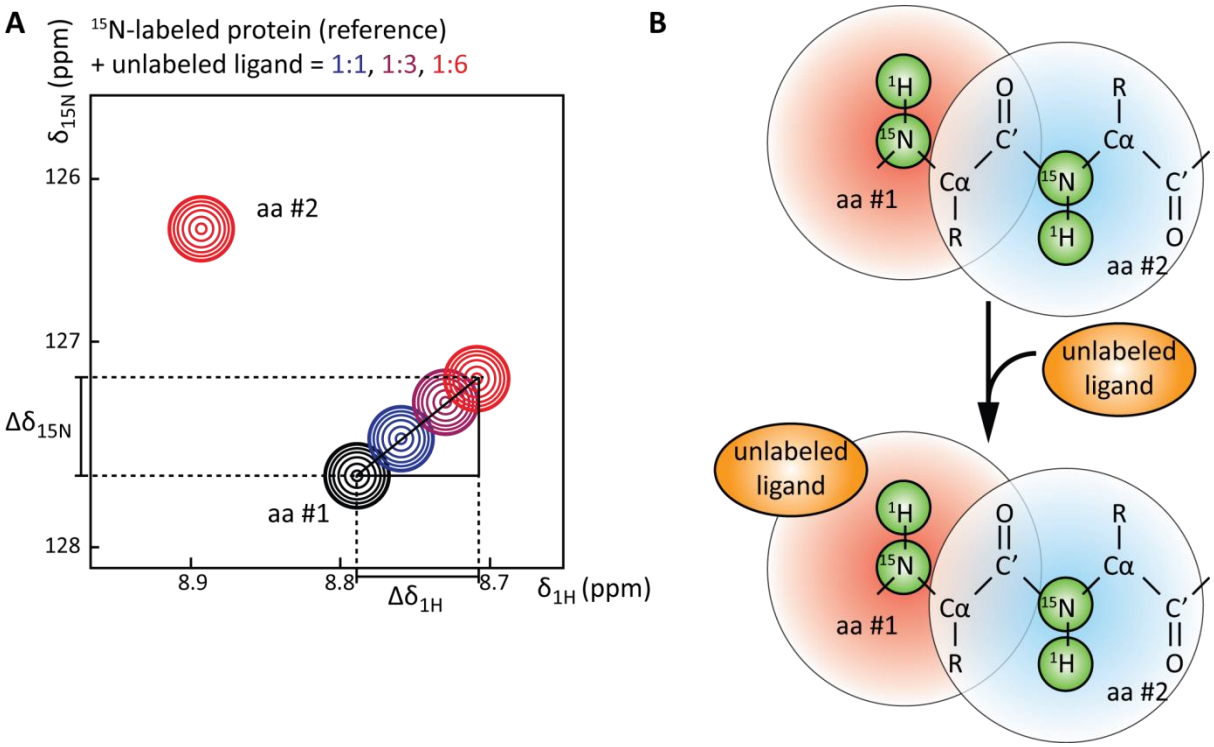

Figure 15: Chemical shift perturbation experiment. (A) $^{1}H,^{15}N$ correlation spectra of a ^{15}N-labeled protein during the course of a chemical shift perturbation experiment. Upon addition of unlabeled ligand, the cross peaks of amino acids (aa #1) which experience a change in their chemical environment upon ligand binding shift. Whereas peaks from amino acids experiencing no change in their chemical environment (aa #2) do no display any chemical shift perturbations. Chemical shift perturbations in the proton ($\Delta\delta_{1H}$) and nitrogen dimension ($\Delta\delta_{15N}$) in ppm can be used to quantify the interaction. **(B)** The chemical environment of a subset of amino acids of a protein changes upon ligand binding. Chemical environments of aa #1 and aa #2 are depicted as red and blue circle, respectively. Unlabeled ligand is depicted as orange sphere and green circles highlight $^{1}H,^{15}N$ pairs observed by $^{1}H,^{15}N$ correlation experiments. Adapted from Renschler et al. (Renschler et al. 2018) and reprinted with permission from AAAS.

Besides the mapping of interaction surfaces onto protein sequences and, if available, structures, it is possible to extract dynamic information from NMR binding studies (Bain 2003; Waudby et al. 2016). In the case of reversible binding to a single site the following equilibrium exists:

Equation 7:

$$P + L \rightleftharpoons PL$$

with the free protein *P*, the free ligand *L* and the protein-ligand complex *PL*. The exchange rate k_{ex} is given by

Equation 8:

$$k_{ex} = k_{on}[L] + k_{off}$$

where k_{on} is the on rate, k_{off} is the off rate and [L] is the ligand concentration. The dissociation constant K_d is given by

Equation 9:

$$K_d = \frac{k_{on}}{k_{off}} = \frac{[P][L]}{[PL]}$$

Where [P] is the protein concentration and [PL] is the protein-ligand complex concentration. Different exchange regimes, that is, different off-rates at constant K_d values, give rise to different line shapes (Figure 16) during NMR titration experiments. If the frequency difference between bound and unbound state in Hz (Δω) is much slower than the exchange rate k_{ex} (k_{ex} << Δω), the peak of the unbound state disappears while the peak of the bound state starts to appear (Figure 16 top). Whereas, if the frequency difference between bound and unbound is much faster than the exchange rate (k_{ex} >> Δω), the peak displays a constant shift during the course of the titration (Figure 16 bottom). At intermediate exchange rates, the intensities of the cross peak experience and decrease with a subsequent increase as well as a shift.

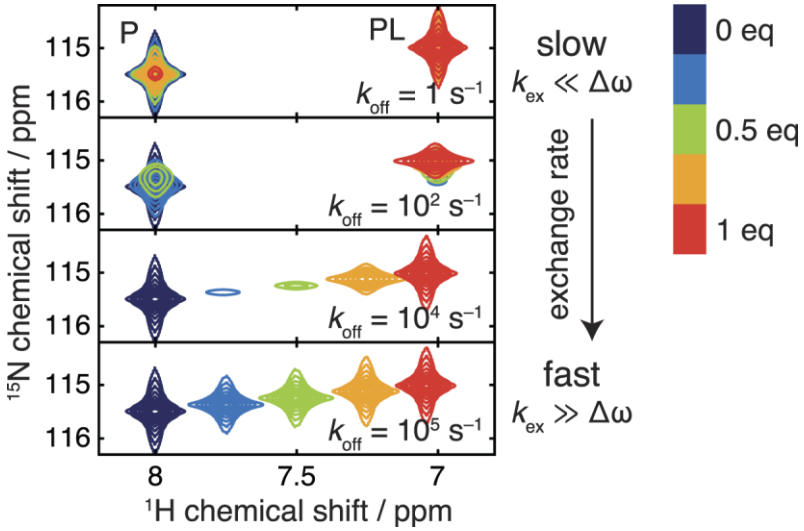

Figure 16: The line shape of cross peaks of an NMR spectrum contains information about exchange rates. Upon ligand addition to a ^{15}N-labeled protein, the line shape of cross peaks that are affected by ligand binding change in an exchange regime dependent manner. P depicts the reference state without ligand; PL depicts the ligand bound state. k_{ex} is the exchange rate and Δω the frequency difference between the bound an unbound state. The ligand concentration increases successively from 0 equivalents (eq, dark blue) to 1 eq of ligand (red). The figure was adapted from Waudby et al. and was simulated with the following parameters: K_d = 2 µM, $\Delta\omega_H$ = 4400 Hz, $\Delta\omega_N$ = 220 Hz, [P] = 1 mM, data recorded at 700 MHz (Waudby et al. 2016).

In this thesis, NMR spectroscopy was used to investigate the PDZ:PBM interactions of the *dm*Par3 PDZ domains with selected ligands. In addition, the influence of the *dm*Par3 FID-motif upon the *dm*Par3 PDZ3 domain was investigated by NMR spectroscopy.

3.2 X-ray Crystallography

The three dimensional structure of a protein defines its function. Hence, the determination of the protein structure enables valuable insights into protein function. One major method to determine protein structures is x-ray crystallography. In x-ray crystallography, protein crystals are exposed to x-rays in order to generate a diffraction pattern. This diffraction pattern can be used to determine the three dimensional structure of the protein inside the crystal.

3.2.1 Crystals

Crystals are repetitions of their smallest non-self-repeating unit, called the asymmetric unit. The asymmetric unit contains the building blocks of a crystal which could be theoretically anything from identical atoms, molecules or ducks (Rupp 2009; Blow 2010). After application of the symmetry operations, defined by the space group of the crystal, the complete crystal unit cell is generated. In turn, the unit cell is repeated via translations in all three dimensions to generate the crystal. Therefore, the crystal is defined by its asymmetric unit together with its space group.

When working with biological macromolecules, such as proteins, the molecules inside a crystal have a fixed stereochemistry. All symmetry operations which facilitate the inversion of such a stereo center, that is mirror planes, inversion centers and gliding planes (combination of mirror planes with translation), cannot be present in protein crystals. Hence, only translation, rotation and combinations thereof (screw axis) are present in protein crystals. Consequently, 65 possible space groups are possible for such crystals (Rupp 2009; Blow 2010).

3.2.2 X-ray diffraction

The key principle underlying x-ray crystallography is the diffraction of x-rays by crystals. The diffraction pattern recorded during an x-ray diffraction experiment contains information about the crystal and its constituents. Information about the electron density inside the crystal is encoded by the intensities of the spots or reflexes of which a diffraction pattern consists. Furthermore, their symmetry and systematic absences of reflexes in the diffraction pattern contain information about the space group. Whereas the position of the reflexes and their distances in respect to each other

encode data about the unit cell angles and dimensions. However, the distances are reciprocal to real space since the diffraction of x-ray is basically a Fourier transformation.

If x-ray waves are passing a crystal, some are scattered by the electrons of the atoms inside the crystal. As all waves, these scattered waves can interfere in a constructive or destructive manner with each other. Only constructive interference results in a diffraction pattern. The condition of constructive interference is described by Bragg's law (Figure 17). In essence, the path difference $2d \sin\theta$ between two or more lattice planes of the crystal with the distance d must be an integer multiple of the wavelength λ (Equation 10).

Equation 10:

$$n\lambda = 2d \sin\theta$$

with $n \in \mathbb{N}$ and the glacial angle θ. In cases where Bragg's law is not fulfilled, the small variances in path difference will lead to destructive interference between the scattered waves, hence canceling each other out.

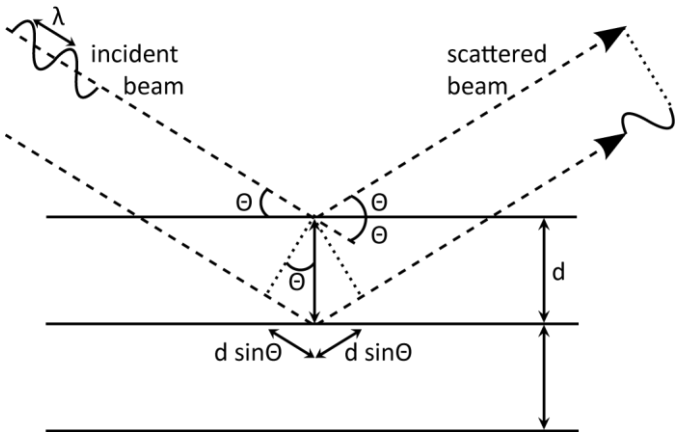

Figure 17: X-ray diffraction represented as reflection on a lattice plane illustrating Bragg's Law. With λ depicting the wavelength of the x-ray beam, Θ depicting the glancing angle between the incident beam and the lattice planes and d depicting the distance between two lattice planes.

The diffraction spots are the result of a Fourier transformation of the x-ray beam with the electron density of the crystal. Therefore, the diffraction pattern describes the electron density in reciprocal space. The structure factor $\boldsymbol{F}_{khl}$ (Equation 11) describes this reciprocal space as the sum of all atomic scattering contributions inside the unit cell (Rupp 2009).

Equation 11:

$$\boldsymbol{F}_{khl} = |\boldsymbol{F}_{khl}| e^{i\Phi_{hkl}} = \sum_{j=1}^{all\ atoms} f_j e^{2\pi i(hx_j + ky_j + lz_j)}$$

with $\boldsymbol{F}_{khl}$ the structure factor, $|\boldsymbol{F}_{khl}|$ being the amplitude F_{khl} of the structure factor, that is the intensity of a reflex with the coordinates h, k and l in the reciprocal space, ϕ being the phase of $\boldsymbol{F}_{khl}$

and f_j the scattering factor of the jth atom. In order to transform the measured intensities into an electron density, Fourier transformation of the structure factor equation (Equation 11) has to be performed and results in the electron density equation (Equation 12).

Equation 12:

$$\rho_{xyz} = \frac{1}{V}\sum_{h}\sum_{k}\sum_{l} F_{khl}\, e^{-2\pi i(hx+ky+lz)}$$

with ρ_{xyz} being the electron density in real space. However, no phase information is present in the recorded data of an x-ray diffraction experiment since only the intensities can be measured.

In order to determine the phases, several methods have been developed. One such method is molecular replacement. During molecular replacement, a structure of a homologous protein is used to search for the localization and orientation of the target structure. Based on the placement of the search model, the phases can be back-calculated which finally enables the Fourier transformation of the structure factor equation (Equation 11) into the electron density equation (Equation 12). The resulting electron density is then used to model the protein structure in an iterative manner.

In this thesis x-ray crystallography has been used to determine the structure of the *dm*Par3 PDZ2:Insc PBM complex.

4. Results and discussion

4.1 Structural basis for the interaction between the cell polarity proteins Par3 and Par6

4.1.1 Contributions

The results presented here are part of the research article “Structural basis for the interaction between the cell polarity proteins Par3 and Par6” published in Science Signaling in 2018 (Renschler et al. 2018). Contributions form coauthors are indicated as follows: SRB (Susanne R. Bruekner), PLS (Paulin L. Salomon), MCS (Mira C. Schütz-Stoffregen), CH (Christine Henzler), AM (Amrita Mukherjee) and SW (Silke Wiesner).

4.1.2 Par6 contains a PBM that associates with the Par3 PDZ1 domain

The Par3:Par6 interaction was previously reported to depend on the PDZ1 domain of Par3 and the PDZ domain of Par6 (Joberty et al. 2000; Lin et al. 2000; Li et al. 2010). In addition, all these reports disagree whether or not the Par6 Crib-motif N-terminal to the PDZ domain is essential for this interaction. Furthermore, the relevance of this interaction *in vivo* has been under debate (Li et al. 2010) and aPKC has been reported as linker, suggesting an indirect Par3:Par6 interaction (Suzuki et al. 2001; Nagai-Tamai et al. 2002). Moreover, PLS, MCS and SW could not show a direct interaction between the Par3 PDZ1 and the Par6 PDZ domain by NMR spectroscopy for several organisms (Renschler et al. 2018). These observations led to the search for an alternative interaction mode between Par3 and Par6. Therefore I revisited the Par6 protein sequence and identified a previously unrecognized class II (φ-X-φ-COO^-) PBM at its C-terminus. Since the motif is highly conserved in metazoans with the notable exception of nematodes (Figure 18), SRB performed NMR CSP experiments with the *Drosophila* proteins.

She observed large chemical shifts perturbations (more than one peak width) and line broadening for numerous residues in the ^{15}N-labeled *Drosophila* Par3 (*dm*Par3) PDZ1 domain upon addition of an unlabeled peptide containing the eight C-terminal residues of *dm*Par6 (Figure 19) (Renschler et al. 2018).

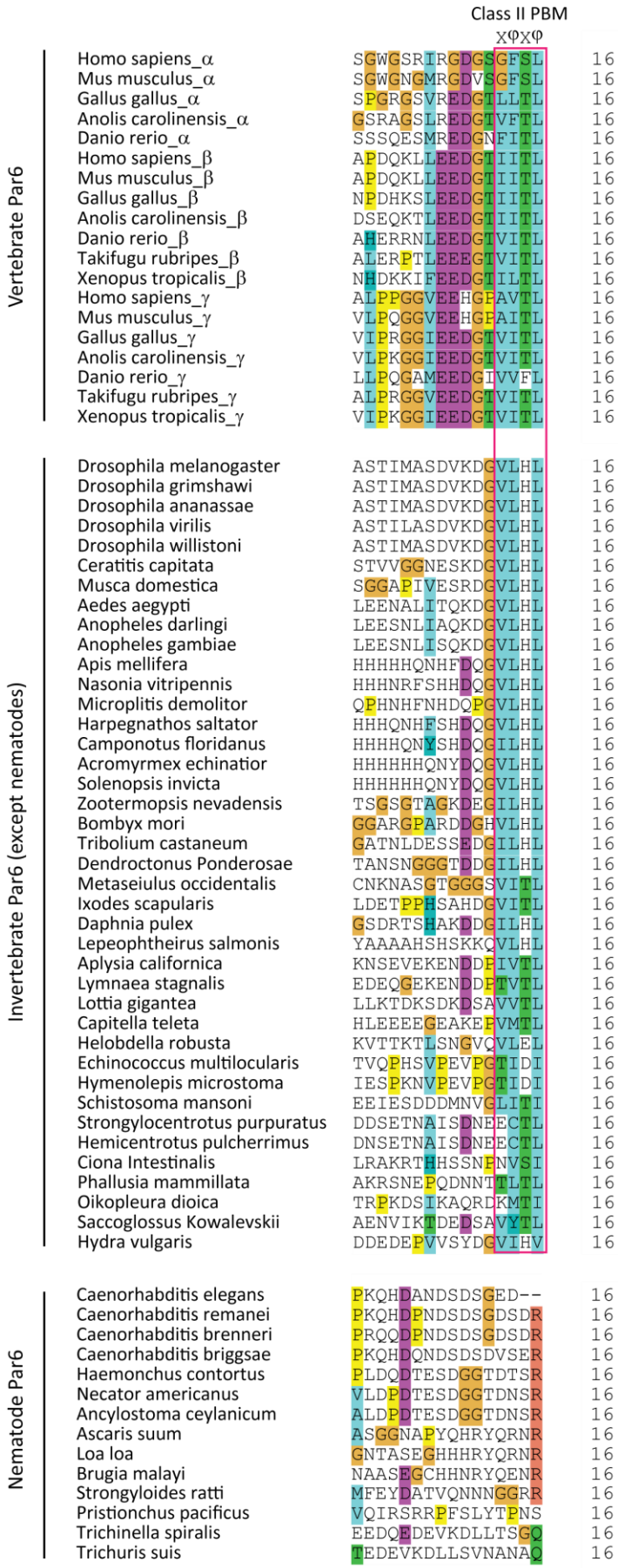

Figure 18: The PBM inside the Par6 C-terminus is highly conserved. Sequence alignment of the C-termini of Par6 proteins from vertebrates (top), invertebrates without nematodes (mid) and nematodes (bottom) are color coded according to conservation by ClustalX (Larkin et al. 2007). The class II PBM discovered that I identified is boxed in red. Adapted from Renschler et al. (Renschler et al. 2018) and reprinted with permission from AAAS.

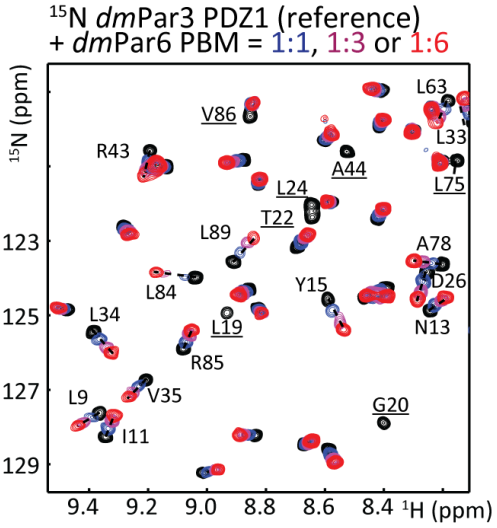

Figure 19: The Par6 PBM interacts with the Par3 PDZ1 domain. Overlay of a representative region of the $^{1}H,^{15}N$-HSQC spectra of the *dm*Par3 PDZ1 domain in the absence (black) and presence of increasing stoichiometric amounts of *dm*Par6 PBM as indicated. For the most affected peaks, chemical shift assignments are shown and underlined if the peaks broaden beyond detection upon binding. Directions of the chemical shift exchanges are indicated by dashed lines. NMR assignments of *dm*Par3 PDZ1 are available under the following BMRB accession code 27197. Spectra were recorded by SRB. Adapted from Renschler et al. (Renschler et al. 2018) and reprinted with permission from AAAS.

This observation is anticipated for two proteins that interact with each other (Figure 15). These results showed that in the *Drosophila* proteins the Par3 PDZ1 domain directly interacts with the Par6 PBM *in vitro*. In support of this, epithelial cell polarity also critically depends on interactions of the Par3 PDZ domains with cell adhesion proteins through PBMs that are highly similar to the Par6 PBM (Figure 26) (Takekuni et al. 2003; Iden et al. 2006; Itoh et al. 2001; Ebnet et al. 2003; Lin et al. 1999).

4.1.3 The Par6 PBM is important for Par3 interaction *in vitro*, in cell culture and *in vivo*

In order to test the importance of the *dm*Par6 PBM in the context of the full length Par6 protein, I performed *in vitro* GST pull down experiments using a recombinant GST-tagged *dm*Par3 fragment containing all three PDZ domains and Sumo-tagged *dm*Par6 variants (Figure 20A).

The PDZ1-3 domains of Par3 were able to pull down efficiently wild-type Par6 (Figure 20B; lane 10). In essence, this interaction was lost upon deletion of the PBM (ΔPBM) (Figure 20B; lane 12), the region C-terminal of the PDZ domain (PB1-CribPDZ) (Figure 20B; lanes 14) or the region C-terminal of the Crib motif (PB1-Crib) (Figure 20B; lanes 16). Notably, GST on its own was not able pull down any of the Par6 constructs in a control experiment (Figure 20B; lanes 9, 11, 13, and 15). Therefore, the pull down experiments confirmed the NMR experiments and showed a direct and crucial *in vitro* interaction of the Par6 PBM with the Par3 PDZ domains.

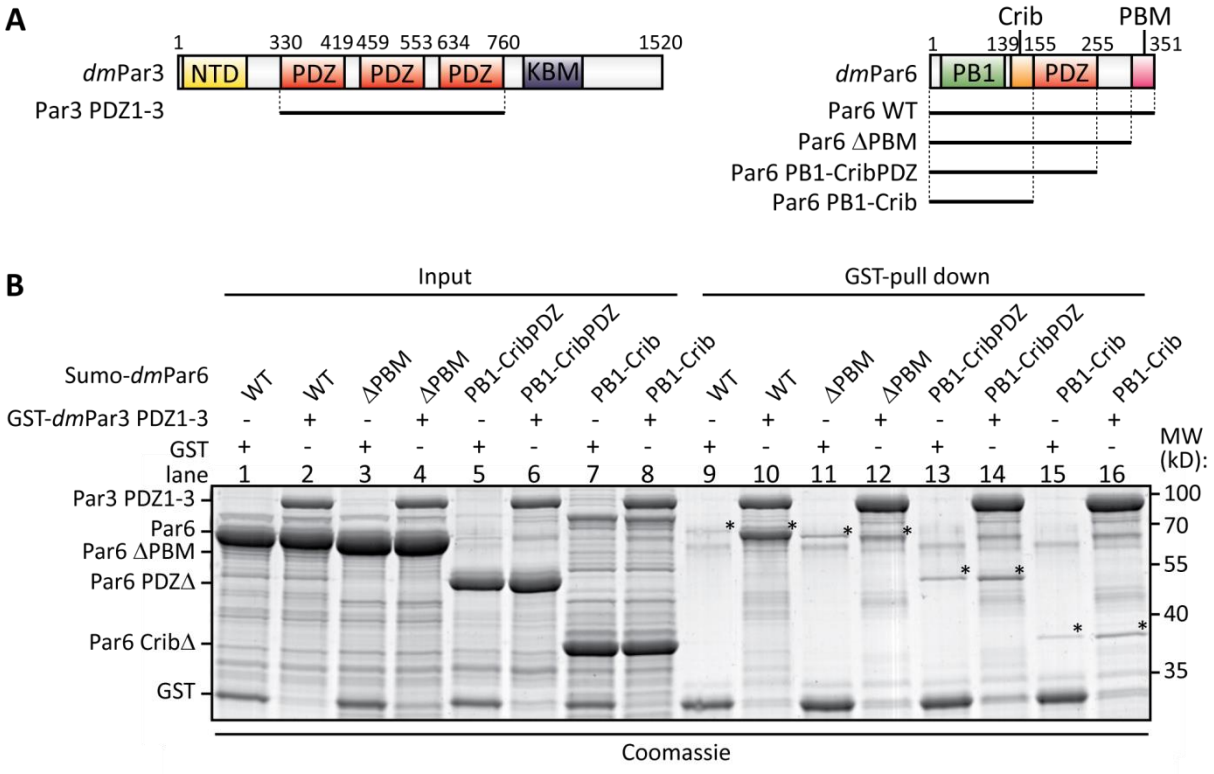

Figure 20: The *dm*Par6 PBM is essential for Par3 interaction. (A) Schematic representation of the *dm*Par3 and *dm*Par6 constructs used for GST pull down experiments. **(B)** GST pull down experiments: GST-tagged *dm*Par3 PDZ1-3 module was incubated with WT or truncated Sumo-tagged *dm*Par6 as indicated. Coomassie staining was used to detect input and associated Par6 as well as GST and GST-*dm*Par3 PDZ1-3. Asterisks highlight Par6 proteins in the pull downs. The pull down is representative of at least three independent experiments. Adapted from Renschler et al. (Renschler et al. 2018) and reprinted with permission from AAAS.

Moreover, my collaboration partners could show that the co-localization of Par3 and Par6 at the plasma membrane in transiently transfected *Drosophila* S2R cells was highly dependent on the presence of the Par6 PBM (Renschler et al. 2018). In addition to the findings in cultured cells, they were also able to show that the *dm*Par6 PBM functions in redundancy with the PDZ domain in Par6 localization *in vivo*. To this end, they investigated the role of the Par6 PBM in Par6 localization in *Drosophila* embryo epithelia at various stages in embryogenesis. Deletion of the Par6 PBM led to a miss-localization of Par6 in fly embryo epithelia. This effect is enhanced in the absence of the Par6 PDZ domain suggesting a possible redundancy in function of the Par6 PBM and PDZ domain *in vivo* (Renschler et al. 2018).

4.1.4 Structural analysis of the *Drosophila* Par3 PDZ1:Par6 PBM complex

Since we could show the *in vivo* and *in vitro* importance of the Par6 PBM in regard of Par3 interaction and Par3-dependent localization of Par6 *in vivo*, SRB solved the structure of the *dm*Par6 PBM octapeptide in complex with the first PDZ domain of *dm*Par3 (Figure 29A, PDB ID: 5oak)

(Renschler et al. 2018). The structure showed binding of the Par6 PBM by canonical β-sheet augmentation to the Par3 PDZ1 domain. Futhermore, a hydrogen bond between H-1 of the Par6 PBM and T22 of the Par3 PDZ1 domain was observed.

In order to validate the importance of the observed interactions, I performed NMR titration experiments. Therefore, I subsituted successively the three C-terminal amino acids of the *dm*Par6 PBM with Alanine (*dm*Par6 L349A (L-2A), H350A (H-1A) and L351A (L0A)) and investigated by NMR experiments their *dm*Par3 PDZ1 binding capacities (Figure 21). In contrast to the changes observed during the titration of the wild type *dm*Par6 PBM in the ^{1}H,^{15}N-HSQC spectrum of *dm*Par3 PDZ1 (Renschler et al. 2018), L-2A and L0A mutations led to almost no CSPs in the ^{1}H,^{15}N-HSQC spectrum of *dm*Par3 PDZ1. In addition, the H-1A mutant weakend the observed CSPs. These observations are consistent with our crystallographic data and indicate the crucial importance of the 0 and -2 positions of the PBM in canonical PDZ PBM interactions as well as the importance of the H-1 hydrogen bond.

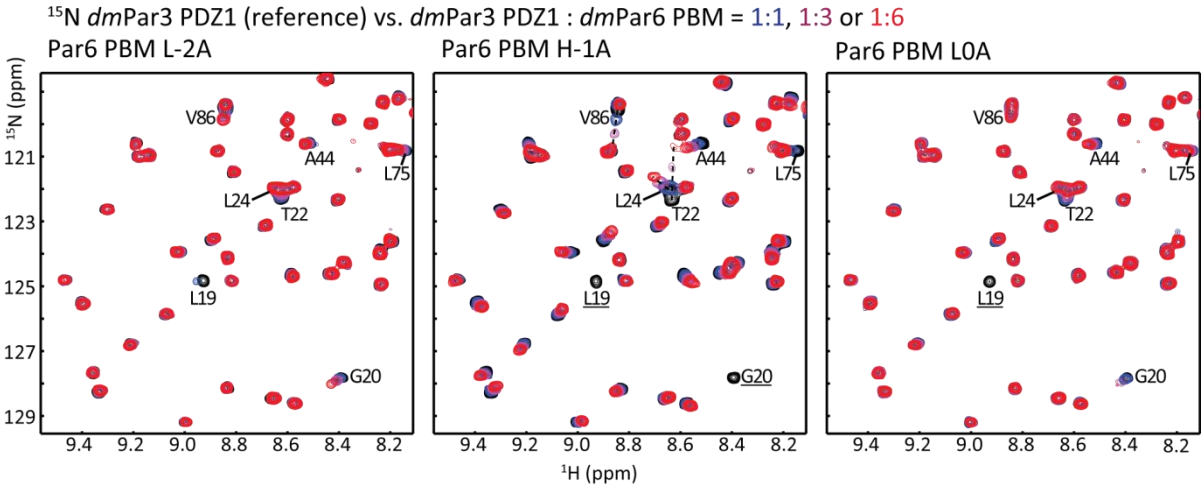

Figure 21: The 0 and -2 position of the *dm*Par6 PBM are important for PDZ interaction. NMR CSPs experiments with ^{15}N-labeled *dm*Par3 PDZ1 domain and *dm*Par6 PBM mutants as indicated. Overlay of a representative region of the ^{1}H,^{15}N-HSQC spectra of the *dm*Par3 PDZ1 domain in the absence (black) and presence of increasing stoichiometric amounts of mutant *dm*Par6 PBMs as indicated. For the most affected peaks, chemical shift assignments are shown and underlined if the peaks broaden beyond detection upon binding. Directions of the chemical shift exchanges are indicated by dashed lines. NMR assignments of *dm*Par3 PDZ1 are available under the following BMRB accession code 27197. Adapted from Renschler et al. (Renschler et al. 2018) and reprinted with permission from AAAS.

4.1.5 The Par3 PDZ1 and PDZ3 domains both interact with the Par6 PBM

Since the residues of the *dm*Par3 PDZ1 domain contacting the *dm*Par6 PBM are well conserved in all three PDZ domains of Par3 (Figure 27), SRB investigated whether the Par6 PBM can also interact with the remaining two *dm*Par3 PDZ domains. In short, she could show that PDZ2 does not interact

with the Par6 PBM whereas the PDZ3 domain interacts with the Par6 PBM (Figure 22) (Renschler et al. 2018).

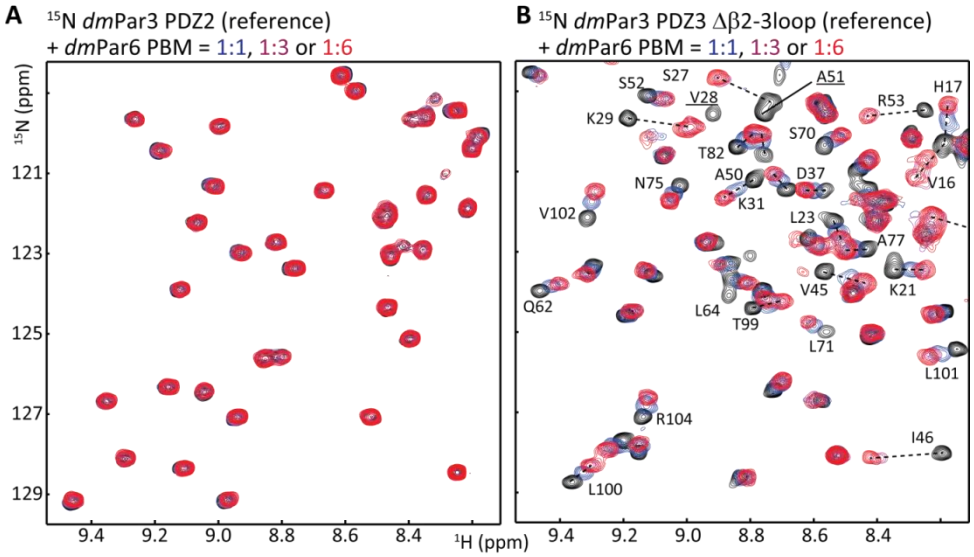

Figure 22: The Par6 PBM interacts with the Par3 PDZ3 domain. (A) Overlay of a representative region of the ^{1}H,^{15}N-HSQC spectra of the *dm*Par3 PDZ2 domain in the absence (black) and presence of increasing stoichiometric amounts of *dm*Par6 PBM as indicated. **(B)** Overlay of a representative region of the ^{1}H,^{15}N-HSQC spectra of the *dm*Par3 PDZ3 Δβ2-3loop domain in the absence (black) and presence of increasing stoichiometric amounts of *dm*Par6 PBM as indicated. For the most affected peaks, chemical shift assignments are shown and underlined if the peaks broaden beyond detection upon binding. Directions of the chemical shift exchanges are indicated by dashed lines. NMR assignments of *dm*Par3 PDZ3 Δβ2-3loop are available under the following BMRB accession code 27198. Spectra were recorded by SRB. Adapted from Renschler et al. (Renschler et al. 2018) and reprinted with permission from AAAS.

In order to quantify the interactions between the *dm*Par3 PDZ domains and the *dm*Par6 PBM, I analyzed the NMR titration data by 2D NMR line shape fitting analysis with TITAN (Waudby et al. 2016) and determined K_d values. Noteworthy, since the *dm*Par3 PDZ2 domain showed no CSPs upon *dm*Par6 PBM titration (Figure 22A), I did not fit these data. The Par6 PBM interacts with the PDZ1 domain with a moderate affinity of 216 ± 4 μM and with the PDZ3 domain with a tighter affinity of 54 ± 1 μM (Table 5, Figure A 4 and Figure A 23). Furthermore, I quantified the affinities of the *dm*Par6 PBM mutants for the PDZ1 domain (Table 4, Figure A 5 – Figure A 7) to gain further insights into the Par3:Par6 interaction. When the C-terminal position (L0A) was mutated, the affinity was weakened to 2486 ± 357 μM. In the case of the -1 position (H1-A), the affinity was weakened to 964 ± 60 μM and in case of the -2 position (L-2A), the affinity was weakened to 4049 ± 1113 μM, respectively. Altogether, the determined affinities showed that mutagenesis of key interacting residues led to a loss of affinity, confirming that these residues are indeed important for the interaction with the Par3 PDZ1 domain.

In general, dissociation constants in the range of hundreds of μM have been reported for physiologically relevant PDZ-PBM interactions (Wiedemann et al. 2004; Stiffler et al. 2007; Fujiwara

et al. 2015). This as well as the results from cultured S2R cells and *Drosophila* embryos (Renschler et al. 2018) shows that the interaction of the Par6 PBM with the Par3 PDZ domains is of importance *in vitro* and *in vivo*.

Table 4: Dissociation constants determined by NMR CSPs experiments and subsequent line shape analysis for the *dm*Par3 PDZ1 domain in complex with different *dm*Par6 PBM mutants.

Ligand	K_d [μM]
***dm*Par6 L-2A**	4049 ± 1113
***dm*Par6 H-1A**	964 ± 60
***dm*Par6 L0A**	2486 ± 357

K_d values were determined by line shape fitting of NMR CSP experiments with TITAN (Waudby et al. 2016). Errors were estimated with bootstrapping statistics on 100 replica. The number of titration points and cross peaks analyzed for each interaction are summarized in Table A 1 and Table A 2. Adapted from Renschler et al. (Renschler et al. 2018) and reprinted with permission from AAAS.

4.1.6 Par3 can interact with two Par6 proteins simultaneously *in vitro*

It is known that the Par complexes form clusters covering the apical plasma membrane in polarized cells. However, the details of this assembly are not well understood. One prerequisite for the formation of higher order complexes is that multivalent proteins are involved. Multivalent proteins contain multiple independent binding sites which engage in a multitude of weak interactions usually in the μM-affinity range. Since both, the first and third PDZ domain of *dm*Par3, fulfill this requirement, I recorded $^{1}H,^{15}N$-TROSY spectra of the ^{15}N-labeled Par3 PDZ1-3 module containing all three PDZ domains (PDZ1-3 $\Delta\beta$2-3loop) and examined its Par6 binding capability.

The NMR spectra of the individual PDZ domains superimpose well with the NMR spectra of the Par3 PDZ1-3 module. Therefore chemical shift resonance assignments of the individual domains could be transferred to the PDZ1-3 module. As the position of a peak in the NMR spectrum depends on its chemical environment, identical chemical shifts mean identical chemical environments. As a conclusion, the Par3 PDZ domains are structurally largely independent from each other. Upon addition of unlabeled *dm*Par6 PBM to the PDZ1-3 construct, CSPs were observed (Figure 23D-F) which were comparable to the CSPs observed for the individual PDZ domains (Figure 19, Figure 22) (Renschler et al. 2018). This confirms that the Par3 PDZ domains can also function independent of each other and that *in vitro* one Par3 molecule can interact with two Par6 proteins via its PDZ domains at the same time. For that reason, Par3 potentially engages in weak, multivalent interactions with Par6 and might thereby promote the assembly of large Par complex cluster at the cell cortex *in vivo*.

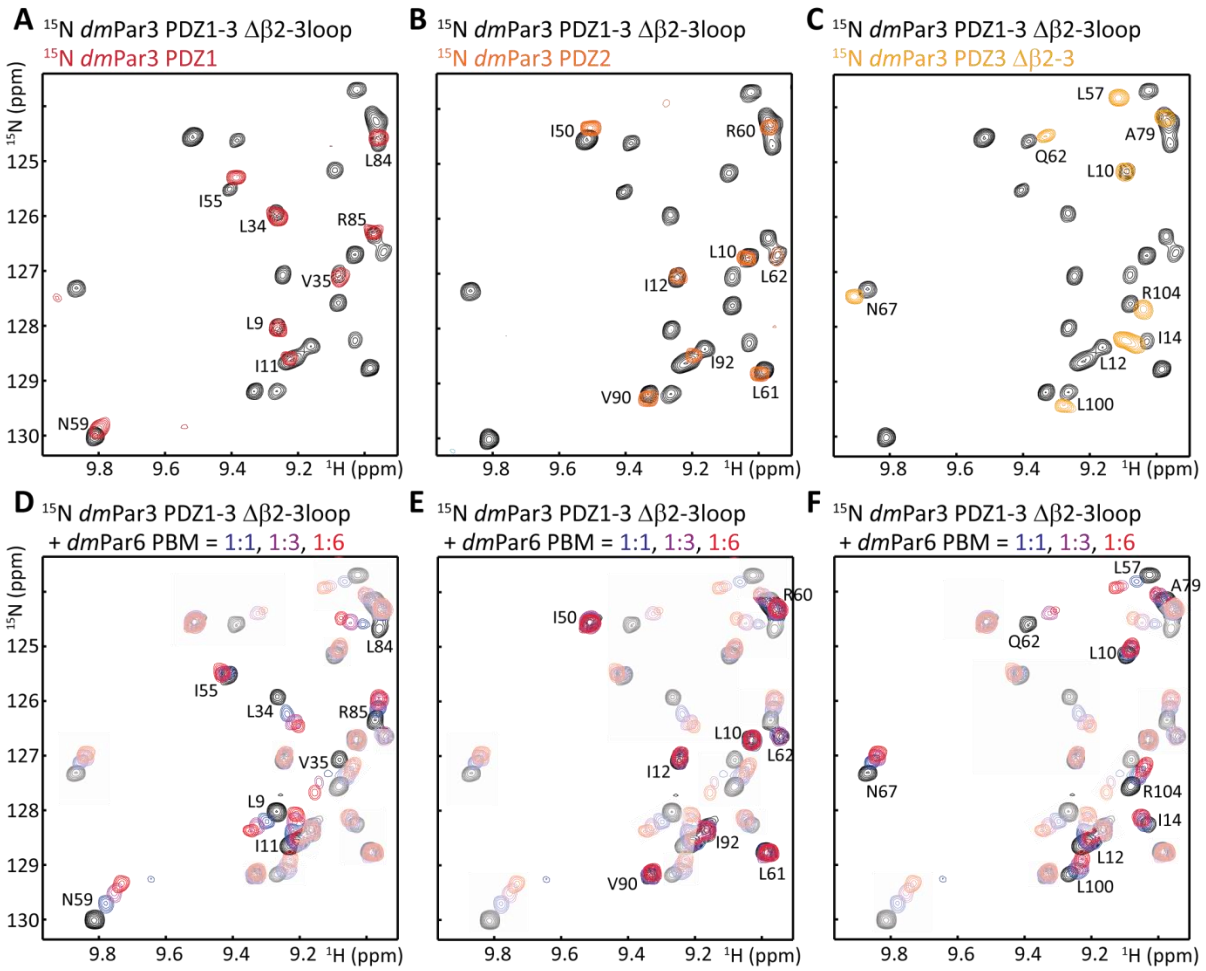

Figure 23: *dm*Par3 can interact simultaneously with two *dm*Par6 proteins. (A) – (C) Overlay of ^{1}H,^{15}N-TROSY spectra of the *dm*Par3 PDZ1-3 Δβ2-3loop module with the isolated PDZ1 **(A)**, PDZ2 **(B)** and PDZ3 Δβ2-3loop domains **(C)**. Resonance assignments are shown for the individual PDZ domains. **(D) – (F)** Overlay of ^{1}H,^{15}N-TROSY spectra of the *dm*Par3 PDZ1-3 Δβ2-3loop module in the absence (black) and presence of dmPar6 PBM as indicated. To highlight the changes of the single domains in the PDZ1-3 Δβ2-3loop module, all peaks not corresponding to PDZ1 **(D)**, PDZ2 **(E)** and PDZ3 Δβ2-3loop domains **(F)** are shown in opaque. NMR assignments were kindly provided by SW, PLS and SRB and are available under BMRB accession codes 27197 (*dm*Par3 PDZ1), 27203 (*dm*Par3 PDZ2) and 27198 (*dm*Par3 PDZ3 Δβ2-3loop). Adapted from Renschler et al. (Renschler et al. 2018) and reprinted with permission from AAAS.

4.1.7 The Par6 PBM can compete with the PBM of E-cadherin for Par3 binding

It is known that cell adhesion molecules from the nectin and cadherin families interact with Par3 and that they contain a conserved class II PBM which is highly similar to the Par6 PBM (Figure 26) (Renschler et al. 2018). For example, the mouse VE-cadherin PBM interacts with the third PDZ of the mouse Par3 protein (*mm*Par3) with a K_d of ~ 6 µM (Tyler et al. 2010) and therefore ~ 9-fold (PDZ3) and ~36-fold (PDZ1) tighter when compared to the *Drosophila* Par6 PBMs (Table 5). To investigate if the Par6 PBM could compete with such ligands, SRB performed NMR CSP-studies with the PBM of the *Drosophila* E-cadherin Shotgun (Shg).

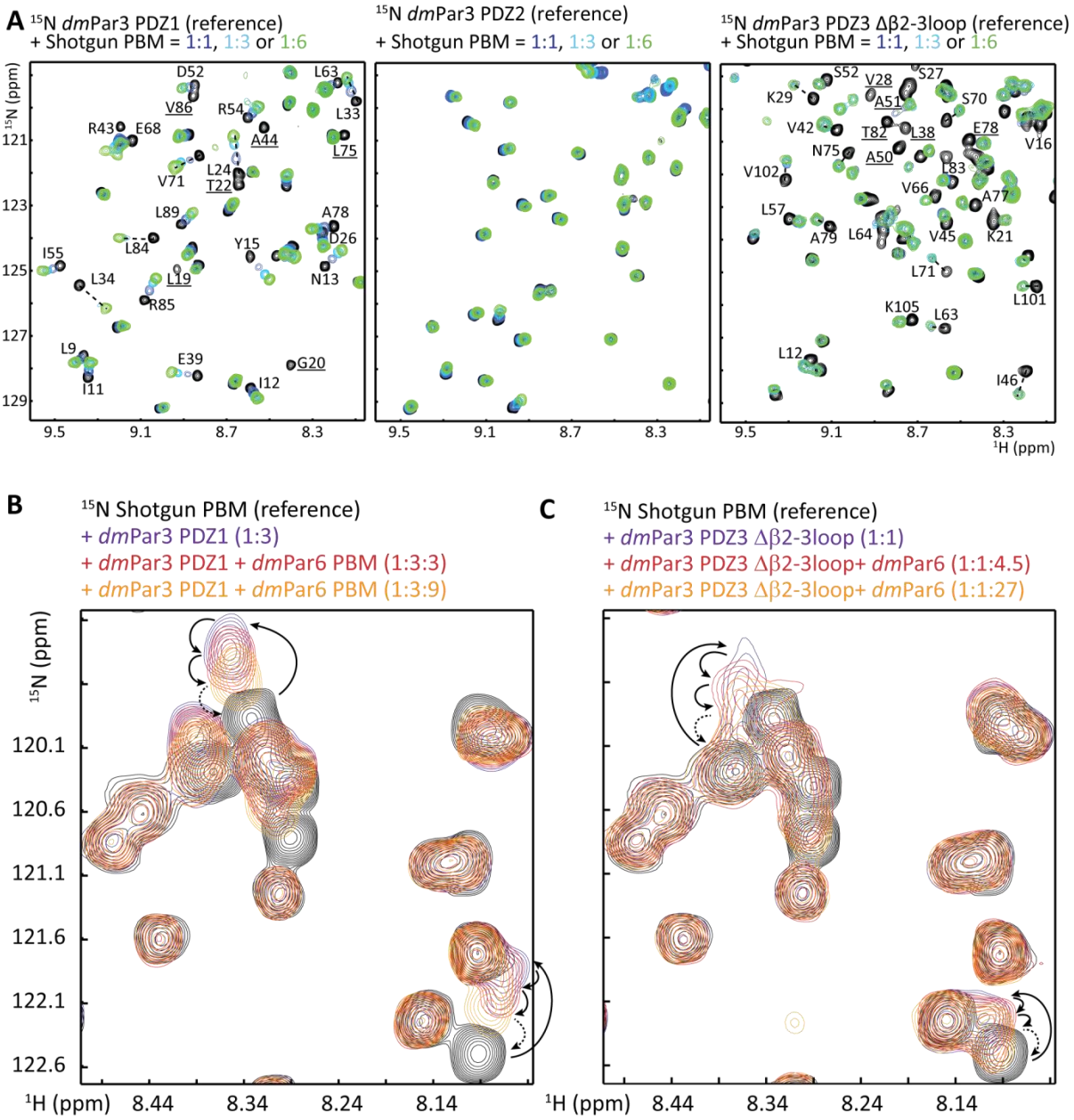

Figure 24: The Shg PBM binds to the Par3 PDZ1 and PDZ3 domains and competes with Par6 for Par3 binding. (A) Overlay of ^{1}H,^{15}N-HSQC spectra of the ^{15}N-labeled *dm*Par3 PDZ1 (left, black), PDZ2 (mid, black) and PDZ3 Δβ2-3loop domains (right, black) in absence and upon step-wise addition of the Shg PBM as indicated. NMR spectra were recorded by SRB. **(B)** Overlay of ^{1}H,^{15}N-HSQC spectra of the ^{15}N-labeled GB1-Shg PBM fusion in the absence (black) or presence of *dm*Par3 PDZ1 domain (purple) and upon step-wise addition of the *dm*Par6 PBM (red and orange). Arrows indicate the successive reversal of the chemical shifts from the Shg PBM:PDZ complex towards the unbound Shg PBM. Spectra were recorded by SW and me. **(C)** as **(B)**, but for the *dm*Par3 PDZ3 Δβ2-3loop domain. Adapted from Renschler et al. (Renschler et al. 2018) and reprinted with permission from AAAS.

To this end, she added increasing amounts of unlabeled Shg PBM to ^{15}N-labeled *dm*Par3 PDZ domains (Figure 24A). These studies revealed that PDZ1 and PDZ3 interact with the Shg-PBM similar to the Par6 PBM and show large CSPs for numerous cross peaks in the ^{1}H,^{15}N-HSQC spectra during the course of the titration (Figure 24A) (Renschler et al. 2018).

Contrary to PDZ1 and PDZ3, PDZ2 showed only few changes (Figure 24A) (Renschler et al. 2018). Subsequent line shape fitting analysis performed by me yielded K_d values 128 ± 4 µM for the PDZ1, 954 ± 45 µM for the PDZ2 and 0.6 ± 0.1 µM for the PDZ3 domain (Table 5, Figure A 8, Figure A 13 and Figure A 22).

Next, I used ^{15}N-labeled Shg PBM to investigate whether the Par6 PBM can compete with the Shg PBM for Par3 PDZ binding in a series of NMR experiments that SW and I recorded. First, we investigated the interaction of PDZ1 or PDZ3 domain with ^{15}N-labeled Shg PBM by recording ^{1}H,^{15}N-correlation spectra of the peptide without and with unlabeled *dm*Par3 PDZ1 or PDZ3 domain. For both PDZ domains, complex formation could be observed by chemical shift changes in the ^{1}H,^{15}N-correlation spectra of the Shg PBM (Figure 24B, C). Then, unlabeled Par6 PBM was added step-wise. This led to changes in the spectra of the Shg-PBM indicating the release of Shg from the Shg PBM:PDZ complex since the chemical shift changes reverted towards the free state of the Shg PBM (Figure 24B, C). This proves the Par6 PBM can directly compete with the Shg PBM for Par3 PDZ binding. Of note, the large difference in binding affinities is reflected in the high stoichiometric excess of Par6 PBM over Shg PBM necessary for PDZ3 competition (Figure 24C). Finally, to address the question of direct competition of different PBMs for Par3 PDZ binding *in vivo* would require additional information. Detailed analyses in cells of the subcellular concentrations of Par3, Par6 and other binding partners, of the dissociation constants of the ligands within the fully assembled Par complex as well as an exact chronological determination of the binding process would be required to answer this question. Without doubt, these questions are challenging but indeed very interesting. A step in this direction is presented in the next chapter of my thesis where I investigate the specificities of the individual Par3 PDZ domains towards different ligands.

4.1.8 The PDZ:PBM interaction is conserved in the human Par3 and Par6 proteins

Co-immunoprecipitation experiments performed by CH and AM with human embryonic kidney (HEK) 293T cells cotransfected with human Par3 (*hs*Par3) and Par6α (*hs*Par6α) constructs demonstrated, that the human Par3 and Par6α proteins also interact in a PBM dependent manner as their *Drosophila* orthologs (Renschler et al. 2018).

In order to investigate whether the specificities as well as the interaction mode of the individual Par3 PDZ domains are conserved between the human and the *Drosophila* proteins, I performed NMR studies on the human Par3 and Par6 proteins. Interestingly, the ^{1}H,^{15}N-HSQC spectra of the human PDZ1 domain of Par3 did not show well dispersed cross peaks (Figure 25A) (Renschler et al. 2018) (PLS and A. Kiessling, personal communication) and thus is characteristic of an unfolded protein (Kwan et al. 2011). Therefore, NMR titration experiments were not feasible. However, fusing the *hs*Par6α PBM to the C-terminus *hs*Par3 PDZ1 separated by a 15-aa GS-linker dramatically increased the quality of the ^{1}H,^{15}N-HSQC spectra and showed well dispersed cross peaks (Figure 25A). For that reason we can conclude that the *hs*Par6α PBM induces the folding of the PDZ1 domain and thus interacts with the *hs*Par3 PDZ1 domain. In contrast to the PDZ1 domain, the PDZ2 and PDZ3 domains of the human protein showed well dispersed cross peaks of folded proteins in the ^{1}H,^{15}N-correlation spectrum. Hence, NMR titration experiments could be performed. The ^{1}H,^{15}N-correlation spectrum of ^{15}N-labeled *hs*Par3 PDZ2 domain displayed some but substantial CSPs (Figure 25B), whereas the ^{1}H,^{15}N-correlation spectrum of ^{15}N-labeled *hs*Par3 PDZ3 domain displayed numerous large CSPs upon Par6α addition (Figure 25C). All CSPs of PDZ2 and PDZ3 could be mapped to the PBM binding groove of the respective PDZ domains from human (PDZ2) or rat (PDZ3) indicating a canonical PDZ:PBM interaction (Figure 25D, E). Taken together, these results show that the Par3 PDZ : Par6 PBM interactions and the Par3 PDZ domain functions are conserved to a large extent in humans and flies.

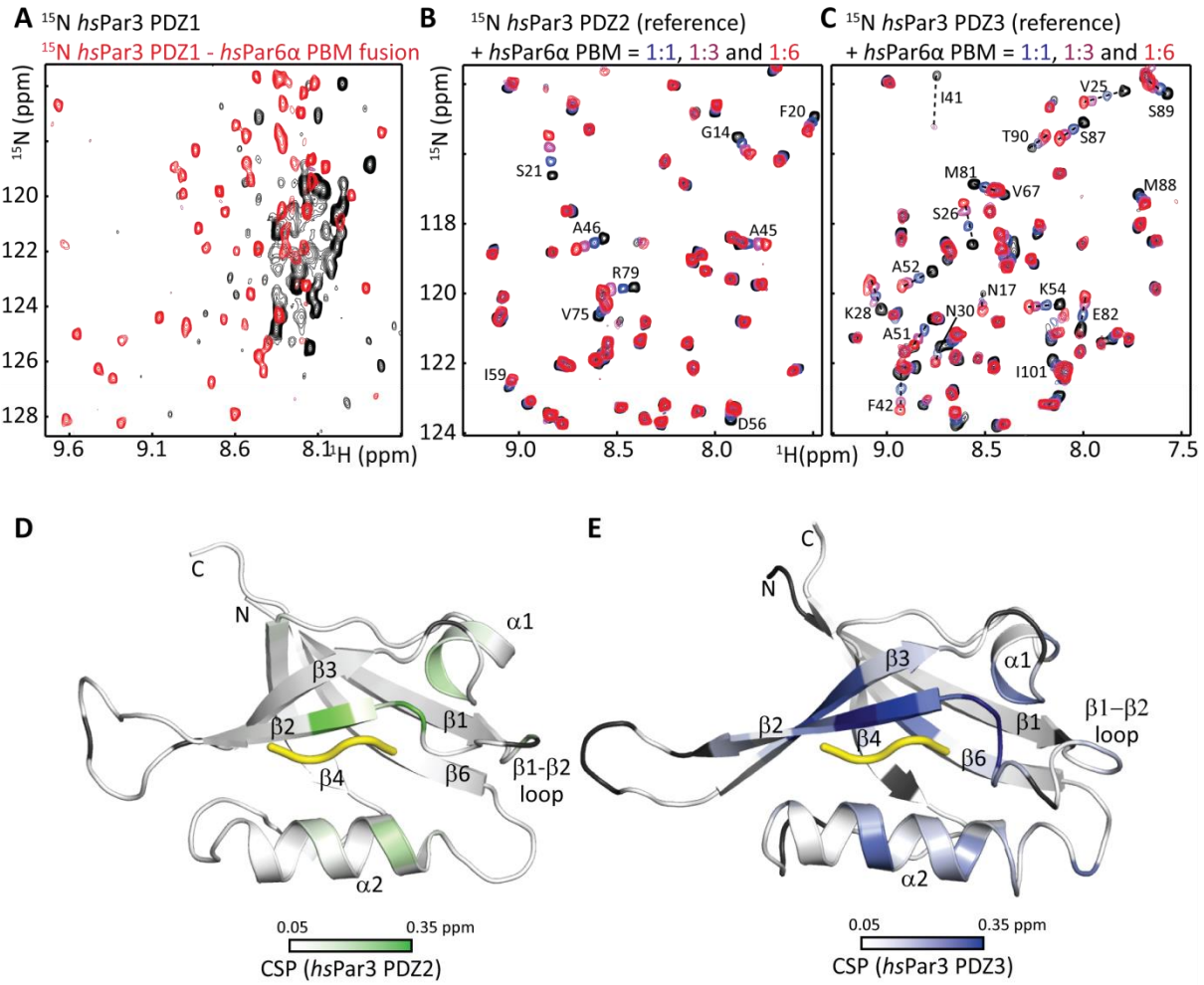

Figure 25: The PDZ:PBM interaction is conserved in the human Par3:Par6 complex. (A) Overlay of ^{1}H,^{15}N-correlation spectra of the *hs*Par3 PDZ1 domain in isolation (black) and the *hs*Par3 PDZ1 domain fused to the *hs*Par6α PBM (red). The absence of well dispersed cross peak indicates the unfolded state of the isolated PDZ1 domain. Data are representative of at least four independent experiments for the PDZ1 domain. **(B,C)** Overlay of ^{1}H,^{15}N-correlation spectra of the PDZ2 **(B)** and the PDZ3 **(C)** domains in the absence and presence of *hs*Par6α PBM peptide as indicated. Assignments of *hs*Par3 PDZ2 and PDZ3 domains were kindly provided by SW and are available under the BMRB accession codes 27204 (*hs*Par3 PDZ2) and 27205 (*hs*Par3 PDZ3). **(D,E)** *hs*Par6α induced CSPs mapped onto the human Par3 PDZ2 domain **(D)** (PDB ID: 2kom (Jensen et al. 2010)) and rat Par3 PDZ3 domain **(E)** (PDB ID: 2k20 (Feng et al. 2008)) and colored from white (CSP ≤ 0.05 ppm) to green **(D)** or blue **(E)** (CSP = 0.35 ppm). Dark blue indicates residues broadened beyond detection in PDZ3. Secondary structure elements are labeled (for PDZ2 β1: aa 5-12, β2: aa 20-24, β3: aa 35-40, α1: aa 45-49, β4: aa 56-61, β5: aa 64-65, α2: aa 71-80, β6: aa 86-93; for PDZ3 β1: aa 6-14, β2: aa 25-31, β3: aa 38-46, α1: aa 51-54, β4: aa 62-67, β5: aa 70-71, α2: aa 77-89, β6: aa 97-105). The Par6 core PBM is shown in yellow and was modeled by superposition of the *dm*Par3 PDZ1:PBM and PDZ2 and PDZ3 structures. Adapted from Renschler et al. (Renschler et al. 2018) and reprinted with permission from AAAS.

4.1.9 The Par6 PBM is important for PAR complex formation

In this study, I identified a previously unknown PBM in the C-terminus of Par6 that interacts canonically with the Par3 PDZ1 and PDZ3 domains. I could show that this interaction is conserved in human and *drosophila* Par3 and Par6 proteins. Furthermore, I was able to show that the interaction is crucial *in vitro*. However, *in vivo* data suggests that the PBM and the PDZ domain of Par6 function in redundancy for Par6 localization in *Drosophila* embryonic epithelia (Renschler et al. 2018).

In previous studies, the Par3:Par6 interaction has been controversial (Joberty et al. 2000; Li et al. 2010; Lin et al. 1999; Nagai-Tamai et al. 2002; Suzuki et al. 2001). However, no heterodimerization of the Par3 PDZ1 and Par6 PDZ domains was detected by GST-pull down (Figure 20), NMR or CoIP studies or in recruitment assays in S2R cells (Renschler et al. 2018). Worth mentioning are the interactions of the first PDZ domain Par3 homologs in humans and mice with highly similar class II PBM ligands of cell adhesion proteins (Figure 26) (Ebnet et al. 2001; Takekuni et al. 2003; Iden et al. 2006; Itoh et al. 2001; Ebnet et al. 2003; Lin et al. 1999; Latorre et al. 2005; Nakayama et al. 2013).

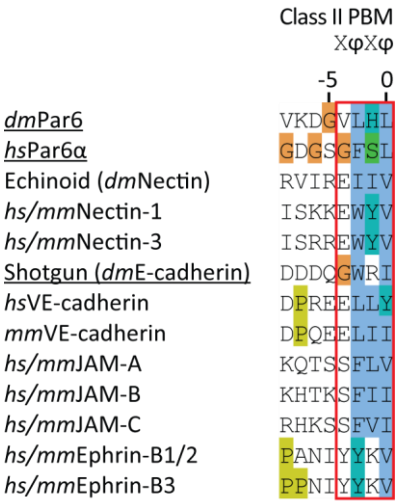

Figure 26: Known cell adhesion interaction partners of Par3. Amino acid sequences of known Par3 interaction partners in the context of cell adhesion (Ebnet et al. 2001; Takekuni et al. 2003; Iden et al. 2006; Itoh et al. 2001; Ebnet et al. 2003; Lin et al. 1999; Latorre et al. 2005; Nakayama et al. 2013) are aligned with the *dm*Par6 PBM and color coded according to conservation by ClustalX (Larkin et al. 2007). PBMs used for NMR competition assays (Figure 24) as well as the *0*Par6α (Figure 25) are underlined. The residues equivalent to the *dm*Par6 PBM facilitating interactions with the *dm*Par3 PDZ1 (Figure 29A) (Renschler et al. 2018) are boxed in red. Adapted from Renschler et al. (Renschler et al. 2018) and reprinted with permission from AAAS.

In addition, SRB showed that the class II PBM of Shg (the *Drosophila* E-cadherin) interacts with *dm*Par3 PDZ1 and PDZ3 domain (Figure 19 and Figure 22) (Renschler et al. 2018). Hence, the Par3:Cadherin interaction is also conserved between *Drosophila* and humans. Taken together, there is strong support of the Par3 PDZ1 and PDZ3 favoring class II PBMs to recruit cell adhesion and polarity proteins in order to establish and maintain cell polarity via the PAR complex. However, a more detailed analysis of the individual binding specificities of the Par3 PDZ domains including a broader range of ligands is needed to support this notion. Scaffolding complexes often use multivalent interactions to assemble different parts of signaling cascades since protein domains can fold and function independently (Pawson & Nash 2003). One well-known mechanism is the tandem arrangement of PDZ domains inside scaffolding proteins (Tsunoda et al. 1997). This holds true for Par3 as PDZ1 and PDZ3 can independently interact with the Par6 and Shg PBM *in vitro* (Figure 24) (Renschler et al. 2018). Therefore, the Par3 PDZ1 and PDZ3 domains function redundantly and allow

one Par3 molecule to interact with two PBMs simultaneously. Additionally, homo-oligomerization of Par3 (Zhang et al. 2013) and hetero-dimerization of Par6 and aPKC (Hirano et al. 2005) provide further scaffolds to assemble large self-organizing PAR complex networks at the cell cortex *in vivo*.

4.2 Specificities of the individual *dm*Par3 PDZ domains for cell polarity proteins

Many different ligands of the Par3 PDZ domains which interact with at least one of the three Par3 PDZ domains have been reported in literature (Figure 10). Those ligands include class I PBMs such as Smash (Beati et al. 2018), Insc (Schober et al. 1999; Wodarz et al. 1999; Culurgioni & Mapelli 2013; Lu & Johnston 2013) and Stan (Wasserscheid et al. 2007), class II PBMs such as Ed (Wei et al. 2005), Shg (Figure 24A) (Wei et al. 2005; Bulgakova et al. 2013; Renschler et al. 2018) and Par6 (Figure 19 and Figure 22) (Renschler et al. 2018) as well as the class III PBM of α-cat (Iden et al. 2006). Besides known interaction partners, other PBMs are present within the cellular environment of Par3 (Figure 2 and Figure 5) such as the Crb class I PBM and the aPKC class III PBM. The Crb PBM has been reported to interact with the PDZ domains of Par6 (Lemmers et al. 2004; Whitney et al. 2016) and Pals1/ Std (Li et al. 2014; Ivanova et al. 2015) whereas no interaction partners of the aPKC PBM are known to date. All those PBMs might link Par3 with its functions in adherens junction assembly (Figure 2), sequestration of the Par6/aPKC module (Figure 2) as well as cortical assembly of the Pins complex (Figure 5) (Harris 2017). However, only sparse information about the specificities of the Par3 PDZ domain is available. These specificities are derived from biased phage display data over-represented in hydrophobic amino acids (Yu et al. 2014). In addition, structural information of the Par3 PDZ domains in complex with ligands is limited to the third PDZ domain of the rodent proteins (Feng et al. 2008; Tyler et al. 2010). Of note, sequence comparison between the Par3 PDZ domains revealed a high degree of similarity between the individual domains (Figure 27). However, based on the structural information and the sequence comparison it seemed unlikely to expect large differences in the specificities between the Par3 PDZ domains.

Figure 27: (continued) Par3 PDZ domain protein sequences were aligned with MUSCLE (Edgar 2004), edited manually if necessary to match Par3 PDZ structures (PDB ID: 5oak for PDZ1, the PDZ2:Insc complex presented in Figure 29C and D for PDZ2 and PDB ID 2koh for PDZ3) and color-coded with ClustalX according to conservation (Larkin et al. 2007). Secondary structure elements are depicted as blue boxes. Residues interacting with the *dm*Par6 PBM (Figure 29A), the Shg PBM (Figure 29B), or the Insc PBM (Figure 29C, D) are indicated by cyan, dark blue and green spheres on top of the corresponding PDZ domain. The region deleted in the *dm*Par3 PDZ3 Δβ2-3 loop construct is indicated by a black box. Dashed lines highlight conserved residues in PDZ3 important for ligand binding in PDZ1 and PDZ2. Residues interacting with the *dm*Par3 FID-motif (Figure 35C, D) are highlighted by purple spheres on top of the sequence of the *dm*Par3 PDZ3 domain.

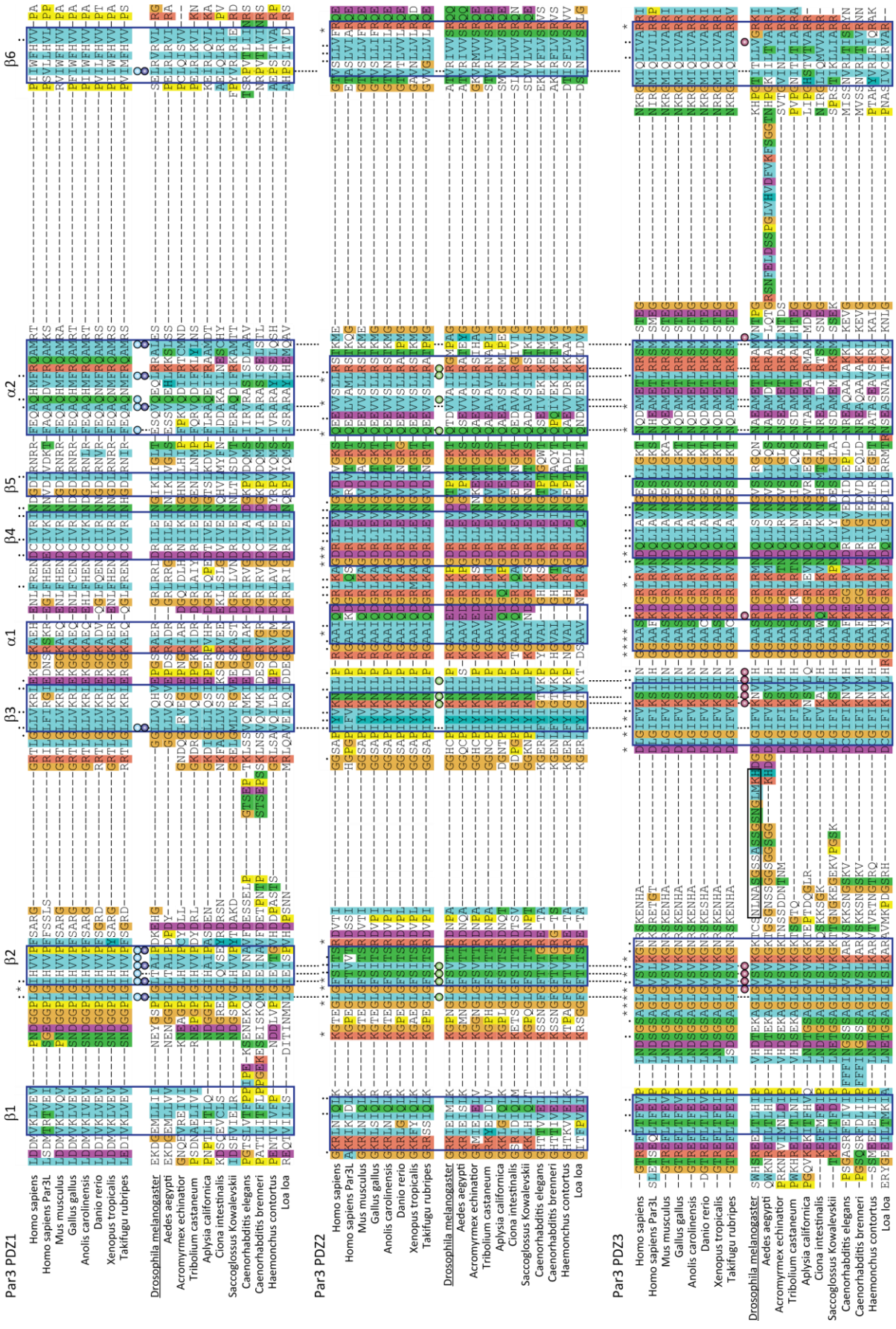

Figure 27: Structure-based sequence alignment of the Par3 PDZ domains. Legend continued on previous page.

In order to provide insights into the specificities of the Par3 PDZ domains and to provide information about the structural basis of these specificities, I performed NMR and x-ray crystallography studies of the PBM listed above and the *dm*Par3 PDZ domains.

Furthermore, I included the internal PBM of Std in this analysis. The Std PBM interacts with the Par6 PDZ domain (Penkert et al. 2004; Wang et al. 2004; Kempkens et al. 2006). At the same time, Std and Par3 interact independently of the Std PBM (Krahn, Bückers, et al. 2010). However, the Par3:Std interaction relies on a region C-terminal of the Par3 KBD (Krahn, Bückers, et al. 2010). Therefore, the Std PBM serves as a negative control.

4.2.1 Contributions

The results presented here have been obtained during the course of my PhD thesis. Previous diploma and bachelor studies conducted in the laboratory of Silke Wiesner by Paulin L. Salomon (Salomon 2012), myself (Renschler 2013), Susanne R. Bruekner (Brückner 2014) and Benjamin Schroeder (Schroeder 2014) already set the foundation of this research and contributions are indicated as follows: SRB (Susanne R. Bruekner), PLS (Paulin L. Salomon), BS (Benjamin Schroeder), SW (Silke Wiesner). Results obtained by myself and already published are indicated by citing the respective papers (Renschler et al. 2018; Beati et al. 2018).

4.2.2 *dm*Par3 PDZ1 and PDZ2, but not the PDZ3 have distinct ligand specificities

To assess the specificities of the individual Par3 PDZ domains in greater detail, I examined the binding capabilities of a variety of reported Par3 PDZ ligands with biological relevance in order to sample the natural PBM sequence space of the *dm*Par3 PDZ domains.

To this end, the C-terminal eight amino acids of the class I PBMs of Insc, Crb and Stan as well as the class II PBMs of Ed and the class III PBM of α-cat were fused to GB1, expressed and purified for NMR titration experiments (Figure 15 and Figure 28). In addition, the previously published interactions of the class I PBM of Smash (Figure 28) (Beati et al. 2018) and the class II PBMs of *dm*Par6 (Figure 19 and Figure 22) and Shg (Figure 24A) (Renschler et al. 2018) with the *dm*Par3 PDZ domains were included in this analysis. Furthermore, the class III PBM of aPKC was added to investigate the possibility of an additional interaction site between aPKC and Par3 besides the well-studied Par3 KBD:aPKC kinase domain interaction (Figure 28) (Wang et al. 2012; Soriano et al. 2016). In order to probe binding to an internal PBM, we choose the Std PBM that is a known ligand of the Par6 PDZ domain (Penkert et al. 2004; Wang et al. 2004; Kempkens et al. 2006).

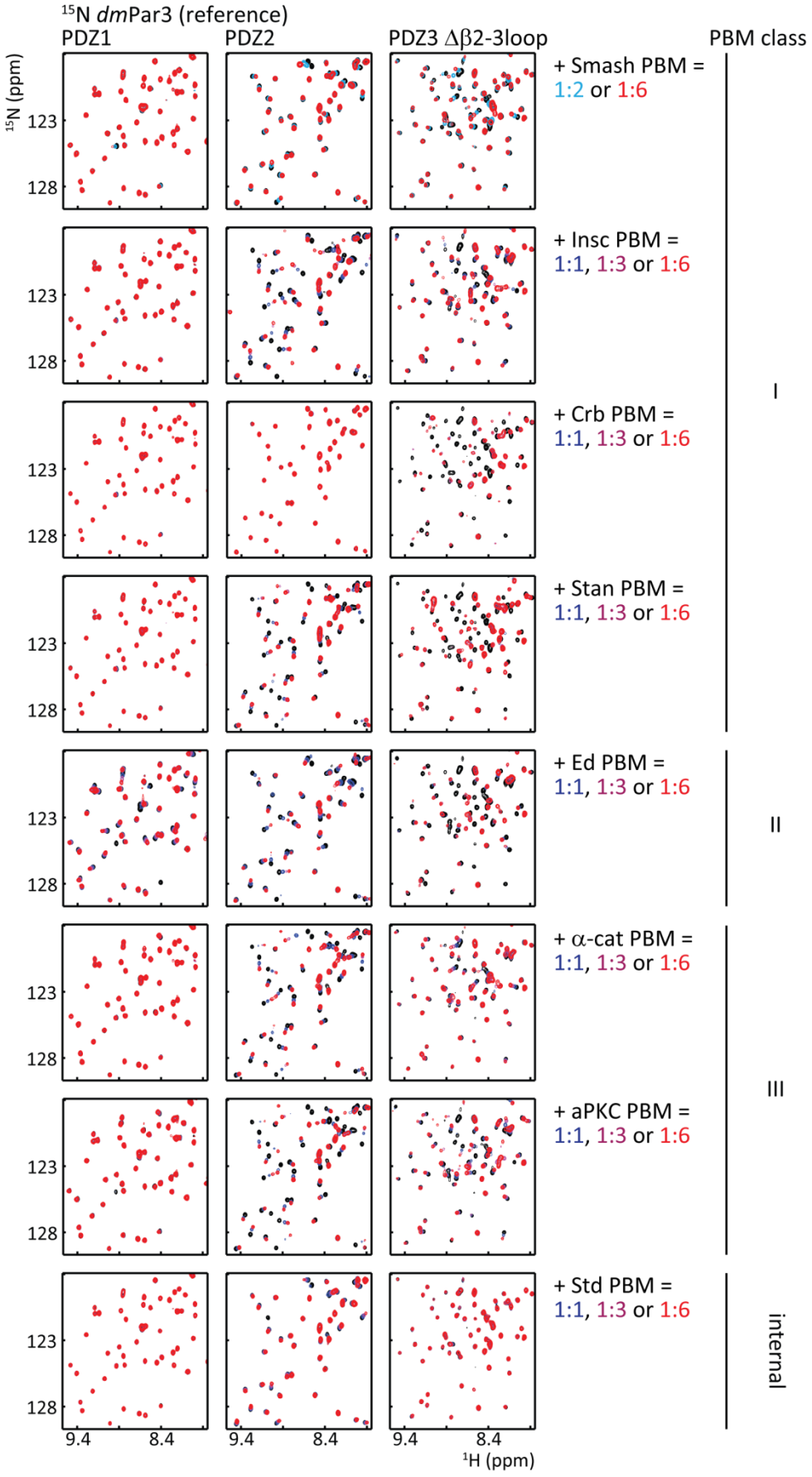

Figure 28: NMR titration experiments of the *dm*Par3 PDZ domains with different PBMs. Legend continued on next page.

Figure 28: (continued) Overlay of a representative region of the $^{1}H,^{15}N$-correlation spectra of the *dm*Par3 PDZ1, PDZ2 and the PDZ3 Δβ2-3loop domains in the absence (black) and presence of stoichiometric amounts of PBM peptides as indicated. SRB recorded data of the Insc and Ed PBMs. BS recorded data of the α-cat and aPKC PBMs. Spectra of the Smash NMR titration experiments are already published (Beati et al. 2018).

Interestingly, despite containing an internal PBM the Std PDZ domain can interact with Par3 via a region C-terminal of the Par3 KBD (Krahn, Bückers, et al. 2010).

Binding affinities of the individual dmPar3 PDZ domains reveal a distinct specificity profile for PDZ1 and PDZ2

To obtain specificity profiles for the individual *dm*Par3 PDZ domains, I evaluated existing NMR CSP data recorded by SRB (Insc, Ed, Shg and *dm*Par6 with PDZ1, PDZ2 and PDZ3 Δβ2-3loop, Figure 19, Figure 22, Figure 24A and Figure 28, respectively) (Brückner 2014; Renschler et al. 2018) and BS (α-cat and aPKC with PDZ1, PDZ2 and PDZ3 Δβ2-3loop, Figure 28) (Schroeder 2014) by 2D lineshape fitting analysis with TITAN (Waudby et al. 2016). Additionally, I performed CSP experiments and analyzed CSP data for Smash, Crb, Stan and Std for PDZ1, PDZ2 and PDZ3 Δβ2-3loop (Figure 28). Lineshape fits are presented in Figure A 3 to Figure A 25 in the appendix.

Interestingly, the *dm*Par3 PDZ1 domain shows a clear selectivity profile. Out of the ten tested PBMs, the *dm*Par3 PDZ1 domain only interacts with class II ligands (Ed, Shg and *dm*Par6) and shows a clear preference for PBMs with a large hydrophobic residue at the very C-terminus of the PBM as in Shg (128 ± 4 μM) and *dm*Par6 (216 ± 4 μM) (Table 5). No significant CSPs were observed for the other PBMs (Figure 28) and therefore K_d values could not be determined for these ligands. In contrast, the Par3 PDZ2 domain showed a clear preference for a number of PBMs (Table 5). However, in contrast to the PDZ1 domain this specificity does not seem to be limited to the general classification of PBMs. The PDZ2 domain interacted with the class I PBM of Stan (31 ± 1 μM) and Insc (107 ± 2 μM), the class III PBM of aPKC (22 ± 1 μM) and α-cat (84 ± 2 μM) and with the class II PBM of Ed (226 ± 6 μM) (Table 5). In contrast, binding of the PBMs of Smash (880 ± 33 μM), Shg (954 ± 45 μM) and Std (762± 60 μM) was weak (Table 5) or not detectable in the case of Crb (Figure 28) and Par6 (Figure 22) (Renschler et al. 2018). The weak interaction with the Std PBM may be expected as this PBM was selected as a negative control since the Par3:Std interaction relies on the Std PDZ domain and not on the Std PBM (Krahn, Bückers, et al. 2010). This is supported by the notion that high micromolar PDZ:PBM affinities may not be physiological relevant.

Table 5: Dissociation constants determined by NMR CSPs experiments and subsequent 2D line shape fitting analysis for the *dm*Par3 PDZ domains in complex with different PBMs.

ligand	class	sequence	K_d [µM]		
			PDZ1	PDZ2	PDZ3 Δβ2-3loop
Smash	I	DGIKF**S**C**V**	n.d.	880 ± 33	561 ± 29
Insc		LTRQE**S**F**V**	n.d.	107 ± 2	275 ± 8
Crb		KPPPE**R**L**I**	n.d.	n.d.	16 ± 1
Stan		IDDDE**T**T**V**	n.d.	31 ± 1	5.5 ± 0.3
Ed	II	RVIRE**I**I**V**	656 ± 58	226 ± 6	19 ± 1
Shg *		DDDQG**W**R**I**	128 ± 4	954 ± 45	0.6 ± 0.1
***dm*Par6 ***		VKDGV**L**H**L**	216 ± 4	n.d.	54 ± 1
α-cat	III	FQSPA**D**A**V**	n.d.	84 ± 2	643 ± 30
aPKC		LMSLE**D**C**V**	n.d.	22 ± 1	101 ± 3
Std	internal	PHRE**M**A**VD**CPD	n.d.	762 ± 60	n.d.

K_d values were determined by 2D line shape fitting of NMR CSP experiments with TITAN (Waudby et al. 2016). Errors were estimated with bootstrapping statistics on 100 replicates. The number of titration points and cross peaks analyzed for each interaction as well contributions from others are summarized in Table A 1 and Table A 2. n.d. refers to not detectable and means no detectable CSPs in NMR CSPs experiments. Asterisks indicate K_d values already published in Renschler *et al.* (Renschler et al. 2018) and reprinted with permission from AAAS.

The dmPar3 PDZ3 has highly promiscuous binding capabilities

In contrast to the PDZ1 and PDZ2 domain, the third PDZ domain of *dm*Par3 did not show a distinct specificity profile in my CSP studies. CSPs in the $^{1}H,^{15}N$-HSQC spectrum of *dm*Par3 PDZ3 Δβ2-3loop were observed for all tested PBMs with the notable exception of the internal PBM of Std (Figure 28 and Table 5). Subsequent line shape fitting analysis revealed a very tight binding of the Shg PBM (class II) with a dissociation constant of 0.6 ± 0.1 µM. Nonetheless, other tight interactions include Stan (5.5 ± 0.3 µM, class I), Crb (16 ± 1 µM, class I), Ed (19 ± 1 µM, class II), *dm*Par6 (54 ± 1 µM, class II) and somewhat weaker aPKC (101 ± 3 µM, class III) and Insc (275 ± 8 µM, class I). Besides, the class I PBM of Smash (561 ± 29 µM) and the class III PBM of α-cat (643 ± 30 µM) bind the *dm*Par3 PDZ3 domain with affinities in the high micromolar range. We can thus conclude that the third PDZ domain of *dm*Par3 has a unique but highly promiscuous specificity.

4.2.3 The ligand specificities of *dm*Par3 PDZ1 and PDZ2 can be related to their complex structures

To investigate the interactions probed by NMR CSPs experiments in more detail, we aimed at solving the 3D structures of Par3 PDZ:PBM complexes for each PDZ domain with ligands of the different PBM classes.

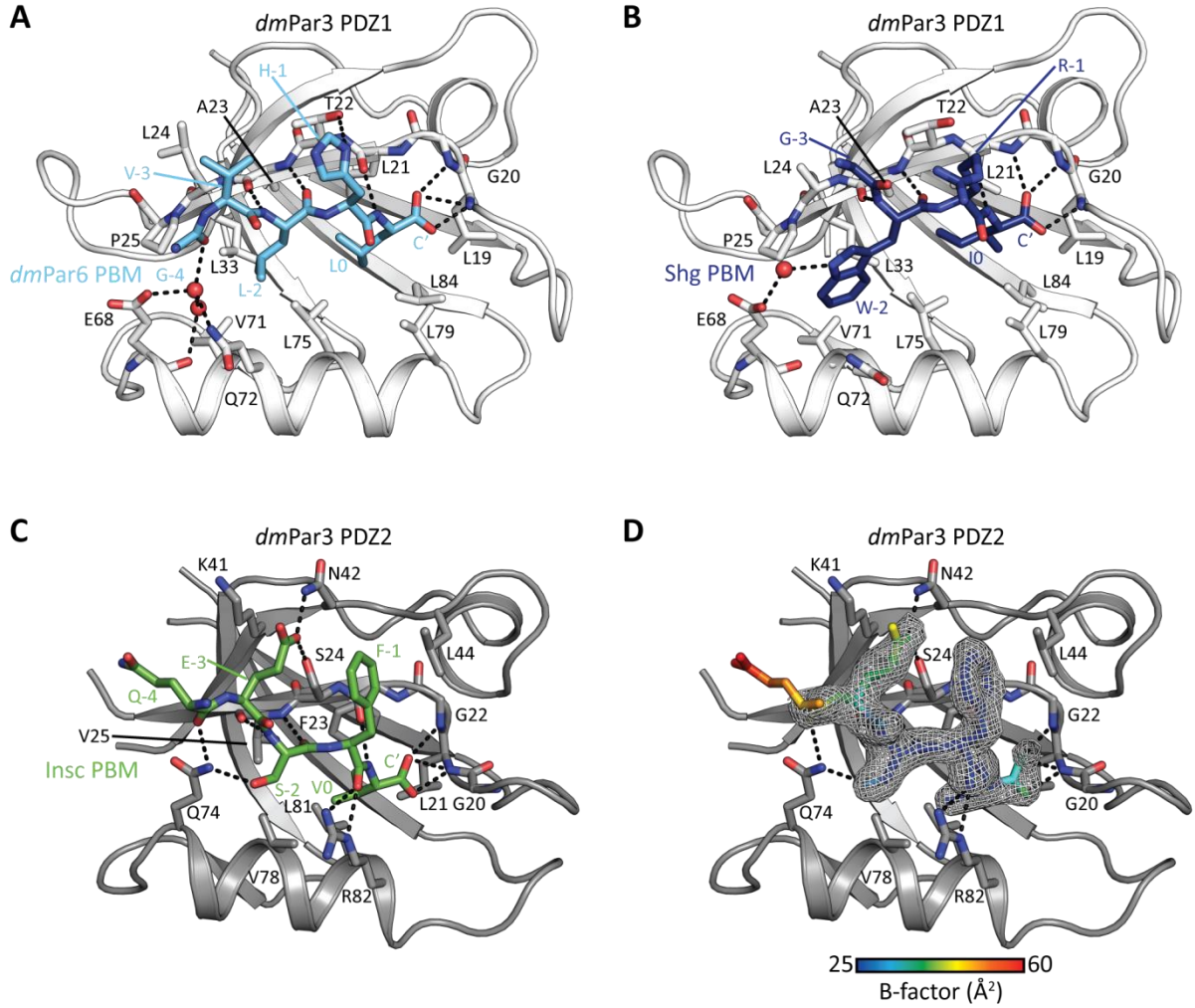

Figure 29: Ligand recognition by the *dm*Par3 PDZ1 and PDZ2 domains. (A) Cartoon representation of the *dm*Par3 PDZ1 domain (white) in complex with the *dm*Par6PBM (cyan) (pdb ID: 5oak). Hydrogen bonds are depicted as dashed black lines. Adapted from Renschler et al. (Renschler et al. 2018) and reprinted with permission from AAAS. **(B)** Cartoon representation of the *dm*Par3 PDZ1 domain (white) in complex with the Shg PBM (darkblue) (PLS and (Renschler 2013)), otherwise as in **(A)**. **(C)** Cartoon representation of the *dm*Par3 PDZ2 domain (grey) in complex with the Insc PBM (green), otherwise as in **(A).** The structure statistics for the *dm*Par3 PDZ2:Insc PBM complex are detailed in Table 32. **(D**) Cartoon representation of the *dm*Par3 PDZ2 domain (grey) in complex with the Insc PBM. The atoms of the PBM are colored according to their B-factor ranging from blue (25 ≤ Å) to red (60 ≥ Å), otherwise as in **(C)**. The iterative-build OMIT electron density map (Terwilliger et al. 2008) of the Insc PBM is shown as 2Fo-Fc map contoured at a sigma level of 1.0 to highlight the presence of the PBM in the PBM binding groove.

So far, we were successful in determining two crystal structures of the *dm*Par3 PDZ1 domain, namely the PDZ1 domain in complex with the class II PBMs of Par6 (SRB; PDB ID: 5oak; Figure 29A) (Renschler et al. 2018) and Shg (PLS and (Renschler 2013); Figure 29B) as well as the crystal structure of the PDZ2 domain in complex with the class I PBM of Insc (Figure 29C, D and Table 32). All structures show the canonical interaction of a PBM with a PDZ domain by augmentation of the β-sheet consisting of the PDZ β2- and β3-strands (Figure 29). That is, the backbone NH and CO groups of the PBM positions 0, -1 and -2 participate in hydrogen bonds with the backbone NH and CO groups of the β2-strand of the PDZ domain. In addition, as for all canonical PDZ-PBM interactions, the C-termini are forming extensive hydrogen bonding networks with the respective carboxylate binding loops comprising of L19, G20 and L21 (Figure 29).

The structures of the Par3 PDZ1 domain in complex with the PBMs of *dm*Par6 (Figure 29A) (Renschler et al. 2018) and Shg (Figure 29B) reveal the structural basis for the narrow specificity profile of PDZ1 domain (Figure 31A and Table 5). The residues of both PBMs at the 0 position, I and L, respectively, are buried in a deep hydrophobic pocket of the PDZ1 domain. This pocket consists of residues in the carboxylate binding loop (L19), the β2- (L21, A23) and β6- strands (L84, V86) and the α2-helix (L75, L79). The hydrophobic residues at the -2 position W (Shg) and L (*dm*Par6) are inserted into a wide hydrophobic pocket consisting of residues in the β2- (A23, P25) and β3- strands (L33) and the α2-helix (V71, L75). In contrast to the *dm*Par3 PDZ1:Shg complex, the *dm*Par3 PDZ1 domain and the *dm*Par6 PBM engage in additional interactions. H-1 of the *dm*Par6 PBM forms a hydrogen bridge to the hydroxyl group of T22 of the PDZ1 domain and V-3 interacts with a hydrophobic patch formed by the methyl group of T22 and L24. Noteworthy, the CO group of G-4 of the *dm*Par6 PBM forms a hydrogen bond network mediated by two water molecules with the sidechains of E68 and Q72 (Figure 29A). In contrast, only the side chain of E68 is involved in a water mediated hydrogen bond network with the W-2 indole NH group in the *dm*Par3 PDZ1:Shg complex (Figure 29B). In the *dm*Par3 PDZ1:*dm*Par6 complex, the hydrophobic pocket surrounding the -2 PBM position is sealed by water-mediated hydrogen bond network between the E68-Q72 residues that orients Q72 towards the -2 binding groove. Moreover, electron density was observed for additional residues of the Par6 PBM forming a second antiparallel β-strand (Renschler et al. 2018). However, since those residues displayed a high B-factor, it is not likely that those residues form a stable structure. In line with this argument, additional NMR experiments conducted by SRB and SW did not provide any evidence of the presence of the second β-strand in the *dm*Par3 PDZ1:*dm*Par6 complex in solution (SW, SRB personal communication).

To determine the structure of the *dm*Par3 PDZ2 domain in complex with a class I ligand, I fused the Insc PBM (LTRQESFV) with a seven amino acid long GS linker sequence to the C-terminus of the

*dm*Par3 PDZ2 domain. Crystals of this construct diffracted to 1.8 Å and I was able to determine the crystallographic phases by molecular replacement using the second PDZ domain of *hs*Dlg3 (PDB ID: 2fe5) as well as the PDZ domain variant C378S of the rat homolog of Dlg (2awx) as search models (Figure 29C, D, Table 32).

The structure of the *dm*Par3 PDZ2:Insc complex highlights the structural differences in ligand recognition between the Par3 PDZ1 and PDZ2 domains. The hydrophobic binding pocket enclosing the valine side chain of the 0 position (Figure 29C) is smaller than the pocket of the PDZ1 domain (Figure 29A, B). The PDZ2 pocket consists of the carboxylate binding loop (L21), the β2-strands (F23) and the α2-helix (L81). In contrast to the PDZ1 domain, there is no hydrophobic pocket present at the -2 position since the β2-strand (V25) and the α2-helix (V78) are spatially too close. Furthermore, the F-1 of the Insc PBM lies on a hydrophobic surface containing L44 of the *dm*Par3 PDZ2 domain. The serine side chain at the -2 position of the Insc PBM forms a hydrogen bond with Q74 of the α2-helix of the PDZ2 domain. Q74 also participates in a hydrogen bond with the backbone CO group of Q-4 of the Insc PBM. Of note, the glutamine at the -3 position of the Insc PBM engages in a hydrogen bond network with S24 and N42 of the PDZ2 domain. Worth mentioning is the close distance of the amino group of the K41 side chain to the carboxylate group of the E-3 side chain. However, the amino group faces into the opposite direction since it is part of a crystal contact involving a sulfate ion. The presence of the Insc PBM in the PBM binding groove of the *dm*Par3 PDZ2 domain was verified by calculating a iterative built OMIT electron density map (Terwilliger et al. 2008) and critically observing the B-factors of the PBM (Figure 29D). The OMIT map shows clear density for the PBM positions 0 to -3. Noteworthy, the side chain of Q-4 shows no OMIT density and high B-factors indicating no stable conformation. However, the backbone CO group involved in the hydrogen bond with Q74 shows a lower B-factor and OMIT map electron density. In addition, the density of the C-terminal carboxyl group of the Insc PBM is incomplete and B-factors associated with the corresponding oxygen and carbon atoms are higher than for the surrounding residues. This might be the result of radiation damage of the crystal which can lead to the decarboxylation of carboxyl groups (Weik et al. 2000; Garman 2010).

In sum, the distinct specificity profiles of the *dm*Par3 PDZ2 domain in comparison to the PDZ1 domain can be explained on a structural level. The most striking difference between the two PDZ domains is the size of the pocket facilitating the interaction with the -2 PBM position. In the *dm*Par3 PDZ1 domain, this pocket is large enough to encompass a large hydrophobic residue such as leucine or trypthophane (Figure 29A, B) whereas the PDZ2 binding pocket is very shallow (Figure 29C, D).

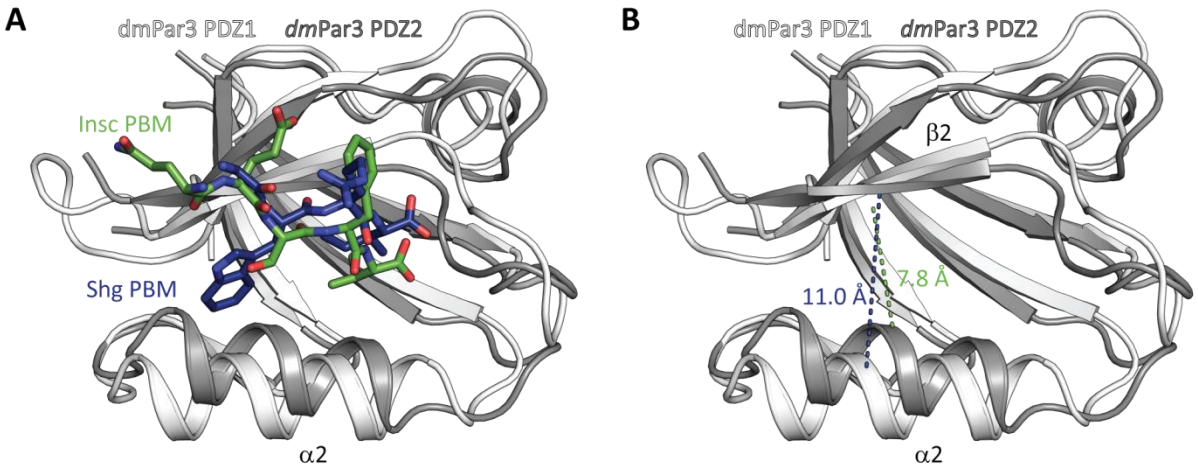

Figure 30: Structural comparison of the *dm*Par3 PDZ1 and PDZ2 domains. (A) Cartoon representation structural alignment of the *dm*Par3 PDZ1 domain (white) in complex with the Shg PBM (dark blue sticks) (PLS and (Renschler 2013)) and of the *dm*Par3 PDZ2 domain (grey) in complex with the Insc PBM (green sticks). The rmsd between the two structures is 2.725 Å. **(B)** As **(A)** but without the PBMs. The distances between the C_α-atoms of equivalent positions in the β2-strand and α2-helix of the PDZ domains (A23 and Q72 in the case of PDZ1 and V25 and V78 in the case of PDZ2, respectively) are given as dark blue and green dashed lines for the *dm*Par3 PDZ1 and PDZ2 domains, respectively.

This difference results in the displacement of the α2-helix of the PDZ domain in respect of the β2-strand (Figure 30). This fact is reflected in the high rmsd of 2.725 Å between the two structures as well as the larger difference in distance between equivalent positions inside the 2-helix and the β2-strand (C_α-atoms of A23 and Q72 in the case of PDZ1 and V25 and V78 in the case of PDZ2, respectively). The distance between these atoms in the *dm*Par3 PDZ1 domain is 11.0 Å compared to 7.8 Å in the PDZ2 domain. Therefore, the *dm*Par3 PDZ1 domain is able to interact with bulkier residues as compared to the *dm*Par3 PDZ2 domain.

Despite my efforts to crystallize various combinations of the *dm*Par3 PDZ3 domain with different PBMs and different GS-linker, no high quality diffraction data could be collected (Table 31).

4.2.4 Discussion

The dmPar3 PDZ domains have unique but redundant binding specificities

Despite high levels of sequence conservation of the residues forming the PBM binding pocket (Figure 27), my analysis of the binding specificities of the *dm*Par3 PDZ domains (Figure 28, Table 5) revealed that the first PDZ domain of *dm*Par3 prefers class II ligands with large hydrophobic residues at the 0 and -2 position (Table 5, Figure 29A, B, Figure 30 and Figure 31A), while the second PDZ domain selects class I and class III PBMs with negatively charged or polar residues at the -2 position as well as glutamine at position -3 and valine at position 0 (Table 5, Figure 29C, D, Figure 30 and Figure 31B). Moreover, the PDZ2 domain is capable of recognizing class II PBMs (Ed), containing V at position 0

and E at position -3, to some extent. Surprisingly, the *dm*Par3 PDZ3 domain displays a highly promiscuous binding profile (Table 5 and Figure 31C) preferring hydrophobic residues at position 0 and E at position -3.

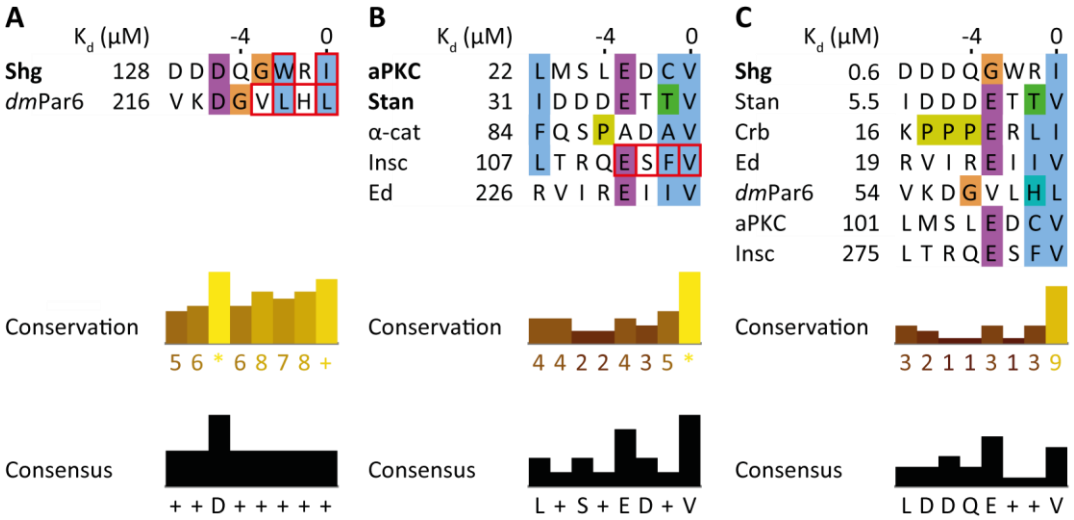

Figure 31: Selectivity profiles of the individual *dm*Par3 PDZ domains. (A) PBMs interacting with the *dm*Par3 PDZ1 domain. PBMs are aligned according to their K_d values (Table 5) and colored with ClustalX according to conservation (Larkin et al. 2007), red boxes indicate interactions between side chain atoms of the PBM with the respective PDZ domain (Figure 29), conservation and consensus sequences were generated in Jalview (Waterhouse et al. 2009). **(B)** PBMs interacting with the *dm*Par3 PDZ2 domain, otherwise as in **(A)**. **(C)** PBMs interacting with the *dm*Par3 PDZ3 Δβ2-3loop domain, otherwise as in **(A)**.

Of note, artificial high affinity PBMs for the *dm*Par3 PDZ domains have been identified by phage display screens (Yu et al. 2014) which coincide partially with the results of my 2D line shape fitting data (Table 5 and Figure 31). In short, PDZ1 interacts with class II PBMs containing W at position -2 and F at position 0, PDZ2 interacts with class II PBMs containing E at position -3 and V at position 0, and PDZ3 interacts with class II PBMs preferring F or in rare cases I at position 0 with very high affinities in the nanomolar range (Yu et al. 2014). However, phage display screens tend to be biased to select for PBMs containing Tryptophan or Phenylalanine residues at various positions as well as artificially low K_d values (Yu et al. 2014; Luck & Travé 2011). Therefore, it is not surprising that Yu et al. found only class II ligands. In addition, protein-protein interactions are not necessary optimized *in vivo*.

The redundant and distinct binding specificities of the dmPar3 PDZ domains may enable the assembly of large polarity protein networks

Overall, the specificities of the three *dm*Par3 PDZ domains share overlapping specificities (Figure 31, Table 5). This observation is intriguing taking into account that one Par3 molecule can simultaneously interact with two Par6 PBMs *in vitro* (Figure 20 and Figure 23) (Renschler et al. 2018)

and probably also with any other PBM which interacts with two Par3 PDZ domains. However, Par3 contains three PDZ domains of which at least one would be able to interact with another PBM if two of its PDZ domains are occupied. Therefore, it is highly possible, that Par3 forms large networks at the cell cortex involving a vast variety of different ligands (Figure 32). However, there is also evidence present for the crucial role of the Par3 oligomerization in Par3 function (Rodriguez et al. 2017; Dickinson et al. 2017; Wang et al. 2017). Hence, large assemblies of Par3 containing several PDZ modules are present in polarized cells. These Par3 clusters are therefore able to interact with many different PBMs at once (Figure 32).

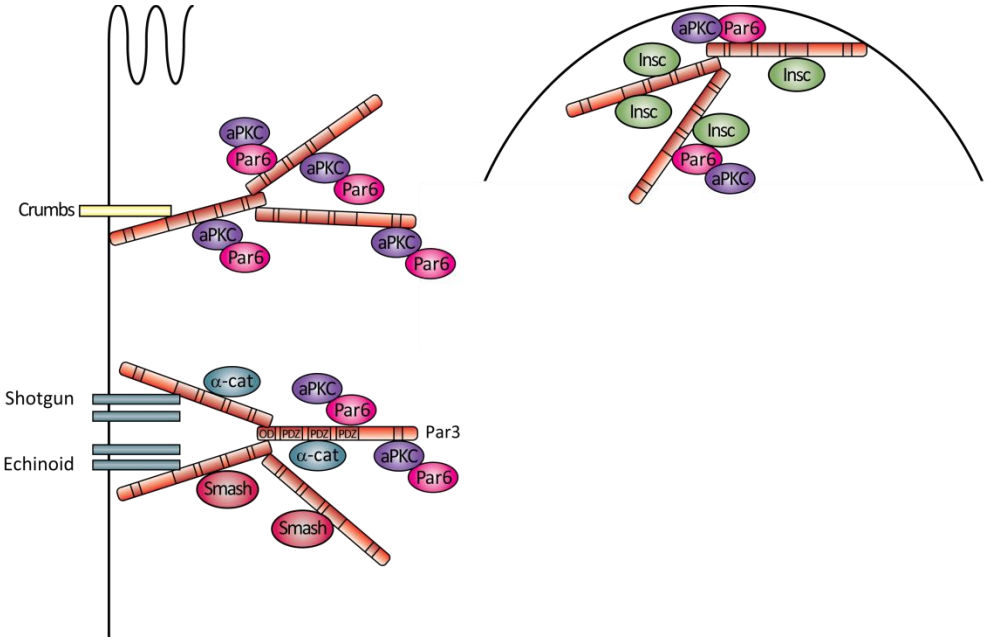

Figure 32: Par3 is a multivalent interaction hub. The Par3 PDZ domains can form multivalent interaction networks in various cellular contexts e.g. in epithelia cells (left) or during asymmetric cell division (right).

Moreover, a study in the *Drosophila* embryo ectoderm indicated specialized functions for the *dm*Par3 PDZ domains (McKinley et al. 2012). The authors proposed that *dm*Par3 recruitment to the apical domain depends on PDZ1 and PDZ3 while PDZ2 mediates downstream effects on epithelial structure. In addition, *dm*Par3 removal form the apical cell cortex is increased by PDZ1. In agreement with the reported functions of the *dm*Par3 PDZ domains, the ligands assigned here (Table 5 and Figure 31) can be related to the individual functions. As for PDZ1, apical recruitment is probably due the interaction with Shg (Figure 32) (Wei et al. 2005; Bulgakova et al. 2013), the E-cadherin of *Drosophila*, whereas *dm*Par3 turnover is probably linked with the *dm*Par6 interaction (Renschler et al. 2018) which might result in a recruitment of the Par6/aPKC module. The downstream effects such as planar cell polarity, Golgi orientation, asymmetric cell division and maybe apical constriction are probably mediated by the interactions of the Par3 PDZ2 domain with Stan (Wasserscheid et al. 2007), α-cat (Odell et al. 2012), Insc (Lu & Johnston 2013; Culurgioni & Mapelli 2013; Lang & Munro

2017) and Smash (Beati et al. 2018), respectively. In addition, the interaction of aPKC via its PBM with the Par3 PDZ2 domain might facilitate Par3 mediated recruitment of aPKC to various substrates independent of the Par3 KBD. The interactions of the third *dm*Par3 PDZ domain with Shg (Wei et al. 2005; Bulgakova et al. 2013), with Crb during epitheliogenesis (Tepass 2012; Lang & Munro 2017) and with Ed (Wei et al. 2005) most probably result in its apical localization (Figure 32). The interactions of the *dm*Par3 PDZ3 domain with Stan, aPKC and Insc (Figure 31C) might result in additional redundancies enabling Par3 to interact with multiple downstream effectors at the same time similar to the multiple interactions between *dm*Par3 and *dm*Par6 (Renschler et al. 2018).

In addition to the multiple possible interactions, the regulation of the involved proteins plays an important role. Surprisingly, my analysis of the Par3 PDZ domain specificities revealed that the third *dm*Par3 PDZ domain is able to interact with the well-studied Par6 PDZ domain interaction partner Crb (Whitney et al. 2016) (Figure 31C and Table 5). However, those two interactions might be linked with different stages of epitheliogenesis. After formation of initial spot-like cell-cell junctions, Par3 recruits members of the Crumbs and PAR complex to these initial junctions (Tepass 2012; Lang & Munro 2017). At this stage, the interaction between the Crb PBM and the *dm*Par3 PDZ3 domain might be of importance. After maturation of the cell-cell junctions and exclusion of Par3, Par6 and aPKC localize with the Crumbs complex (Tepass 2012; Lang & Munro 2017). This is probably a Cdc42-dependent process since the affinity of the Par6 PDZ domain for the Crb PBM can be increased by an factor of 10 in the presence of GTP-bound Cdc42 to $K_d \approx 1.2$ µM (Whitney et al. 2016) that is 13-fold stronger when compared to the Par3 PDZ3:Crb PBM interaction ($K_d \approx 16$ µM, Table 5).

Additionally, the weak interaction of the Std PBM with the *dm*Par3 PDZ2 domain (Figure 31B and Table 5) was observed. This interaction might be less important compared to the interaction of the Std PDZ with the C-terminal region of Par3 (Krahn, Bückers, et al. 2010). However, no biophysical data investigating the Std PDZ:*dm*Par3 complex is present to date. Yet it is known that the Std PBM can interact with the Par6 PDZ domain with an $K_d \approx 6$ µM (Penkert et al. 2004) that is 127-fold stronger than the Par3 PDZ2:Std PBM interaction ($K_d \approx 762$ µM, Table 5).

Furthermore, the cellular context may differ in which those interactions occur. For example, during the gastrulation of the *Drosophila* embryo, Std is expressed and present before stage 6. Crb however, is only present at later stages (Krahn, Bückers, et al. 2010; Sen et al. 2015). Therefore, multiple and redundant interaction might be necessary to ensure correct cell polarization in various developmental and cellular contexts. In line with that is the observation that Par is dispensable for the maintenance of cell polarity in the *Drosophila* follicular epithelium (Shahab et al. 2015).

Besides the previously reported interaction between the Par6 PBM and the Par3 PDZ1 and PDZ3 domains (Renschler et al. 2018), I discovered another PBM-based interaction between the aPKC PBM

and the Par3 PDZ2 and PDZ3 domains (Figure 31B, C and Table 5). Interestingly, to date this interaction was not reported. Instead much emphasis in the research of the aPKC:Par3 interaction was focus on the Par3 KBD and its duality as substrate and inhibitor of the aPKC kinase domain (Wang et al. 2012; Soriano et al. 2016). However, the interaction of the aPKC PBM with the Par3 PDZ2 and PDZ3 domains increases the multivalency and redundancy between the Par6/aPKC module and Par3 thereby enabling different binding modes independent of the Par3 KBD. This might be of importance since active aPKC seems to be associated with Par3 present at adherens junctions enriched with Shg (E-cadherin) (Soriano et al. 2016). As I and my co-authors could show (Figure 19, Figure 22, Table 5) (Renschler et al. 2018), the interaction of the Par6 PBM and Par3 relies on the interaction with Par3 PDZ1 and PDZ3 and can compete with Shg for Par3 PDZ1 and PDZ3 binding (Figure 24). However, an additional interaction between the aPKC PBM and the *dm*Par3 PDZ2 and PDZ3 domains might strengthen the interaction of the Par6/aPKC module. This might be off importance keeping active aPKC associated with Par3 at adherens junctions, since the tight interaction between the Par6 KBD and the aPKC kinase domain is released upon Par3 KBD phosphorylation by aPKC (Wang et al. 2012; Soriano et al. 2016). Nevertheless, detailed *in vivo* analysis of the Par3 PDZ:aPKC PBM interactions has to be done in order to draw further conclusion about the function of the aPKC PBM in context of the PAR complex.

Structural investigations are required to decipher the specificity profiles of the Par3 PDZ domains

The presented x-ray structures of the *dm*Par3 PDZ1 domain in complex with the *dm*Par6 PBM (Figure 29A) (Renschler et al. 2018) and the Shg PBM (Figure 29B, PLS and (Renschler 2013)) as well as the *dm*Par3 PDZ2 domain in complex with the Insc PBM (Figure 29C, D) provide important insights into the recruitment of natural ligands to the *dm*Par3 PDZ domains and their specificities. Although a fairly comprehensive structural study (Ernst et al. 2014) has been performed to determine specificity determining components of PDZ domains for high affinity ligands derived from phage display screens, this approach suffers from the over representation of aromatic residues in the selected PBMs as well as very low K_d values (Yu et al. 2014; Luck & Travé 2011; Tonikian et al. 2008; Ernst et al. 2014). Yet, the ability of PDZ1 to enclose large hydrophobic residues such as W or L inside its position -2 binding pocket was not observed before. In contrast, the strict selectivity for V at position 0 of *dm*Par3 PDZ2 ligands (Figure 31) largely confers to the presence of F23 which constricts the position 0 binding pocket in PDZ2 (Figure 29C, D) compared to PDZ1 (Figure 29A, B) as described previously (Ernst et al. 2014). Moreover, the insights gained from the *dm*Par3 PDZ2:Insc complex (Figure 29C, D) can be extrapolated to explain the PDZ2 specificities (Figure 29 and Figure 31B). K41 and N42 are the reason for the presence of a glutamine at the PBM -3 position as in the *dm*Par3

PDZ2:Insc complex. In addition, it is possible to substitute S-2 with threonine or aspartate in order to form hydrogen bonds with Q74 of the PDZ2 domain. Likewise, the phenylalanine at the -1 position can be replaced by other hydrophobic residues such as I, A, C or the methyl group of a threonine in order to maintain the hydrophobic interaction with L44.

Besides, all residues at the interaction surfaces of *dm*Par3 PDZ1 and PDZ2 are highly conserved (Figure 27), suggesting conserved binding specificities of the Par3 PDZ domains. In fact, I also showed that PDZ1 and PDZ3 of the human Par3 protein are able to bind to the human Par6 PBM (Figure 25) (Renschler et al. 2018). Furthermore, residues involved in PBM binding in *dm*Par3 PDZ1 and PDZ2 are conserved to some extent in PDZ3 (Figure 27), highlighting the ability of PDZ3 to interact with PBMs also recognized by PDZ1 and PDZ2 (Table 5 and Figure 31). In line with this observation, the PDZ3 domains of the human, mice and rat Par3 proteins bind to JAMs, Nectins and Ephrins (Ebnet et al. 2001; Takekuni et al. 2003; Iden et al. 2006; Itoh et al. 2001; Ebnet et al. 2003; Lin et al. 1999; Latorre et al. 2005; Nakayama et al. 2013) as well as PTEN (von Stein et al. 2005; Feng et al. 2008) which contain similar class II PBMs as *dm*Par6, Ed and Shg in *Drosophila* (Figure 26). Taking together, the structures presented here form the basis for understanding the specificities of the *dm*Par3 PDZ1 and PDZ2 domains.

The Par3 PDZ3 domain carries specificity determining residues from both the PDZ1 and PDZ2 domain

In addition, the third PDZ domain of *dm*Par3 seems to be an intermediate of PDZ1 and PDZ2. This is reflected in the fact that residues contacting PBMs in *dm*Par3 PDZ1 and 2 are conserved in PDZ3 (Figure 27 and Figure 33). All residues identified in the x-ray structures of the *dm*Par3 PDZ1 domain in complex with the *dm*Par6 PBM (Figure 29A), the Shg PBM (Figure 29B) and the *dm*Par3 PDZ2 domain in complex with the Insc PBM (Figure 29C, D) are present in the *dm*Par3 PDZ3 domain (Figure 33). This is most likely the explanation of the promiscuous binding specificity of the *dm*Par3 PDZ3 domain (Figure 25, Figure 31C and Table 5). Therefore, the Par3 PDZ3 domain is a chimera of the Par3 PDZ1 and PDZ2 domains in regard of ligand selectivity and selectivity determining features.

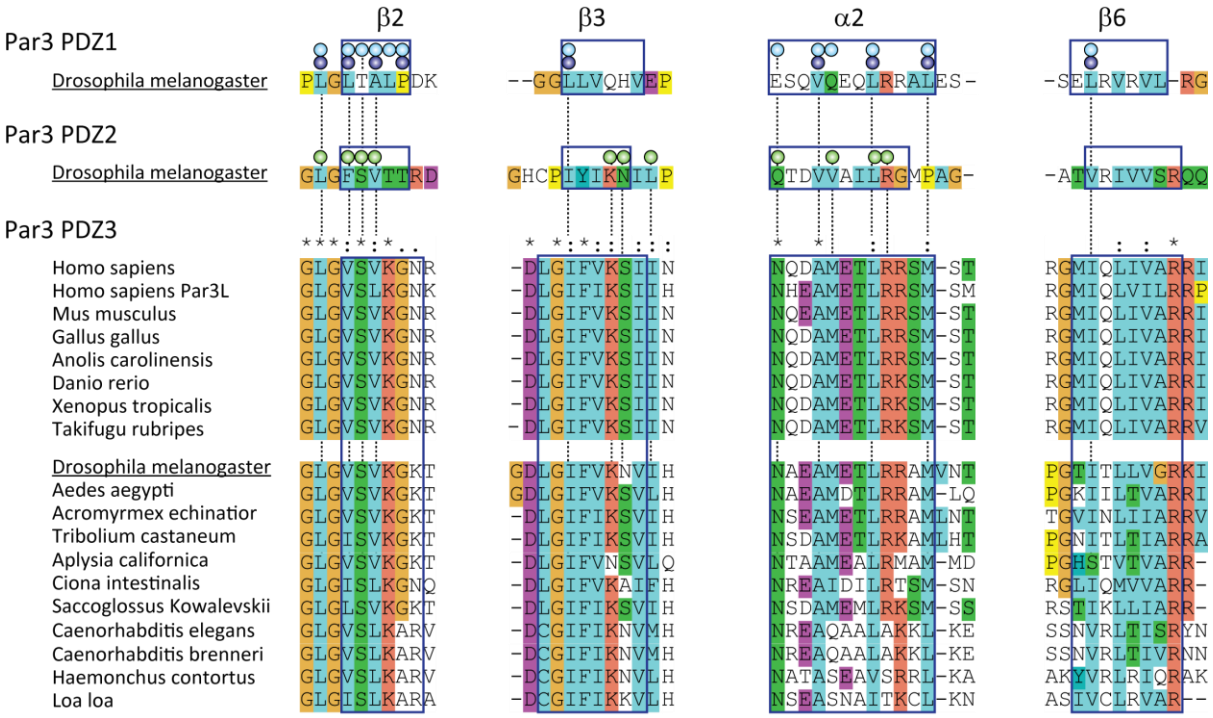

Figure 33: The Par3 PDZ3 domain is a chimera of the Par3 PDZ1 and PDZ2 domains. Detail of the structure-based sequence alignment of the Par3 PDZ1, PDZ2 and PDZ3 domains (Figure 27) highlighting the conservation of specificity determining residues from the *dm*Par3 PDZ1 and PDZ2 domains in the *dm*Par3 PDZ3 domain. Residues interacting with the *dm*Par6 PBM (Figure 29A), the Shg PBM (Figure 29B), or the Insc PBM (Figure 29C, D) are indicated by cyan, dark blue and green spheres on top of the corresponding PDZ domain, respectively. Otherwise as Figure 27.

In sum I could show that the *dm*Par3 PDZ1 and PDZ2 domains have unique ligand binding properties (Figure 25, Figure 31A, B and Table 5) which are based on the structure in the case of the PDZ1 (Figure 29A, B) and PDZ2 domains (Figure 29C, D). However, they share redundant ligand specificities with the Par3 PDZ3 domain (Figure 25, Figure 31C and Table 5) enabling Par3 to form multivalent interactions networks in different cellular contexts (Figure 32). This redundant ligand specificity of the Par3 PDZ3 domain with the PDZ1 and PDZ2 domains are resulting from the fact that the PDZ3 domain contains all ligand specificity determining residues of the other two Par3 PDZ domains (Figure 33).

4.3 A short N-terminal motif regulates the function of the *dm*Par3 PDZ3 domain

During my thesis, I discovered that the *dm*Par3 PDZ3 domain does not display a conclusive specificity profile (Figure 31C, Table 5) since it is able to recognize almost all PBMs tested in a promiscuous fashion. Moreover, it seems to be a chimera between the Par3 PDZ1 and PDZ2 domains on the sequence level (Figure 33) and thus in its PBM binding profile (Figure 31). Of note, during the investigation of the Par3 PDZ module comprising all three PDZ domains (Figure 23), all PDZ domains seemed to be structurally and functionally largely independent (Renschler et al. 2018). But nevertheless, the third PDZ domain showed $^{1}H,^{15}N$-chemical shifts changes noticeably larger than the first and second PDZ domain (Figure 23). Together with the fact that PDZ domains are known to be influenced by sequences adjacent to them (Ivarsson 2012; Luck et al. 2012; Ye & Zhang 2013), I wanted to investigate this observation further.

4.3.1 Contributions

The results presented here have been obtained during the course of my PhD thesis. Results obtained by myself and already published are indicated by citing the respective papers.

4.3.2 The *dm*Par3 PDZ3, but not PDZ1 and PDZ2, displays structural changes when embedded in the PDZ module

NMR spectra of the entire *dm*Par3 PDZ module (PDZ1-3) in comparison with the individual PDZ domains showed, that the PDZ domains of *dm*Par3 are structurally and functionally largely independent (Figure 23) (Renschler et al. 2018). However, changes in the $^{1}H,^{15}N$-chemical shifts of the third Par3 PDZ domain were consistently larger than for the PDZ1 and PDZ2 domains (Figure 23C). The fact that the cross peaks originating from PDZ1 and PDZ2 in the $^{1}H,^{15}N$ TROSY spectrum of the PDZ1-3 Δβ2-3loop construct overlaid well with the individual domains (Figure 23A, B) demonstrates that a region within the linker sequence between the second and third PDZ domain interacts *in cis* with the PDZ3 domain and thereby causes the CSPs in this domain.

4.3.3 The PDZ2-3 linker contains an FID-motif that interacts *in cis* with the PDZ3 domain

To probe which part of the linker between the *dm*Par3 PDZ2 and PDZ3 domains caused the CSPs in the Par3 PDZ3 domain, I generated a construct that comprised of the entire linker sequence starting from the C-terminus of the PDZ2 domain and contains the PDZ3 domain without the loop between

the second and third β-strand (Figure 34A, linker-PDZ3 Δβ2-3 loop). Comparison of the ^{1}H,^{15}N-HSQC spectrum of the ^{15}N-labeled *dm*Par3 linker-PDZ3 Δβ2-3 loop construct with the ^{1}H,^{15}N-HSQC spectrum of the ^{15}N-labeled *dm*Par3 PDZ3 Δβ2-3 loop construct displayed chemical shift changes in the peaks of the PDZ3 domain as observed previously (Figure 34B). This demonstrates that residues in the PDZ2-3 linker influence the PDZ3 domain.

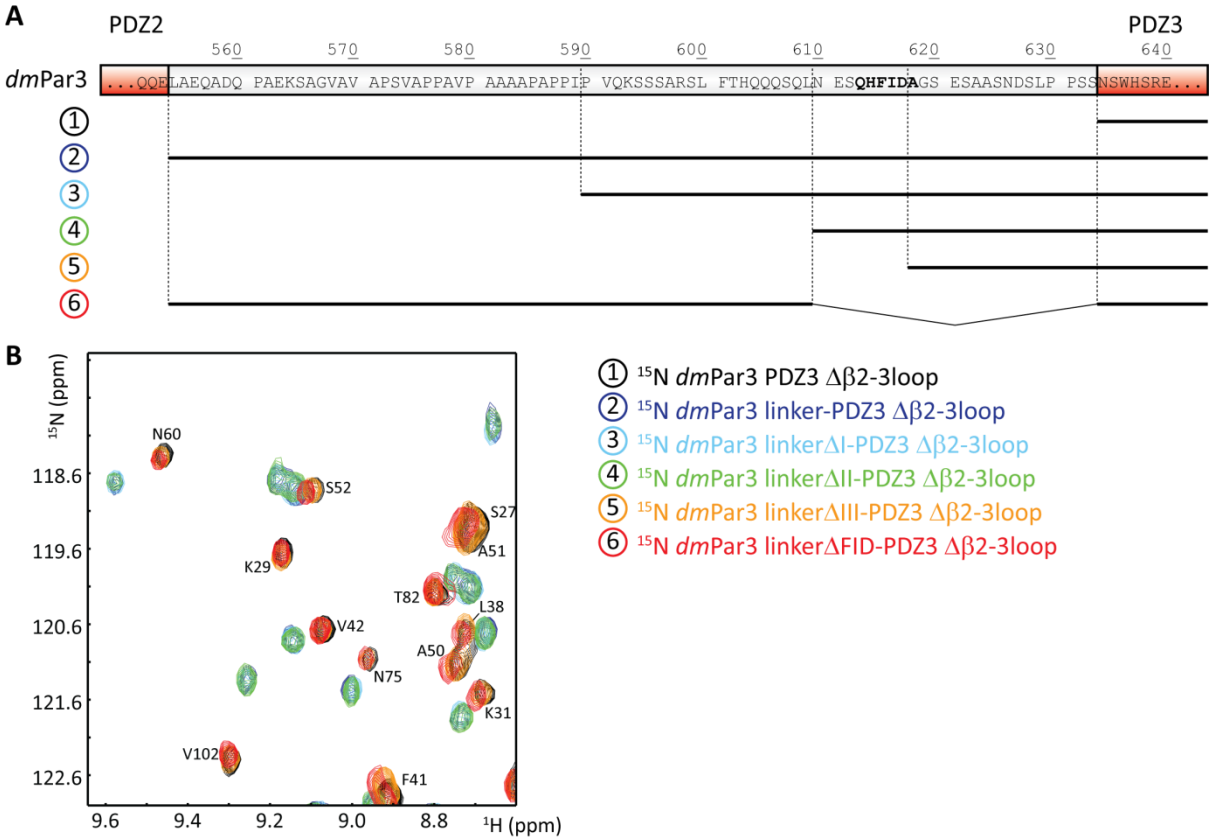

Figure 34: The FID-motif N-terminal of *dm*Par3 PDZ3 causes structural changes in PDZ3. (A) Schematic representation of *dm*Par3 PDZ3 Δβ2-3loop constructs used for mapping the motif N-terminal of PDZ3 which influences PDZ3. The sequence of the linker between *dm*Par3 PDZ2 and PDZ3 is shown and numbered according to FL *dm*Par3 protein (FBpp0110299). The FID-motif folding back onto PDZ3 is highlighted in bold. Numbers to the left indicate construct names and are colored as in **(B)**. **(B)** Overlay of ^{1}H,^{15}N-HSQC spectra of *dm*Par3 PDZ3 Δβ2-3loop constructs described in **(A)**. *dm*Par3 PDZ3 Δβ2-3loop is shown in black, *dm*Par3 linker-PDZ3 Δβ2-3loop in dark blue, *dm*Par3 linkerΔI-PDZ3 Δβ2-3loop in light blue, *dm*Par3 linkerΔII-PDZ3 Δβ2-3loop in green, *dm*Par3 linkerΔIII-PDZ3 Δβ2-3loop in orange, *dm*Par3 linkerΔFID-PDZ3 Δβ2-3loop in red. Chemical shift assignments are shown according to *dm*Par3 PDZ3 Δβ2-3loop as published previously under the BMRB accession code 27198 (Renschler et al. 2018).

To map the linker residues involved in the interaction, I truncated the N-terminus of the linker sequence in several steps (Figure 34A). Comparison of the ^{1}H,^{15}N-HSQC spectra of these truncation constructs displayed changes in the PDZ3 domain similar to the complete linker sequence until a sequence of 24 amino acids N-terminal of the Par3 PDZ3 domain was left (Figure 34B, *dm*Par3 linkerΔII-PDZ3 Δβ2-3 loop). In contrast, further truncation of the linker (*dm*Par3 linkerΔIII-PDZ3 Δβ2-3 loop) leaving just 16 residues N-terminal of the Par3 PDZ3 domain as well excision of the 24 aa N-

terminal of the Par3 PDZ3 domain (*dm*Par3 linkerΔFID-PDZ3 Δβ2-3 loop) did not yield significant CSPs in the $^{1}H,^{15}N$-HSQC spectra between these constructs and *dm*Par3 PDZ3 domain (Figure 34B). Therefore, the 24 amino acids N-terminal of the PDZ3 domain interact with the third PDZ domain of *dm*Par3 *in cis*.

4.3.4 The FID-motif folds back onto PDZ3 next to the PBM binding grove

To determine the interaction surface between the linker residues and the PDZ3 domain, I first investigated the interaction of the ^{15}N-labeled ten N-terminal linker amino acids with the *dm*Par3 PDZ3 domain *in trans* with NMR CSP experiments.

To this end, I fused the linker sequence (aa 610-620 of *dm*Par3) to the B1 domain of the *streptococcal* protein G (denoted as *dm*Par3 FID-motif) with two linking serine and glycine residues and assigned the H,N-resonances of the linker residues in this construct (Figure 35A and Figure A 2). In order to assign secondary structure elements to the *dm*Par3 FID-motif in isolation, I quantified $^{3}J_{HN\text{-}H\alpha i}$-coupling constants which directly correlate with the secondary structure of proteins (Bystrov 1976) and used qualitative information present in the 3D $^{1}H,^{15}N$-HNH-NOESY spectrum of the *dm*Par3 FID-motif to resolve ambiguities. This analysis revealed the presence of one α-helical turn at the N-terminus of the FID-motif (aa 610-614) whereas the C-terminal part (aa 615-620) adopts an elongated random coil structure (Table 6).

Table 6: Secondary structure assignment of the *dm*Par3 FID-motif in isolation.

residue #			**610**						**615**				**620**
aa	*S**	*G**	N	E	S	Q	H	F	I	D	A	G	S
$^{3}J_{HN\text{-}H\alpha i}$ (Hz)	6.61	7.17	7.21	6.15	6.66	7.07	4.51	6.32	7.89	6.69	6.69	6.01	7.43
2nd structure *	rc	α	α	α	α	α	α	rc	rc	rc	rc	rc	rc

* 2nd structure assignment after qualitative inspection of the 3D $^{1}H,^{15}N$-HNH-NOESY strips to resolve ambiguous $^{3}J_{HN\text{-}H\alpha i}$-coupling constants ($6 \leq {}^{3}J_{HN\text{-}H\alpha i}$ (Hz) ≤ 8).

Next, I added increasing amounts of unlabeled *dm*Par3 PDZ3 Δβ2-3loop domain to the ^{15}N-labeled *dm*Par3 FID-motif (Figure 35A). As expected for two proteins interacting with each other, I observed several CSPs (Figure 35A, B) of the cross peaks of amino acids 610 and 613-618 (QHFIDA) but no CSPs for peaks originating from the GB1 domain or from the remaining SG-linker sequence. Of note, N610 is approximately facing into the same direction as residues 613-618 since it is at the other end of the α-helical turn identified previously in the FID-motif in isolation (Table 6). Therefore, the FID motif and in particular residues 610 and 613-618 (Figure 35B) interact with a single surface with the third PDZ domain of *dm*Par3.

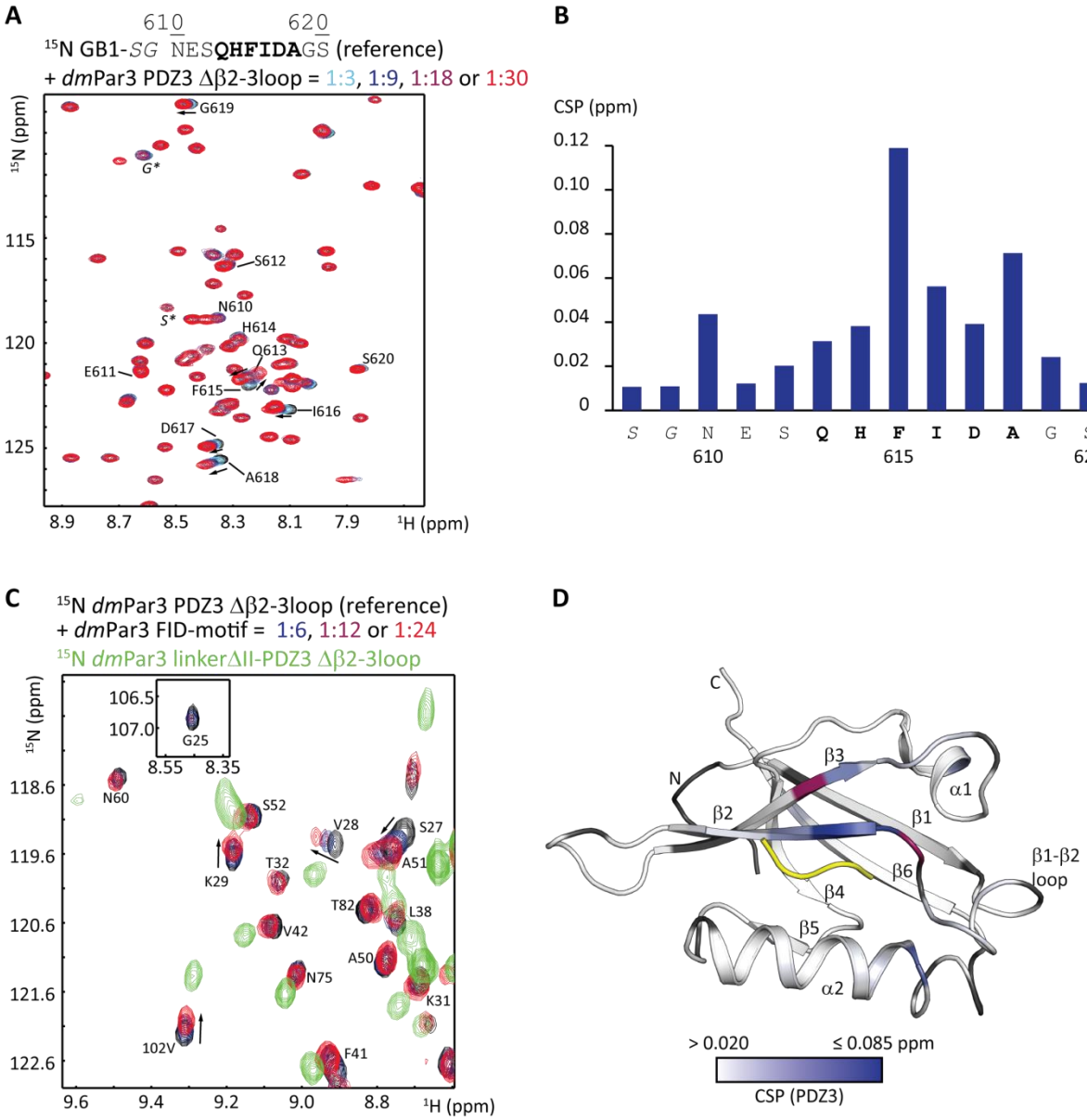

Figure 35: The FID-motif interacts with a surface close to the PBM binding grove of *dm*Par3 PDZ3. (A) Overlay of a representative region of the ^{1}H,^{15}N-HSQC spectra of the FID-motif containing linker of *dm*Par3 fused to GB1 domain in the absence (black) and presence of increasing stoichiometric amounts of *dm*Par3 PDZ3 Δβ2-3loop domain as indicated. Arrows indicate the direction of chemical shift changes. Chemical shift assignments are shown for the residues originating from the *dm*Par3 FID-motif. **(B)** CSPs induced by the *dm*Par3 PDZ3 Δβ2-3loop domain are mapped onto the sequence of the FID-motif. Italic residues originate from the linker between GB1 and the *dm*Par3 FID-motif and core residues of the FID-motif are highlighted in bold. **(C)** Overlay of a representative region of the ^{1}H,^{15}N-HSQC spectra of the *dm*Par3 PDZ3 Δβ2-3loop domain in the absence (black) and presence of increasing stoichiometric amounts of the FID-motif containing linker of *dm*Par3 fused to GB1 as indicated. Arrows indicate the directions of chemical shift changes. The ^{1}H,^{15}N-HSQC spectrum of *dm*Par3 linkerΔII-PDZ3 Δβ2-3loop is shown in green in order to highlight the end point of the titration. Chemical shift assignments are shown for the residues of *dm*Par3 PDZ3 Δβ2-3loop as published previously (Renschler et al. 2018). **(D)**

CSPs induced by the FID-motif containing linker of *dm*Par3 are mapped onto a homology model of *dm*Par3 PDZ3 Δβ2-3loop (Renschler et al. 2018). Legend continued on next page.

Figure 35: (D) (continued) CSPs are color coded with a linear gradient from white (CSP ≤ 0.020 ppm) to blue (CSP = 0.085 ppm). Residues broadened beyond detection are shown in purple and not assigned residues of PDZ3 are shown in dark grey. The PBM binding groove of the dmPar3 PDZ3 domain is indicated by the Shg PBM in yellow from the *dm*Par3 PDZ1:Shg complex and was generated by aligning both structures in pymol. Secondary structure elements are labeled (α1: aa 51-55, α2: aa 76-88, β1: aa 8-15, β2: aa 26-31, β3: aa 38-45, β4: aa 61-66, β5: aa 69-71, β6: aa 97-104).

To map the interaction surface of the FID-motif onto the PDZ3 domain, I added unlabeled *dm*Par3 FID-motif to the ^{15}N-labeled *dm*Par3 PDZ3 Δβ2-3loop domain. Again, CSPs were observed for a subset of cross peaks (Figure 35C). As expected, all PDZ3 cross peaks affected by the presence of the FID-motif shifted into the direction of the corresponding cross peaks in the *dm*Par3 linkerΔII-PDZ3 Δβ2-3loop construct that is the state where the FID-motif is bound in an intramolecular manner. In general, the observed CSPs for both, the FID-motif (Figure 35A, B) and the PDZ3 domain (Figure 35C, D), are not very pronounced at high stoichiometric ratios which suggests a weak interactions *in trans*. Since the backbone amides of the *dm*Par3 PDZ3 domain and a homology model of the *dm*Par3 PDZ3 Δβ2-3loop domain were published previously (Renschler et al. 2018), I was able to map the CSPs onto the PDZ3 domain (Figure 35D). Interestingly, this showed that residues most affected by the FID-motif are located β2- and β3-strands and hence in close vicinity to the PBM binding groove.

4.3.5 The FID-motif weakens the affinities of *dm*Par3 PDZ3

The chemical shift mapping demonstrated that the FID-motif binds to the *dm*Par3 PDZ3 domain in close vicinity to the PBM binding groove (Figure 35D). Additionally, residues involved in the binding surface of the FID-motif (Figure 35D) are partially conserved between all three *dm*Par3 PDZ domains (Figure 27) and are likely important for ligand recognition in PDZ1 and PDZ2 (Figure 29). Thus, the FID-motif might represent a regulatory element to influence the affinities of the *dm*Par3 PDZ3 domain. Therefore, I investigated the effects of the FID-motif onto the specificity of the PDZ3 domain. As my line shape fitting analysis of the isolated *dm*Par3 PDZ3 domain reveled a very broad specificity of the PDZ3 domain for all tested PBMs (Table 5), I performed CSPs experiments (
Figure 36) with ^{15}N-labeled *dm*Par3 linkerΔII-PDZ3 Δβ2-3loop and the strongest binding ligands (Insc, Crb, Stan, Ed, Shg, *dm*Par6 and aPKC). In order to test the effect on weak interaction partners, the α-cat PBM (K_d (*dm*Par3 PDZ3 Δβ2-3loop) = 663 ± 40 µM) was incorporated. Next, I determined K_d values (Table 7) using 2D lineshape fitting with TITAN (Figure A 26 – Figure A 32) (Waudby et al. 2016).

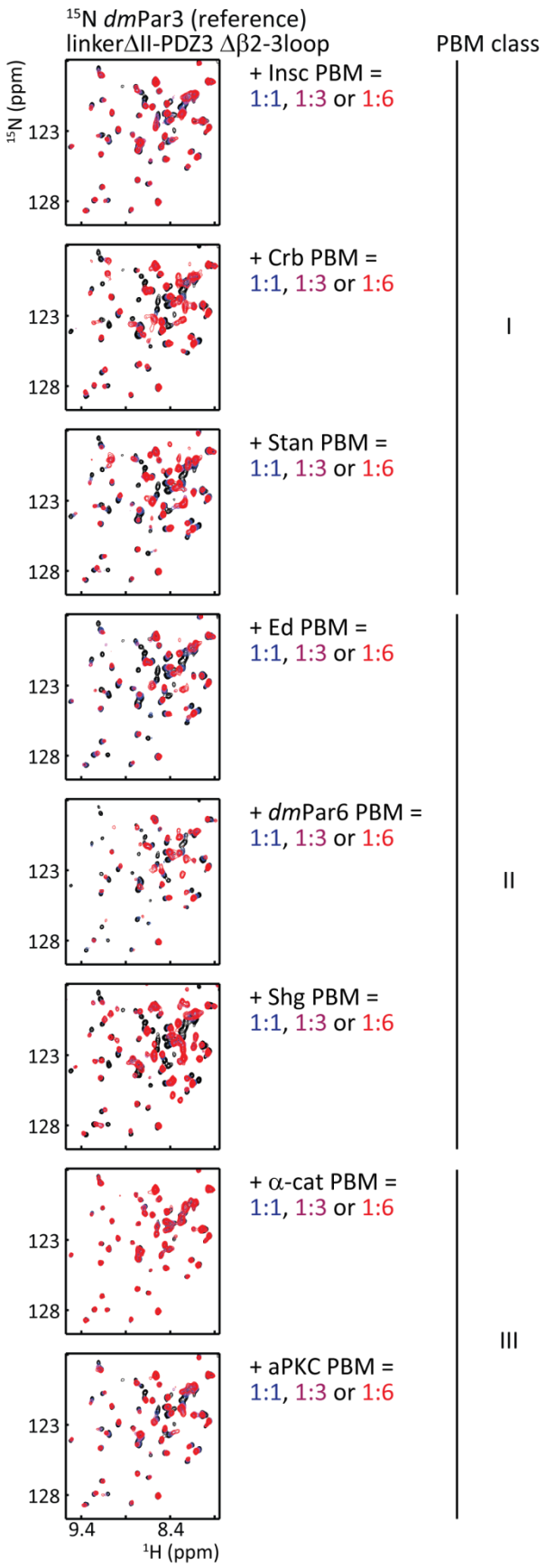

Figure 36: NMR titration experiments of the *dm*Par3 linkerΔII-PDZ3 Δβ2-3loop domain with different PBMs. Overlay of a representative region of the ^{1}H,^{15}N-correlation spectra of the *dm*Par3 linkerΔII-PDZ3 Δβ2-3loop domain in the absence (black) and presence of stoichiometric amounts of PBM peptides as indicated.

Overall, all affinities were reduced by the presence of the FID-motif (Table 7). However, the affinities of tight binding PBMs such as Shg and Stan were reduced more drastically (from 0.6 µM and 5.5 µM to 11 µM and 73 µM, respectively) which is 18- and 13-fold weaker, respectively. In comparison, the affinity of *dm*Par6 which binds with an intermediate affinity was only reduced by an factor of 3 (Table 7) form 54 µM to 155 µM. In addition, the interaction with ligands with an already rather weak affinity (Insc and aPKC) for the PDZ3 domain was further reduced from 275 µM to 844 µM (3 fold decrease) in the case of Insc and from 101 µM to 663 µM (7-fold decrease) in the case of aPKC, respectively. Of note, no CSPs could be observed for the α-cat PBM (

Figure 36). Therefore, no interaction takes place between the PDZ3 domain and the α-cat PBM if the FID-motif is present with the PDZ3 domain *in cis*.

Table 7: Differences in dissociation constants (in µM) between PDZ3 Δβ2-3loop and linkerΔII-PDZ3 Δβ2-3loop for different PBMs.

PBM	class	sequence	PDZ3 Δβ2-3loop	linkerΔII-PDZ3 Δβ2-3loop	fold difference
***dm*Par6**	II	VKDGV**L**H**L**	54 ± 1 *	155 ± 10	2.9
Insc	I	LTRQE**S**F**V**	275 ± 8	844 ± 90	3.1
Ed	II	RVIRE**I**I**V**	19 ± 1	117 ± 5	6.1
aPKC	III	LMSLE**D**C**V**	101 ± 3	663 ± 40	6.6
Crb	I	KPPPE**R**L**I**	16 ± 1	134 ± 7	8.2
Stan	I	IDDDE**T**T**V**	5.5 ± 0.3	73 ± 3	13.1
Shg	II	DDDQG**W**R**I**	0.6 ± 0.1 *	11 ± 1	18.3
α-cat	III	FQSPA**D**A**V**	663 ± 40	n.d.	-

K_d values were determined by 2D line shape fitting of NMR CSP experiments with TITAN (Waudby et al. 2016). Errors were estimated with bootstrapping statistics on 100 replicates. The number of titration points and cross peaks analyzed for each interaction as well contributions from others are summarized in Table A 1 and Table A 2. n.d. refers to not detectable and means no detectable CSPs in NMR CSPs experiments. Asterisks indicate K_d values already published in Renschler *et al.* (Renschler et al. 2018) and reprinted with permission from AAAS.

Taking together, these results demonstrate that the FID-motif is decreasing the affinities of the *dm*Par3 PDZ3 domain. Thereby the FID-motif counters the promiscuity of the Par3 PDZ3 domain to some extent.

4.3.6 Discussion

The FID-motif enables the dmPar3 PDZ3 domain to discriminate between different PBMs

My binding analyses of the PDZ3 domain in presence of the FID-motif showed that the FID-motif weakens the affinities of the PDZ domain towards PBMs (Figure 36, Table 7). Besides, the FID-motif seems to level out the huge affinity differences between the highest affinity PBM tested in this study, Shg, and intermediate affinity PBMs such as *dm*Par6. The affinity of the *dm*Par3 PDZ3 domain decreases from 90-fold (K_d(*dm*Par3 PDZ3 Δβ2-3loop) vs Shg of 0.6 µM or *dm*Par6 of 54 µM) to 14-fold (K_d(*dm*Par3 linkerΔII-PDZ3 Δβ2-3loop) vs Shg of 11 µM or *dm*Par6 of 155 µM) thereby reducing the affinity difference by a factor of more than 6 (Table 7, Figure 37A, B).

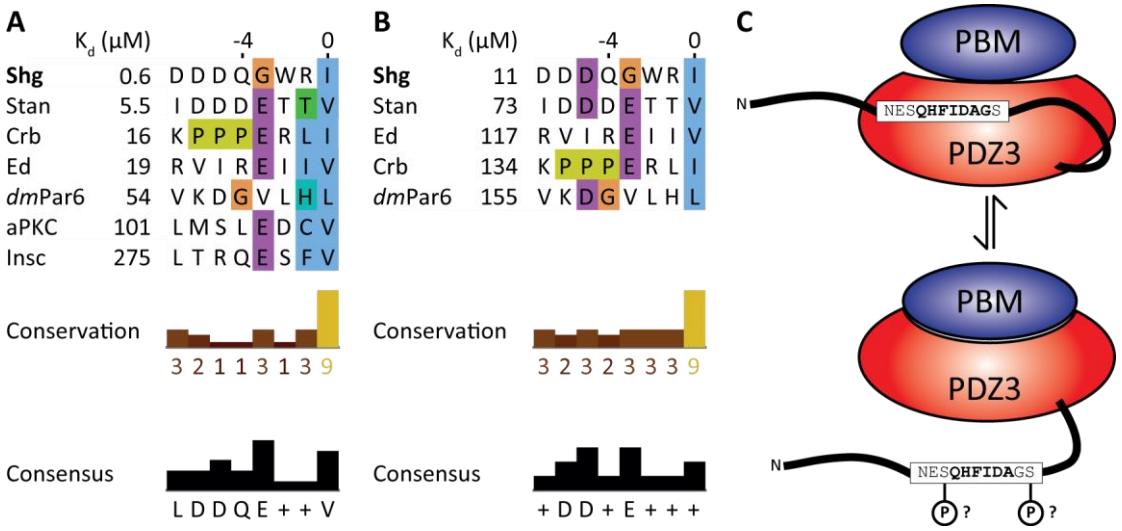

Figure 37: The selectivity of the *dm*Par3 PDZ3 domain is influenced by the FID-motif. (A) PBMs interacting with the *dm*Par3 PDZ3 Δβ2-3loop domain, otherwise as in Figure 31A. **(B)** PBMs interacting with the *dm*Par3 linkerΔII-PDZ3 Δβ2-3loop domain, otherwise as in Figure 31A. **(C)** The FID-motif might modulate the *dm*Par3 PDZ3 domain affinities and switch the PDZ3 domain from an low affinity state (top) to a high affinity state (bottom).

Based on the comparison of the binding affinities of the strongest interaction partners of the *dm*Par3 PDZ domain in absence and presence of the FID-motif (Table 7, Figure 37A, B) it seems that the FID-motif transforms the PDZ3 domain into a low affinity state (Figure 37C, top). Interestingly, sequence comparison of the highest affinity PBMs of both states (Figure 37A, B) reveals that apparently position -5 becomes much more conserved as three out of five high affinity PBMs of the *dm*Par3 linkerΔII-PDZ3 domain contain a aspartate at this position. Interestingly, this position is far-off from the FID-interaction surface (Figure 35D).

Several models could explain the reduced affinity of the *dm*Par3 PDZ domain in presence of the FID-motif. In a competitive model, the residues of the FID-motif would bind the same residues within the PDZ3 domain involved in the interaction with a PBM. Thereby the FID-motif would sterically block the access of the PBM to the PBM binding groove of the PDZ3 domain. Alternatively, the FID-motif could allosterically influence residues inside the PBM binding groove thus altering its binding properties. However, based on the data of my CSPs experiments (Figure 35D), the close vicinity of the FID-motif interaction surface and the PBM binding groove would favor the first model in which the FID-motif sterically interferes with PBM binding especially of residues at the very C-terminus of the PBM. Thereby contributions in regard of selectivity of residues outside the core PBM become more critical as reflected in the fact that almost all PBMs interacting with the PDZ3 domain in presence of the FID-motif contain an aspartate residue at position -5. Non-surprising, the residues of the *dm*Par3 PDZ3 domain interacting with the FID-motif (Figure 35C, D) are also important for PBM recognition (Figure 27) further strengthening the first model.

Extensions at the C- and N-termini of PDZ domains have been described previously and can form a variety of different interactions with their PDZ domains (Ivarsson 2012; Luck et al. 2012; Ye & Zhang 2013). PDZ extensions can occur as additional α-helices or β-strands on both termini. In general, those extensions are directly adjacent to the respective PDZ domain or in very close vicinity. However, an element which is present more than ten amino acids upstream of the N-terminus of a PDZ domain has to my knowledge not been described previously. However, there are elements present extending more than ten amino acids from the respective PDZ domain termini such as the Crib motif N-terminal of the Par6 PDZ domain (Peterson et al. 2004; Whitney et al. 2011; Whitney et al. 2013; Whitney et al. 2016). The Par6 Crib motif forms two additional β-strands in the presence of GTP-bound Cdc42 and enhances the affinity of the Par6 PDZ domain for C-terminal ligands such as the Crb PBM. However, the FID-motif represents an extension with an inverse effect on the PDZ domain affinities compared to the Par6 Crib domain.

The FID-motif is only conserved in fruit flies

The FID-motif N-terminal of the *dm*Par3 PDZ3 domain enables the PDZ3 domain to discriminate PBMs within its otherwise promiscuous interaction space (Figure 37). Since the interactions of the Par3 PDZ3 domain are conserved to some extent between human and *Drosophila* (Figure 25, Figure 26) (Renschler et al. 2018) the question arose whether the *dm*Par3 FID-motif is conserved in humans. However, sequence alignments of the linker region between the PDZ2 and PDZ3 domain of the vertebrate and invertebrate proteins were not feasible since the linker sequence is not conserved. Of note, alignment of several invertebrate Par3 proteins was much more successful (Figure 38). However, the *dm*Par3 FID-motif is only conserved in *Drosophila* and related species whereas the FID-interaction surface is much more conserved on the PDZ3 domain. Interestingly, bees and ants possess a very similar motif as fruit flies at the same location inside the Par3 PDZ2-PDZ3 linker sequence (Figure 38). Therefore, the FID-motif might be a feature the Par3 PDZ3 domain acquired late and convergent in the evolution of fruit flies, ants and bees which is consistent with the observation of rapid evolution of short linear motifs (Davey et al. 2015). In addition, other Par3 PDZ3 domains might have similar features which are not visible in sequence alignments due to their low conservation. Hence, detailed structural and biophysical analysis of the Par3 PDZ1-3 module is crucial to discover these short motifs.

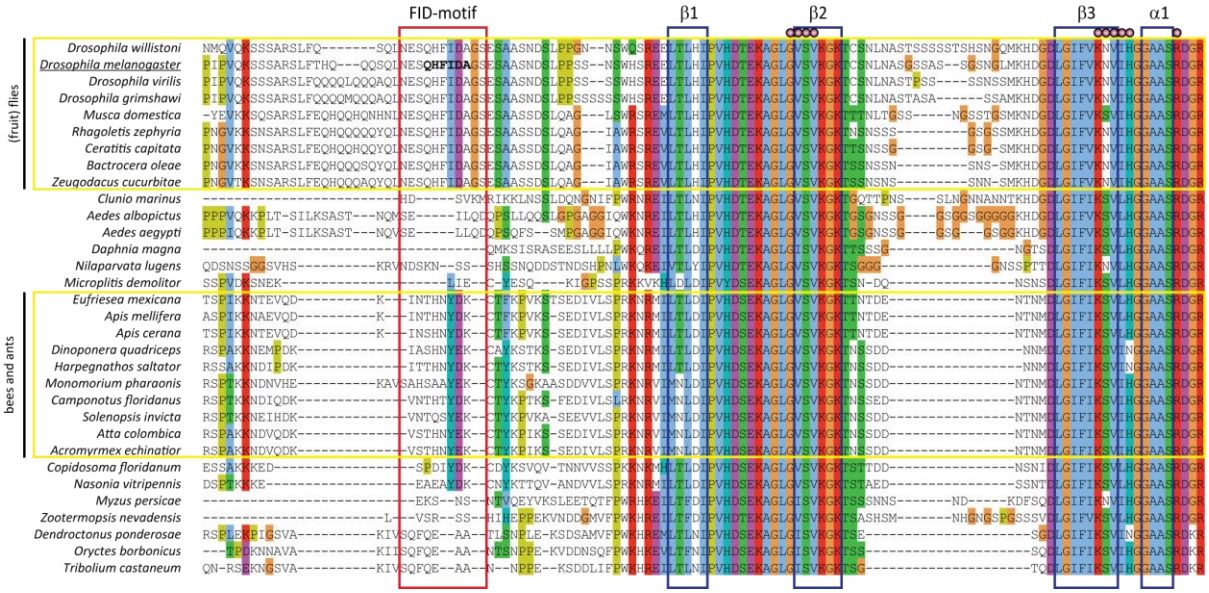

Figure 38: Sequence alignment of the Par3 FID-motif. Sequences of invertebrate Par3 proteins were aligned using clustalΩ (Sievers et al. 2011) and color coded according to conservation with clustalX (Larkin et al. 2007). The FID-motif (boxed in red) is only conserved in a subset of invertebrates closely related to *Drosophila melanogaster*. Of note, bees and ants contain a similar motif N-terminal of the Par3 PDZ3 domain. The secondary structure elements of the N-terminal part of the dmPar3 PDZ3 domain are indicated as in Figure 27. The residues interacting with the FID-motif (Figure 35C, D) are indicated by purple spheres.

The FID-motif might act as a modulator of the Par3 PDZ3 domain specificity

Moreover, the *dm*Par3 FID motif might have a regulatory function similar to known PDZ extensions (Ivarsson 2012; Luck et al. 2012; Ye & Zhang 2013). Since the binding of the FID-motif to the PDZ3 domain of *dm*Par3 reflects an auto-inhibited state with lowered affinities (Table 7, Figure 37), regulation of this inhibited state by post-translational modifications may be a mechanism to release auto-inhibition and enable a high affinity state. For example, phosphorylation of adjacent sequences may represent such a release mechanism since S612 and S621 are located at both sides of the *dm*Par3 FID-motif (Figure 37C) as well as six serine residues are present between the FID-motif and the N-terminus of the PDZ3 domain (Figure 34A). However, further studies have to be performed to investigate such regulatory mechanisms as well as the function of the FID-motif *in vivo*. Interestingly, the influence of the *dm*Par3 FID-motif on the *dm*Par3 PDZ3 domain specificity seems to almost exclusively exclude proteins involved in asymmetric cell division such as Insc or with catalytic activity such as aPKC (Figure 37). In contrast, the FID-motif still allows interactions with PBMs involved in apical localization such as Shg, Stan, Ed and Crb as well as *dm*Par6. Thereby, the FID-motif allows to fine tune the specificities of the *dm*Par3 PDZ3 domain.

In sum, I have identified here a non-conserved, N-terminal extension of the *dm*Par3 PDZ3 domain, called the FID-motif, which weakens the affinities of the *dm*Par3 PDZ3 domain for a subset of ligands. The FID-motif might be a modulator of the Par3 PDZ domain specificity. However, in depth analysis is necessary to investigate the influence of the FID-motif *in vivo*.

5. General Discussion

The main challenges in characterizing the individual functions of cell polarity proteins and especially their individual domains and motifs are functional coupling, redundant interactions, functional differences in organism strains, protein constructs (different alleles, isoforms, tags etc.) and paralogs used in different studies (Nagai-Tamai et al. 2002; Fievet et al. 2013). Moreover, the developmental context as well as the cell type have a severe impact on the composition of cell polarity complexes (Henrique & Schweisguth 2003). Lastly, polarity proteins can be part of different complexes within a single cell at the same time (Goehring et al. 2011; Rodriguez et al. 2017). Taken together, all these points are enormous obstacles for the analysis of protein functions in mutational studies as each single point may obscure phenotypes. Therefore, detailed structural studies are essential to elucidate the molecular basis of complex formation in cell polarity. Additionally, PDZ domains require a free C-terminus to recognize canonical PBMs. Therefore, C-terminal tagging as used in some cases for fluorescence microscopy or immunoblotting may abolish PDZ:PBM association and thus interfere with discovering other, hitherto unidentified PDZ:PBM interactions. In sum, this may be the reason of some of the controversies not only associated with the Par3:Par6 interaction. Nevertheless, my coauthors and I have been able to dissect the Par3:Par6 interaction in atomic detail and investigate its function *in vivo* (Renschler et al. 2018). We were able to show that the Par3:Par6 interaction relies on the Par6 PBM interacting with the Par3 PDZ1 and PDZ3 domain *in vitro* and that these interactions are conserved between human and fly (Figure 19, Figure 20-Figure 23, Figure 25). Furthermore we could show that the Par6 PBM can compete with the Par3 PDZ domain ligand Shg *in vitro* (Figure 24). In addition, my coauthors could show that the *dm*Par6 PBM seems to be functional redundant in terms of Par6 localization *in vivo* (Renschler et al. 2018). Hence, out study was able to solve the ambiguities about the details of the Par3:Par6 interaction and show the importance of the Par6 PBM in Par6 localization *in vivo*.

Interestingly, almost all polarity and cell adhesion proteins contain a PBM or at least one PDZ domain. This highlights the importance of PDZ:PBM interactions in cell polarity and cell adhesion networks. My work demonstrates the necessity of investigating PDZ domain specificities since distinct specificity profiles of the Par3 PDZ1 and PDZ2 domains as well as the promiscuity of PDZ3 and the influence of the FID-motif were impossible to infer on the sequence level (Figure 27, Figure 28, Figure 31, Figure 37, Table 5 and Table 7). Hence a thorough investigation of function, specificity and redundancy of PDZ domains, as presented here, is essential to dissect their roles in polarity protein function and localization.

Of note, it is worth mentioning that not all interaction partners of the *dm*Par3 PDZ domains are present in the same cellular environment at the same time due to difference in their expression

patterns as well as due to their regulation. Therefore, the Par3 PDZ domains have to maintain their specificities to multiple PBMs in order to fulfill all functions of Par3 in different developmental and cellular contexts (Figure 39). Hence Par3 has to be able to participate in different complexes. Nevertheless it is a recurring theme of the Par3 PDZ module to have multivalent interactions with its ligands (Figure 39) thereby enabling Par3 to form network-like structures.

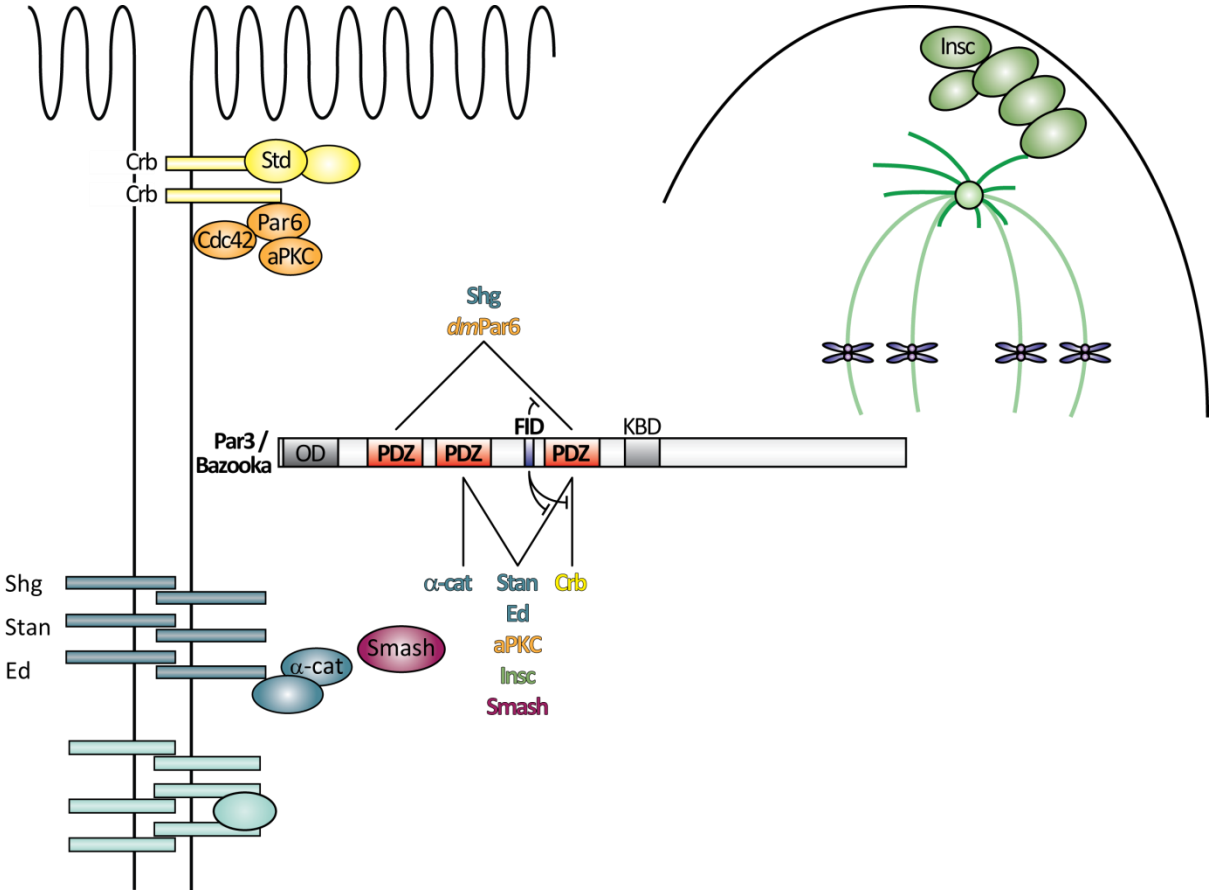

Figure 39: Interaction network of the *dm*Par3 PDZ domains. Approximate subcellular localizations of the Par3 PDZ domain interaction partners are shown. The interactions of the Par3 PDZ domains with different PBMs are color according to the localization of the binding partners with yellow indicating the Crumbs complex, orange members of the PAR complex, green-blue adherens junctions, merlot zonula adherens and green asymmetric cell division. Abbreviations according to Figure 2, Figure 3 and Figure 5.

In addition, recent investigations of the N-terminal oligomerization domain of Par3 highlight the importance of Par3 clustering for proper establishment of cell polarity (Harris 2017). Moreover, Par3 clusters have distinct activities depending on whether they dock to centrosomes or whether they are located at the cell cortex or in assembly scaffolds of adherens junctions, or as part of the PAR complex (Harris 2017). Since the Par3 OD mediates Par3 oligomerization, but no other protein-protein interactions, the recruitment of Par3 interaction partners is mediated by the PDZ domains of Par3. My analyses have shown that each individual Par3 PDZ domain possesses its unique but redundant binding profile (Figure 28, Figure 31, Table 5) determined by their structures (Figure 29

and Figure 30). Of note, the *dm*Par3 PDZ3 domain possesses overlapping PBM binding specificities (Figure 29, Figure 30, Figure 39) and conserved specificity determining residues of PDZ1 and PDZ2 (Figure 33). Hence the Par3 PDZ domain can be seen as a chimera in regard of PDZ:PBM interactions between the PDZ1 and PDZ2 domains. Worth mentioning is the fact that not all tested PBMs are present at the same subcellular localization at the same time in every cell type. For example, during gastrulation in *Drosophila* embryos Crb is expressed in late stages (Krahn, Bückers, et al. 2010; Sen et al. 2015). However, epitheliogenesis also takes place in the embryo before Crb is expressed. In line with that observation, it is known for Par3 and Crb to function redundantly in polarity maintenance in mature follicular epithelia cells (Shahab et al. 2015). In contrast, Par3 knockouts have a server effect on epithelial morphology during *Drosophila* development (Shahab et al. 2015). Another example is the interaction between Par3 and Insc which takes place during asymmetric cell division but not during epitheliogenesis (Lu & Johnston 2013; Culurgioni & Mapelli 2013). Besides different expression patterns, post-translational modifications influence the function and localization of proteins. As such, the aPKC mediated phosphorylation of Par3 is a well-studied process by which Par3 is excluded from the PAR complex at the most apical domain of epithelia cells and enriched on adherens junctions (Tepass 2012; Lang & Munro 2017). Hence, the ability of the Par3 PDZ domains to interact with different ligands would be necessary to ensure correct Par3 localization and function in different complexes in a huge variety of developmental and cellular processes. Therefore, my analyses contribute to a better understanding of the function of the Par3 PDZ3 module as a whole and of the individual Par3 PDZ domains. Clustering increases the valency of Par3 assemblies as well as the ability of Par3 to recruit multiple interaction partners via the individual PDZ domains simultaneously. This enables the assembly of Par3 and its interaction partners into cluster with liquid-like properties and may enhance the segregation and thereby the polarization process (Recouvreux & Lenne 2016; Banani et al. 2017). Furthermore, I could show that the FID-motif folds back onto the *dm*Par3 PDZ3 domain (Figure 35) and enables the PDZ3 domain to discriminate between different PBMs (

Figure 36 and Table 7). Moreover fine tuning of the Par3 PDZ3 domain affinities as well as the PDZ3 domain specificities by post-translational modifications of the FID-motif might pose an way to carefully adjust these large assemblies (Banani et al. 2017) (Figure 37 and Figure 39). Nevertheless, *in vivo* investigations addressing this hypothesis are necessary to fully understand the function of the Par3 FID-motif.

Finally, this study will help to understand the underlying principles of the Par3 interaction networks that establish, maintain and disrupt cell polarity and therefore are essential for development and carcinogenic processes.

6. Materials

6.1 Equipment

Table 8: Equipment

Instrument	Manufacturer
37 °C plate incubator	Hereaus
37 °C shaker incubator, HT Multitron Standard and HT Ecotron	Infors
Acculab-balance	Sartorius
Advanced Primus 25 Thermocycler	Peqlab
Advanced Primus 96 Thermocycler	Peqlab
Agarose gel chamber, HE 99X	Amersham Biosciences
Avance AVIII (600 MHz) spectrometer	Bruker
Avance AVIII (800 MHz) spectrometer	Bruker
Avanti J-26 XP centrifuge	Beckmann Coulter
Bio-5000 Scanner	Microtek
Centrifuge 5424 + 5417C	Eppendorf
Centrifuge bucket, 1 L	Beckmann Coulter
Centrifuge bucket, 50 mL	Beckmann Coulter
Digital Sonifier 450	Branson
DNA sequencer (3730XL)	Applied Biosystems
dragonfly	ttp labtech
E-Box 1000/26M system	Vilbert Lormat
Electrophoresis power supply, EP 301	GE Healthcare
EmulsiFlex-C3	AVESTIN, Inc.
FPLC Äkta prime plus	GE Healthcare
FPLC NGC	BioRad
freezer (-20 °C)	Liebherr
freezer (-80 °C)	Liebherr
French press Emulsiflex-C3	Avestin
Gyro-Rocker SSL3	Stuart
Heating block	VWR
HERAEUS multifuge 3SRü centrifuge	Thermo Scientific
Hi Load 16/600, Superdex 75, preg grade (120 ml)	GE Healthcare
Hi Load 26/600, Superdex 75, preg grade (320 ml)	GE Healthcare
HisTrap HP, 1 x 1 ml	GE Healthcare
HisTrap HP, 1 x 5 ml	GE Healthcare
HiTrap Q HP	GE Healthcare
HiTrap SP HP	GE Healthcare
JA-25.50 rotor	Beckmann Coulter
JLA-8.100 rotor	Beckmann Coulter
Light box prolite Basic 2	Kaiser
Magnetic stirrer, MR hei-Mix L and MR Hei-Mix S	Heidolph
Microwave	Bosch
Mighty small II gel caster	GE Healthcare

NanodropTM 100 spectrometer	Thermo Scientific
PD-10 Desalting Columns	GE Healthcare
Peristaltic Pump P1	GE Healthcare
pH meter HI 2221	HANNA Industries
Photometer, bio photometer plus	Eppendorf
Pipetman neo P1000, P200, P100, P20, P10, P2	Gilson
Precision balance 440-47N	Kern
SDS-PAGE unit, SE 250	Amersham Biosciences
Sonoplus sonifier	Bandelin
Thermomixer comfort	Eppendorf
Vortex Genie 2	Scientific Industries

6.2 Chemicals and consumables

Table 9: Chemicals

Chemical	Supplier
^{13}C-D-Glucose (99%)	Sigma-Aldrich
^{2}H,^{12}C-D-Glucose (99%)	Sigma-Aldrich
Acrylamide-bis solution (29:1), 40 % (w/v)	Roth
Agarose	Sigma-Aldrich
Ammonium chloride	Alfa Aesar
Ammonium chloride ($^{15}NH_4Cl$)	Sigma-Aldrich
Ammonium persulfate (APS)	AppliChem
Ampicillin sodium salt	Roth
BigDye Terminator v3.1 Sequencing reagents	ABI
Biotin	Roth
Boric acid	Sigma-Aldrich
Bradford protein assay reagent (5x)	Serva
Bromophenol blue 0.04 % (w/v)	Alfa-Aesar
Calcium chloride ($CaCl_2$ x 2 H_2O)	Merck
Chloramphenicol	Sigma-Aldrich
Cobalt chloride ($CoCl_2$ x 6 H_2O)	Sigma-Aldrich
Coomassie Brilliant Blue G250	Fisher Scientific
Copper (II) chloride	Alfa Aesar
Copper (II) sulfate ($CuSO_4$ x 5 H_2O)	VWR
D_2O	Sigma-Aldrich
D-Glucose	Baker
Disodium hydrogen phosphae (Na_2HPO_4)	Merck
Dithiothreitol (DTT)	Enzo Life Science
DNA loading dye (6x)	Thermo Scientific
dNTPs	Thermo Scientific
EDTA disodium salt	Promega
Ethanol	Sigma-Aldrich

Gene ruler 100bp DNA ladder	Fermentas
Gene ruler 1kbp DNA ladder	Fermentas
Glycerol	Roth
GSH (reduced)	Sigma-Aldrich
HEPES	Roth
Hydrochloric acid (HCl), 6M	Roth
Imidazole	Roth
IPTG (Isopropyl β-D-1-thiogalactopyranoside)	Roth
Iron (III) chloride ($FeCl_3$ x 6 H_2O)	Alfa Aesar
Kanamycin sulfate	Roth
L-Arginine	SAFC
L-Methionine (methyl-labeled)	CIL
Magnesium chloride	Acros Organics
Manganese (II) sulfate ($MnSO_4$ x 4 H_2O)	VWR
MOPS	Sigma-Aldrich
N,N,N‘,N‘,-tetramethylethylenediamine (TEMED)	Sigma-Aldrich
Ni^{2+}-NTA-agarose beads	Quiagen
PageRuler prestained protein ladder	Thermo Scientific
Potassium phosphate, monobasic (KH_2PO_4)	CalBiochem
Protino® Glutathione Agarose 4B	Macherey-Nagel
Rotiphorese® 50x TAE buffer	Roth
SafeView nucleic acid stain	Applied biological materials Inc.
SDS, 20 % (w/v) solution	AppliChem
SDS-PAGE buffer 10x (Tris, glycine, SDS)	National Diagnostics
Sodium azide (NaN_3)	Sigma-Aldrich
Sodium chloride (NaCl)	Merck
Sodium dihydrogen phosphate monohydrate	Merck
Sodium hydroxide 10N (NaOH)	Alfa-Aesar
Sodium L-glutamate monohydrate	Merck
TEMED (N,N,N',N'-tetramethylethylene diammine)	Sigma-Aldrich
Thiamine hydrochloride	Sigma-Aldrich
Tris-HCl	Roth
Triton X-100	Sigma-Aldrich
Zinc sulfate ($ZnSO_4$ x 7 H_2O)	VWR

Table 10: Enzymes

Enzyme	Vendor
DNaseI	Appli Chem
DpnI	NEB
Kapa Polymerase	Roche
Lysozyme (fromm henn egg white)	Fluka
Tobacco etch virus (TEV) protease	own production

Table 11: Consumables

Product	Manufacturer
5 mm NMR tubes	Norell
96 well plate	Greiner
96-3 low profile INTELLI-PLATE®	Art Robbins Instruments
Concentrator Vivaspin 20	Sartorius
Cuvettes (plastic)	Roth
Dialysis membrane, MWCO 3500	Spectrum Laboratories
Falcon tubes (14 mL and 50 mL)	Greiner
Inoculation loop	Greiner
Inoculation spreader	Sarstedt
Membrane filters	Millipore
NucleoSpin® Gel and PCR Clean-up	Machery-Nagel
NucleoSpin® Plasmid EasyPure	Machery-Nagel
Parafilm	Pechney
Pasteur piptes	Willmad Lab Glass
PCR plastic tubes	Greiner
Pipet tips	Greiner
Pipets (single use, sterile)	Simport
Plastic cups (1.5 mL and 2 mL)	Eppendorf
Plastic cups (1.5 mL capless)	Fisher Scientific
Snap cap inoculation tubes	Simport
Syringe filter (0.22 µm, 0.45 µm)	Millex
Syringes (6, 20 and 60 mL)	Fisher Scientific
UV cuvettes (plastic)	Eppendorf
Vacuum sterile filter	Millipore

6.3 Buffers and media

Table 12: Buffer and media composition

Buffer	Ingredients
Agarose (1 %) stock solution	5 g of agarose is dissolved in 500 mL heated 1x Rotiphorese TAE-buffer and stored at 65 °C
Ampicillin (1,000x)	2.5 g / 25 mL H2O (100 mg/mL)
APS (10 %)	1 g / 10 mL (0.1 g/mL)
Biotin (1,000x)	20 mg / 20 mL H2O (1 mg/mL; add some 1M NaOH to dissolve)
Chloramphenicol (1,000x)	0.85 g / 25 mL pure EtOH (34 mg/mL)
Coomassie stain solution	0.5 g Coomassie Brilliant Blue G250 (0.025%) in 30 mM HCl, 10% EtOH
crystallization buffer	20 mM HEPES pH 7.5, 150 mM NaCl, 1 mM DTT
DTT (1 M)	3.1 g DTT / 20 mL (155 mg/mL)
DTT (5 M)	7.7 g DTT / 10 mL (770 mg/mL)
EDTA pH 8.0 (100 mM)	37.22 g/L, pH 8,0
elution buffer	lysis buffer with 333 mM Imidazol

HEPES pH 8.0 (1 M)	238.3 g HEPES in 1L H2O, adjust pH
Imidazole (1 M)	68.08 g Imidazole / 1000 mL
IPTG (1 M)	4.8 g / 20 mL (240 mg/mL)
Kanamycin (1,000x)	1.25 g / 25 mL H2O (50 mg/mL)
LB	10 g bactotryptone, 5 g yeast extract, 10 g NaCl in 1 l of H2O, pH 7.4, autoclaved
LB-Agar	5 g bactotryptione, 2.5 g yeast extract, 5 g NaCl, 7.5 g agar (1.5 %) in 500 ml H_2O, pH 7.4, autoclaved
lysis buffer	NaP buffer with 10 mM Imidazol, 1 mM DTT, pH 7.5
lysis buffer +	lysis buffer with Lysozyme, RNAse, Triton X-100
lysis buffer EDTA	NaP buffer with 10 mM Imidazol, 1 mM DTT, 0.5 mM EDTA, pH 7.5
M9 (10x)	60 g Na_2HPO_4, 28.6 g KH_2PO_4, 5g NaCl dissolved in 1 L H_2O, pH 7.4
M9 (1x, D2O)	1 L D_2O, 6 g Na_2HPO_4, 2.86 g KH_2PO_4, 0.5 g NH_4CL (unlabelled or ^{15}N), pH 7.4, 4 g glucose unlabelled or 2 g glucose labelled (^{1}H,^{13}C or ^{2}H,^{13}C or ^{2}H,^{12}C), 1 mL trace elements (1,000x), 0.1 mL trace elements (10,000x), 1 mL $MgSO_4$ (1M), 1 mL biotin (1000x), 1 mL thiamine (1000x), 1 mL of each antibiotic (1000x), 0.3 mL $CaCl_2$ (1M)
M9 (1x, H2O)	100 mL M9 (10x) in 1 L of H_2O, pH 7.4, 0.5 g NH_4CL (unlabelled or ^{15}N), 4 g glucose unlabelled or 2 g glucose labelled (^{1}H,^{13}C or ^{2}H,^{13}C or ^{2}H,^{12}C), 1 mL trace elements (1,000x), 0.1 mL trace elements (10,000x), 1 mL $MgSO_4$ (1M), 1 mL biotin (1000x), 1 mL thiamine (1000x), 1 mL of each antibiotic (1000x), 0.3 mL $CaCl_2$ (1M)
MOPS pH 7.5 (1 M)	209.26 g MOPS in 1 L H_2O, adjust pH
NaP (10x)	87.6 g/L NaCl, 71 g/L Na_2HPO_4, pH 7.1
NaP (1x)	50 mM NaP, 150 mM NaCl, pH 7.5
NMR	20 mM NaP, 150 mM NaCl, pH 7.5 or 6.5, 1-2 mM DTT, (0.5 mM EDTA), (0.02 % NaN_3)
nonreducing SDS loading buffer (5x)	3 mL Tris-HCl (1 M, pH 6.8), 2.5 mL glyercol (25 % final), 4.5 mL 20% SDS, 1 mg bromophenol blue (0,01% final)
PD	50 mM NaP pH 7.5, 150 mM NaCl, 10% glycerol, 2 mM DTT
Q high salt	20 mM bis-Tris pH 7, 1000 mM NaCl, 1 mM DTT
Q low salt	20 mM bis-Tris pH 7, 10 mM NaCl, 1 mM DTT
reducing SDS loading buffer (5x)	3 mL Tris-HCl (1 M, pH 6.8), 2.5 mL glyercol (25 % final), 4.5 mL 20% SDS, 1 mg bromophenol blue (0,01% final), 1 mL of DTT (5 M final)
SP high salt	20 mM HEPES pH 7.5, 1000 mM NaCl, 1 mM DTT
SP low salt	20 mM HEPES pH 7.5, 10 mM NaCl, 1 mM DTT
Thiamine (1000x)	20 mg / 20 mL H_2O (1 mg/mL)
Trace elements (1,000x)	5 g EDTA in 100 mL H_2O (adjust to pH 7.5); 0.833 g $FeCl_3$ x 6 H_2O, 84 mg $ZnCl_2$, 13 mg $CuCl_2$ x 2 H_2O, 10 mg $CoCl_2$ x 6 H_2O, 10 mg H_3BO_3
Trace elements (10,000x)	3.37 g $CuSO_4$ x 5 H_2O, 3.0 g $MnCl_2$ x 4 H_2O, 0.43 g $ZnSO_4$ x 7 H_2O, 0.5 $CoCl_2$ x 6 H_2O in 100 mL H_2O
Tris-HCl pH 6.8 (1 M)	60.5 g Tris-HCl in 500 mL H_2O, pH 6.8
Tris-HCl pH 8.0 (1 M)	121 g Tris-HCl in 1 L H_2O, pH 8

Tris-HCl pH 8.8 (1.5 M)	90.75 g Tris-HCl in 500 mL H_2O, pH 8.8
XTAL	20 mM HEPES pH 7.5, 150 mM NaCl, 1 mM DTT

6.4 Protein expression constructs

Table 13: Protein expression constructs

protein	domain	# aa	# aa NMR/ X-ray construct	expression tag (cleavage)	vector
Chlamydia trachomatis					
GST (A0A0E9AVJ1)	N-terminal domain	1-217		His_6 (no) … HA (no)	pET M30-HA
D. melanogaster					
aPKC (FBgn0261854)	PBM	599-606	-7 - 0	His6-GB1 (no)	pRT Duet
Crb (FBgn0259685)	PBM	2246-2253	-7 - 0	His6-GB1 (no)	pRT Duet
Ed (FBgn0000547)	PBM	1315-1322	-7 - 0	His6-GB1 (no)	pRT Duet
Insc (FBgn0011674)	PBM	852-859	-7 - 0	His6-GB1 (no)	pRT Duet
Par3 (FBpp0110299)	FID-motif	610-620		His6-GB1 (no)	pRT Duet
	PDZ1	330-419	5-94	His6-MBP (yes)	pET M41
	PDZ2	459-553	5-99	His6-MBP (yes)	pET M41
	PDZ3	634-760		His6-MBP (yes)	pET M41
	PDZ3 Δβ2-3loop	634-666, 686-760	2-109	His6-MBP (yes)	pET M41
	linker-PDZ3 Δβ2-3loop	554-666, 686-760		His6-GST (yes)	pET M30
	linkerΔI-PDZ3 Δβ2-3loop	590-666, 686-760		His6-GST (yes)	pET M30
	linkerΔII-PDZ3 Δβ2-3loop	610-666, 686-760		His6-GST (yes)	pET M30
	linkerΔIII-PDZ3 Δβ2-3loop	618-666, 686-760		His6-GST (yes)	pET M30
	linkerΔFID-PDZ3 Δβ2-3loop	554-609,634-666, 686-760		His6-GST (yes)	pET M30
	PDZ1-3	330-760		His6-GST-HA (no)	pET M30-HA
	PDZ1-3 Δβ2-3loop	330-666, 686-760		His6-GST (yes)	pET M30
Par3-Par6	PDZ1:PBM fusion	330-419, 344-351	5-94, -7 - 0	His6-MBP (yes)	pET M41
Par3-Shg	PDZ1:PBM fusion	330-419,	5-94, -7 - 0	His6-MBP (yes)	pET M41
Par3-Insc	PDZ2:PBM fusion	459-553	5-99, -7 - 0	His6-MBP (yes)	pET M41
Par6 (FBpp0074229)	Full length	1-351		His6-Sumo (no)	pET M11 Sumo
	ΔPBM	1-343		His6-Sumo (no)	pET M11 Sumo
	PB1-Crib	1-255		His6-Sumo (no)	pET M11 Sumo
	PB1-CribPDZ	1-155		His6-Sumo (no)	pET M11 Sumo
	PBM	344-351	-7 - 0	His6-GB1 (no)	pRT Duet
	PBM L349A	344-351	-7 - 0	His6-GB1 (no)	pRT Duet
	PBM H350A	344-351	-7 - 0	His6-GB1 (no)	pRT Duet
	PBM L351A	344-351	-7 - 0	His6-GB1 (no)	pRT Duet
	PDZ	155-255		His6-MBP (yes)	pET M41
	Crib-PDZ	139-255		His6-MBP (yes)	pET M41
Shg (FBgn0003391)	PBM	1500-1507	-7 - 0	His6-GB1 (no)	pRT Duet
Smash (Dmel_CG43427)	PBM	1526-1533	-7 - 0	His6-GB1 (no)	pRT Duet
Std (FBgn0261873)	PBM	13-23	-8 - 1	His6-GB1 (no)	pRT Duet
Stan (FBgn0024836)	PBM	3542-3549	-7 - 0	His6-GB1 (no)	pRT Duet

α-cat (FBgn0010215)	PBM	900-907	-7 - 0	His6-GB1 (no)	pRT Duet
H. sapiens					
Par3 (NP_001171714)	PDZ1	246-364	4-122	His6-GST (yes)	pET M30
	PDZ2	457-549	4-96	His6-GST (yes)	pET M30
	PDZ3	583-685	5-107	His6-GST (yes)	pET M30
Par3-Par6a	PDZ1:PBM fusion	246-364, 339-346	4-122, -7 - 0	His6-GST (yes)	pET M30
Par6a (NP_058644)	PBM	339-346	-7 - 0	His6-GB1 (no)	pRT Duet
S. cerevisiae					
Sumo (Q12306)	FL	1-105		His_6 (no)	pET M11 Sumo
Streptococcus sp. group G					
protein G (P19909)	B1 F353Y K358E	304-358		His_6 (no)	pRT Duet

6.5 Primers

Table 14: Primers

construct	primer name	sequence
***dm*Par3 linkerΔFID-PDZ3 Δβ2-3loop**	FR98_Baz_linker-NII_fw	CTCATCAGCAGCAATCGCAGCTCAACAGTTGGCACTCCCGCGAG
	FR98_Baz_linker-NII_rv	CGCGGGAGTGCCAACTGTTGAGCTGCGATTGCTGCTGATG
***dm*Par3 linkerΔIII-PDZ3 Δβ2-3loop**	FR99_Baz_delNII_1_fw	CTTTATTTTCAGGGCGCCATGGGCGCGGGCAGCGAGTCGGC
	FR99_Baz_delNII_1_rv	GCCGACTCGCTGCCCGCGCCCATGGCGCCCTGAAAATAAAG
***dm*Par3 linkerΔII-PDZ3 Δβ2-3loop**	FR88_Baz_PDZ3+N_I_fw	CTTTATTTTCAGGGCGCCATGGGCAACGAATCTCAGCACTTTATTGATGCGG
	FR88_Baz_PDZ3+N_I_rv	CCGCATCAATAAAGTGCTGAGATTCGTTGCCCATGGCGCCCTGAAAATAAAG
***dm*Par3 linkerΔI-PDZ3 Δβ2-3loop**	FR89_Baz_PDZ3+N_II_fw	CTTTATTTTCAGGGCGCCATGGGCCCGGTACAAAAATCCAGCAGCGC
	FR89_Baz_PDZ3+N_II_rv	GCGCTGCTGGATTTTTGTACCGGGCCCATGGCGCCCTGAAAATAAAG
GB1-Crb PBM	FR93_GB1-Crb_fw	GAAGAAAACCTGTATTTTCAGGGAAAACCGCCTCCGGAAGAACGCCTGATTTAAACCGGCTTTCTGACCGAATAT
	FR93_GB1-Crb_fv	ATATTCGGTCAGAAAGCCGGTTTAAATCAGGCGTTCTTCCGGAGGCGGTTTTCCCTGAAAATACAGGTTTTCTTC
GB1-*dm*Par3 FID-motif	FR120_GB1-dmPar3_linker_fw	CAGAAGAAAACCTGTATTTTCAGGGAAGCGGCAACGAATCTCAGCACTTTATTGATGCGGGCAGCTAAGATCCGGATCATGATCATACCG
	FR120_GB1-dmPar3_linker_rc	CGGTATGATCATGATCCGGATCTTAGCTGCCCGCATCAATAAAGTGCTGAGATTCGTTGCCGCTTCCCTGAAAATACAGGTTTTCTTCTG
GB1-*hs*Par6α PBM	FR32_GB1-hPar6a_fw	GAAAACCTGTATTTTCAGGGAGGCGATGGCAGCGGCTTTAGCCTGTAACGGTAAAACCCTGAAAGG
	FR32_GB1-hPar6a_rv	CCTTTCAGGGTTTTACCGTTACAGGCTAAAGCCGCTGCCATCGCCTCCCTGAAAATACAGGTTTTC
GB1-Smash PBM	FR65_GB1-unchar_fw	GAAGAAAACCTGTATTTTCAGGGAGATGGCATTAAATTTAGCTGCGTGTAACGGTAAAACCCTGAAAGGTG
	FR65_GB1-unchar_rv	CACCTTTCAGGGTTTTACCGTTACACGCAGCTAAATTTAATGCCATCTCCCTGAAAATACAGGTTTTCTTC
GB1-Stan PBM	FR95_GB1-Stan_fw	GAAGAAAACCTGTATTTTCAGGGAATTGATGATGACGAAACCACGGTGTAAACCGGCTTTCTGACCGAATAT
	FR95_GB1-Stan_rv	ATATTCGGTCAGAAAGCCGGTTTACACCGTGGTTTCGTCATCATCAATTCCCTGAAAATACAGGTTTTCTTC
GB1-Std PBM	FR94_GB1-Std_fw	GAAGAAAACCTGTATTTTCAGGGACCACACCGTGAGATGGCCGTCGATTGTCCGGACAGTGGATCTGGTTAAACCGGCTTTCTGACCGAATAT
	FR94_GB1-Std_rv	ATATTCGGTCAGAAAGCCGGTTTAACCAGATCCACTGTCCGGACAATCGACGGCCATCTCACGGTGTGGTCCCTGAAAATACAGGTTTTCTTC

7. Methods

7.1 Molecular biology

7.1.1 Agarose gel electrophoresis

Deoxyribonucleic nucleic acid polymers can be easily separated by their length by agarose gel electrophoresis no matter whether they are linear fragments such as PCR products or circular such as plasmids. Since their intrinsic negative charge of the phosphate deoxyribose backbone, they move towards the cathode in an electric field. Within a mesh like environment of agarose gels, this fact can be employed to separate different sized molecules due to the faster migration of smaller fragments.
A 1% (w/v) Agarose solution is pepared with 1x TAE Buffer (Table 12) and 50 mL are mixed with 2 µL of SyberGreen™ dye and cast. Agarose gels are run at 175 V for 14-18 min in 1x TAE buffer.

7.1.2 Heat shock transformation of chemical competent *E.coli* cells

Transformation describes the process by which bacteria take up foreign DNA either spontaneously or enhanced via certain methods. Any method is based on the perforation of the bacterial membrane by liposomes or by mechanical forces generated by an electric discharge, ultrasonic sound, or a short heat shock. The perforated membrane allows DNA to diffuse into the cells. The affinity of bacterial membranes for DNA can be enhanced by chemicals i.e. Ca^{2+}-ions and by incubation of the bacteria with DNA prior to transformation.
1 µL of purified plasmid DNA (~ 100 ng/ µL) or 5 µL of a ligation reaction, QC PCR or RF cloning PCR are added to 50 µL chemical competent cells and incubated 5 min on ice. Cells are heat shocked for 1 min at 42°C. Cells are transferred immediately afterwards on ice and 500 µL LB medium (Table 12) are added. Cells are incubated for recovery for 30 min (purified plasmid DNA) or 90 min (ligation, QC, RF) at 37°C shaking at low rpm in order to allow expression of antibiotic resistance genes. After recovery, cells are plated on LB agar plates with the respective selection markers (Table 12) and incubated o/n at 37°C.

7.1.3 PCR based methods

The polymerase chain reaction (PCR) is used to amplify DNA fragments. To this end, a heat stable DNA polymerase, short DNA primers complementary to sequences at both ends of the DNA fragment and deoxy nucleotides (dNTPs) are added to a DNA template. By cycling the temperature, a series of steps are permutated which lead to an amplification of the template DNA. First, the DNA double helix is denatured with high temperatures around 95-98°C. Next, the temperature is

decreased to the annealing temperature of the primer (Table 14). The annealing temperature Tm is the temperature at which the primer binds specifically to is complementary sequence and can be calculated e.g. according to (Wallace et al. 1979; Green & Sambrook 2012):

Equation 13:

$$Tm = 64.9 + \frac{41 \times (yG + zC - 16.4)}{(wA + xT + yG + zC)}$$

Where wA, xT, yG and zC are the number of bases of A, T, G anc C, respectively. Last, the temperature is increased to 72°C to allow the polymerase to elongate the primer at its temperature optimum. Finally, the cycle is repeated again. Since the product of the previous cycle is another template for the subsequent cycle, in general an exponential amplification of DNA is achieved.

7.1.3.1 QuickChange™ mutagenesis

The QuickChange (QC) Kit developed by Stratagene is a technique to introduce site specific mutations into a DNA sequence. QC reaction parameters are given in Table 15 and Table 16.

Table 15: QC reaction

Amount/ Volume	
25 ng	target vector
2.5 µL	10 µM Mix of fwd and rev Primers
5 µL	5x High GC Kapa Buffer
1 µL	Kapa dNTP Mix
0.5 µL	Kapa HiFi Polymerase
Adjust volume to 25 µL with sterile H_2O	

Table 16: QC and RF reaction parameters

Temperature	**Duration**	**Step**	**No of cycles**
98°C	3 min	initialization	
98°C	30 sec	denaturing	20-25
X* °C	15 sec	annealing	
72°C	**	elongation	
72°C	10 min	final elongation	
4°C	forever	storage	

* calculated according to Equation 13, ** calculated according to an extension rate of 2kb/ min

7.1.3.2 Restriction free cloning

Cloning without the need of restriction sites and restriction enzymes is possible with restriction free (RF) cloning (van den Ent & Löwe 2006). RF cloning is a PCR based cloning approach. In short, a PCR product or any other linear double stranded DNA fragment encoding the gene of interest and flanked by priming regions complementary to the target vector insertion site is inserted into the target vector. In a linear amplification reaction, the DNA fragment acts as a primer for the amplification of the target vector. This leads to a nicked product with the gene of interest incorporated site specific into the target vector. Since the parental target vector is methylated, digestion with DpnI, a DNase specific for methylated DNA, degrades the parental target vector. Subsequently, the nicked product is transformed into a suitable host and can be used further.

Inserts larger than 120 nt have to be PCR amplified. The primers used (Table 12) are designed according to the following specifications. The 5' (forward) primer included ~25 bp overlapping with the sequence upstream of the target vector insertion site followed by ~25 bp of the gene of interest whereas the 3' (reverse) primer was designed in a reversed order having ~25 bp of the antisense strand of the gene of interest at its 5' end followed by ~25 bp of the antisense strand of the target vector insertion site. It is advisable to have some nucleotides in between the two insertion site of the target vector to reduce sterical hindrance. Additionally, care of reading frames present in the target sequence has to be taken in order to avoid frame shift mutations. Insert DNA was amplified by a PCR with a proofreading polymerase, analyzed by agarose gel electrophoresis, purified and served as "primers" for the subsequent RF cloning reaction. Inserts smaller than 120 nt can be synthesized by solid phase synthesis. However, the annealing sequences were designed according to the annealing sequences of longer inserts.

The final RF cloning reaction is described in Table 17 with the reaction parameters in Table 16. After addition of 0.5 µL DpnI and incubation for 30 min at 37°C, RF cloning products are analyzed by agarose gel electrophoresis. Successful reactions are transformed into DH5α cells and plated on LB-agar plates with appropriate antibiotics for selection.

Table 17: RF cloning reaction

Amount/ Volume	
25 ng	target vector
150 ng	forward primer (alternatively, double-stranded PCR product for large inserts)
150 ng	reverse primer (not necessary if working with large inserts)
5 µL	5x High GC Kapa Buffer
1 µL	Kapa dNTP Mix
0.5 µL	Kapa HiFi Polymerase
Adjust volume to 25 µL with sterile H_2O	

7.1.4 DNA purification

DNA is purified with the NucleoSpin® Gel and PCR Clean-up Kit (Machery-Nagel) according to the manufacturer's instructions.

7.1.5 Isolation of plasmid DNA

Plasmids are small circular DNA fragments encoding genes outside the bacterial genome. In nature, they usually contain resistance genes and can be transferred between different bacterial cells. These attributes make them a great tool for genetic manipulation of bacteria cells since plasmids can be modified according to the needs of the experimenter by molecular methods.

E.coli DH5α cells transformed with the desired plasmid were grown o/n at 37°C in 8 ml of LB medium (Table 12) supplemented with the respective selection marker. Cells were harvested at 4000 rpm (HERAEUS Multifuge 3SR+) at room temperature for 10 min and the supernatant was discarded. DNA was purified with the NucleoSpin® Plasmid EasyPure PCR Kit (Machery-Nagel) according to the manufacturer's instructions.

7.1.6 DNA sequencing

The dideoxy method for DNA sequencing was invented by Sanger (Sanger et al. 1977). In short, dideoxy nucleotides (ddNTPs) fluorescently labeled according to their base as well as deoxy nucleotides (dNTPs) are added to a PCR mix. If a labeled ddNTP is incorporated by the polymerase instead of a dNTP, chain elongation is terminated and results in a fluorescently labeled DNA strand according to the last base incorporated at the 3'-end. The resulting mixture of differently sized and labeled DNA strands can be separated by HPLC and the 3'-base can be analyzed by fluorescent read out giving a chromatogram which represents the sequence of the template DNA.

Standard sequencing primers can be found in Table 18 and reaction set up in Table 19 and Table 20.

Table 18: Standard sequencing primer

Primer	Sequence	annealing region	direction	Plasmid
T7 terminator	GCTAGTTATTGCTCAGCGG	T7 terminator	3' to 5'	pET M30, pET M30 HA pET M41, pRT Duet
T7 promotor	TAATACGACTCACTATAGGG	T7 promotor	5' to 3'	pET M30, pET M41
GST fw	GGGCTGGCAAGCCACGTTTGGTG	C-terminus of GST	5' to 3'	pET M30, pET M30 HA
MBP fw	CGTCAGACTGTCGATGAAG	C-terminus of MBP	5' to 3'	pET M41

Table 19: Sequencing PCR

Amount/ Volume	
100 - 200 ng	plasmid DNA
1 µL	10 µM sequencing primer
0.5 µL	BDT mix
2 µL	5x sequencing buffer
Adjust volume to 10 µL with sterile H_2O	

Table 20: Sequencing PCR parameters

Temperature	**Duration**	**Step**	**No of cycles**
96°C	20 sec	initialization	
96°C	20 sec	denaturing	30
50°C	10 sec	annealing	
60°C	4 min	elongation	
60°C	10 min	final elongation	
4°C	forever	storage	

7.2 Protein biochemistry

7.2.1 Sodium dodecyl sulfate polyacrylamide gel electrophoresis (SDS-PAGE)

Each protein has its unique sequence and all physical properties can be derived from this sequence. One of those properties is the molecular weight (MW) which can be calculated as the sum of all MWs of all amino acids in the sequence of a protein. SDS-PAGE is one method to separate proteins according to their MW. To this end, the proteins are denatured by SDS in the loading buffer which forms a negatively charged complex with the proteins. Next, the sample is loaded on a polyacrylamide gel and a current is applied across the gel. The negative charged protein-SDS complexes will move towards the cathode of the electric field. During this movement, large protein-SDS complexes will move slower than small ones since large protein-SDS complexes are retained more by the polyacrylamide gel. Thus, differently sized proteins are separated. If marker proteins with known MW are run on the same gel, the MW of the proteins inside the sample can be estimated.

SDS-polyacrylamide gels are cast according to Table 12, Table 21 and Table 22 and run at 180 – 220 V. Gels are stained with Coomassie for protein detection.

Table 21: Gel recipe for polyacrylamide separating gels.

Gel percentage (separation range)	8% (30 - 250 kD)	12% (14 - 150 kD)	16% (5 - 70 kD)
40% acrylamide (29:1)	14 mL	21 mL	28 mL
H2O	37.5 mL	30.5 mL	23.5 mL
1.5M Tris-HCl pH 8.8 (0.375 M)	17.5 mL		
20% SDS (0.1%)	0.35 mL		
10% APS (0.1%)	0.35 mL		
TEMED (0.5 uL / mL)	35 µL		

Table 22: Gel reipe for polyacrylamide stacking gel.

	4%
40% acrylamide (29:1)	3.5 mL
H2O	26.5 mL
1.0M Tris-HCl pH 6.8 (0.125M)	4.35 mL
20% SDS (0.1%)	0.175 mL
10% APS (0.1%)	0.175 mL

7.2.2 Coomassie staining

Coomassie Brilliant Blue G250 is a bright blue dye which interacts with proteins in a nonspecific manner via hydrophobic interactions. Therefore, Commassie can be used to detect proteins which have been separated by SDS-PAGE.

Rinse gel three times in water and boil it in the microwave. Rinse again with water and cover the gel with Coomassie staining solution (Table 12 and Table 23). Boil gel in staining solution and incubate 5 min shaking. Replace staining solution with water for destaining.

Table 23: Coomassie staining solution

Amount/ Volume	
Coomassie Brilliant Blue G250	**0.8g**
Ethanol	100 mL
H_2O	900 mL
6 M HCl	5 mL
stir o/n	

7.2.3 Pull down assays

The interactions of two different proteins can be probed via pull down assays. To this end, one binding partner is immobilized via an affinity tag at Sepharose beads. The other binding partner is then incubated with those beads. If both proteins interact, the binding partner not immobilized should be detectable after several washing steps in the eluted fraction.

First, a 1:1 slurry of glutathione beads (Macherey-Nagel) in PD buffer (Table 12) is prepared. Next, 0.27 nmol of N-terminal His_6-GST-HA-tagged *dm*Par3 PDZ1-3 or His_6-GST-HA in PD buffer as well as 16.2 nmol of His_6-GST-SUMO-*dm*Par6 variants (see Figure 20A for details) are added and the volume is adjusted to 250 µL. After incubation for 60 minutes at 4°C, unbound proteins are removed by four washing steps. Each washing steps consists of centrifugation of the beads for 90 sec at 1500 g at 4°C and subsequent buffer exchange to 200 µL fresh PD buffer. Finally, bound proteins are eluted with PD buffer supplemented with 25 mM reduced GSH for 60 minutes at 4°C and precipitated with 10% (w/v) TCA for 30 minutes on ice. Precipitated proteins are pelleted by centrifugation (20 min, 20000 g, 4°C) and resuspended in 20 µL SDS loading buffer, resolved by SDS-PAGE and detected by Coomassie staining for analysis.

7.2.4 Recombinant protein expression

Structural biology methods such as X-ray crystallography and NMR spectroscopy usually require vast amounts of pure protein. The method of choice to produce those high amounts is the overexpression of proteins recombinant in bacteria cells such as *E.coli* with subsequent purification steps.

7.2.4.1 Unlabeled protein expression

50 ml LB supplemented with the respective antibiotics (Table 12) are inoculated with *E.coli* BL21-CodonPlus (DE3)-RIL cells carrying the desired protein expression construct (Table 13) and incubate o/n at 37 °C. The next morning, 500 mL LB supplemented with the respective antibiotics are inoculated with the o/n preculture at an OD600 of 0.2 – 0.3. The suspension culture is expanded at 37 °C until the desired volume (usually 2 L for GB1-fusion constructs) is reached with an OD600 of 0.8 – 0.9. At this point, the culture is shifted to 20 °C. After temperature equilibration (30 – 60 min) protein expression is induced by the addition of IPTG (0.5 – 1 mM final concentration) for 16 h. Cells are harvested by centrifugation (6000 g, 10 min, 4°C) and cell pellets are stored at -20°C until use.

7.2.4.2 Isotope labeling

NMR studies require the labeling of the protein to be investigated with specific isotopes such as ^{15}N and ^{13}C (Table 3). To this end, recombinant proteins are expressed in minimal media containing bioavailable forms of the isotopes such as $^{15}NH_4Cl$ as sole nitrogen source or ^{13}C-Glucose as sole carbon source. Furthermore, for NMR studies of larger proteins (≥ 25 kDa) it is desirable to enrich Deuterium in order to minimize Hydrogen mediated T_2-relaxation.

50 ml LB supplemented with the respective antibiotics (Table 12) are inoculated with *E.coli* BL21-CodonPlus (DE3)-RIL cells carrying the desired protein expression construct (Table 13) and incubate o/n at 37 °C. The next morning, 500 mL M9 minimal media containing the appropriate isotopes and supplemented with the respective antibiotics (Table 12) are inoculated with the o/n preculture at an OD600 of 0.15 – 0.3. To this end, a sufficient amount of the preculture is pelleted by centrifugation and resuspended in M9 minimal media. The suspension culture is expanded at 37 °C until the desired volume (usually 1 L ^{15}N M9 (H_2O) for ^{15}N-labeled PDZ domains constructs) is reached with an OD600 of 0.8 – 0.9. At this point, the culture is shifted to 20 °C. After temperature equilibration (30 – 60 min) protein expression is induced by the addition of IPTG (0.5 – 1 mM final concentration) for 16 h. Cells are harvested by centrifugation (6000 g, 10 min, 4°C) and cell pellets are stored at -20°C until use.

7.2.5 Protein purification

All methods in structural biology require sufficient amounts of pure protein. The following section covers several methods for protein purification. Depending on the needs of the methods used, different purification strategies combining different purification steps were chosen to fulfill these needs. Protein purification strategies are summarized in Table 24.

Table 24: Protein purification strategies used for the studies of the *dm*Par3 PDZ domains.

method	proteins	purification steps
CSPs analysis/	GB1-fusion constructs	Ni-NTA, GF
NMR titrations	^{15}N-labeled PDZ domain	Ni-NTA, TEV, GF
	^{15}N-labeled *dm*Par3 linkerPDZ3 Δβ2-3 loop constructs	Ni-NTA, TEV, reverse Ni-NTA, (GF)
backbone assignment	^{13}C,^{15}N-labeled linkerΔNII-PDZ3 Δβ2-3 loop	Ni-NTA, TEV, reverse Ni-NTA, GF
crystallization trials	PDZ-ligand fusion	Ni-NTA, TEV, IEX, GF

Abbreviations as follows: Ni-NTA: Ni^{2+}-NTA-affinity chromatography, GF: gel filtration, TEV: TEV protease cleavage, reverse Ni-NTA: Reverse Ni^{2+}-NTA-affinity chromatography, IEX: Ion exchange chromatography.

7.2.5.1 Ni^{2+}-NTA-affinity chromatography

Ni^{2+}-Ions can form complexes with Imidazole and Imidazole ring containing molecules. Since histidine contains an Imidazole ring in its side chain, proteins can form complexes with Ni^{2+}-Ions. This can be exploited to affinity purify proteins containing an appropriate number of histidine residues in an appropriate conformation. Therefore, an N-terminal histidine tag consisting of six histidines can be integrated into protein expression constructs. Those fusion proteins are able to bind to Ni^{2+}-Ions

immobilized on Nitrilotriacetic acid agarose beads and can be separated from a protein mixture such as cell lysates.

35 ml lysis buffer + (Table 12) per 1 L medium is used to resuspend cell pellets by vortexing for 10 min at 4°C. Large lysis volumes (≥ 1 L culture volume) are lysed with an EmulsiFlex for 2-3 rounds at 4°C, small lysis volumes are sonicated (KE 76 tip, 2 sec pulse, 1 sec pause, 20 % amplitude, total time 1 min) on ice two times. Cell debris are removed by centrifugation (40 000 g, 4°C, 30 min). After filtration, the supernatant is mixed with Ni^{2+}-NTA beads (5 mL per 1 L of culture) and incubated at 4°C for 10 min. Next, the mixture is poured into a column and washed with lysis buffer until no protein is detected with a Bradford assay in the wash fraction. Bound proteins are eluted with elution buffer. Fractions are analyzed by SDS-PAGE and Coomassie staining.

7.2.5.2 Dialysis and TEV protease cleavage

Various protein purification steps require specific buffer conditions to ensure proper separation. For example, reverse Ni^{2+}-NTA-affinity chromatography requires a Imidazole concentration below 5 mM and ion exchange chromatography require a low buffer conductivity (< 5 mS/cm). Simultaneously, the expression tag can be cut off by TEV protease since all protein expression constructs used in this thesis harbor a TEV protease recognition site (ENLYFQG) between the C-terminus of the expression tag and the N-terminus of the protein of interest.

To this end, the protein solution is mixed with 1 aliquot of TEV protease (1 mL, 0.5 mg/mL), packed into a 5 kDa cut-off dialysis tube and dialyzed against an appropriate volume of the buffer (Table 12) with the desired characteristics for downstream applications (Table 24) o/n at 4°C.

7.2.5.3 Reverse Ni^{2+}-NTA-affinity chromatography

After TEV protease cleavage, the cut off expression tag can be removed by a second Ni^{2+}-affinity column.

Beforehand, the Imidazole concentration has to be reduced at least below 5 mM preferably by a combined dialysis and TEV protease cleavage step. The protein mixture is batch incubated with an appropriate amount of Ni^{2+}-NTA beads equilibrated with dialysis buffer, beads are washed with dialysis buffer until no protein is detected with a Bradford assay and eluted with dialysis buffer supplemented with 300 mM Imidazol. Fractions are analyzed by SDS-PAGE and Coomassie staining.

7.2.5.4 Ion exchange chromatography

Each protein has charged residues. The sum of these charged residues define the overall charge of a protein which is reflected by its pI. In turn, this charge can be used to separate proteins from each other. In addition, those charges are influenced via protonation and deprotonation or simplified by the pH of the buffer. Moreover, charged particles interact with each other. These interactions can be used to immobilize proteins on charged beads such as sulphonated Sepharose (HiTrap SP) or quaternary amide Sepharose (HiTrap Q) at low ionic buffer strengths. Upon an increase of the ionic buffer strengths, proteins can be eluted again.

Before running an ion exchange chromatography (IEX), the ionic strength of the protein solution has to be adjusted below 5 mS/cm which usually corresponds to a NaCl concentration about 10 mM. In addition, the buffer ion and buffer pH should not interfere with the binding of the protein of interest to the IEX matrix used. In general, if the pH is 1 unit below the pI of the protein of interest, it will bind to a cation exchanger such as a SP column, if the pH is 1 unit above the pI of the protein of interest, it will bind to an anion exchanger such as a Q column. The buffer should not bear the opposite charge of the exchange column since it would otherwise occupy the charged surface of the column matrix and would compete with the protein of interest for binding. Therefore, before running HiTrap SP column, buffer is exchanged to SP low salt buffer (Table 12) or Q low salt buffer (Table 12) before running a HiTrap Q column. 5 mL IEX columns are run at 2.5 mL/min on a NGC system (BioRad) and absorptions at 280 nm and 215 nm are monitored to identify protein containing fractions. Bound proteins are eluted by a gradient ranging from 0 – 40 % high salt buffer containing 1000 mM NaCl. Protein containing fractions are analyzed by SDS-PAGE and Coomassie staining.

7.2.5.5 Gel filtration chromatography

Another method for protein separation is gel filtration (GF) or size exclusion chromatography. Hereby, the different sizes of proteins are used for separation. The matrix of GF columns is porous. Since smaller molecules therefore have a larger volume to diffuse through when passed over a GF column, they need longer to transverse the column than bigger molecules. Hence, small and large molecules are separated.

S75 16/600 or S75 26/600 columns (GE Healthcare) are equilibrated with an appropriate buffer (e.g. NMR buffer for subsequent NMR measurements (Table 12)) and run on a NGC system (BioRad). Absorptions at 280 nm and 215 nm are monitored to identify protein containing fraction. Protein containing fractions are analyzed by SDS-PAGE and Coomassie staining.

7.3 Structural biology and biophysics

7.3.1 NMR spectroscopy

7.3.1.1 Data acquisition

5 mm NMR tubes (Norell) were used to record all NMR experiments and NMR data was acquired with a 600 MHz Bruker Advance III spectrometer equipped with a TXIz probe head. All experiments were set up with Bruker Topspin 2.1 software. Furthermore, the standard set up used by laboratory coworkers was used for excitation pulses, decoupling sequences and gradient pulses. A summary of temperatures and spectra recorded can be found in Table 25.

Table 25: Overview of NMR experiments conducted during my thesis.

constructs/ experiments	spectra	temperature
individual *dm*Par3 PDZ domains / titrations	^{1}H,^{15}N-HSQC	293 K
***dm*Par3 linker-PDZ3 Δβ2-3 loop / titrations**	^{1}H,^{15}N-HSQC	293 K
***dm*Par3 linker-PDZ3 Δβ2-3 loop / constructs**	^{1}H,^{15}N-HSQC	303 K
***dm*Par3 PDZ1-3 module**	^{1}H,^{15}N-TROSY	303 K
individual *hs*Par3 domains	^{1}H,^{15}N-HSQC	303 K
GB1-*dm*Par3 FID-motif / assignment	^{1}H,^{15}N-HSQC, -HNHA, -HNHB, -HNH-NOESY	293 K
GB1-*dm*Par3 FID-motif / titration	^{1}H,^{15}N-HSQC	293 K

7.3.1.1.1 ^{1}H,^{15}N-HSQC experiments

2D ^{1}H,^{15}N-HSQC experiments were recorded with 1024 complex points for a sweep width of 13 ppm in the ^{1}H dimension, and 128 complex points for a sweep width of 26 ppm in the ^{15}N dimension.

7.3.1.1.2 ^{1}H,^{15}N-TROSY experiments

2D ^{1}H,^{15}N-TROSY experiments were recorded with 768 complex points for a sweep width of 13 ppm in the ^{1}H dimension, and 128 complex points for a sweep width of 26 ppm in the ^{15}N dimension.

7.3.1.1.3 Assignment of the *dm*Par3 FID-motif

In order to assign the residues of the *dm*Par3 FID motif (NESQHFIDAGS) in context of the GB1-fusion construct, an unusual assignment strategy was chosen. Excellent technical support and advice was provided by Dr. Vincent Truffault.

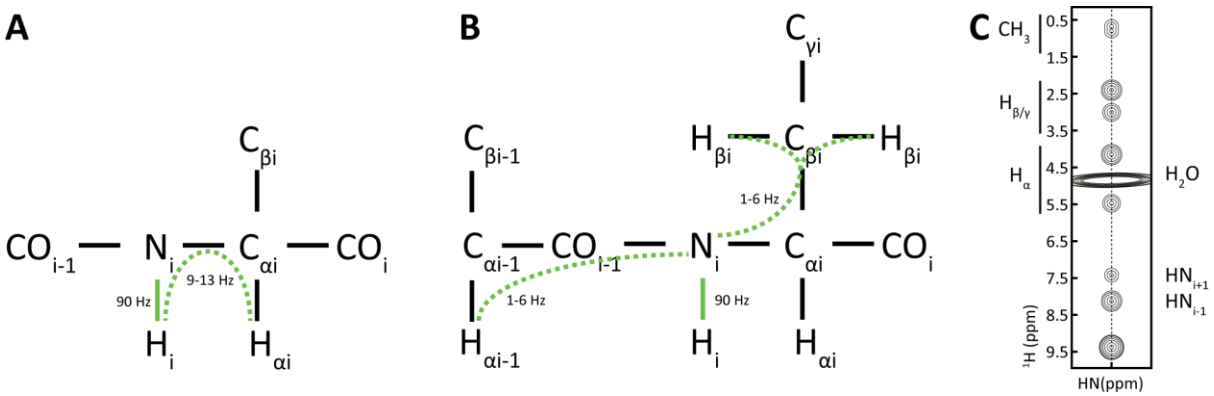

Figure 40: Assignment strategy of the *dm*Par3 FID-motif. (A) J-couplings used for 3D $^{1}H,^{15}N$-HNHA spectra are shown as solid green line ($^{1}J_{HN}$) and as dashed green line ($^{3}J_{HN\text{-}H\alpha i}$). **(B)** J-couplings used for 3D $^{1}H,^{15}N$-HNHB spectra are shown as solid green line ($^{1}J_{HN}$) and as dashed green line ($^{3}J_{HN\text{-}H\alpha i\text{-}1}$ and $^{3}J_{HN\text{-}H\beta i}$). **(C)** A hypothetical stripe of a $^{1}H,^{15}N$-HNH-NOESY spectrum is shown highlighting the information content of a $^{1}H,^{15}N$-HNH-NOESY spectrum. Characteristic positions of H_{β}-, $H_{\beta/\gamma}$-, H_{α}-, HN_{i-1}-, HN_{i+1}- and H_2O- cross peaks are indicated at the right and at the left.

A highly concentrated sample of the ^{15}N-labeled GB1-*dm*Par3 FID motif fusion construct (1.7 mM) in NMR buffer (Table 12) was available. In addition, only eleven cross peaks originating from the FID-motif in the spectrum of the GB1 fusion had to be assigned (Figure 35A, Figure A 2). Hence, 2D $^{1}H,^{15}N$-HSQC as well as 3D $^{1}H,^{15}N$-HNHA, $^{1}H,^{15}N$-HNHB and $^{1}H,^{15}N$-HNH-NOESY spectra were recorded. The 3D $^{1}H,^{15}N$-HNHA spectrum contains HN cross peaks of the backbone and the C_{α}-proton of the same residue ($H_{\alpha i}$) (Figure 40A). The 3D $^{1}H,^{15}N$-HNHB spectrum contains HN cross peaks of the backbone and the C_{β}-protons of the same residue ($H_{\beta i}$) (Figure 40B). However, at high concentrations (> 0.5 mM), the 3D $^{1}H,^{15}N$-HNHB spectrum also contains cross peaks of the C_{α}-proton of the previous residue ($H_{\alpha i-1}$). Therefore, sequential information can be extracted from this spectrum. Additionally, the 3D $^{1}H,^{15}N$-HNH-NOESY spectrum contains cross peaks of protons in the vicinity of HN pairs (usually around 5 Å) at characteristic positions (Figure 40C) further enriching the available information. All of these information combined enabled Dr. Truffault and me to assign the residues of the FID-motif inside the GB1-*dm*Par3 FID-motif fusion protein (Figure 35A). The assignment was carried out at 20°C, spectra were analyzed with TopSpin 2.1 (Bruker) and Sparky (Lee et al. 2015). Table 26 summarizes the acquisition parameters used. In order to identify peaks originating from the *dm*Par3 FID-motif, the $^{1}H,^{15}N$-HSQC spectrum of the ^{15}N-labeled GB1-*dm*Par3 FID-motif fusion was compared with a $^{1}H,^{15}N$-HSQC spectrum of ^{15}N-labeled GB1 without the FID-motif. Cross peaks only present in the $^{1}H,^{15}N$-HSQC spectrum of the ^{15}N-labeled GB1-*dm*Par3 FID-motif (Figure A 2) were selected for subsequent assignment of the $^{1}H,^{15}N$-resonaces of the *dm*Par3 FID-motif.

Table 26: Acquisition parameters for *dm*Par3 FID-motif backbone assignment.

	dimension ^{1}H		^{15}N		^{1}H	
spectra	**complex points**	**sw [ppm]**	**complex points**	**sw [ppm]**	**complex points**	**sw [ppm]**
$^{1}H,^{15}N$-HSQC	1024	13	128	26	-	-
$^{1}H,^{15}N$-HNHA	1024	13	58	26	72	13
$^{1}H,^{15}N$-HNHB	1024	13	58	26	72	13
$^{1}H,^{15}N$-HNH-NOESY	1024	13	64	26	112	13

7.3.1.2 Data processing and visualization

All NMR spectra were processed with the NMRPipe/NMRDraw package (Delaglio et al. 1995) and visualized with NMRview (Johnson & Blevins 1994).

7.3.1.3 Chemical shift perturbation experiments

Chemical shift perturbation (CSP) experiments of NMR titrations are a powerful tool to study protein interactions. Since the position of a cross peak in a NMR spectrum depends on the local magnetic field and thus on the chemical environment, changes in this environment can be observed by NMR spectroscopy.

Since proton based NMR experiments are very sensitive towards changes in buffer composition such as pH (Hayes et al. 1975; Patel et al. 1975) and ionic strength (Mildvan & Cohn 1963), variations in buffer composition of the ^{15}N-labeled protein and its unlabeled ligand have to be avoided. To this end, all ^{15}N-labeled proteins with their respective ligands are dialyzed against a large volume of NMR buffer (Table 12) o/n at 4°C or exchanged into the same buffer by gel filtration. ^{15}N-labeled protein concentration was adjusted to 67-113 µM (Table 27) with NMR buffer containing 5-10% D_2O. After recording the reference spectra, highly concentrated unlabeled ligand was added at defined molar ratios. During the course of the titrations, the number of scans was increased to compensate for ^{15}N-labeled protein dilution due to volume increase.

Table 27: Concentration of ^{15}N-labeled *dm*Par3 PDZ domains used for CSP experiments

PBM	^{15}N-labeled *dm*Par3 PDZ1	*dm*Par3 PDZ2	*dm*Par3 PDZ3	*dm*Par3 linkerΔII-PDZ3 Δβ2-3 loop	*dm*Par3 PDZ1-3 Δβ2-3 loop
Smash	67	100	100	-	-
Insc	75	100	100	113	-
Crb	83	80	105	105	-
Stan	70	82	100	105	-
Ed	75	100	100	105	-
Shg	75	100	100	107	-
***dm*Par6**	75	100	100	109	74
a-cat	100	100	108	110	-
aPKC	75	108	75	95	-
Std	100	100	104	-	-
***dm*Par6 L0A**	75	-	-	-	-
***dm*Par6 H-1A**	75	-	-	-	-
***dm*Par6 L-2A**	80	-	-	-	-
Shg vs *dm*Par6	104	-	103	-	-

7.3.1.4 Chemical shift perturbation analysis

Chemical shift perturbations can be used to semi-quantify the interaction of two binding partners and to map the interacting regions if resonance assignments are available. To this end, the average CSPs are used and are calculated in ppm:

Equation 14:

$$CSP = \sqrt{{\Delta\delta_{1H}}^2 + \left(\frac{\Delta\delta_{15N}}{4}\right)^2}$$

where $\Delta\delta_{1H}$ is the difference in proton chemical shift and $\Delta\delta_{15N}$ is the difference in nitrogen chemical shift at a 30-fold stoichiometric excess of *dm*Par3 PDZ3 Δβ2-3loop domain compared to the respective reference in the absence of ligand in chase of ^{15}N-labeled *dm*Par3 FID-motif titration with unlabeled *dm*Par3 PDZ3 Δβ2-3loop domain (Figure 35B), 24-fold stoichiometric excess of *dm*Par3 FID-motif compared to the respective reference in the absence of ligand in chase of ^{15}N-labeled *dm*Par3 PDZ3 Δβ2-3loop titration with unlabeled *dm*Par3 FID-motif (Figure 35D) or at a nine-fold stoichiometric excess of PBM compared to the respective reference in the absence of ligand in the case of *dm*Par3 PDZ domain titrations with PBMs (Renschler et al. 2018). Chemical shifts were extracted using Sparky (Lee et al. 2015), CSPs were quantified using Equation 14 and mapped and color coded onto a suitable protein structures (x-ray, NMR or homology model) via pymol or are mapped onto the protein sequence.

7.3.1.5 Two dimensional line shape analysis

Each NMR spectra contains a vast amount of data about the local chemical environments of the observed nuclei as well as the change of that environment over time. In order to extract this data, line shape fitting analysis is performed. During two dimensional line shape analysis performed with TITAN (Waudby et al. 2016), each spectrum is simulated and the parameters used for simulation are fitted against the experimental data.

^{1}H,^{15}N-CSP studies for the *dm*Par3 PDZ domains were quantified using TITAN according to instructions and online documentation (http://www.nmr-titan.com and https://bitbucket.org/cwaudby/titan/wiki/Home). Spectra were acquired with 1024 and 128 points in the ^{1}H and ^{15}N dimensions, respectively, and processed with the NMRPipe/NMRDraw package (Delaglio et al. 1995) with exponential window functions with a line broadening of 4 Hz in the proton dimension and 8 Hz in the nitrogen dimension. Spectra were zero-filled to 4096 and 1024 points in the ^{1}H and ^{15}N dimensions, respectively. In order to obtain comparable results for different ligands, the same cross peaks were used for the analysis of each PDZ domain (Table A 1). Errors were estimated with bootstrapping statistics on 100 replicates. Figures for line shape analyses were prepared with TITAN.

7.3.1.6 Secondary structure determination

The ^{3}J-coupling constants are directly linked with the stereochemistry of the atoms between which J-coupling occurs and can be used to extract information about the angles between them (Bystrov 1976). In addition, it is possible to directly correlate $^{3}J_{HN\text{-}H\alpha i}$-coupling constants with secondary structure elements which are defined by the torsion angle ϕ of the peptide backbone.

$^{3}J_{HN\text{-}H\alpha i}$-coupling constants in Hz were determined according to Equation 15 from 3D ^{1}H,^{15}N-HNHA spectra:

Equation 15:

$$^{3}J_{HN-H\alpha i} = \frac{arctan\sqrt{I_{H\alpha i}/I_{HN}}}{2\pi \cdot D3 \cdot f}$$

with $I_{H\alpha i}$ being the intensity of the $H_{\alpha i}$ cross peak, I_{HN} being the intensity of the HN_i diagonal peak, $D3$ being the evolution time of the $^{3}J_{HN\text{-}H\alpha i}$-coupling (here 14 ms) and f being an empirical determined relaxation factor. f accounts for the loss of magnetization during $D3$ and was determined to be 0.9 (V. Truffault, personal communication). Characteristic $^{3}J_{HN\text{-}H\alpha i}$-coupling constants found in secondary structure elements are summarized in Table 28.

Table 28: Characteristic $^{3}J_{HN\text{-}H\alpha i}$-coupling constants in secondary structure elements

Secondary structure element	$^{3}J_{HN\text{-}H\alpha i}$-coupling constant (Hz)
α-helix	< 6
random coil/ ambiguous	6 – 8
β-strand	> 8

In order to assign secondary structure elements, the intensifies of the $H_{\alpha i}$ cross peak and H_{HN} diagonal peak in the 3D $^{1}H,^{15}N$-HNHA spectra of ^{15}N-labeled GB1-*dm*Par3 FID-motif were quantified using Sparky (Lee et al. 2015). $^{3}J_{HN\text{-}H\alpha i}$-coupling constants were calculated using Equation 15. Secondary structure elements were subsequently assigned by comparison with characteristic $^{3}J_{HN\text{-}H\alpha i}$-coupling constants in secondary structure elements (Table 28). Additionally, qualitative analysis of 3D $^{1}H,^{15}N$-HNH-NOESY strips was performed to resolve amgibuities. In 3D $^{1}H,^{15}N$-HNH-NOESY spectra, spacial distances correlate with the peak intensities. Therefore, it is possible to gain information of the secondary structure since in α-helices the $H_{\alpha i-3}$ is in close proximity of the HN_i giving rise to a detectable cross peak in the corresponding $^{1}H,^{15}N$-HNH-NOESY strip of residue i. Furthermore, in elongated conformations of the protein chain such as β-strands and random coils, the intensities of HN_{i-1} cross peaks are significant less intense compared to HN_{i-1} cross peaks found in α-helices. Hence, qualitative analysis of $^{1}H,^{15}N$-HNH-NOESY spectra aids in resolving ambiguous $^{3}J_{HN\text{-}H\alpha i}$-coupling constants.

7.3.2 X-ray crystallography

7.3.2.1 Crystallization condition screening

In order to grow protein crystals, the proteins in solution has to pass the phase barrier between a under saturated solution and a supersaturated solution (Blow 2010; Rupp 2009). However, if proteins are concentrated in concentrators above their saturation point, they usually tend to aggregate and do not form crystals. In order to prevent this aggregation, the transition has to be smooth to allow crystal nucleus formation. In addition, other variables influencing the crystal growth such as salt concentration, pH and additives favoring crystal contacts should be adjusted. One gentle way to increase the protein concentration is the extraction of water from the protein solution via vapor diffusion. In sitting drop vapor diffusion, a mixed drop of protein solution and reservoir solution is sitting above a well filled with reservoir solution inside an air-tight chamber. The reservoir solution consists of various ingredients such as buffers, additives, salts and hygroscopic crystallizing agents. Since the concentration of the crystallizing agent is higher in the reservoir, water diffuses from the drop into the reservoir. This diffusion leads to an increase of the protein concentration in

the drop. Finally, the protein concentration reaches supersaturation and hopefully crystal growth starts. The exact crystallization conditions for each protein differ. Therefore the crystallization conditions have to be determined empirically by screening the crystallization space by varying pH, crystallization agent, crystallization agent concentration, temperature, protein concentration as well as other parameters such as additives (salts, volatile agents, etc.) and their concentrations. To this end, commercially available screens have been developed.

The Insc PBM was fused with a seven amino acid long GS-linker to the C-terminus of the *dm*Par3 PDZ2 domain, expressed in LB and purified by Ni-NTA affinity chromatography, SP ion exchange chromatography and gel filtration. The *dm*Par3 PDZ2-Insc fusion was concentrated to 25 mg/mL in XTAL buffer (Table 12) and initial crystallization screening was performed with the commercially available screens listed in Table 29. Initial crystallization screening was performed in sitting drop 96-well plates (96-3 low profile INTELLI-PLATE®, Art Robbins Instruments) with drops consisting of 0.3 µL protein solution and 0.3 µL reservoir solution. Crystal growth was observed in various wells after seven to 14 days at 20°C. Next, crystals obtained were tested by mechanical stability or by synchrotron irradiation whether or not they were protein crystals. Therefore, crystals were cryo-protected, flash frozen in liquid nitrogen and diffraction quality was measured at the Swiss Light Source (SLS, Villingen, Switzerland). Although some crystals diffracted well showing diffraction spots at 2 Å, the overall quality of the datasets was low since the completeness was low.

Table 29: Initial crystallization screens

Screen	Manufacturer
Classics	QIAGEN
Classics II	QIAGEN
PEGs	QIAGEN
PEGs II	QIAGEN
Protein Complex	QIAGEN
JCSG+	QIAGEN
AmSO$_4$	QIAGEN

Consequently, the most promising conditions in terms of resolution were chosen to improve the crystallization conditions (Table 30). Crystal improvement screens were set up with a dragonfly pipetting robot (ttp labtech) and screening was performed in sitting drop 96-well plates (96-3 low profile INTELLI-PLATE®, Art Robbins Instruments) with drops consisting of 0.3 µL protein solution and 0.3 µL reservoir solution. Protein solution contained the *dm*Par3 PDZ2-Insc fusion protein at concentrations of 25.8 mg/mL or 13.2 mg/mL. Crystal growth was observed in various wells within 12 h to seven days at 20°C. Crystals were cryo-protected and diffraction data was recorded at the SLS. The highest quality crystal used for structure determination of the *dm*Par3 PDZ2 : Insc PBM

complex was grown in 63.64 mM MES pH 6, 36.36 mM HEPES pH 7, 0.1 M NH_4SO_4, 30 % (w/v) PEG 5000 MME.

Table 30: Crystal improvement screens

initial condition		**screen**	
		from	**to**
Classics II/ D3	0.1 M HEPES pH 7	0.1 M MES pH 6.5	0.1 M HEPES pH 7.5
	30 % (w/v) Jeffamine ED 2001 pH 7	20 % (w/v)	40 % (w/v)
PEGs II/ G2	0.1 M MES pH 6.5	0.1 M MES pH 6	0.1 M HEPES pH 7
	0.2 M NH_4SO_4	0 M NH_4SO_4	0.7 M NH_4SO_4
	30 % (w/v) PEG 5000 MME	constant	

In addition to the *dm*Par3 PDZ2:Insc PBM construct mentioned above, several other constructs have been generated to solve crystal structures of *dm*Par3 PDZ domains in complex with various PBMs (Table 31). Although all constructs were expressed in sufficient amounts and soluble and pure protein could be obtained, none of the constructs tested yielded high-quality diffraction data (Table 31).

Table 31: Crystallization construct of *dm*Par3 PDZ domains not yielding high-quality diffracting crystals

***dm*Par3 PDZ domain**	**PBM**	**linker length (position)**	**expression**	**solubility**	**final purity**	**crystals grown**	**crystal quality**
PDZ2	Insc	15 GS (PDZ-PBM)	ok	ok	ok	no	
PDZ3 Δβ2-3 loop	*dm*Par6	5 GS (PDZ-PBM)	ok	ok	ok	ok	no diffraction
		15 GS (PDZ-PBM)	ok	ok	ok	ok	diffraction to 12 Å after crystal improvement
	Shg	7 GS (PDZ-PBM)	ok	ok	ok	ok	diffraction to 4 Å after crystal improvement
		15 GS (PDZ-PBM)	ok	ok	ok	ok	no diffraction
	Ed	7 GS (PDZ-PBM)	ok	ok	ok	ok	no diffraction
linker-PDZ3 Δβ2-3 loop	-	-	ok	ok	ok	no	
	Shg	7 GS (PDZ-PBM)	ok	ok	ok	no	
	*dm*Par6	7 GS (PDZ-PBM)	ok	ok	ok	no	
	Ed	7 GS (PDZ-PBM)	ok	ok	ok	no	
MBP-linker-PDZ3 Δβ2-3 loop	-	-	ok	ok	ok	no	
	-	4 A (MBP-linker)	ok	ok	ok	no	

7.3.2.2 Cryogenic protection of protein crystals

Protein crystals consist of huge amounts of water. In contrast, x-ray diffraction data is usually acquired at temperatures of 100-120 K in order to reduce radiation damage to the protein molecules

inside the crystal. At these low temperatures the water would freeze and the water molecules would form crystal lattices. Hence, the frozen water would also cause a diffraction pattern. Therefore, x-ray diffraction of the water molecules inside the protein crystals has to be avoided. In order to avoid water crystallization, the protein crystals are incubated with cryo-protectants such as glycerol, PEG-400, salts etc. which lead to the formation of amorphous ice with no defined crystal lattice. Since amorphous ice has no lattice, diffraction from water molecules of amorphous is always destructive and thus leads to no observable diffraction spots on the detector.

In order to cryo-protect protein crystals, suitable cryo-protectant solutions have to be found. To this end, reservoir solution is mixed with glycerol or PEG-400 at 30 % (v/v) and flash frozen in liquid N_2. If the frozen solution stays transparent, a suitable cryo-protectant solution is found. However, if the frozen solution is opaque or cracks and/or other forms of deformation, phase separation etc. are observed the cryo-protectant has to be changed or the cryo-protectant concentration has to be adjusted. After establishing a suitable cryo-protectant solution, protein crystals are transferred into the cryo-protectant solution, shortly incubated, flash frozen in liquid N_2 and stored in liquid N_2 until recording diffraction data at the synchrotron. *Dm*Par3 PDZ2-Insc fusion crystals used for *dm*Par3 PDZ2 : Insc PBM complex diffraction data collection were cryo-protected in reservoir solution supplemented with 30 % (v/v) PEG-400.

7.3.2.3 Data acquisition

The *dm*Par3 PDZ2 : Insc PBM complex diffraction data was collected at the SLS at the PXII beamline with a PILATUS 6M pixel detector with 0.5° oscillation per image, a filter transmission of 0.1, a detector distance of 0.295 m, and λ = 1 Å in a cryostream.

7.3.2.4 Data processing

During data processing, each spot recorded in the diffraction data set is indexed, i.e. the Miller indices h, k and l are assigned. Therefore, during indexing, the diffraction spots are assigned to their coordinates in the reciprocal space. Next, the space group is assigned. To this end, all possible space groups are scored according to their probability to produce the diffraction pattern and the highest scoring one is chosen. Subsequently, the intensity of each spot is determined by integration. Finally, scaling takes place. During scaling, all data is merged into one file and partial reflections from several frames are added up. To this end, intensities obtained from partial reflections in different orientations on each of the frames are variably scaled together. In addition, during scaling, the R_{free}-set of reflections (Brünger 1992) is generated.

The *dm*Par3 PDZ2 : Insc PBM complex X-ray diffraction data was processed using images from 0°-360° in XDS (Kabsch 2010), no anomalous signal was observed. The space group was determined by pointless (Evans 2006). Data set statistics are provided in Table 32.

Table 32: Statistics of X-ray data collection and refinement of the *dm*Par3 PDZ2 : Insc PBM complex

Data collection	
Wavelength (Å)	1.0
Resolution range (Å)	41.49 - 1.767 (1.83 - 1.767)
Total reflections	104544 (9415)
Unique reflections	8254 (803)
Multiplicity	12.7 (11.7)
Completeness (%)	99.60 (98.04)
I / σI	28.04 (3.74)
Wilson B-factor (Å^2)	29.42
CC1/2	1 (0.92)
Crystal properties	
Space group	I 2 2 2
Unit cell dimensions	
a, b, c (Å)	42.203, 48.851, 78.576
α, β, γ (°)	90, 90, 90
Refinement	
Resolution range (Å)	41.49 - 1.767 (1.83 - 1.767)
Reflections used in refinement	8252 (802)
Reflections used for R_{free}	413 (40)
R_{work} / R_{free} (%)	0.1763 (0.2222) / 0.2059 (0.2910)
CC_{work} / CC_{free} (%)	0.947 (0.920) / 0.952 (0.832)
RMS(bonds)	0.006
RMS(angles)	0.77
Ramachandran favored / allowed / outliers (%)	98.78 / 1.22 / 0
Rotamer outliers (%)	0
Clashscore	2.23
Number of non-hydrogen atoms	691
macromolecules	653
ligands	5
solvent	33
Average B-factor (Å^2)	36.64
macromolecules (overall) (Å^2)	36.06
PDZ domain (Å^2)	36.05
Insc PBM (Å^2)	33.91
solvent (Å^2)	43.06
Sulfate (Å^2)	69.99

7.3.2.5 Phase determination by molecular replacement

During X-ray data acquisition, only intensities are recorded. However, phase information is needed in order to transform the reciprocal space into real space. Therefore, the phases have to be determined. If homologous structures are available, it is feasible to use these structures for phasing (Rossmann & Blow 1961). PHASER uses log-likelihood methods to place the search model in order to obtain phase information (McCoy et al. 2007).

Phases of the *dm*Par3 PDZ2 : Insc PBM complex X-ray diffraction data were obtained by PHASER (McCoy et al. 2007). The second PDZ domain of *hs*Dlg3 (2fe5, 37 % identity) as well as the PDZ domain variant C378S of the rat homolog of Dlg (2awx, 34 % identity) were used as search models. The search modes were trimmed by chainsaw (Stein 2008) to the last common atom with *dm*Par3 PDZ2. Additionally, loops were removed from the models manually and both models were used in an ensemble search. PHASER found a single solution with a LLG of 269 and a TFZ of 15.7. Inspection in coot did not reveal any clashes. Furthermore, no density was present in solvent channels and the crystal packing seemed to be reasonable. Initial refinement with Phenix (Adams et al. 2010) including simulated annealing resulted in R_{work} / R_{free} of 36.96 / 37.26. Therefore, phase determination by molecular replacement was successful.

7.3.2.6 Structure refinement

During refinement, the model and the phases are improved. Successive rounds of model building and subsequent refinement lead to improved phases which in turn lead to better maps to build in. Therefore, the model explains the experimental data better after refinement since it represents the data better. This progress can be monitored by the crystallographic R-factor:

Equation 16:

$$R = \frac{\sum ||F_{obs}| - |F_{calc}||}{\sum |F_{obs}|}$$

The crystallographic R-factor compares the observed structure factors F_{obs} with the back calculated structure factors F_{calc} derived from the model. If the R-factor lowers during refinement, the model explains the data better. However, the R-factor has to be cross validated in order to avoid over fitting. To this end, approximately 5 % of the observed reflexes are not included into refinement. Similar to the R-factor, a R_{free}-factor is calculated (Brünger 1992). If both R (also called R_{work}) and R_{free} decrease during refinement, the refinement is valid and the resulting model explains the experimental data better than the previous model.

The initial model obtained from PHASER was refined successively using alternating rounds of refinement in Phenix (Adams et al. 2010) using anisotropic B-factors and model building in Coot

(Emsley et al. 2010). Figures displaying structures were prepared using PyMOL (www.pymol.org). Final refinement statistics are provided in Table 32.

7.3.2.7 Iterative-build OMIT map

During refinement, the previously build model is used to calculate the crystallographic phases for the next refinement cycle. However, this model is biased e.g. by wrongly placed atoms. Since the refinement of the model adjusts the parameters describing the correctly placed atoms (e.g. position, B-factors), these parameters are also adjusted to compensate for errors in the model. Therefore, the improved phases contain reminiscences of the errors even though if they are corrected at a later stage during refinement. Consequently, memories of their positions are present as model bias and validation of such bias is necessary.

One effective way to remove or to check for model bias was introduced by T. Terwiliger *et al.* as iterative-build OMIT maps (Terwilliger et al. 2008). To this end, parts of the model are iteratively omitted and with these OMIT models, model building, density modification and refinement is carried out. Since the resulting map has never been affected by a model in the OMIT region, this map is bias free inside the OMIT region. As a result, OMIT maps for each OMIT region are generated and can be combined to an iterative-build composite OMIT map without any model bias. The iterative-build OMIT map routine has been implemented in phenix (Adams et al. 2010) and was applied for OMIT map generation of the Insc PBM of the *dm*Par3 PDZ2:Insc complex (Figure 29D).

8. Appendix

8.1 ^{1}H,^{15}N-HSQC spectra of *dm*Par3 linker-PDZ3 Δβ2-3loop constructs and *dm*Par3 PDZ3 Δβ2-3loop CSPs experiments with the *dm*Par3 FID-motif

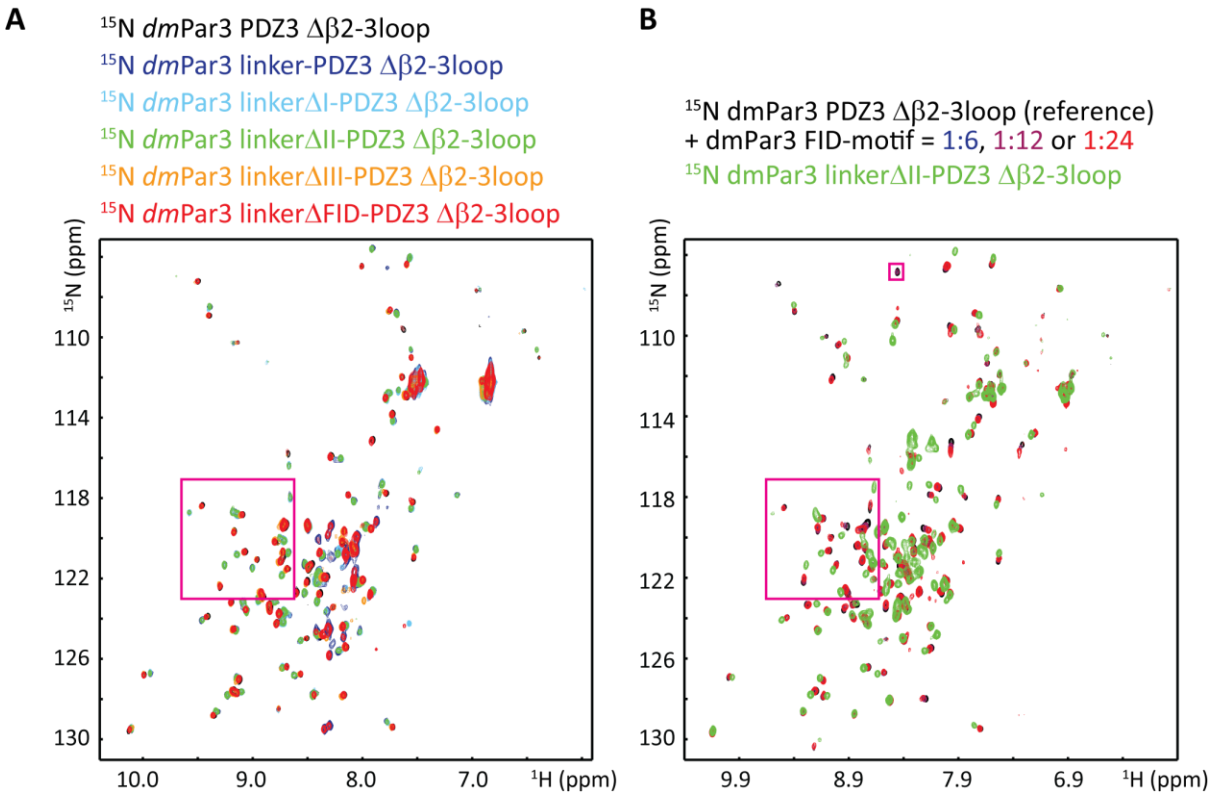

Figure A 1: ^{1}H,^{15}N-HSQC spectra of *dm*Par3 PDZ3Δβ2-3loop constructs and *dm*Par3 PDZ3Δβ2-3loop CSPs experiments with the *dm*Par3 FID-motif. (A) Overlay of ^{1}H,^{15}N-HSQC spectra of *dm*Par3 PDZ3 Δβ2-3loop constructs described in Figure 34A. *dm*Par3 PDZ3 Δβ2-3loop is shown in black, *dm*Par3 linker-PDZ3 Δβ2-3loop in purple, *dm*Par3 linkerΔI-PDZ3 Δβ2-3loop in light blue, *dm*Par3 linkerΔII-PDZ3 Δβ2-3loop in green, *dm*Par3 linkerΔIII-PDZ3 Δβ2-3loop in orange, *dm*Par3 linkerΔFID-PDZ3 Δβ2-3loop in red. The magenta box indicates the region of the spectra displayed in Figure 34A. **(B)** Overlay of the ^{1}H,^{15}N-HSQC spectra of the *dm*Par3 PDZ3 Δβ2-3loop domain in the absence (black) and presence of increasing stoichiometric amounts of the FID-motif containing linker of *dm*Par3 fused to GB1 as indicated. Data are shown for three out of eight titration points (Table A 2). The magenta box indicates the region of the spectra displayed in Figure 34.

8.2 Assignment of the $^{1}H,^{15}N$-resonances of the *dm*Par3 FID-motif

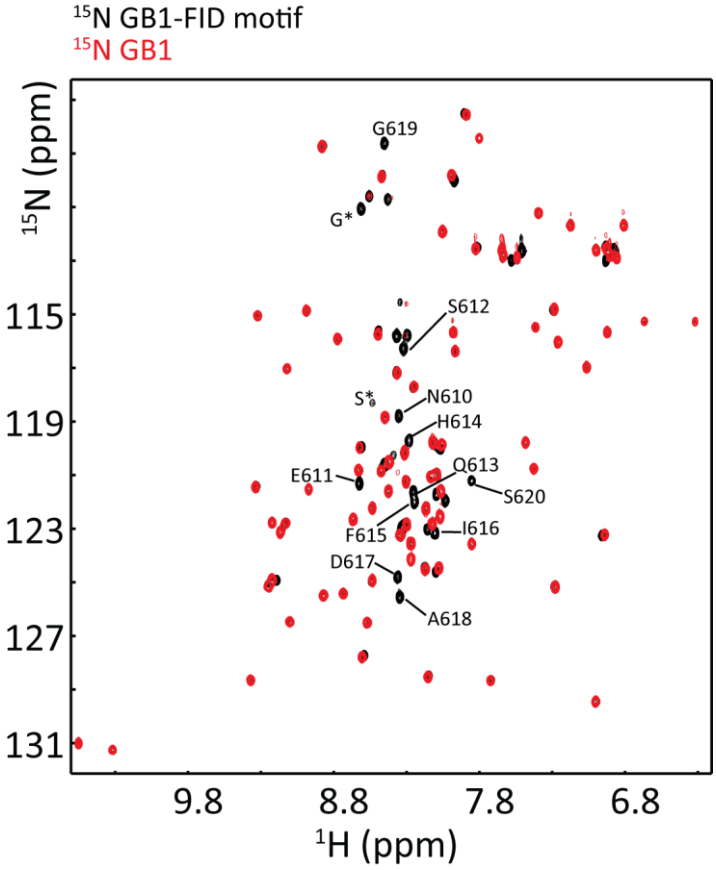

Figure A 2: Assignment of the $^{1}H,^{15}N$-resonances of the *dm*Par3 FID-motif in context of the GB1-*dm*Par3 FID construct. Overlay of the $^{1}H,^{15}N$-HSQC spectra of GB1-*dm*Par3 FID-motif (black) and GB1 (red). Peaks originating from the GB1 domain display no CSPs in presence of the *dm*Par3 FID-motif. Cross peaks originating from the *dm*Par3 FID-motif are labeled. In addition to cross peaks originating from the *dm*Par3 FID-motif, two additional peaks not present in the GB1 spectrum are present and could be assigned to serine (*S**) and glycine (*G**) residues introduced as a linker between the GB1 and the *dm*Par3 FID-motif.

8.3 NMR line shape fitting analysis of the *dm*Par3 PDZ domains

8.3.1 Cross peaks and number of titration steps used for line shape fitting analysis

Table A 1: Cross peaks used for line shape analysis of the individual *dm*Par3 PDZ domains

PDZ1	PDZ2	PDZ3	linker-PDZ3
I11	G17	T19	G23
Y15	F23	G23	N67
L34	27T	V26***	Q74
Q36	41K	K43	E81
N59	46R	I46	V102
E73	51E	A50	
L79*	61L	N67****	
E80	80I	Q74	
L84	82R**	E81	
L89	92I	V88*****	
	96R	V102	

*not Ed; **just Insc, Shg; *** not aPKC, Crb, Ed; **** not *dm*Par6; ***** just *dm*Par6

Table A 2: Number of titration steps used for line shape fitting analysis

PDZ1	PDZ2	PDZ3	linker-PDZ3
5 (Ed)^{SB}	4 (Smash)	4 (Smash)	7 (Insc)
8 (Shg)$^{SRB,SW, MCS, FAR}$	5 (Insc)^{SRB}	5 (Insc)^{SRB}	7 (Crb)
10 (*dm*Par6)$^{SRB,SW,MCS, FAR}$	5 (Stan)	5 (Crb)	7 (Stan)
6 (*dm*Par6 L0A)	5 (Ed)^{SRB}	5 (Stan)	7 (Ed)
5 (*dm*Par6 H-1A)	5 (Shg)^{SB}	5 (Ed)^{SRB}	7 (Shg)
5 (*dm*Par6 L-2A)	5 (α-cat)^{BS}	8 (Shg)$^{SRB,SW, MCS, FAR}$	7 (*dm*Par6)
	5 (aPKC)^{BS}	13 (*dm*Par6)$^{SRB,SW, MCS, FAR}$	7 (aPKC)
	5 (Std)	5 (α-cat)^{BS}	
		5 (aPKC)^{BS}	

The following abbreviations indicate persons who acquired NMR titration data used for line shape fitting analysis: SRB (Susanne R. Bruekner), PLS (Paulin L. Salomon), BS (Benjamin Schroeder), SW (Silke Wiesner) and FAR (Fabian A. Renschler).

8.3.2 Line shape fitting analysis of *dm*Par3 PDZ1

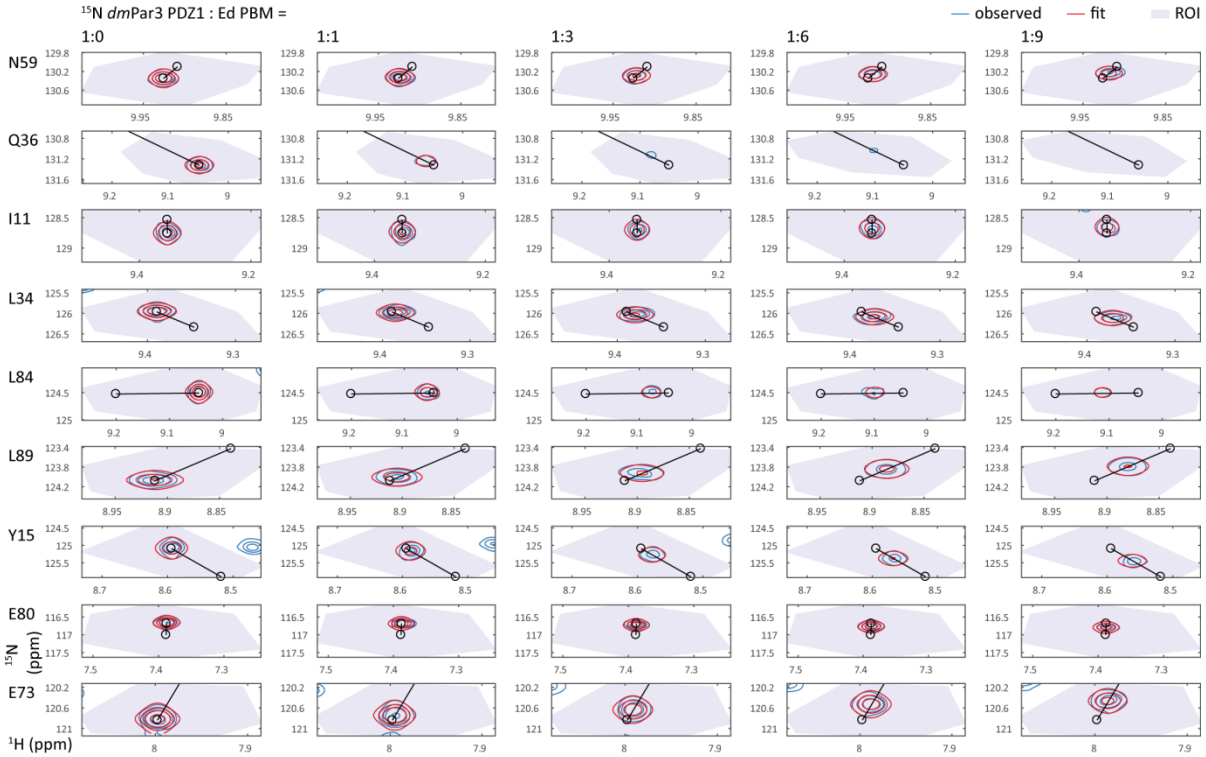

Figure A 3: Line shape fitting analysis of the *dm*Par3 PDZ1 interaction with the Ed PBM. Contour plots of $^{1}H,^{15}N$-HSQC spectra of each cross peak used in TITAN line shape fitting analysis (Waudby et al. 2016) at each titration point are shown. Observed cross peaks are shown in blue whereas fits are shown in red. Black lines indicate the course of the titration between the reference point and an estimated saturation point of the fit CSPs. The grey area around the cross peaks indicates the region of interest selected to fit the data in TITAN. Titration points are indicated above each column. Plots were generated by TITAN. NMR titration data was provided by Susanne Bruekner.

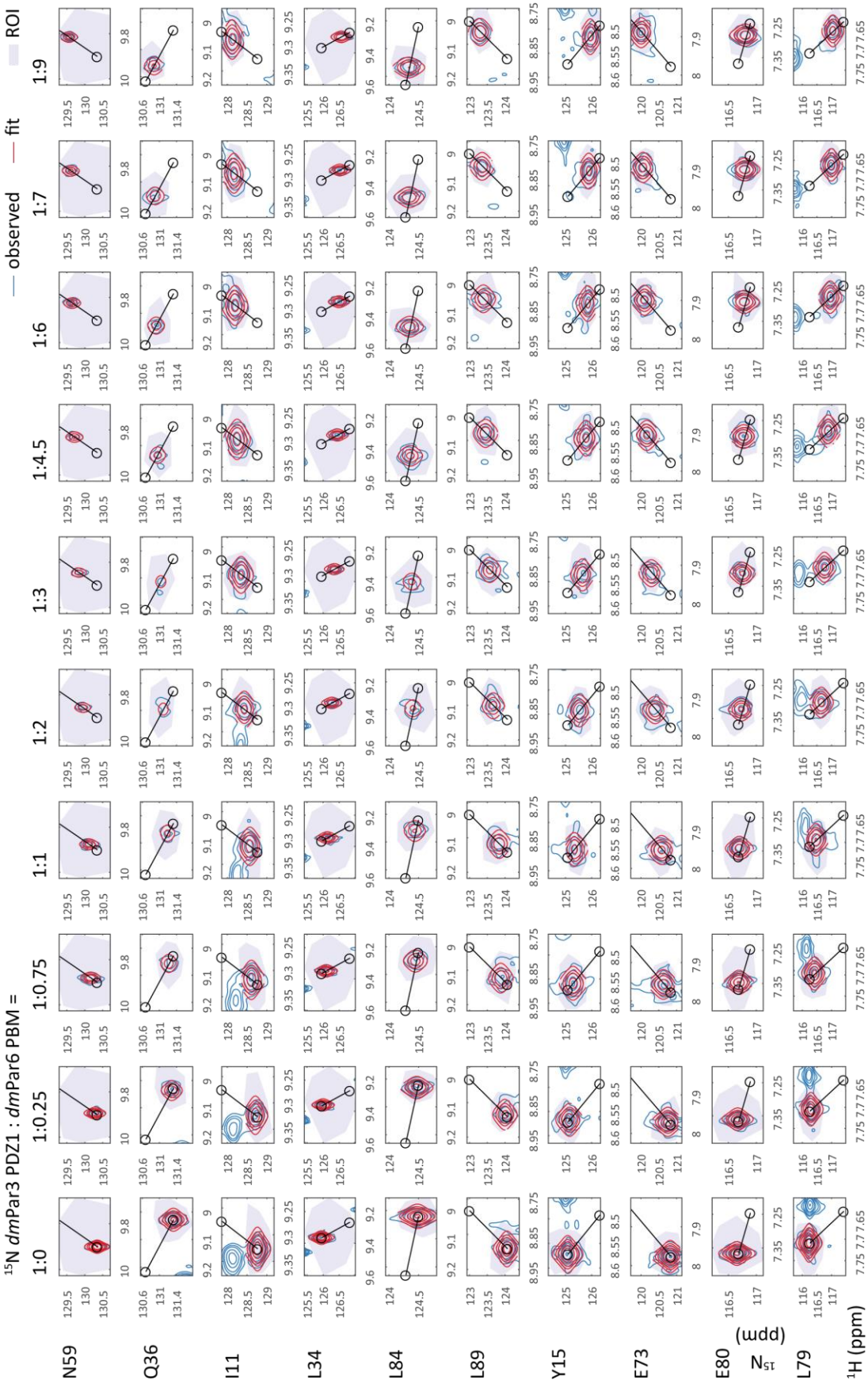

Figure A 4: Line shape fitting analysis of the *dm*Par3 PDZ1 interaction with the *dm*Par6 PBM. NMR titration data was provided by Susanne Bruekner, Silke Wiesner, Mira C. Schütz-Stoffregen and me. Otherwise as in Figure A 3.

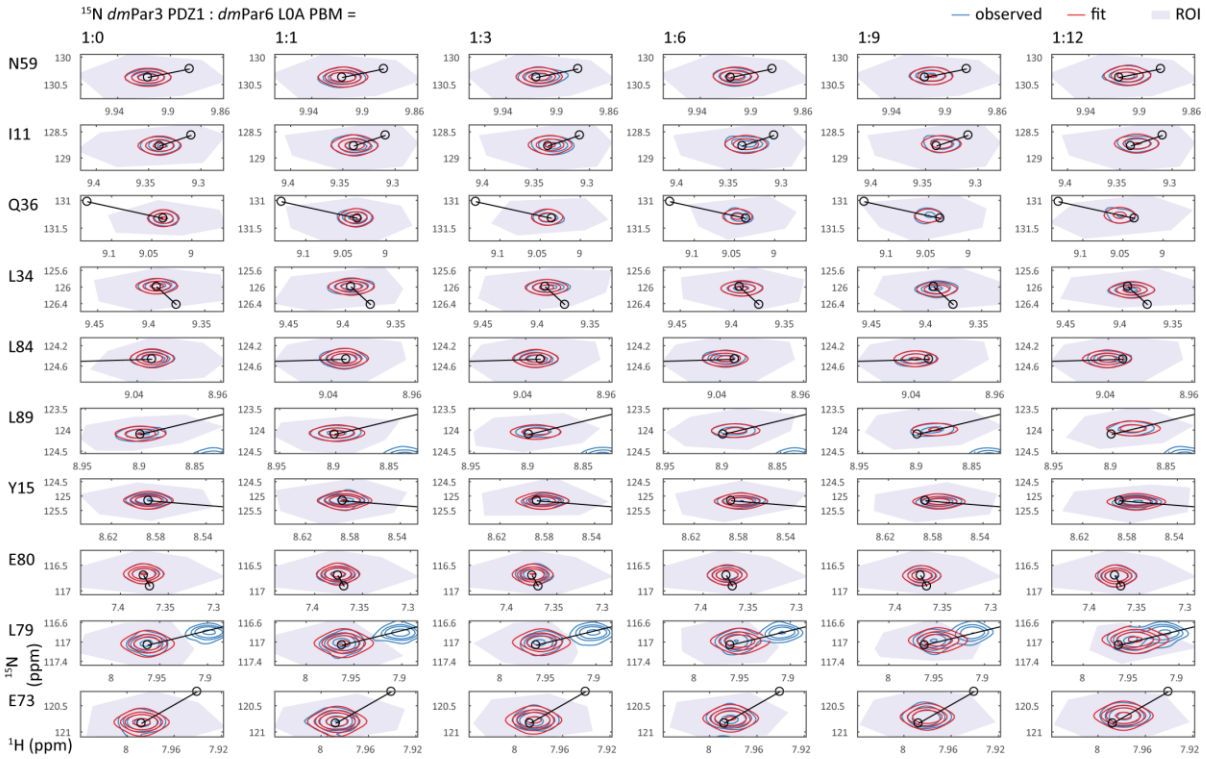

Figure A 5: Line shape fitting analysis of the *dm*Par3 PDZ1 interaction with the *dm*Par6 L0A PBM. Otherwise as in Figure A 3.

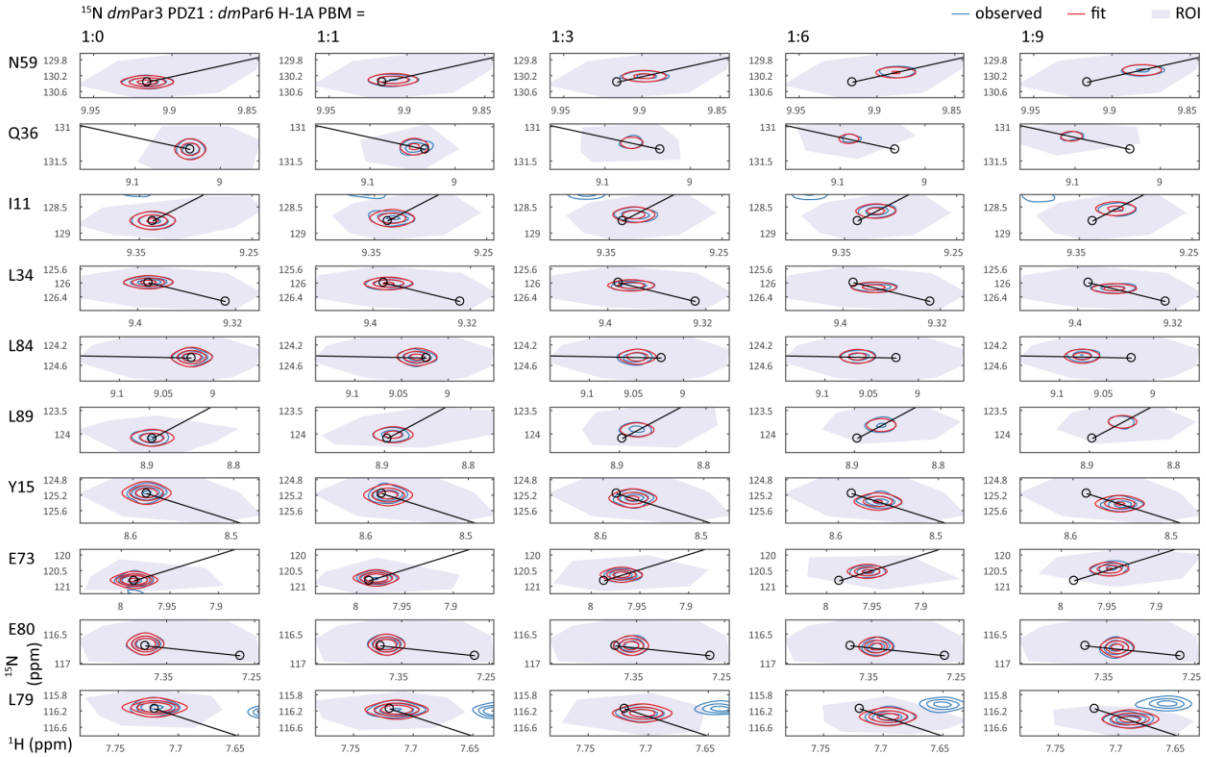

Figure A 6: Line shape fitting analysis of the *dm*Par3 PDZ1 interaction with the *dm*Par6 H-1A PBM. Otherwise as in Figure A 3.

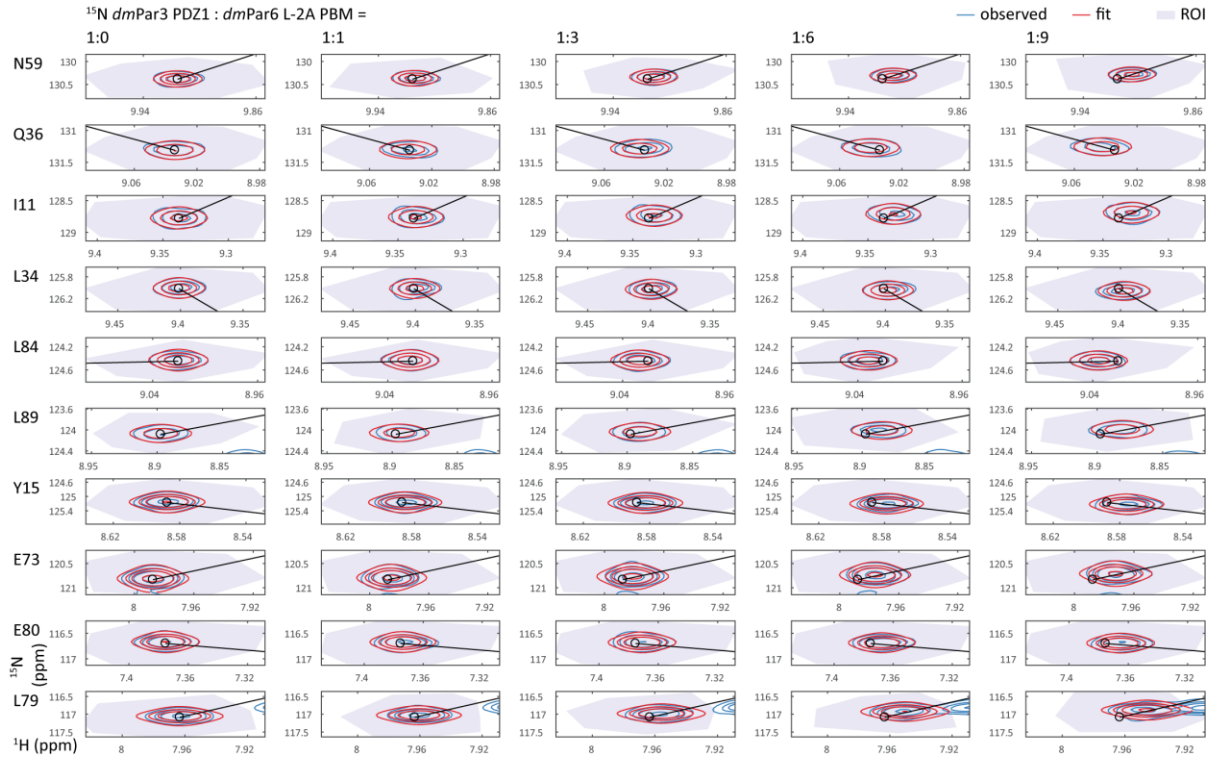

Figure A 7: Line shape fitting analysis of the *dm*Par3 PDZ1 interaction with the *dm*Par6 L-2A PBM. Otherwise as in Figure A 3.

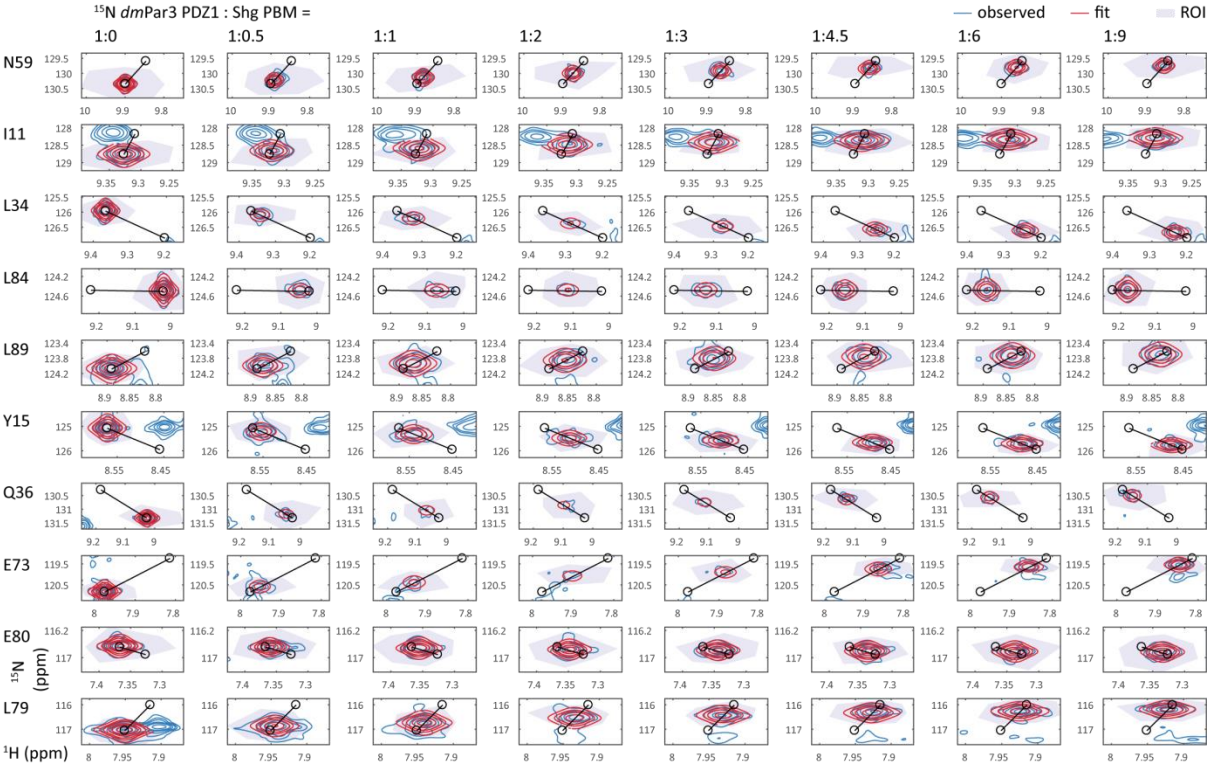

Figure A 8: Line shape fitting analysis of the *dm*Par3 PDZ1 interaction with the Shg PBM. NMR titration data was provided by Susanne Bruekner, Silke Wiesner, Mira C. Schütz-Stoffregen and me. Otherwise as in Figure A 3.

8.3.3 Line shape fitting analysis of *dm*Par3 PDZ2

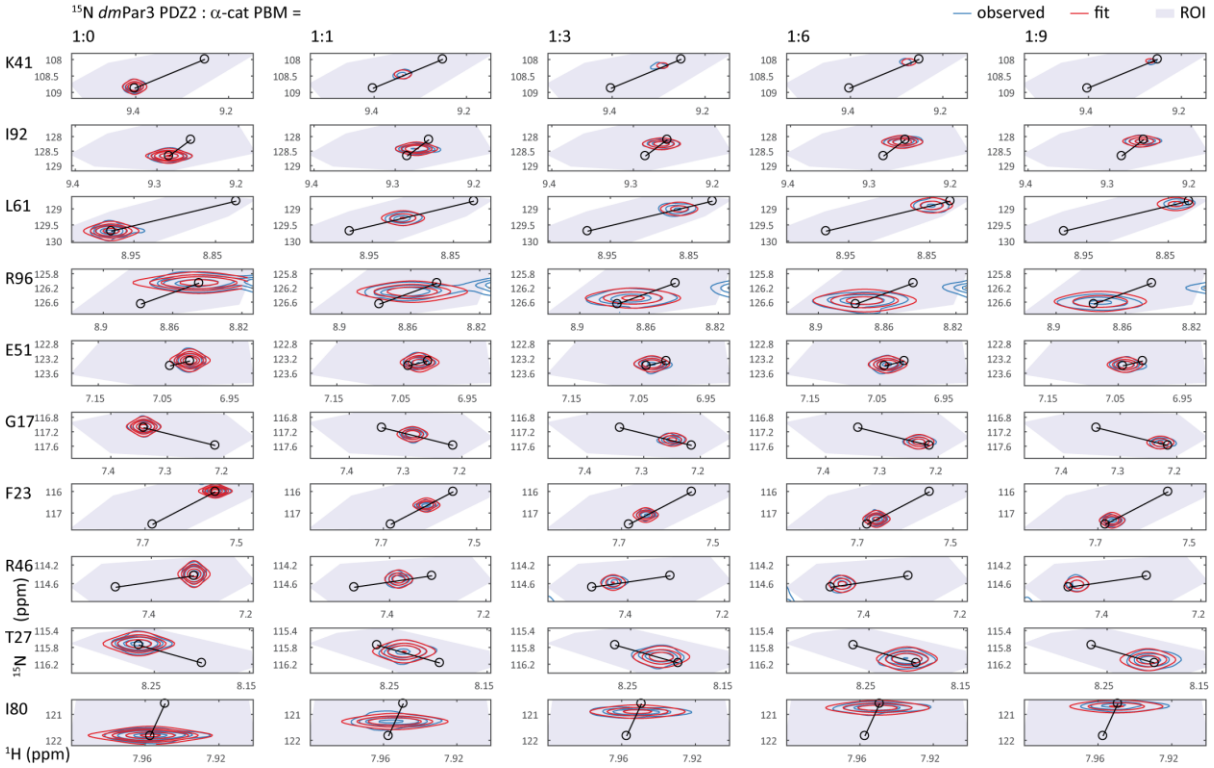

Figure A 9: Line shape fitting analysis of the *dm*Par3 PDZ2 interaction with the α-cat PBM. NMR titration data was provided by Benjamin Schroeder. Otherwise as in Figure A 3.

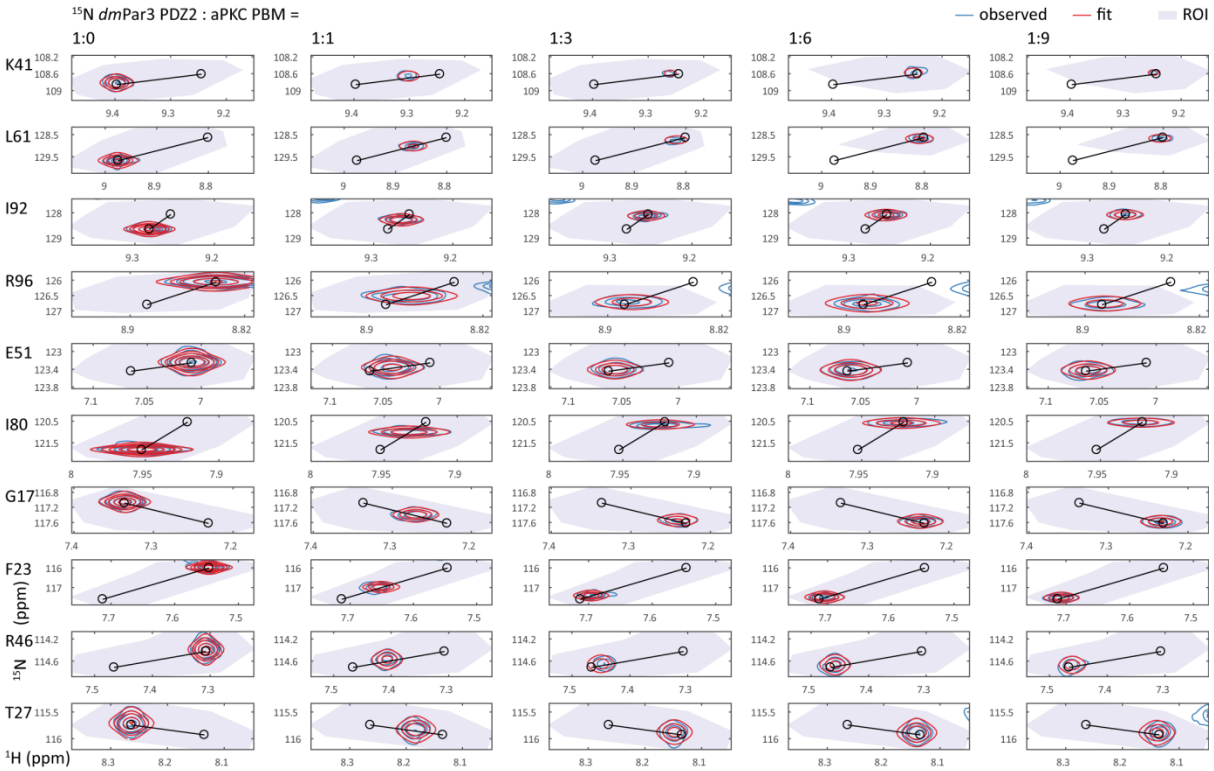

Figure A 10: Line shape fitting analysis of the *dm*Par3 PDZ2 interaction with the aPKC PBM. NMR titration data was provided by Benjamin Schroeder. Otherwise as in Figure A 3.

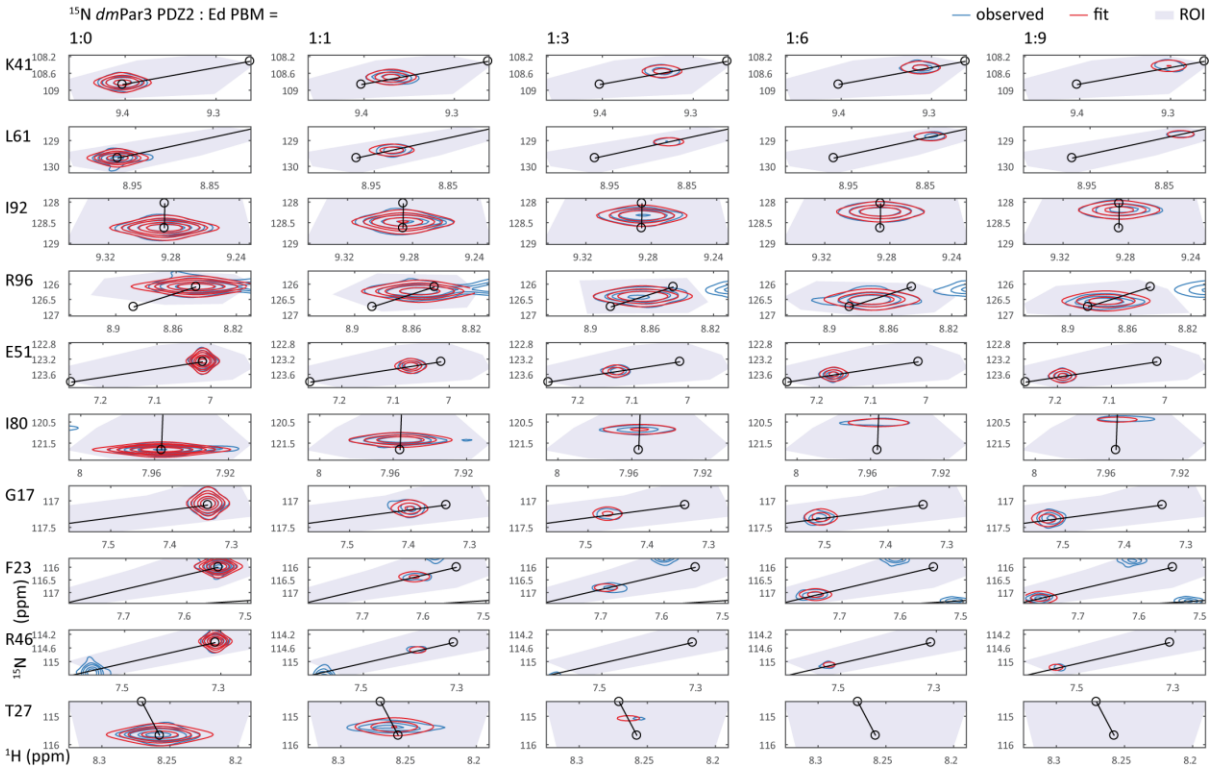

Figure A 11: Line shape fitting analysis of the *dm*Par3 PDZ2 interaction with the Ed PBM. NMR titration data was provided by Susanne Bruekner. Otherwise as in Figure A 3.

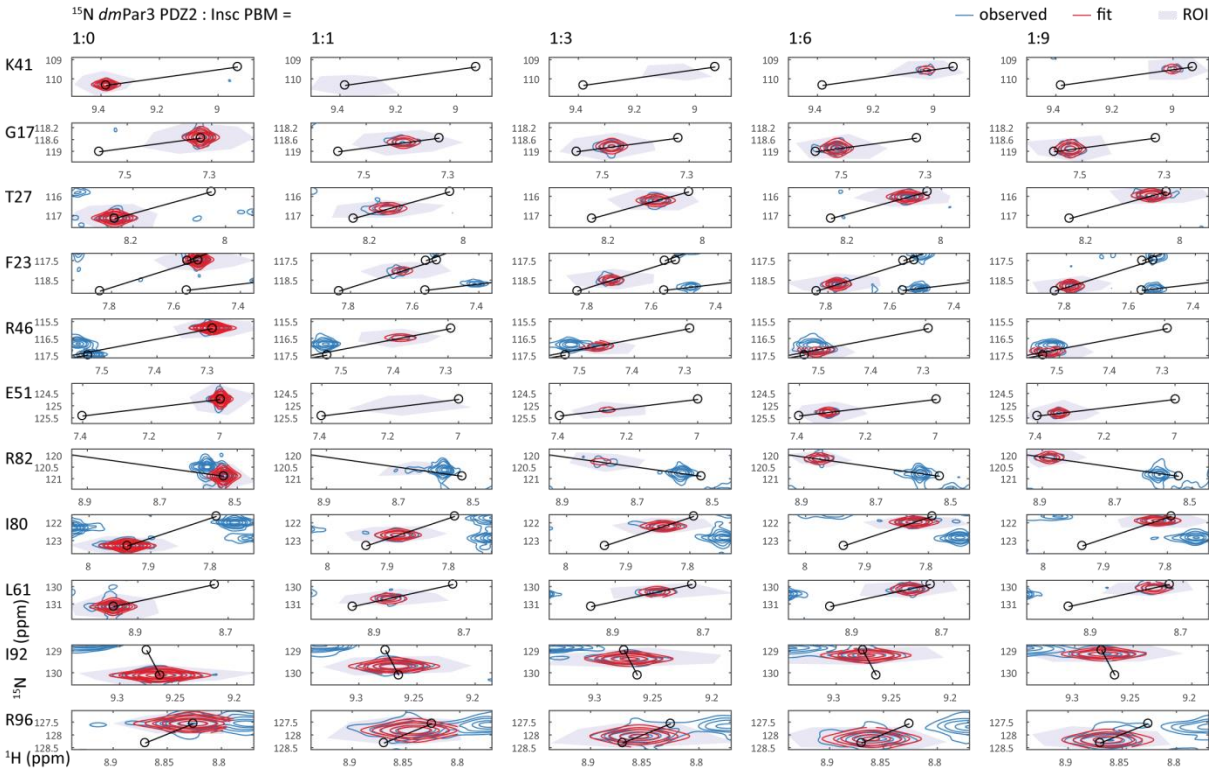

Figure A 12: Line shape fitting analysis of the *dm*Par3 PDZ2 interaction with the Insc PBM. NMR titration data was provided by Susanne Bruekner. Otherwise as in Figure A 3.

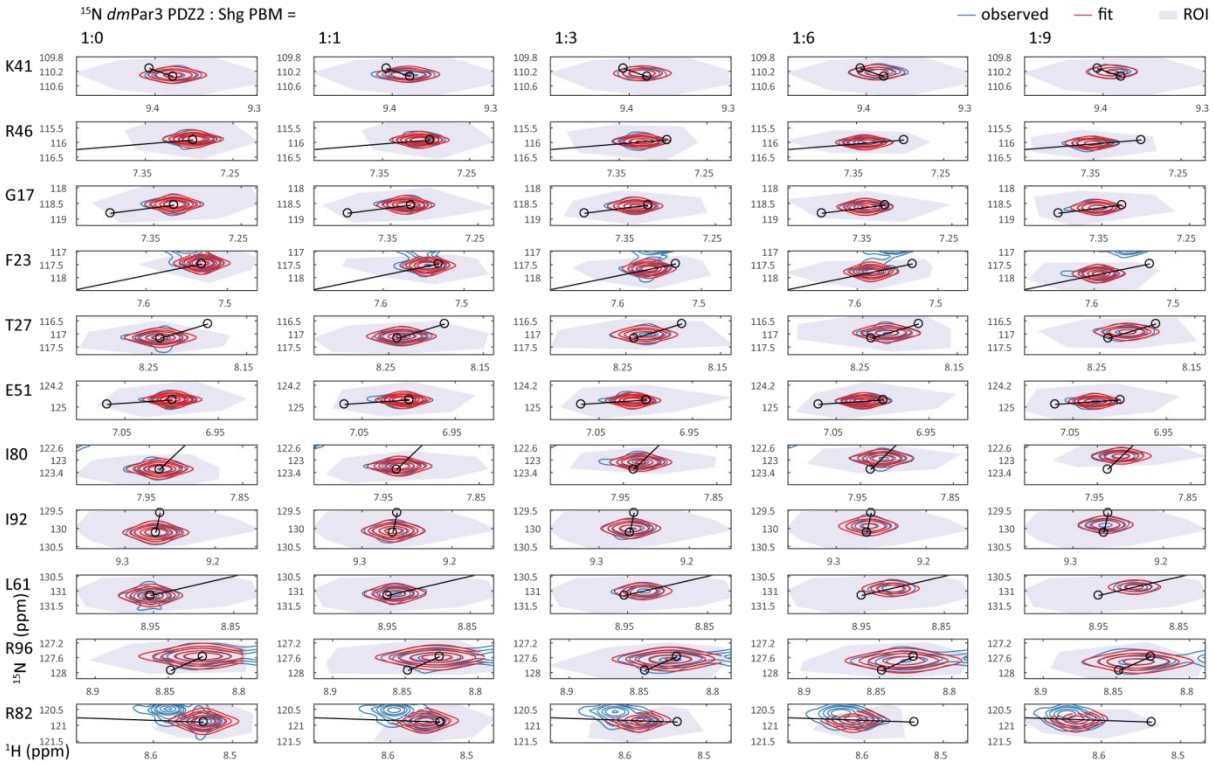

Figure A 13: Line shape fitting analysis of the *dm*Par3 PDZ2 interaction with the Shg PBM. NMR titration data was provided by Susanne Bruekner. Otherwise as in Figure A 3.

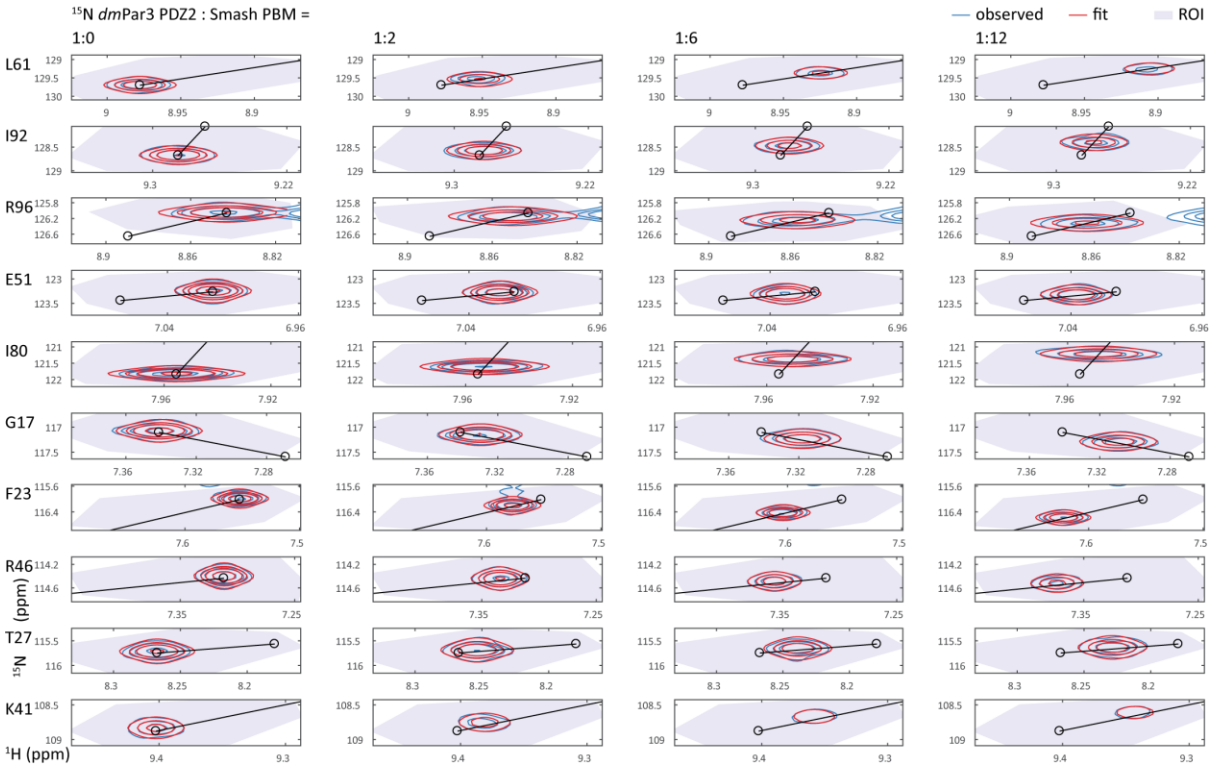

Figure A 14: Line shape fitting analysis of the *dm*Par3 PDZ2 interaction with the Smash PBM. Otherwise as in Figure A 3.

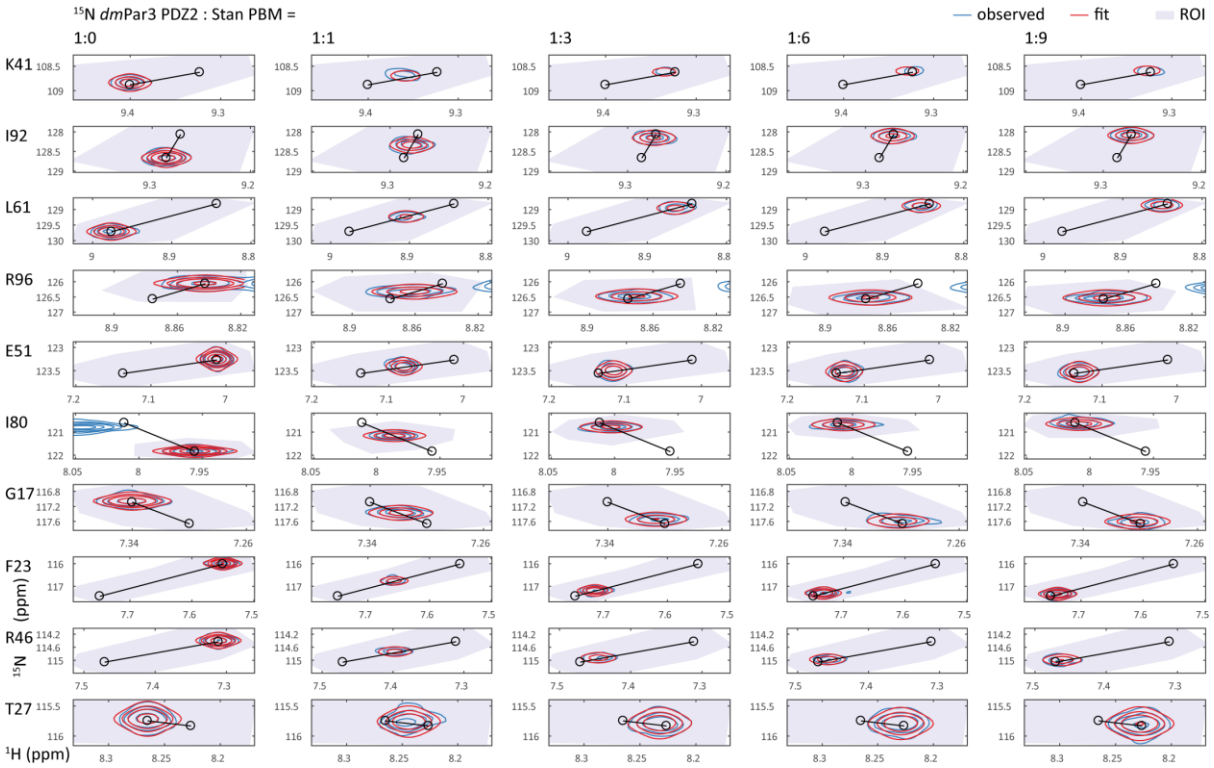

Figure A 15: Line shape fitting analysis of the *dm*Par3 PDZ2 interaction with the Stan PBM. Otherwise as in Figure A 3.

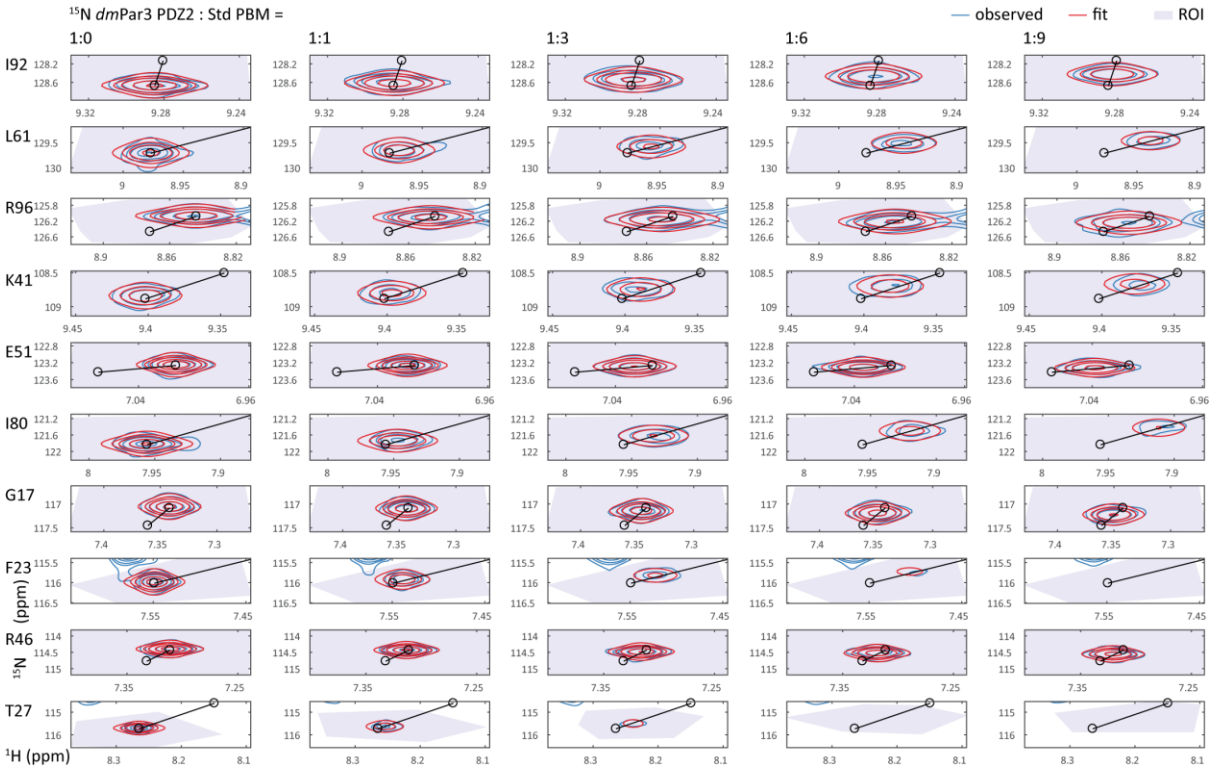

Figure A 16: Line shape fitting analysis of the *dm*Par3 PDZ2 interaction with the Std PBM. Otherwise as in Figure A 3.

8.3.4 Line shape fitting analysis of *dm*Par3 PDZ3 Δβ2-3loop

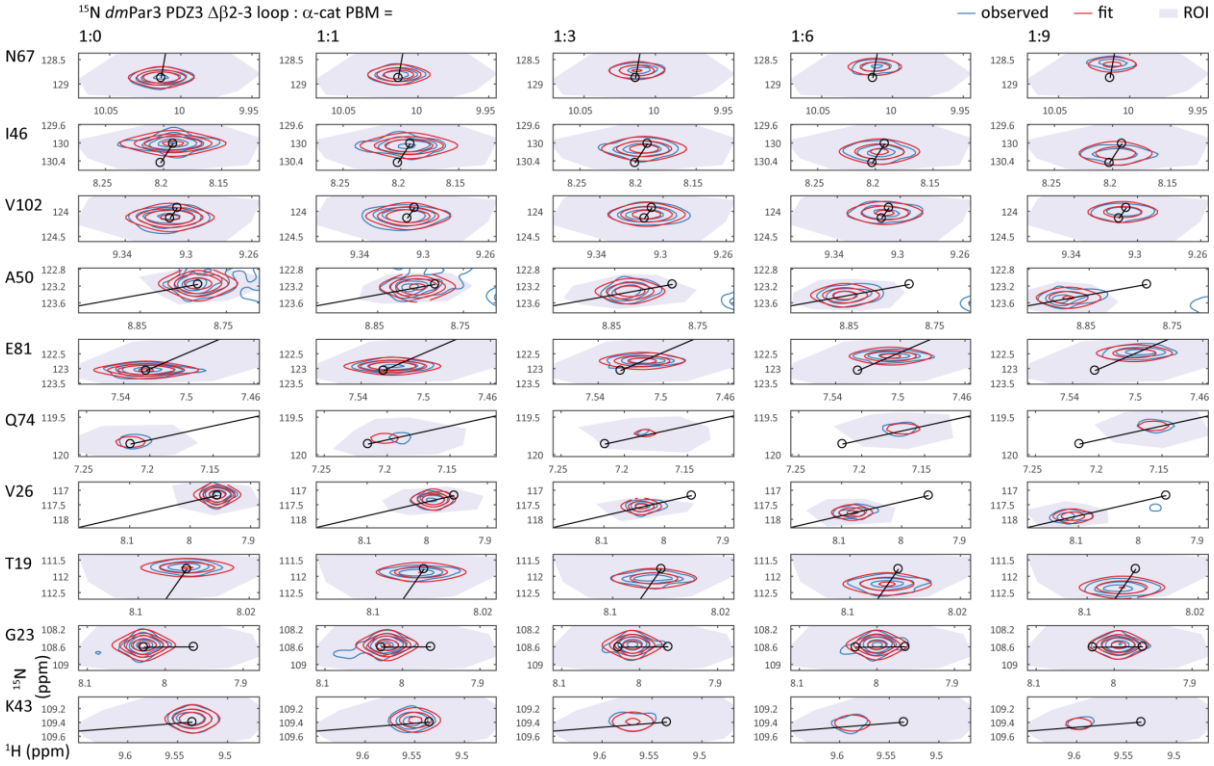

Figure A 17: Line shape fitting analysis of the *dm*Par3 PDZ3 Δβ2-3loop interaction with the α-cat PBM. NMR titration data was provided by Benjamin Schroeder. Otherwise as in Figure A 3.

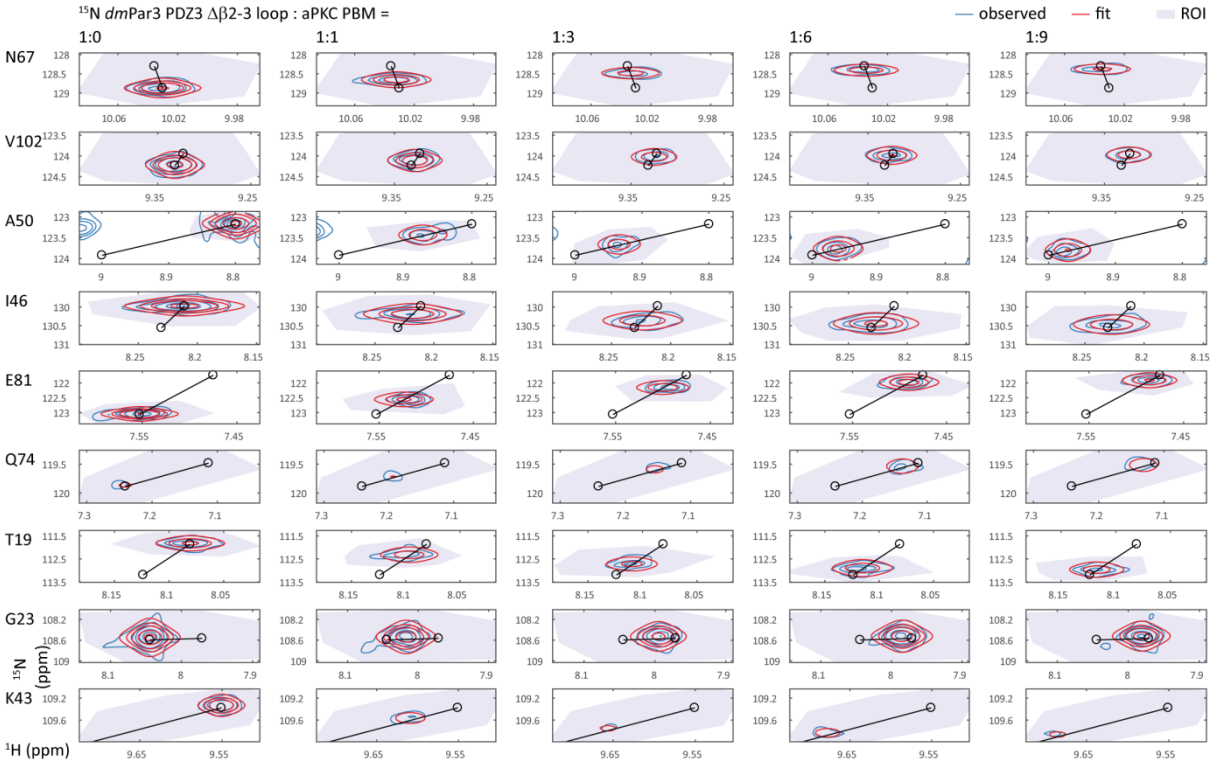

Figure A 18: Line shape fitting analysis of the *dm*Par3 PDZ3 Δβ2-3 loop interaction with the aPKC PBM. NMR titration data was provided by Benjamin Schroeder. Otherwise as in Figure A 3.

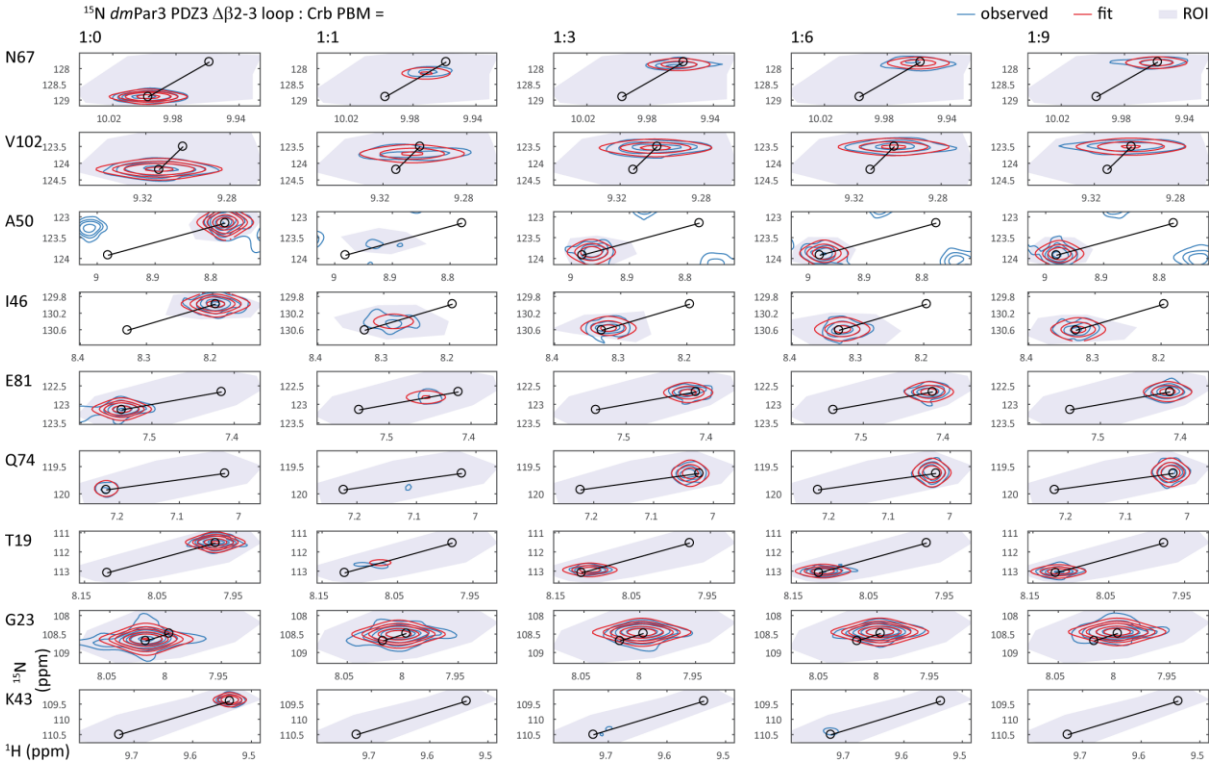

Figure A 19: Line shape fitting analysis of the *dm*Par3 PDZ3 Δβ2-3 loop interaction with the Crb PBM. Otherwise as in Figure A 3.

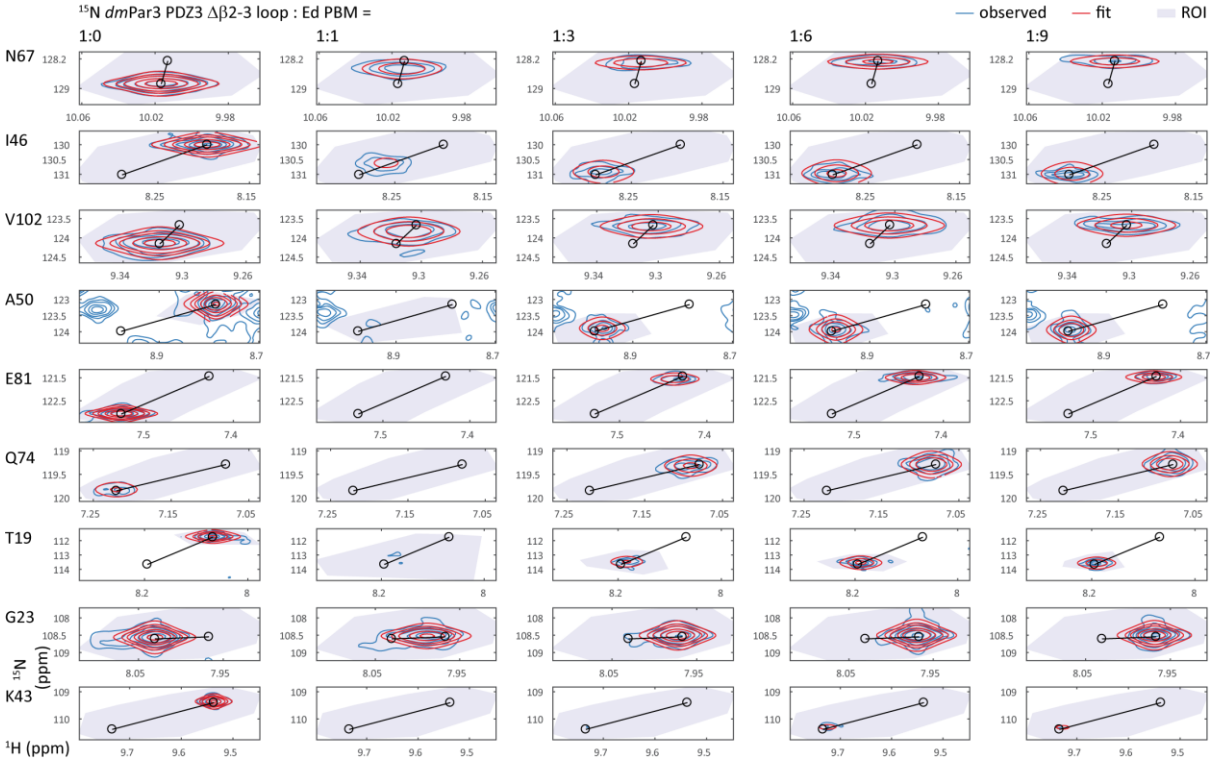

Figure A 20: Line shape fitting analysis of the *dm*Par3 PDZ3 Δβ2-3 loop interaction with the Ed PBM. NMR titration data was provided by Susanne Bruekner. Otherwise as in Figure A 3.

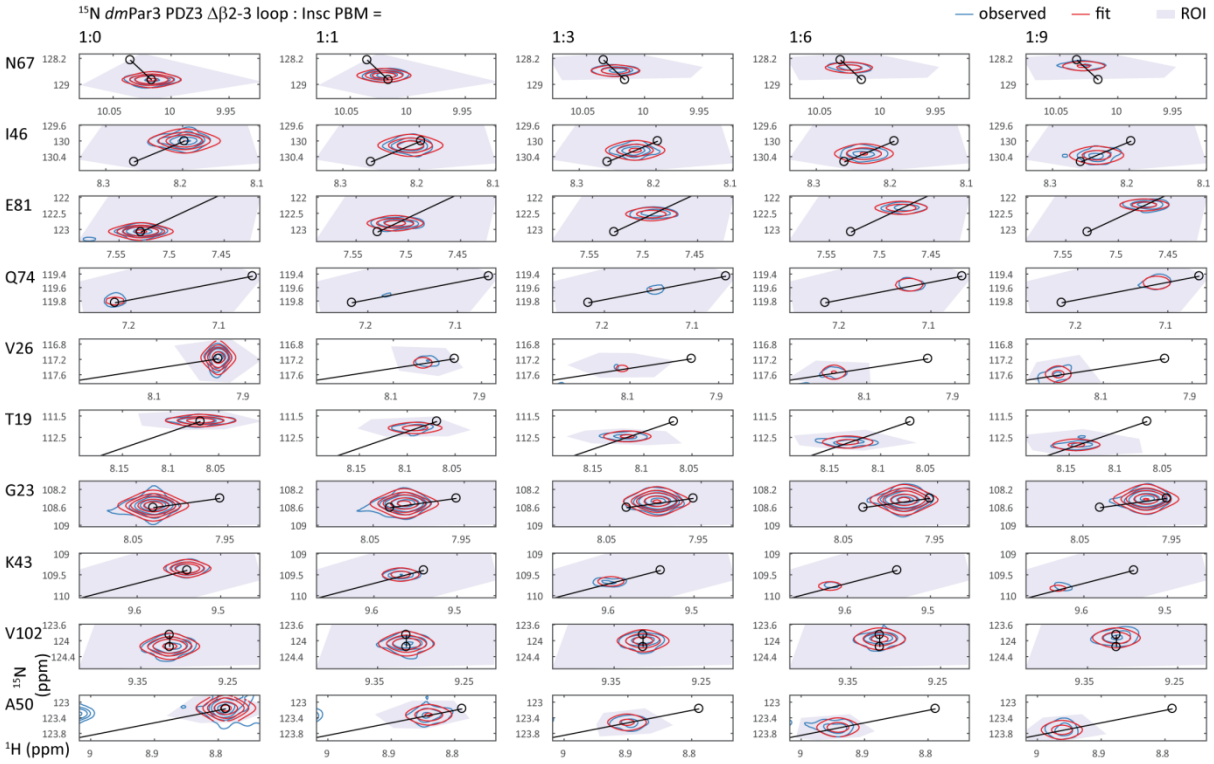

Figure A 21: Line shape fitting analysis of the *dm*Par3 PDZ3 Δβ2-3loop interaction with the Insc PBM. NMR titration data was provided by Susanne Bruekner. Otherwise as in Figure A 3.

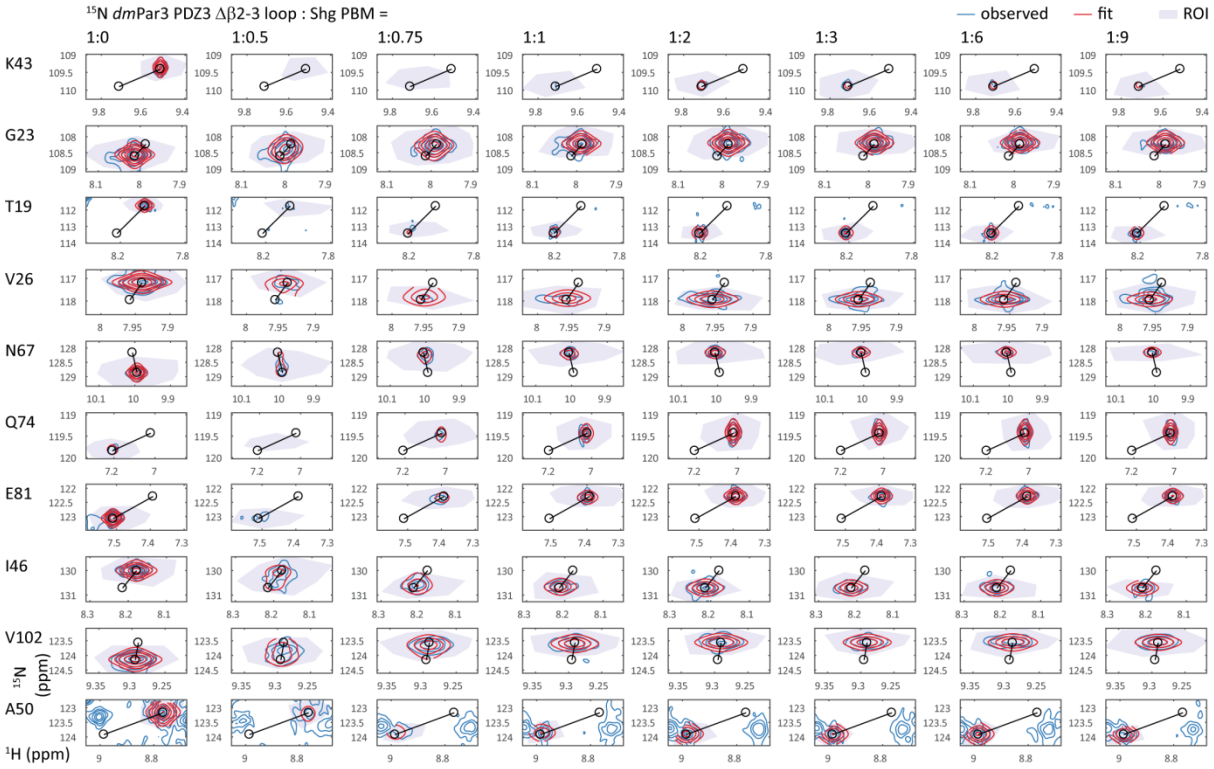

Figure A 22: Line shape fitting analysis of the *dm*Par3 PDZ3 Δβ2-3loop interaction with the Shg PBM. NMR titration data was provided by by Susanne Bruekner, Silke Wiesner Mira C. Schütz-Stoffregen and myself. Otherwise as in Figure A 3.

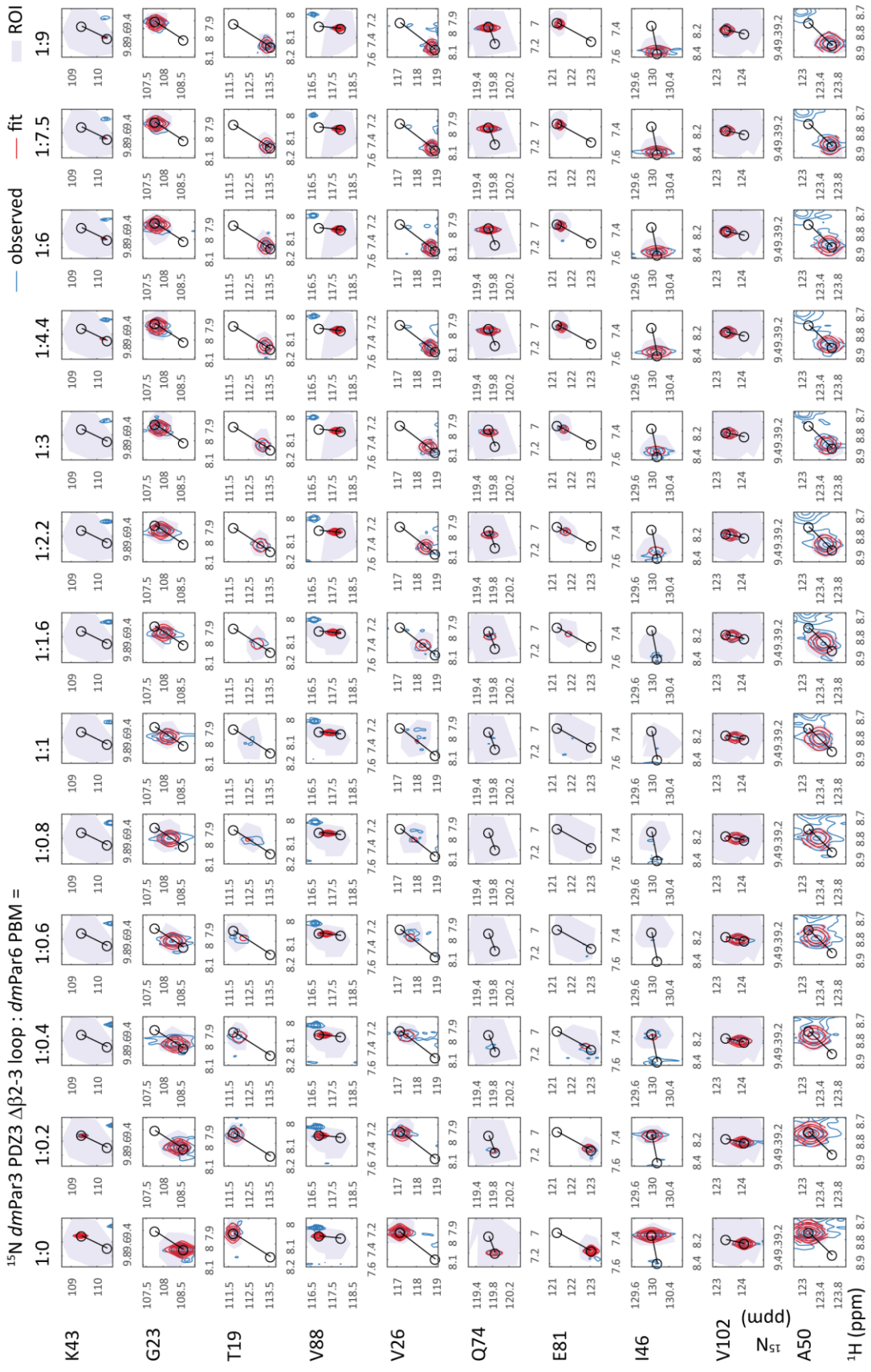

Figure A 23: Line shape fitting analysis of the *dm*Par3 PDZ3 Δβ2-3loop interaction with the *dm*Par6 PBM. NMR titration data was provided by Susanne Bruekner, Silke Wiesner, Mira C. Schütz-Stoffregen and myself. Otherwise as in Figure A 3.

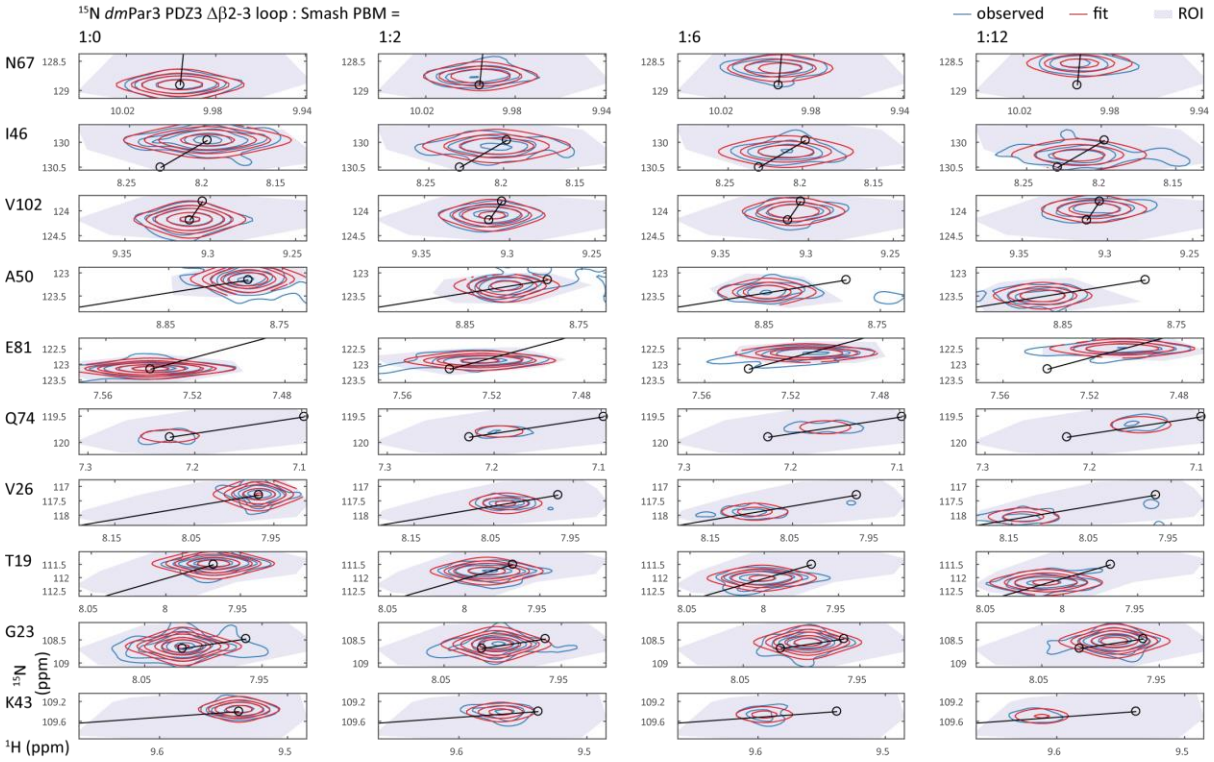

Figure A 24: Line shape fitting analysis of the *dm*Par3 PDZ3 Δβ2-3loop interaction with the Smash PBM. Otherwise as in Figure A 3.

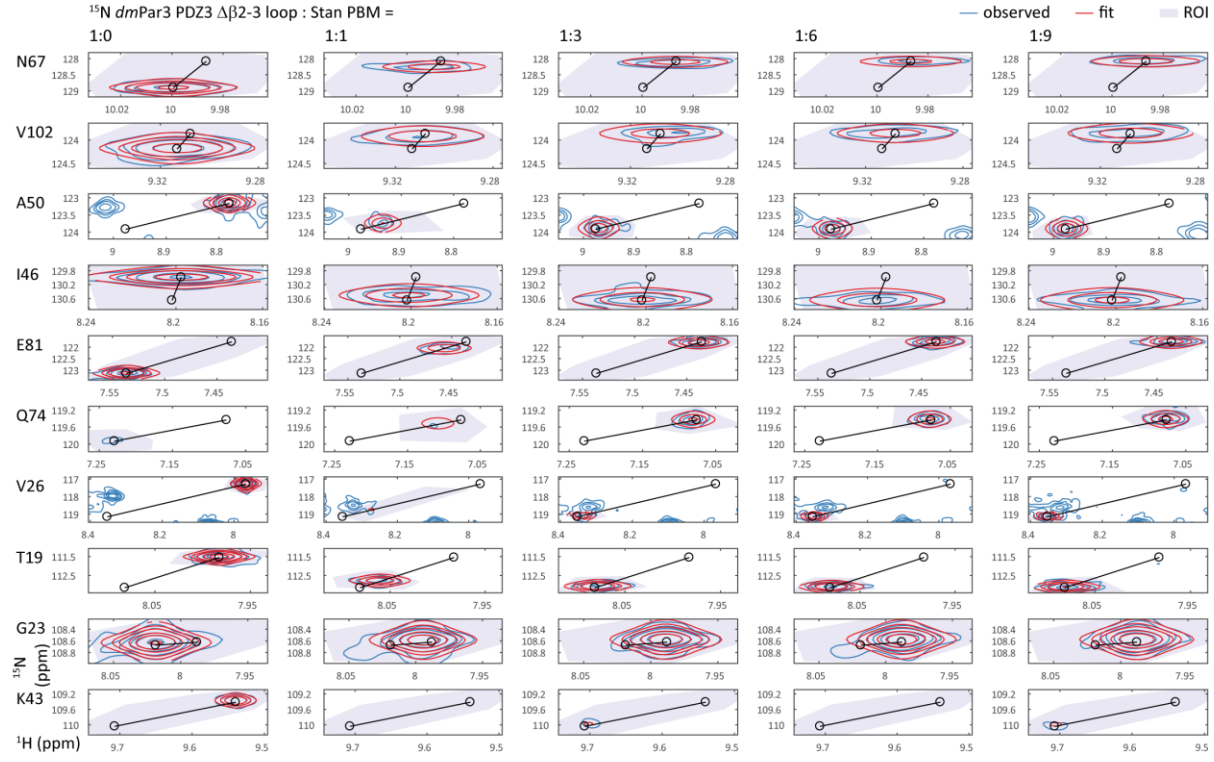

Figure A 25: Line shape fitting analysis of the *dm*Par3 PDZ3 Δβ2-3loop interaction with the Stan PBM. Otherwise as in Figure A 3.

8.3.5 Line shape fitting analysis of *dm*Par3 linkerΔII-PDZ3 Δβ2-3loop

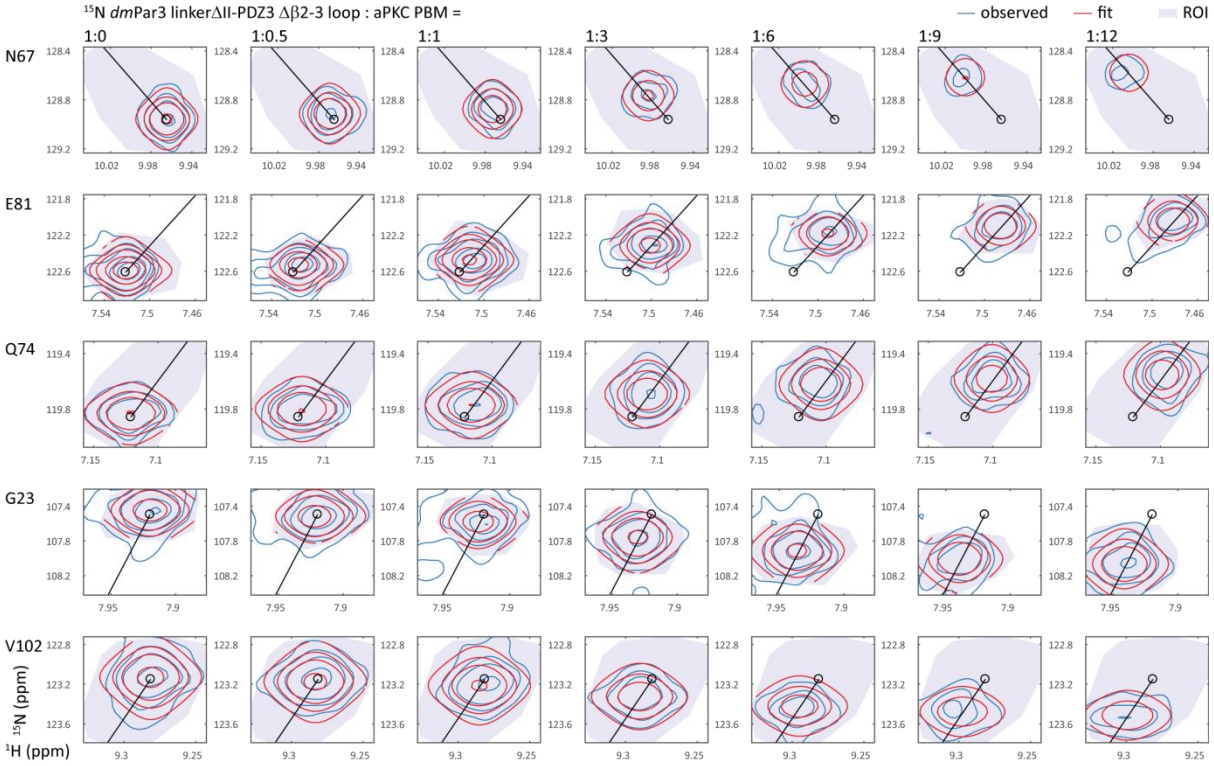

Figure A 26: Line shape fitting analysis of the *dm*Par3 linkerΔII-PDZ3 Δβ2-3loop interaction with the aPKC PBM. Otherwise as in Figure A 3.

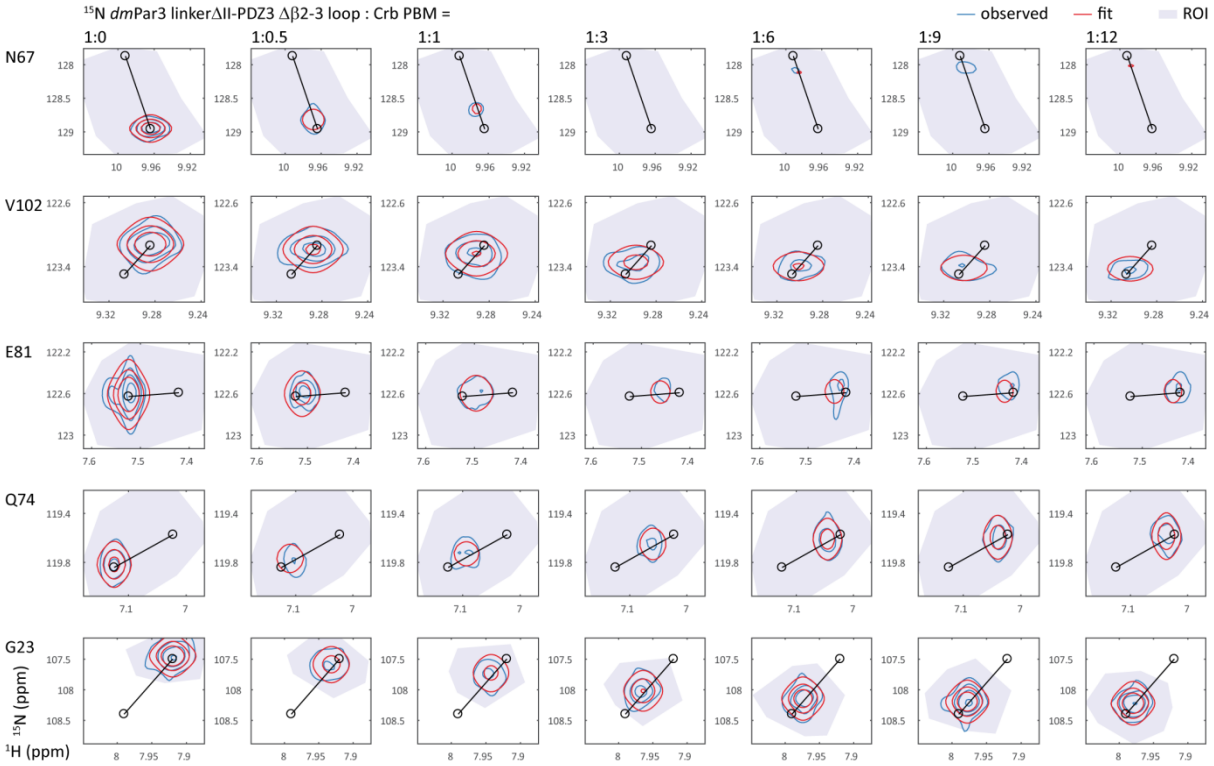

Figure A 27: Line shape fitting analysis of the *dm*Par3 linkerΔII-PDZ3 Δβ2-3 loop interaction with the Crb PBM. Otherwise as in Figure A 3.

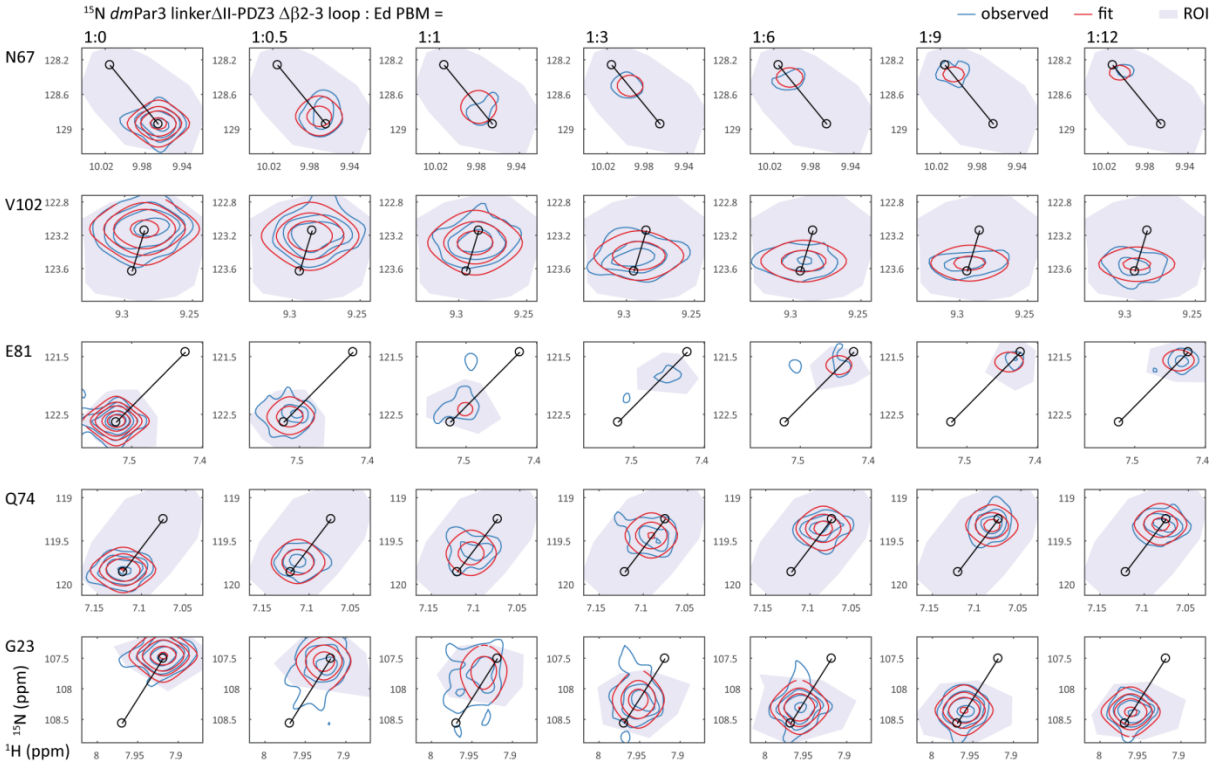

Figure A 28: Line shape fitting analysis of the *dm*Par3 linkerΔII-PDZ3 Δβ2-3loop interaction with the Ed PBM. Otherwise as in Figure A 3.

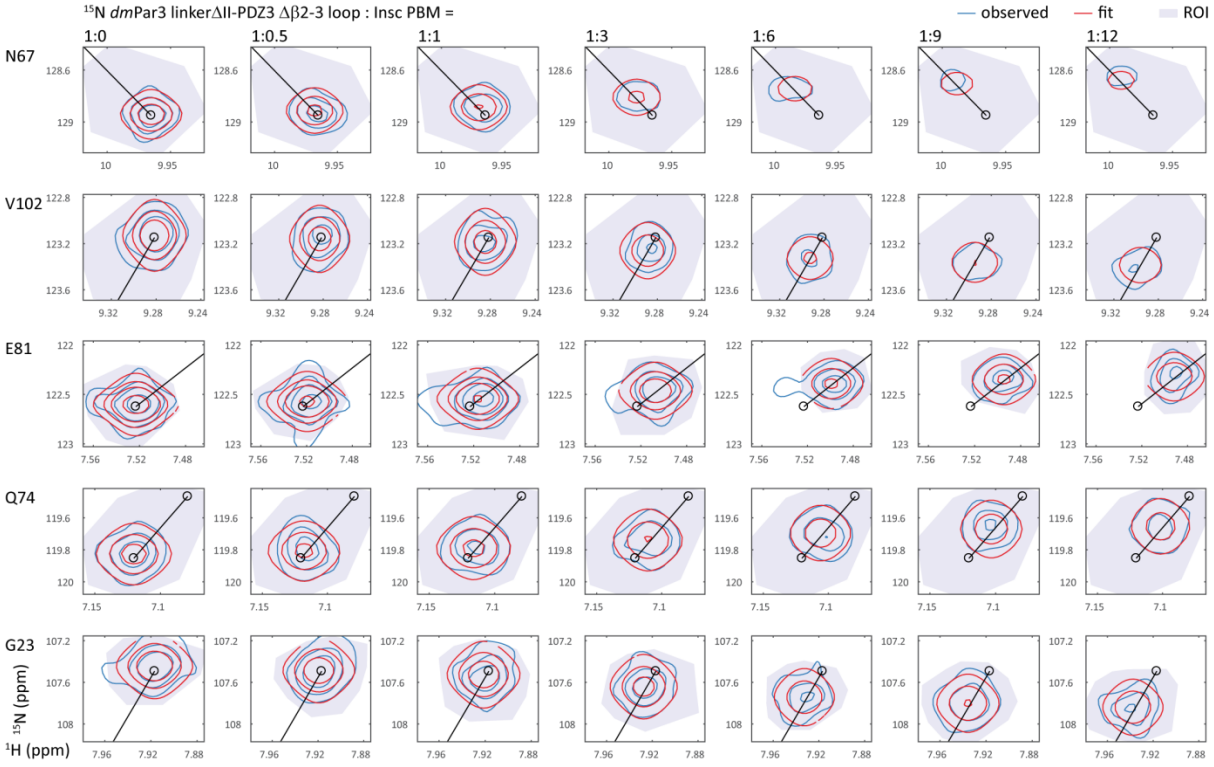

Figure A 29: Line shape fitting analysis of the *dm*Par3 linkerΔII-PDZ3 Δβ2-3loop interaction with the Insc PBM. Otherwise as in Figure A 3.

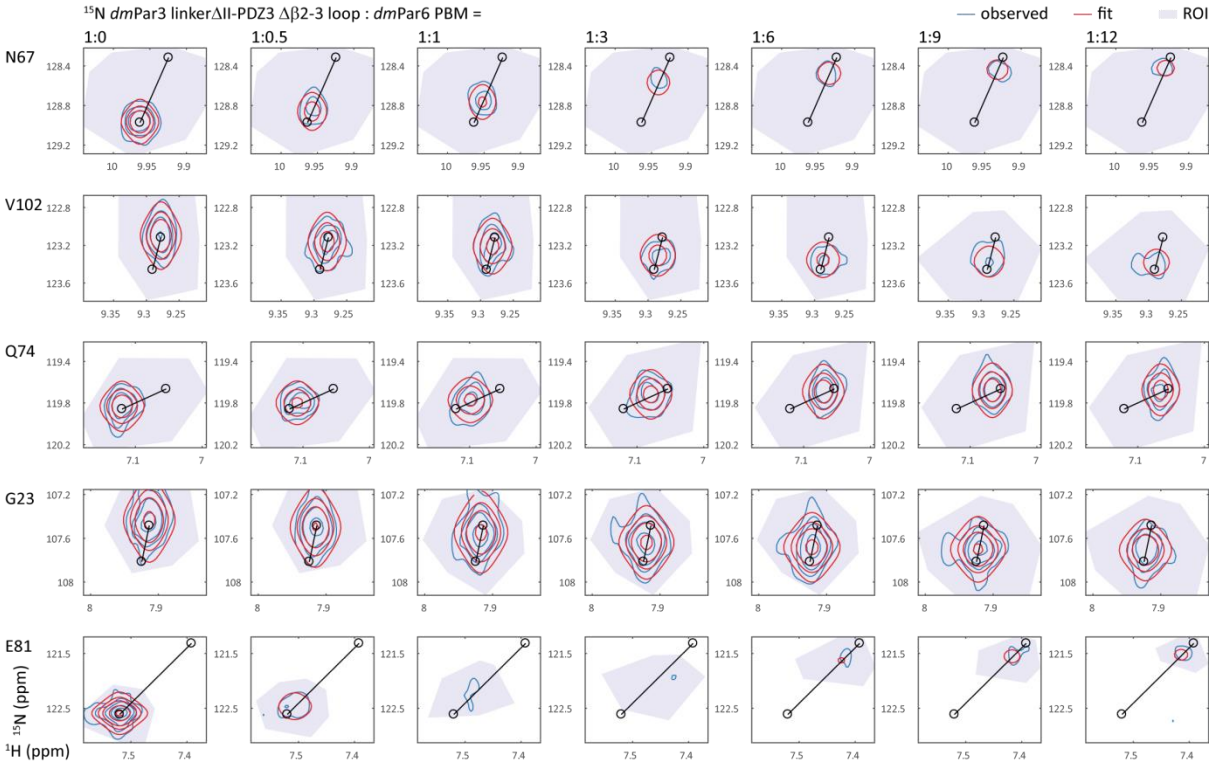

Figure A 30: Line shape fitting analysis of the *dm*Par3 linkerΔII-PDZ3 Δβ2-3loop interaction with the *dm*Par6 PBM. Otherwise as in Figure A 3.

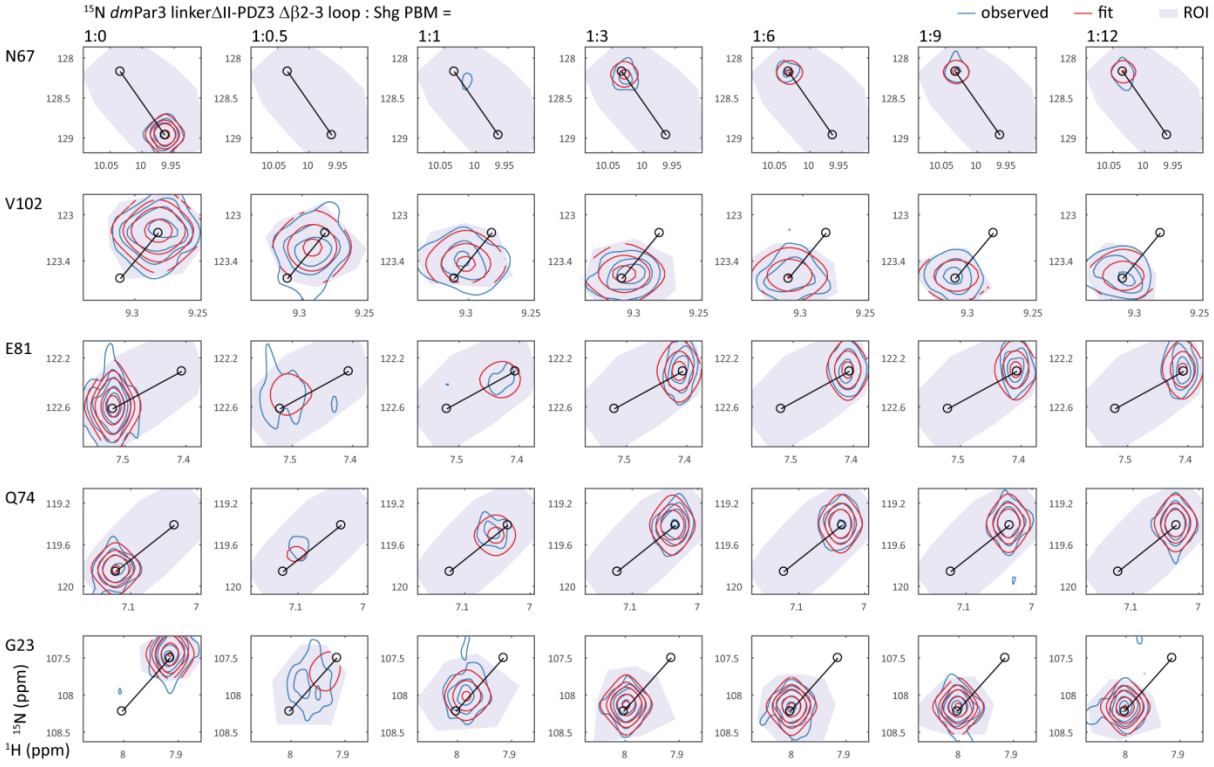

Figure A 31: Line shape fitting analysis of the *dm*Par3 linkerΔII-PDZ3 Δβ2-3loop interaction with the Shg PBM. Otherwise as in Figure A 3.

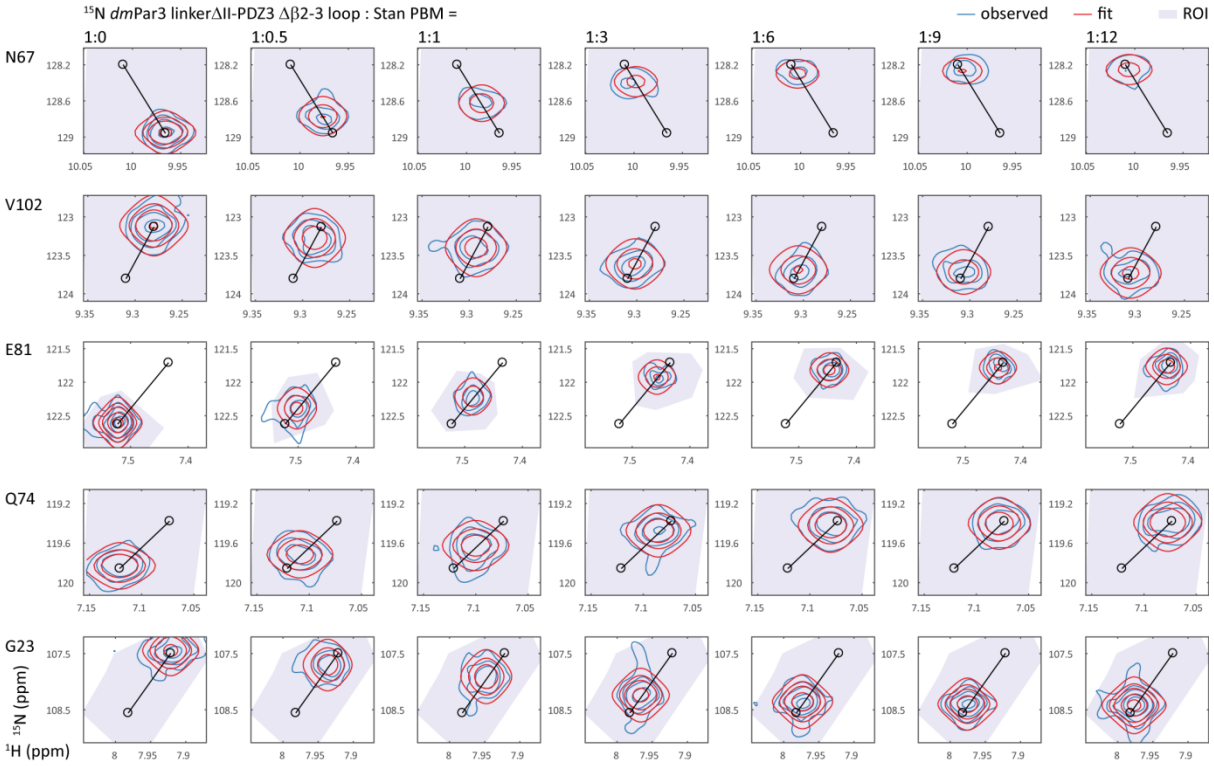

Figure A 32: Line shape fitting analysis of the *dm*Par3 linkerΔII-PDZ3 Δβ2-3loop interaction with the Stan PBM. Otherwise as in Figure A 3.

9. Acknowledgments

First, I have to thank my family and especially my wife for all the support during the past four years. I know it wasn't always easy, but look, that peak IS shifting! Desirée, you are the one ;-) :-* I want to thank my parents and my parents-in-law for taking care of the kids and all the delicious food. Finally, I must thank the smallest biggest greatest persons on earth: Karl, Johanna and Franz for all the nonsense, dirty cloths and sand in my shoes – you are amazing!

I would like to thank Silke for her support during the last seven years in her lab. For the opportunities and support she offered me as well as for the advice she gave. It was a great pleasure to discuss science with you and to exchange baby stories with you.

I would like to thank Thilo Stehle for being my university supervisor. I enjoyed your lectures not only during my PhD but also during my diploma studies. Your enthusiasm about biomolecular structures was very inspiring. I would like to thank the members of my examination committee, Dirk Schwarzer and Frank Böckler, for agreeing to be part of this committee. I would like to thank Wolfram Antonin for being a member of my TAC. Furthermore, I would like my whole TAC (Thilo, Silke, Wolfram) for the fruitful discussions and insights from our meetings.

I would like to thank Mira for teaching me how to purify proteins and all the other very important stuff about the AKTA and the lab. In line with that I would like to thank all past and present Wiesner lab members for the amazing atmosphere, in particular Samira, Magnus, Natalia, Carsten, Philip (spin that chair), Susi, Benni, Andreas, Paulin and Christine. I would like to thank Amrita and Christine for their work with the human Par proteins in cell culture. I would like to thank Andreas Wodarz and Michael Krahn as well as the members of their laboratories for the interesting collaborations.

I would like to thank Remco Sprangers and the members of his lab for the shared group meetings and the thoughtful comments. Furthermore, I would like to thank Ancilla for the advice and assistance during my crystallization efforts.

I would like to thank Sarah Danes for the organization of the IMPRS events and all the support she offered.

I would like to thank Vincent Truffault for all the advice on NMR spectroscopy in theory and praxis as well as for all the discussions on the latest topics. Additionally, I would like to thank Christian Feldhaus for the support offered by the light microscope facility.

I would like to thank the coffee crowd (Daniela, Magnus, Phillip, Carsten, Jan) for most delightful conversation topics. I would like to thank the HotS stack for flaming, raging, farming, trolling and memeing. I would like to thank Tobi for even more delightful coffee conversations. And wine conversations. And Mexicana conversations.

Finally, for the horde! For Azeroth! For Sine P! For Drykorn! For Ciquala! For Molaf!

10. References

Adams, P.D. et al., 2010. PHENIX: a comprehensive Python-based system for macromolecular structure solution. *Acta crystallographica. Section D, Biological crystallography*, 66(Pt 2), pp.213–21.

Amacher, J.F. et al., 2014. Stereochemical preferences modulate affinity and selectivity among five PDZ domains that bind CFTR: comparative structural and sequence analyses. *Structure (London, England : 1993)*, 22(1), pp.82–93.

Aue, W.P., Bartholdi, E. & Ernst, R.R., 1976. Two-dimensional spectroscopy. Application to nuclear magnetic resonance. *The Journal of Chemical Physics*, 64(5), pp.2229–2246.

Bain, A.D., 2003. Chemical exchange in NMR. *Progress in Nuclear Magnetic Resonance Spectroscopy*, 43(3–4), pp.63–103.

Banani, S.F. et al., 2017. Biomolecular condensates: organizers of cellular biochemistry. *Nature reviews. Molecular cell biology*, 18(5), pp.285–298.

Barrett, P.J. et al., 2013. The quiet renaissance of protein nuclear magnetic resonance. *Biochemistry*, 52(8), pp.1303–20.

Beati, H. et al., 2018. The adherens junction-associated LIM domain protein Smallish regulates epithelial morphogenesis. *The Journal of cell biology*, 217(3), pp.1079–1095.

Bieri, M. et al., 2011. Macromolecular NMR spectroscopy for the non-spectroscopist: beyond macromolecular solution structure determination. *The FEBS journal*, 278(5), pp.704–15.

Blow, D., 2010. *Outline of Crystallography for Biologists* 1st cor., OXFORD University Press.

Brückner, S., 2014. *PDZ Domains of Bazooka: Small Domains, but Big Players in Cell Polarity - A Structural Study*,

Brünger, A., 1992. Free R value: a novel statistical quantity for assessing the accuracy of crystal structures. *Nature*, 355(6359), pp.472–5.

Bulgakova, N.A. et al., 2013. Dynamic microtubules produce an asymmetric E-cadherin-Bazooka complex to maintain segment boundaries. *The Journal of cell biology*, 201(6), pp.887–901.

Bystrov, V.F., 1976. Spin—spin coupling and the conformational states of peptide systems. *Progress in Nuclear Magnetic Resonance Spectroscopy*, 10(2), pp.41–82.

Chen, J.R. et al., 2008. Predicting PDZ domain-peptide interactions from primary sequences. *Nature biotechnology*, 26(9), pp.1041–5.

Chen, Y. et al., 2012. Genome-wide functional annotation of dual-specificity protein- and lipid-binding modules that regulate protein interactions. *Molecular cell*, 46(2), pp.226–37.

Culurgioni, S. & Mapelli, M., 2013. Going vertical: functional role and working principles of the protein Inscuteable in asymmetric cell divisions. *Cellular and molecular life sciences : CMLS*.

Czeslik, C., Seemann, H. & Winter, R., 2007. *Basiswissen Physikalische Chemie* 2nd rev. C. Elschenbroich, F. Hensel, & H. Hopf, eds., B.G. Teubner Verlag/ GWV Fachverlag.

Davey, N.E., Cyert, M.S. & Moses, A.M., 2015. Short linear motifs - ex nihilo evolution of protein regulation. *Cell communication and signaling : CCS*, 13(1), p.43.

Delaglio, F. et al., 1995. NMRPipe: a multidimensional spectral processing system based on UNIX pipes. *Journal of biomolecular NMR*, 6(3), pp.277–93.

Dickinson, D.J. et al., 2017. A Single-Cell Biochemistry Approach Reveals PAR Complex Dynamics during Cell Polarization. *Developmental cell*, 42(4), p.416–434.e11.

Drummond, M.L. & Prehoda, K.E., 2016. Molecular Control of Atypical Protein Kinase C: Tipping the Balance between Self-Renewal and Differentiation. *Journal of molecular biology*, 428(7), pp.1455–64.

Ebnet, K. et al., 2001. The cell polarity protein ASIP/PAR-3 directly associates with junctional adhesion molecule (JAM). *The EMBO journal*, 20(14), pp.3738–48.

Ebnet, K. et al., 2003. The junctional adhesion molecule (JAM) family members JAM-2 and JAM-3 associate with the cell polarity protein PAR-3: a possible role for JAMs in endothelial cell polarity. *Journal of cell science*, 116(Pt 19), pp.3879–91.

Edgar, R.C., 2004. MUSCLE: multiple sequence alignment with high accuracy and high throughput. *Nucleic acids research*, 32(5), pp.1792–7.

Elsum, I. et al., 2012. The Scribble-Dlg-Lgl polarity module in development and cancer: from flies to man. *Essays in biochemistry*, 53, pp.141–68.

Emsley, P. et al., 2010. Features and development of Coot. *Acta crystallographica. Section D, Biological crystallography*, 66(Pt 4), pp.486–501.

van den Ent, F. & Löwe, J., 2006. RF cloning: a restriction-free method for inserting target genes into plasmids. *Journal of biochemical and biophysical methods*, 67(1), pp.67–74.

Ernst, A. et al., 2014. A structural portrait of the PDZ domain family. *Journal of molecular biology*, 426(21), pp.3509–19.

Ernst, R.R., Bodenhausen, G. & Wokaum, A., 1987. *Principles of Nuclear Magnetic Resonance in One and Two Dimensions*, Clarendon Press, Oxford.

Evans, P., 2006. Scaling and assessment of data quality. *Acta crystallographica. Section D, Biological crystallography*, 62(Pt 1), pp.72–82.

Fanning, A.S. et al., 2007. Domain swapping within PDZ2 is responsible for dimerization of ZO proteins. *The Journal of biological chemistry*, 282(52), pp.37710–6.

Feng, W. et al., 2008. Par-3-mediated junctional localization of the lipid phosphatase PTEN is required for cell polarity establishment. *The Journal of biological chemistry*, 283(34), pp.23440–

9.

Fievet, B.T. et al., 2013. Systematic genetic interaction screens uncover cell polarity regulators and functional redundancy. *Nature cell biology*, 15(1), pp.103–12.

Fletcher, G.C. et al., 2012. Positive feedback and mutual antagonism combine to polarize Crumbs in the Drosophila follicle cell epithelium. *Current biology : CB*, 22(12), pp.1116–22.

Fujiwara, Y. et al., 2015. Crystal structure of afadin PDZ domain-nectin-3 complex shows the structural plasticity of the ligand-binding site. *Protein science : a publication of the Protein Society*, 24(3), pp.376–85.

Gallardo, R. et al., 2010. Structural diversity of PDZ-lipid interactions. *Chembiochem : a European journal of chemical biology*, 11(4), pp.456–67.

Gao, L., Macara, I.G. & Joberty, G., 2002. Multiple splice variants of Par3 and of a novel related gene, Par3L, produce proteins with different binding properties. *Gene*, 294(1–2), pp.99–107.

Garman, E.F., 2010. Radiation damage in macromolecular crystallography: what is it and why should we care? *Acta crystallographica. Section D, Biological crystallography*, 66(Pt 4), pp.339–51.

Garrard, S.M. et al., 2003. Structure of Cdc42 in a complex with the GTPase-binding domain of the cell polarity protein, Par6. *EMBO Journal*, 22(5), pp.1125–1133.

Goehring, N.W. et al., 2011. PAR proteins diffuse freely across the anterior-posterior boundary in polarized C. elegans embryos. *The Journal of cell biology*, 193(3), pp.583–94.

Goldstein, B. & Macara, I.G., 2007. The PAR proteins: fundamental players in animal cell polarization. *Developmental cell*, 13(5), pp.609–22.

Green, M.R. & Sambrook, J., 2012. *Molecular Cloning A LABORATORY MANUAL*, COLD SPRING HARBOR LABORATORY PRESS.

Harris, T.J.C., 2017. Protein clustering for cell polarity: Par-3 as a paradigm. *F1000Research*, 6(0), p.1620.

Harris, T.J.C. & Tepass, U., 2010. Adherens junctions: from molecules to morphogenesis. *Nature reviews. Molecular cell biology*, 11(7), pp.502–14.

Hayes, M.B., Hagenmaier, H. & Cohen, J.S., 1975. Nuclear magnetic resonance titration curves of histidine ring protons. Human metmyoglobin and the effects of azide on human, horse, and sperm whale metmyoglobins. *The Journal of biological chemistry*, 250(18), pp.7461–72.

Henrique, D. & Schweisguth, F., 2003. Cell polarity: the ups and downs of the Par6/aPKC complex. *Current opinion in genetics & development*, 13(4), pp.341–50.

Hirano, Y. et al., 2005. Structure of a cell polarity regulator, a complex between atypical PKC and Par6 PB1 domains. *The Journal of biological chemistry*, 280(10), pp.9653–61.

Hui, S., Xing, X. & Bader, G.D., 2013. Predicting PDZ domain mediated protein interactions from

structure. *BMC bioinformatics*, 14, p.27.

Iden, S. et al., 2006. A distinct PAR complex associates physically with VE-cadherin in vertebrate endothelial cells. *EMBO reports*, 7(12), pp.1239–46.

Im, Y.J. et al., 2003. Crystal structure of the Shank PDZ-ligand complex reveals a class I PDZ interaction and a novel PDZ-PDZ dimerization. *The Journal of biological chemistry*, 278(48), pp.48099–104.

Itoh, M. et al., 2001. Junctional adhesion molecule (JAM) binds to PAR-3: a possible mechanism for the recruitment of PAR-3 to tight junctions. *The Journal of cell biology*, 154(3), pp.491–7.

Ivanova, M.E. et al., 2015. Structures of the human Pals1 PDZ domain with and without ligand suggest gated access of Crb to the PDZ peptide-binding groove. *Acta crystallographica. Section D, Biological crystallography*, 71(Pt 3), pp.555–64.

Ivarsson, Y. et al., 2014. Large-scale interaction profiling of PDZ domains through proteomic peptide-phage display using human and viral phage peptidomes. *Proceedings of the National Academy of Sciences of the United States of America*, 111(7), pp.2542–7.

Ivarsson, Y., 2012. Plasticity of PDZ domains in ligand recognition and signaling. *FEBS letters*, 586(17), pp.2638–47.

Jensen, D.R. et al., 2010. Rapid, robotic, small-scale protein production for NMR screening and structure determination. *Protein science : a publication of the Protein Society*, 19(3), pp.570–8.

Joberty, G. et al., 2000. The cell-polarity protein Par6 links Par3 and atypical protein kinase C to Cdc42. *Nature cell biology*, 2(8), pp.531–9.

Johnson, B.A. & Blevins, R.A., 1994. NMR View: A computer program for the visualization and analysis of NMR data. *Journal of biomolecular NMR*, 4(5), pp.603–14.

Kabsch, W., 2010. XDS. *Acta crystallographica. Section D, Biological crystallography*, 66(Pt 2), pp.125–32.

Keeler, J., 2010. *Understanding NMR Spectroscopy*, John Wiley & Sons.

Kemphues, K.J. et al., 1988. Identification of genes required for cytoplasmic localization in early C. elegans embryos. *Cell*, 52(3), pp.311–20.

Kempkens, O. et al., 2006. Computer modelling in combination with in vitro studies reveals similar binding affinities of Drosophila Crumbs for the PDZ domains of Stardust and DmPar-6. *European journal of cell biology*, 85(8), pp.753–67.

Krahn, M.P., Bückers, J., et al., 2010. Formation of a Bazooka-Stardust complex is essential for plasma membrane polarity in epithelia. *The Journal of cell biology*, 190(5), pp.751–60.

Krahn, M.P., Klopfenstein, D.R., et al., 2010. Membrane targeting of Bazooka/PAR-3 is mediated by direct binding to phosphoinositide lipids. *Current biology : CB*, 20(7), pp.636–42.

Kuchinke, U., Grawe, F. & Knust, E., 1998. Control of spindle orientation in Drosophila by the Par-3-related PDZ-domain protein Bazooka. *Current biology : CB*, 8(25), pp.1357–65.

Kundu, K. & Backofen, R., 2014. Cluster based prediction of PDZ-peptide interactions. *BMC genomics*, 15 Suppl 1(Suppl 1), p.S5.

Kwan, A.H. et al., 2011. Macromolecular NMR spectroscopy for the non-spectroscopist. *The FEBS journal*, 278(5), pp.687–703.

Lang, C.F. & Munro, E., 2017. The PAR proteins: from molecular circuits to dynamic self-stabilizing cell polarity. *Development (Cambridge, England)*, 144(19), pp.3405–3416.

Larkin, M.A. et al., 2007. Clustal W and Clustal X version 2.0. *Bioinformatics (Oxford, England)*, 23(21), pp.2947–8.

Latorre, I.J. et al., 2005. Viral oncoprotein-induced mislocalization of select PDZ proteins disrupts tight junctions and causes polarity defects in epithelial cells. *Journal of cell science*, 118(Pt 18), pp.4283–93.

Lee, H.-J. & Zheng, J.J., 2010. PDZ domains and their binding partners: structure, specificity, and modification. *Cell communication and signaling : CCS*, 8, p.8.

Lee, W., Tonelli, M. & Markley, J.L., 2015. NMRFAM-SPARKY: enhanced software for biomolecular NMR spectroscopy. *Bioinformatics (Oxford, England)*, 31(8), pp.1325–7.

Lemmers, C. et al., 2004. CRB3 binds directly to Par6 and regulates the morphogenesis of the tight junctions in mammalian epithelial cells. *Molecular biology of the cell*, 15(3), pp.1324–33.

Li, J. et al., 2010. Binding to PKC-3, but not to PAR-3 or to a conventional PDZ domain ligand, is required for PAR-6 function in C. elegans. *Developmental biology*, 340(1), pp.88–98.

Li, Y. et al., 2014. Structure of Crumbs tail in complex with the PALS1 PDZ-SH3-GK tandem reveals a highly specific assembly mechanism for the apical Crumbs complex. *Proceedings of the National Academy of Sciences of the United States of America*, 111(49), pp.17444–9.

Lin, D. et al., 2000. A mammalian PAR-3-PAR-6 complex implicated in Cdc42/Rac1 and aPKC signalling and cell polarity. *Nature cell biology*, 2(8), pp.540–7.

Lin, D. et al., 1999. The carboxyl terminus of B class ephrins constitutes a PDZ domain binding motif. *Journal of Biological Chemistry*, 274(6), pp.3726–3733.

Lu, M.S. & Johnston, C.A., 2013. Molecular pathways regulating mitotic spindle orientation in animal cells. *Development (Cambridge, England)*, 140(9), pp.1843–56.

Luck, K., Charbonnier, S. & Travé, G., 2012. The emerging contribution of sequence context to the specificity of protein interactions mediated by PDZ domains. *FEBS Letters*, 586(17), pp.2648–2661.

Luck, K. & Travé, G., 2011. Phage display can select over-hydrophobic sequences that may impair

prediction of natural domain-peptide interactions. *Bioinformatics (Oxford, England)*, 27(7), pp.899–902.

Macara, I.G., 2004. Parsing the polarity code. *Nature reviews. Molecular cell biology*, 5(March), pp.220–231.

McCaffrey, L.M. & Macara, I.G., 2009. Widely conserved signaling pathways in the establishment of cell polarity. *Cold Spring Harbor perspectives in biology*, 1(2), p.a001370.

McCoy, A.J. et al., 2007. Phaser crystallographic software. *Journal of applied crystallography*, 40(Pt 4), pp.658–674.

McKinley, R.F.A., Yu, C.G. & Harris, T.J.C., 2012. Assembly of Bazooka polarity landmarks through a multifaceted membrane-association mechanism. *Journal of cell science*, 125(Pt 5), pp.1177–90.

Merino-Gracia, J. et al., 2016. Insights into the C-terminal Peptide Binding Specificity of the PDZ Domain of Neuronal Nitric-oxide Synthase: CHARACTERIZATION OF THE INTERACTION WITH THE TIGHT JUNCTION PROTEIN CLAUDIN-3. *The Journal of biological chemistry*, 291(22), pp.11581–95.

Mildvan, A.S. & Cohn, M., 1963. MAGNETIC RESONANCE STUDIES OF THE INTERACTION OF THE MANGANOUS ION WITH BOVINE SERUM ALBUMIN. *Biochemistry*, 2(5), pp.910–9.

Morris, G.A. & Freeman, R., 1979. Enhancement of nuclear magnetic resonance signals by polarization transfer. *Journal of the American Chemical Society*, 101(3), pp.760–762.

Müller, H.A. & Wieschaus, E., 1996. armadillo, bazooka, and stardust are critical for early stages in formation of the zonula adherens and maintenance of the polarized blastoderm epithelium in Drosophila. *The Journal of cell biology*, 134(1), pp.149–63.

Muthuswamy, S.K. & Xue, B., 2012. Cell polarity as a regulator of cancer cell behavior plasticity. *Annual review of cell and developmental biology*, 28, pp.599–625.

Nagai-Tamai, Y. et al., 2002. Regulated protein-protein interaction between aPKC and PAR-3 plays an essential role in the polarization of epithelial cells. *Genes to cells : devoted to molecular & cellular mechanisms*, 7(11), pp.1161–71.

Nakayama, M. et al., 2013. Spatial regulation of VEGF receptor endocytosis in angiogenesis. *Nature cell biology*, 15(3), pp.249–60.

Nelson, W.J., 2003. Adaptation of core mechanisms to generate cell polarity. *Nature*, 422(6933), pp.766–74.

Noda, Y. et al., 2001. Human homologues of the Caenorhabditis elegans cell polarity protein PAR6 as an adaptor that links the small GTPases Rac and Cdc42 to atypical protein kinase C. *Genes to cells : devoted to molecular & cellular mechanisms*, 6(2), pp.107–19.

Odell, A.F. et al., 2012. A VE-cadherin-PAR3-α-catenin complex regulates the Golgi localization and

activity of cytosolic phospholipase A(2)α in endothelial cells. *Molecular biology of the cell*, 23(9), pp.1783–96.

Ooshio, T. et al., 2007. Cooperative roles of Par-3 and afadin in the formation of adherens and tight junctions. *Journal of cell science*, 120(Pt 14), pp.2352–65.

Patel, D.J. et al., 1975. Assignment of the imidazole ring nitrogen protons of histidine 48 in the proton NMR spectrum of ribonuclease A in water solution. *Biochimica et biophysica acta*, 400(2), pp.275–82.

Pawson, T. & Nash, P., 2003. Assembly of cell regulatory systems through protein interaction domains. *Science (New York, N.Y.)*, 300(5618), pp.445–52.

Penkert, R.R., DiVittorio, H.M. & Prehoda, K.E., 2004. Internal recognition through PDZ domain plasticity in the Par-6-Pals1 complex. *Nature structural & molecular biology*, 11(11), pp.1122–7.

Pervushin, K., 2000. Impact of transverse relaxation optimized spectroscopy (TROSY) on NMR as a technique in structural biology. *Quarterly reviews of biophysics*, 33(2), pp.161–97.

Peterson, F.C. et al., 2004. Cdc42 regulates the Par-6 PDZ domain through an allosteric CRIB-PDZ transition. *Molecular cell*, 13(5), pp.665–76.

Rattle, H., 1995. *An NMR Primer for Life Scientists* 1st ed., Partnership Press.

Recouvreux, P. & Lenne, P.-F., 2016. Molecular clustering in the cell: from weak interactions to optimized functional architectures. *Current opinion in cell biology*, 38, pp.18–23.

Renschler, F.A. et al., 2018. Structural basis for the interaction between the cell polarity proteins Par3 and Par6. *Science signaling*, 11(517), p.eaam9899.

Renschler, F.A., 2013. *Structural Studies of PAR-3 Recruitment to Cell-Cell Junctions in Vertebrate and Invertebrate Epithelia.*,

Rodriguez, J. et al., 2017. aPKC Cycles between Functionally Distinct PAR Protein Assemblies to Drive Cell Polarity. *Developmental cell*, 42(4), p.400–415.e9.

Rossmann, M.G. & Blow, D.M., 1961. The refinement of structures partially determined by the isomorphous replacement method. *Acta Crystallographica*, 14(6), pp.641–647.

Rupp, B., 2009. *Biomolecular Crystallography: Principles, Practice, and Application to Structural Biology* 1st ed., New York: Garland Science.

Salomon, P., 2012. *NMR Studies of a PDZ-PDZ Domain Interaction between the Polarity Proteins Par-3 and Par-6*,

Sanger, F., Nicklen, S. & Coulson, A.R., 1977. DNA sequencing with chain-terminating inhibitors. *Proceedings of the National Academy of Sciences of the United States of America*, 74(12), pp.5463–7.

Schober, M., Schaefer, M. & Knoblich, J. a, 1999. Bazooka recruits Inscuteable to orient asymmetric

cell divisions in Drosophila neuroblasts. *Nature*, 402(6761), pp.548–51.

Schroeder, B., 2014. *Structural Studies of Cell Polarity Proteins.*

Sen, A., Sun, R. & Krahn, M.P., 2015. Localization and Function of Pals1-associated Tight Junction Protein in Drosophila Is Regulated by Two Distinct Apical Complexes. *The Journal of biological chemistry*, 290(21), pp.13224–33.

Shahab, J. et al., 2015. Bazooka/PAR3 is dispensable for polarity in Drosophila follicular epithelial cells. *Biology open*, 4(4), pp.528–41.

Sievers, F. et al., 2011. Fast, scalable generation of high-quality protein multiple sequence alignments using Clustal Omega. *Molecular systems biology*, 7(539), p.539.

Soriano, E. V. et al., 2016. aPKC Inhibition by Par3 CR3 Flanking Regions Controls Substrate Access and Underpins Apical-Junctional Polarization. *Developmental cell*, 38(4), pp.384–98.

Stein, N., 2008. CHAINSAW : a program for mutating pdb files used as templates in molecular replacement. *Journal of Applied Crystallography*, 41(3), pp.641–643.

von Stein, W. et al., 2005. Direct association of Bazooka/PAR-3 with the lipid phosphatase PTEN reveals a link between the PAR/aPKC complex and phosphoinositide signaling. *Development (Cambridge, England)*, 132(7), pp.1675–86.

Stiffler, M.A. et al., 2007. PDZ domain binding selectivity is optimized across the mouse proteome. *Science (New York, N.Y.)*, 317(5836), pp.364–9.

Suzuki, A. et al., 2001. Atypical protein kinase C is involved in the evolutionarily conserved par protein complex and plays a critical role in establishing epithelia-specific junctional structures. *The Journal of cell biology*, 152(6), pp.1183–96.

Suzuki, A., Akimoto, K. & Ohno, S., 2003. Protein kinase C lambda/iota (PKClambda/iota): a PKC isotype essential for the development of multicellular organisms. *Journal of biochemistry*, 133(1), pp.9–16.

Tabuse, Y. et al., 1998. Atypical protein kinase C cooperates with PAR-3 to establish embryonic polarity in Caenorhabditis elegans. *Development (Cambridge, England)*, 125(18), pp.3607–14.

Takekuni, K. et al., 2003. Direct binding of cell polarity protein PAR-3 to cell-cell adhesion molecule nectin at neuroepithelial cells of developing mouse. *The Journal of biological chemistry*, 278(8), pp.5497–500.

Tanentzapf, G. & Tepass, U., 2003. Interactions between the crumbs, lethal giant larvae and bazooka pathways in epithelial polarization. *Nature cell biology*, 5(1), pp.46–52.

Tepass, U., 2012. The apical polarity protein network in Drosophila epithelial cells: regulation of polarity, junctions, morphogenesis, cell growth, and survival. *Annual review of cell and developmental biology*, 28, pp.655–85.

Terwilliger, T.C. et al., 2008. Iterative-build OMIT maps: map improvement by iterative model building and refinement without model bias. *Acta crystallographica. Section D, Biological crystallography*, 64(Pt 5), pp.515–24.

Tonikian, R. et al., 2008. A specificity map for the PDZ domain family. *PLoS biology*, 6(9), p.e239.

Tsunoda, S. et al., 1997. A multivalent PDZ-domain protein assembles signalling complexes in a G-protein-coupled cascade. *Nature*, 388(6639), pp.243–9.

Tyler, R.C., Peterson, F.C. & Volkman, B.F., 2010. Distal interactions within the par3-VE-cadherin complex. *Biochemistry*, 49(5), pp.951–7.

Vassilev, V. et al., 2017. Catenins Steer Cell Migration via Stabilization of Front-Rear Polarity. *Developmental cell*, 43(4), p.463–479.e5.

van de Ven, F.J.. M., 1995. *Multidimensional NMR in Liquids - Basic Principles and Experimental Methods* 1st ed., John Wiley & Sons.

Wallace, R.B. et al., 1979. Hybridization of synthetic oligodeoxyribonucleotides to phi chi 174 DNA: the effect of single base pair mismatch. *Nucleic acids research*, 6(11), pp.3543–57.

Wang, C. et al., 2012. Substrate recognition mechanism of atypical protein kinase Cs revealed by the structure of PKCι in complex with a substrate peptide from Par-3. *Structure*, 20(5), pp.791–801.

Wang, C.K. et al., 2010. Extensions of PDZ domains as important structural and functional elements. *Protein and Cell*, 1(8), pp.737–751.

Wang, Q., Hurd, T.W. & Margolis, B., 2004. Tight junction protein Par6 interacts with an evolutionarily conserved region in the amino terminus of PALS1/stardust. *The Journal of biological chemistry*, 279(29), pp.30715–21.

Wang, S.-C. et al., 2017. Cortical forces and CDC-42 control clustering of PAR proteins for Caenorhabditis elegans embryonic polarization. *Nature cell biology*, 19(8), pp.988–995.

Wasserscheid, I., Thomas, U. & Knust, E., 2007. Isoform-specific interaction of Flamingo/Starry Night with excess Bazooka affects planar cell polarity in the Drosophila wing. *Developmental dynamics : an official publication of the American Association of Anatomists*, 236(4), pp.1064–71.

Waterhouse, A.M. et al., 2009. Jalview Version 2--a multiple sequence alignment editor and analysis workbench. *Bioinformatics (Oxford, England)*, 25(9), pp.1189–91.

Watts, J.L. et al., 1996. par-6, a gene involved in the establishment of asymmetry in early C. elegans embryos, mediates the asymmetric localization of PAR-3. *Development (Cambridge, England)*, 122(10), pp.3133–40.

Waudby, C.A. et al., 2016. Two-Dimensional NMR Lineshape Analysis. *Scientific reports*, 6(1), p.24826.

Wei, S.-Y. et al., 2005. Echinoid is a component of adherens junctions that cooperates with DE-Cadherin to mediate cell adhesion. *Developmental cell*, 8(4), pp.493–504.

Weik, M. et al., 2000. Specific chemical and structural damage to proteins produced by synchrotron radiation. *Proceedings of the National Academy of Sciences of the United States of America*, 97(2), pp.623–8.

Whitney, D.S. et al., 2013. Allosteric activation of the Par-6 PDZ via a partial unfolding transition. *Journal of the American Chemical Society*, 135(25), pp.9377–83.

Whitney, D.S. et al., 2016. Binding of Crumbs to the Par-6 CRIB-PDZ Module Is Regulated by Cdc42. *Biochemistry*, 55(10), pp.1455–61.

Whitney, D.S., Peterson, F.C. & Volkman, B.F., 2011. A conformational switch in the CRIB-PDZ module of Par-6. *Structure (London, England : 1993)*, 19(11), pp.1711–22.

Wiedemann, U. et al., 2004. Quantification of PDZ domain specificity, prediction of ligand affinity and rational design of super-binding peptides. *Journal of molecular biology*, 343(3), pp.703–18.

Wieschaus, E. & Noell, E., 1986. Specificity of embryonic lethal mutations in Drosophila analyzed in germ line clones. *Roux's archives of developmental biology : the official organ of the EDBO*, 195(1), pp.63–73.

Wiesner, S. & Sprangers, R., 2015. Methyl groups as NMR probes for biomolecular interactions. *Current opinion in structural biology*, 35, pp.60–67.

Wodarz, A. et al., 1999. Bazooka provides an apical cue for Inscuteable localization in Drosophila neuroblasts. *Nature*, 402(6761), pp.544–7.

Wu, H. et al., 2007. PDZ domains of Par-3 as potential phosphoinositide signaling integrators. *Molecular cell*, 28(5), pp.886–98.

Ye, F. & Zhang, M., 2013. Structures and target recognition modes of PDZ domains: recurring themes and emerging pictures. *The Biochemical journal*, 455(1), pp.1–14.

Yu, C.G. et al., 2014. Peptide binding properties of the three PDZ domains of Bazooka (Drosophila Par-3). *PloS one*, 9(1), p.e86412.

Zhang, Y. et al., 2013. Structural insights into the intrinsic self-assembly of par-3 N-terminal domain. *Structure*, 21(6), pp.997–1006.